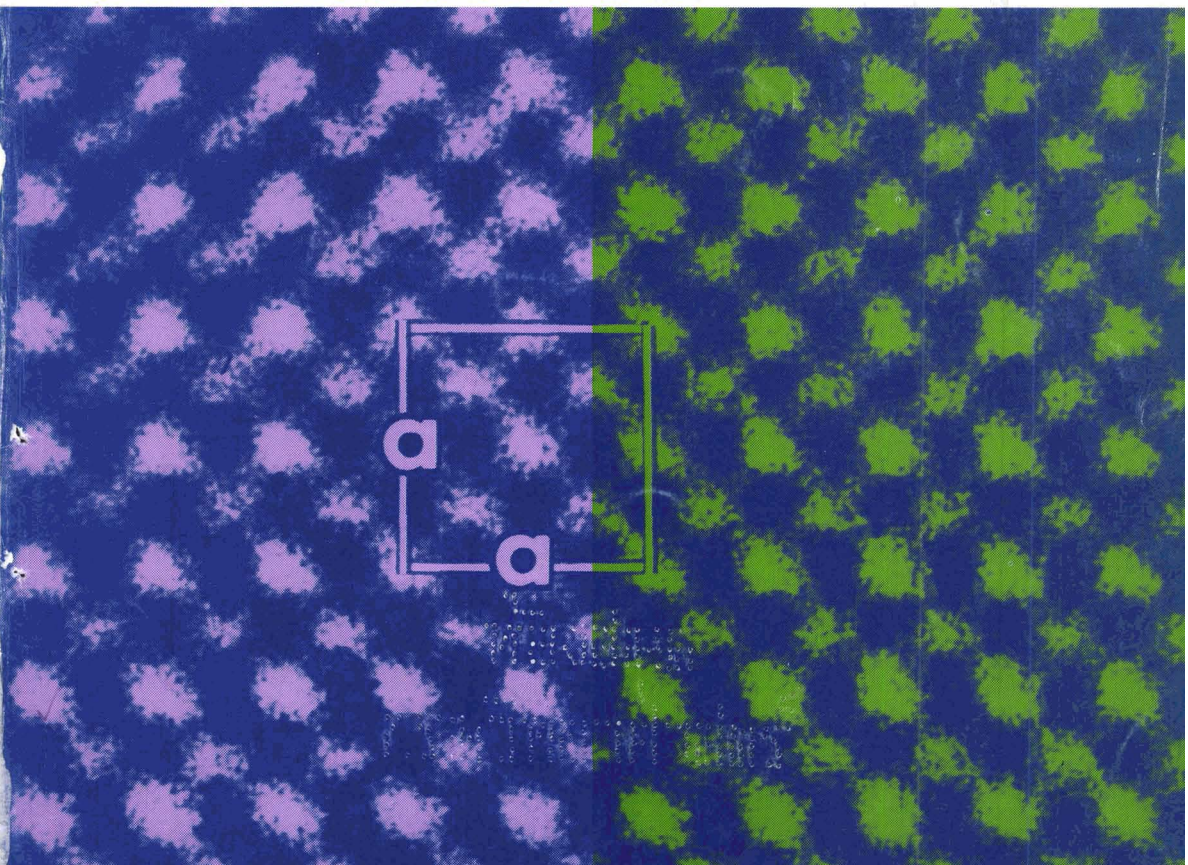


# Journal of the CERAMIC SOCIETY of Japan, *International Edition*

## Vol.99 Nov.1991

■ 22 Papers from Nippon Seramikkusu Kyokai Gakujutsu Ronbunshi, Vol.99 No.11 1991

NIPPON SERAMIKKUSU KYOKAI GAKUJUTSU RONBUNSHI Vol.99 1991



**Editorial Board**

Dr. Teruo Sakaino  
Prof. Emeritus, Tokyo Institute of Technology

Dr. Nobuyasu Mizutani  
Prof., Tokyo Institute of Technology

Dr. Yusuke Moriyoshi  
Director, Nat. Inst. for Res. in Inorganic Materials

Dr. Kitao Takahara  
Prof., Nagoya University

Yukio Endo  
Chairman  
Koyo-sha Co., Ltd.

Dr. Takashi Hanazawa  
Executive Director,  
The Ceramic Society of Japan

Seiji Iwata  
Executive Director,  
Japan Fine Ceramics Association

Keiji Hayashi  
Managing Editor

**Editors**

Managing Editor Keiji Hayashi  
Associate Editor Kohsuke Odani  
Assistant Artists Toshimitsu Irie  
Misao Tomita

Assistant Kiyoe Kojima  
Circulation Youko Matsumoto  
Publisher Keiji Hayashi

**Published Monthly by  
FUJI TECHNOLOGY PRESS LTD.**  
7F Daini Bunsei Bldg.  
11-7, Toranomon 1-chome  
Minato-ku, Tokyo 105, Japan  
Tel:81-3-3508-0051  
Fax:81-3-3592-0648

One year subscription  
Air Mail ¥200,000

Copyright - © 1991 by  
The Ceramic Society of Japan and Fuji  
Technology Press Ltd. All rights reserved.

No part of this publication may be reproduced, stored in a retrieval system, or transmitted, in any form or by any means, electronic, mechanical, photo copying, recording, or otherwise, without the prior written permission of the publishers. The papers, excluding those on information and communications, reviews, etc., were originally received by Nippon Seramikkusu Kyokai Gakujutsu Ronbunshi, and translated for this journal. The responsibility for the translation lies with the publisher.

**Papers:**

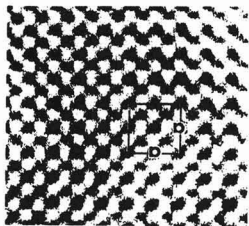
- **Microhardness Anisotropy and the Indentation Load/size Effect in MgO·xAl<sub>2</sub>O<sub>3</sub> Single Crystals** . . . . . 1038  
Hong Li, Hisayuki Suematsu, Takayoshi Iseki and Richard C. Bradt
- **Fabrication and Characterization of CVD-Deposited TiC-SiC Composites** . . . . . 1046  
Chihiro Kawai and Masaya Miyake
- **Preparation of Porous SiO<sub>2</sub>-ZrO<sub>2</sub> Glass from Sol Containing Polyethylene Glycol** . . . . . 1053  
Tetsuo Yazawa, Akiko Miyake and Hiroshi Tanaka
- **Sintering of High Purity ZrSiO<sub>4</sub> Powder** . . . . . 1058  
Toshiyuki Mori, Hiroshi Yamamura, Hidehiko Kobayashi and Takashi Mitamura
- **The Effects of Surface Coating and Orienting of Whiskers on Mechanical Properties of SiC(w)/Si<sub>3</sub>N<sub>4</sub>** . . . . . 1063  
Tatsuji Matsui, Osamu Komura and Masaya Miyake
- **Effect of Coarse Quartz Grains on Mechanical Strength of Porcelain Body** . . . . . 1070  
Kenya Hamano, Yueh-Hong Wu, Zenbe-e Nakagawa and Minoru Hasegawa
- **Quantitative Analysis of Pore Structure on Frost Durability of Inorganic Building Materials** . . . . . 1074  
Masahiko Nakamura, Takaaki Ohnishi and Masataka Kamitani
- **Distribution of Electric Resistance of Dielectric Semiconductor Ceramics** . . . . . 1080  
Miho Uehara and Masakazu Tanahashi
- **High Temperature Oxidation of Si<sub>3</sub>N<sub>4</sub> in O<sub>2</sub>-N<sub>2</sub> Atmospheres** . . . . . 1084  
Makoto Ishikawa, Nobuyuki Takeuchi, Shingo Ishida, Mitsuru Wakamatsu and Koji Watanabe
- **Composition and Microstructure of CVD-C, SiC Coating on SiC Fiber** . . . . . 1090  
J.X. Li, Yohtaro Matsuo and Shiushichi Kimura
- **Mechanical Dampers Using Piezoelectric Composites** . . . . 1096  
Yoji Suzuki, Kenji Uchino, Hironori Gouda, Masao Sumita, R.E. Newnham and A.R. Ramachandran

**Technical reports:**

- **Synthesis of ZSM-5 Zeolite from Silica Stone Occurred in Ioh Island, Kagoshima Prefecture, Japan** . . . . . 1099  
Yoshihiro Hirata, Tadashi Kodama, Kinji Shimada and Yoshimi Ishihara
- **Role of External Additives on the Surface Crystallization of Multi-component Non-Alkali Glasses** . . . . . 1104  
Hideyuki Kuribayashi, Rikuo Ota, Jiro Fukunaga and Tomoyuki Taguchi

**Notes:**

- **Properties of Y<sub>2</sub>O<sub>3</sub>-Al<sub>2</sub>O<sub>3</sub>-SiO<sub>2</sub> Glasses as a Model System of Grain Boundary Phase of Si<sub>3</sub>N<sub>4</sub> Ceramics (Part 2) — Leaching Characteristics —** . . . . . 1110  
Kohei Oda and Tetsuo Yoshio



**Cover:**

This picture shows a high-resolution structure image of zirconia (ZrO<sub>2</sub>) projected along the a-axis of a cubic lattice (a=5.1). As indicated by arrowheads in the micrograph, both zirconium (Zr) and oxygen (O) atom positions appear as strong and weak dark dots, respectively. This is the first electron microscope data in which individual oxygen positions in inorganic compounds can be directly observed as weak dark dots.

The microgram was obtained by the ultra-high-resolution, high-voltage electron microscope (Model: H-1500) developed in 1990 as NIRIM's second high-voltage electron microscope. The device has the world's highest resolution of 1.0Å, which was achieved by employing operating and applicable voltages of 1300kV and 1500kV, respectively. A very low spherical aberration coefficient for the objective (C<sub>s</sub>=1.85mm at 1300kV) was realized by computer-aided design of the electron-magnetic lens system. This new apparatus permits the imaging of not only metal atoms but also light atoms (such as oxygen) in many inorganic materials by means of high-resolution electron microscopy.

- **Thermal Shock Resistance of High Thermal Conductive SiC Ceramics** . . . . . 1113  
Yukio Takeda and Kunihiro Maeda
- **Bending Strength of SiC/Al<sub>2</sub>O<sub>3</sub> Composite Sheet obtained from Polycarbosilane/Alumina Power/Binder Mixture** . . . . 1117  
Kazuro Kawamura
- **Preparation of SiC-Si<sub>3</sub>N<sub>4</sub> Composite Fine Powders from Chrolosilanes by R.F. Thermal Plasma** . . . . . 1120  
Masaaki Suzuki, Yoshinori Nakata and Takeshi Okutani
- **Micro Mechanical Processing for Ordered Structure** . . . . . 1124  
Zenji Kato and Keizo Uematsu
- **Wetting Properties of W by Molten SiO<sub>2</sub>-MgO-Al<sub>2</sub>O<sub>3</sub> Ternary Eutectic Composition** . . . . . 1127  
Gyozou Toda, Shousaku Ishihara and Tsuyoshi Fujita

**Ceramic letter:**

- **Growth of Epitaxial PLZT Film by CVD** . . . . . 1130  
Hiroshi Funakubo, Katsuhiro Imashita and Nobuyasu Mizutani

**Discussion:**

- **Comment on "Synthesis of Titanium Nitride Whiskers from Potassium Fluorotitanate (IV)"** . . . . . 1133  
C. Bamberger and J. Brynestad
- **Reply to "Comment on 'Synthesis of Titanium Nitride Whiskers from Potassium Fluorotitanate (IV)' "** . . . . . 1134  
Mitsuharu Tabuchi, Yasunari Kaneko and Hiromichi Iwasaki

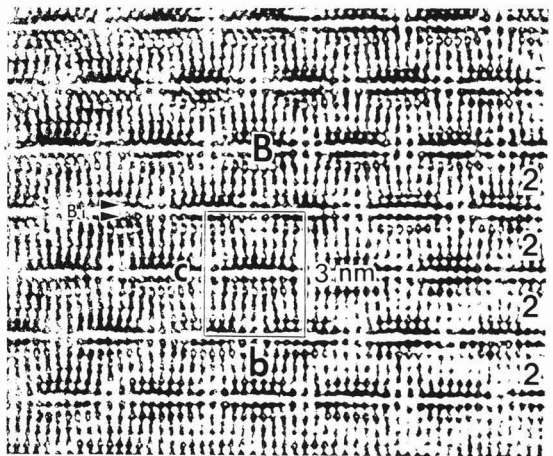
**Information & Communications**

- **News** . . . . . .C-87
- **Abstracts of Articles on Ceramics from Selected Journal of the Academic Societies** . . . . . .C-91

---

## Papers, Letters and Notes

---



High resolution electron microscope photograph of the modulation doped structure of  $\text{Bi}_2\text{Sr}_2\text{CaCu}_2\text{O}_y$  ( $T_c=80\text{K}$ ) in the  $[100]$  direction. Figures at right side indicate number of copper layers, symbol B indicates bismuth rich region.

# Microhardness Anisotropy and the Indentation Load/Size Effect in $\text{MgO}\cdot x\text{Al}_2\text{O}_3$ Single Crystals

Hong Li\*, Hisayuki Suematsu\*\*, Takayoshi Iseki\*\* and Richard C. Bradt\*

\*Mackay School of Mines, University of Nevada-Reno  
Reno, Nevada 89557-0047, U.S.A.

\*\*Department of Inorganic Materials, Tokyo Institute of Technology  
O-okayama, Meguro-ku, Tokyo, 152 Japan

The Knoop microhardness profiles were determined on the (100) of  $\text{MgO}\cdot 1\text{Al}_2\text{O}_3$  and  $\text{MgO}\cdot 3\text{Al}_2\text{O}_3$  single crystals. The  $\langle 100 \rangle$  were the hardness maxima and the  $\langle 110 \rangle$  the hardness minima for both compositions. The nonstoichiometric spinel was the most anisotropic, but the stoichiometric  $\text{MgO}\cdot 1\text{Al}_2\text{O}_3$  crystal had the larger load-independent "true" hardness for all indentation orientations on the (100). The hardness profiles were found to be dominated by the  $\{111\}\langle 1\bar{1}0 \rangle$  primary slip systems from comparison with the calculated ERSS diagrams for the crystals, although differences in the profile shapes were evident. The nonstoichiometric spinel exhibited the greater indentation load/size effect in terms of the Meyer's Law exponent.

[Received May 7, 1991; Accepted July 18, 1991]

**Key-words:** Spinel, Meyer's law, Hardness anisotropy, Microindentation, Stoichiometry

## 1. Introduction

Deformation processes relating to dislocation motion and the active slip systems of  $\text{MgO}\cdot x\text{Al}_2\text{O}_3$  spinel single crystals<sup>1</sup> have been extensively studied for several decades. Following Hornstra's prediction<sup>1)</sup> of the  $\{111\}\langle 1\bar{1}0 \rangle$  primary slip system in stoichiometric spinel ( $\text{MgO}\cdot 1\text{Al}_2\text{O}_3$ ), Choi et al.<sup>2)</sup> studied the high temperature deformation (1600°C) of polycrystalline stoichiometric Mg-Al spinel and confirmed that the  $\{111\}\langle 1\bar{1}0 \rangle$  slip system was active. Single crystal spinel was subsequently studied by Lewis<sup>3)</sup> at high temperatures (1300°C to 1520°C) in one of the first reports on the effect of stoichiometry on the deformation. Lewis reported that the slip system in nonstoichiometric spinel ( $\text{MgO}\cdot x\text{Al}_2\text{O}_3$ ,  $x=1.5, 2.5$  and  $3.5$ ) is the  $\{110\}\langle 1\bar{1}0 \rangle$ . For the  $x=3.5$  spinel, he also observed the  $\{111\}\langle 1\bar{1}0 \rangle$ , but considered that it was because of the high ratio of resolved shear stress ( $\tau_{111}/\tau_{110}=1.5$ ), which resulted from the oriented test specimens.

Newey and Radford<sup>4)</sup> also studied the high temperature deformation of the Mg-Al spinels ( $x=1, 2$  and  $3$ ). They reported the  $\{111\}\langle 1\bar{1}0 \rangle$  slip system for both the  $\text{MgO}\cdot 1\text{Al}_2\text{O}_3$  and the  $\text{MgO}\cdot 3\text{Al}_2\text{O}_3$  spinels, but that the  $\{110\}\langle 1\bar{1}0 \rangle$  was dominant for the  $\text{MgO}\cdot 2\text{Al}_2\text{O}_3$ . Doukhan et al.<sup>5,6)</sup> addressed the creep behavior of  $\text{MgO}\cdot x\text{Al}_2\text{O}_3$  ( $x=1.1$  and  $1.8$ ) spinel single crystals at 1520°C. They confirmed

the  $\{111\}\langle 1\bar{1}0 \rangle$  slip system for the  $x=1.1$  Mg-Al spinel, but also observed the  $\{110\}$  slip system for the  $x=1.1$  Mg-Al spinel, but also observed the  $\{110\}_n$  for the  $x=1.8$  Mg-Al spinel. Donlon et al.<sup>9)</sup> reported dislocation dissociation on the  $\{111\}$  slip system for the nonstoichiometric ( $\text{MgO}\cdot 3.5\text{Al}_2\text{O}_3$ ) spinel at 1500°C, which confirms the previous report by Newey and Radford. Heuer, Mitchell and coworkers<sup>7,9)</sup> have also studied the high temperature deformation of spinel between 1790° and 1895°C. The  $\{111\}\langle 1\bar{1}0 \rangle$  slip system was confirmed for the stoichiometric Mg-Al spinel single crystals and the  $\{110\}\langle 1\bar{1}0 \rangle$  for the nonstoichiometric Mg-Al spinel single crystals. Recently, Suematsu et al.<sup>10,11)</sup> studied nonstoichiometric ( $\text{MgO}\cdot 2.9\text{Al}_2\text{O}_3$ ) single crystal spinel at temperatures between 1100° and 1500°C, where dislocation processes were observed to be those of the  $\{110\}\langle 1\bar{1}0 \rangle$  slip system. The effect of the spinel stoichiometry on the stacking fault energy has been addressed in considerable detail by Welsch et al.,<sup>12)</sup> who suggest that the stacking fault energy of  $\text{MgO}\cdot x\text{Al}_2\text{O}_3$  decreases as the composition ratio,  $x$ , increases. Duclos et al.<sup>13)</sup> have studied the effect of stoichiometry on the creep of  $\text{MgO}\cdot x\text{Al}_2\text{O}_3$  ( $x=1.1, 1.8$  and  $3$ ) spinels and concluded that the ease of glide on the  $\{110\}\langle 1\bar{1}0 \rangle$  slip plane of the nonstoichiometric spinel is the result of the high intrinsic mobility of the dislocations.

Studies addressing the hardness of  $\text{MgO}\cdot x\text{Al}_2\text{O}_3$  single crystal spinels do not appear to be as numerous as those for the slip systems. Mineralogy texts usually report a Moh's hardness of about 8<sup>14)</sup>. In their summary, Young and Millman<sup>15)</sup> have reported that the Vickers microhardness varies from 1378 to 1505 kg/mm<sup>2</sup> on the (111) plane of spinel single crystals, while Akimune and Bradt<sup>16)</sup> reported a Knoop microhardness of 1508kg/mm<sup>2</sup> on the (111). Viechnicki et al.<sup>17)</sup> have studied precipitation effects on the Knoop microhardness of nearly stoichiometric Mg-Al spinel single crystals. They reported 100g test load Knoop microhardness values of 1820kg/mm<sup>2</sup> in the  $\langle 100 \rangle$  directions, but only 1690kg/mm<sup>2</sup> in the  $\langle 110 \rangle$  on the (100). The difference between these hardnesses is about 8%. Bansal and Heuer<sup>18)</sup> measured the Knoop microhardnesses in the  $\langle 100 \rangle$  and the  $\langle 110 \rangle$  on the (100) plane during precipitation in  $\text{MgO}\cdot 3.5\text{Al}_2\text{O}_3$  spinel single crystals. They observed that the  $\langle 100 \rangle$  is consistently harder than the  $\langle 110 \rangle$  by about 10%, although the actual microhardnesses fluctuated during the precipitation process. Only Akimune and Bradt<sup>16)</sup> have specifically addressed the Knoop microhardness anisotropy of stoichiometric ( $\text{MgO}\cdot 1\text{Al}_2\text{O}_3$ ) spinel single crystals, measuring both the (100) and the (111) planes. Their results

\*1 In some of the literature, the nonstoichiometric spinels are specified as  $(\text{Al}_2\text{O}_3)_n\text{MgO}$ .

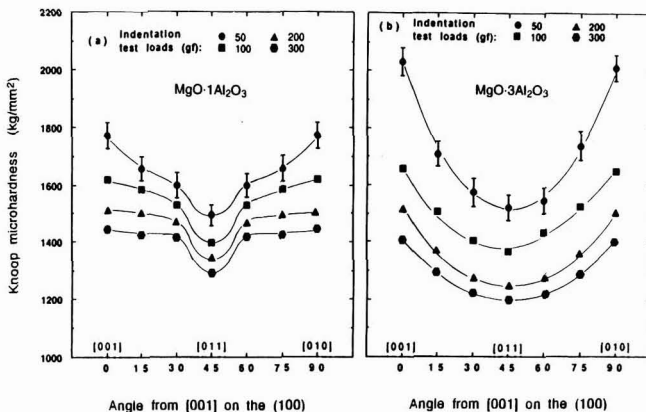


Fig. 1. The Knoop microhardness profiles of the single crystals on their (100) planes: (a) MgO·1Al<sub>2</sub>O<sub>3</sub> and (b) MgO·3Al<sub>2</sub>O<sub>3</sub>.

indicate that the microhardness is highly anisotropic on the (100), but essentially isotropic on the (111) plane. The trend that the <100> is harder than the <110> on the (100) plane, about 1800 to 1500 kg/mm<sup>2</sup>, is consistent with the other spinel microhardnesses that have been reported by Viechnicki et al.<sup>17</sup> and Bansal and Heuer.<sup>18</sup> Zinkle<sup>19</sup> recently studied the effect of ion-implantation on the hardness of polycrystalline MgO·1Al<sub>2</sub>O<sub>3</sub> spinel and observed that the hardness of the irradiated spinels increases about 5%. This increase in hardness by ion-implantation is addressed in terms of the creation of interstitial dislocation loops, which were observed to be of the {111}<1T0> and the {110}<1T0> types.

In spite of these numerous studies of Mg-Al spinels, there has not been a systematic investigations of the influence of the stoichiometry of Mg-Al spinels on either their hardness or their hardness anisotropy. Neither has there been a study of the indentation load/size effect, the ISE, on the microhardness or the microhardness anisotropy of spinel. This paper reports a study of these phenomena. The stoichiometry effect on the microhardness and the related anisotropy profiles of Mg-Al spinel single crystals were determined on the (100) planes of high purity synthetic stoichiometric (MgO·1Al<sub>2</sub>O<sub>3</sub>) and nonstoichiometric (MgO·3Al<sub>2</sub>O<sub>3</sub>) single crystals. The indentation load/size effect on the microhardness of these crystals is considered in terms of both the classical Meyer's Law<sup>20</sup> and a normalized form of Meyer's Law which has been proposed by Li and Bradt.<sup>21</sup>

## 2. Experimental Procedure

According to the earlier study of Akimune and Bradt,<sup>16</sup> the Knoop microhardness anisotropy of Mg-Al spinel is significant on the (100); however, on the (111) plane the microhardness is essentially isotropic. Therefore, in this study, only the Knoop microhardnesses on the (100) of the crystals have been addressed. Single crystals of MgO·1Al<sub>2</sub>O<sub>3</sub><sup>2</sup> and MgO·3Al<sub>2</sub>O<sub>3</sub><sup>3</sup> were obtained from commercial

sources. Previous to the specimen mounting, both surfaces and the <100> crystallographic orientations of specimens were confirmed by X-ray diffraction. Then each specimen was mounted using the cold mounting method with a mixture of epoxy powder and hardener. Subsequent polishing was carried out by using 15, 5, 3, 1 and finally 0.25 μm diamond pastes to achieve scratch free, mirror-like surfaces for the Knoop indentation microhardness measurements.

Using a Shimadzu microindenter, Knoop microhardness measurements were made at room temperature for indentation test loads of 50, 100, 200 and 300g at an indentation rate of 0.017 mm/s for a dwell time of 15s. The crystallographic orientations which were measured on the (100) planes were from the [001] through the [011] to the [010], where the [hkl] is parallel to the long axis of the Knoop indenter. Cracks occasionally initiated from the indentation corners for test loads above 300g, thus not allowing for accurate hardness measurements above that level of test load. In the microindentation hardness test, the long diagonal of the Knoop impression was measured immediately after the indentation. The Knoop hardness number (KHN) at each load level was calculated from the long diagonal of the indentation by applying:

$$KHN = \frac{14229 P}{d^2} \text{ (kg/mm}^2\text{)} \dots \dots \dots (1)$$

where *P* is the indentation test load (in grams) and *d* is the long diagonal of the Knoop indentation (in micrometers). The Knoop microhardness values are reported as the averages for 25 individual indentations at each orientation and test load. The 95% confidence intervals are reported as determined by applying the "t" distribution for the hardnesses and all subsequent parameters derived from the analysis and the graphical presentation.

\*2 Union Carbide Corp; San Diego, CA, USA  
 \*3 Shinko Co., Tokyo, Japan

### 3. Results and Discussion

#### 3.1. Knoop Microhardness Anisotropy

The (100) plane Knoop microhardness profiles for the MgO-1Al<sub>2</sub>O<sub>3</sub> and MgO-3Al<sub>2</sub>O<sub>3</sub> single crystals are depicted in Figs. (1a) and (1b), respectively. The error-bars on the 50g results are the largest 95% confidence intervals for the data. The apparent microhardnesses of these two spinel single crystals are similar, ranging from about 1200 to 2000 kg/mm<sup>2</sup>, dependent on the test load. In terms of the familiar Moh's scale, this is between about 7.6 and 8.3, which compares favorably to the value of 8 that has been reported.<sup>14)</sup> For both of these Mg-Al spinels, the microhardness profiles on the (100) plane exhibit hardness maxima in the <100> and a minima in the <110>. This general microhardness profile is in agreement with the previous results of Akimune and Bradt on the (100) of stoichiometric MgO-1Al<sub>2</sub>O<sub>3</sub>.<sup>16)</sup> It is also similar to the result of Ito on the (100) of MnFe<sub>2</sub>O<sub>4</sub>, which also has the spinel structure<sup>22)</sup> and that of Dekker and Rieck<sup>23)</sup> for the (100) plane of a Mn<sub>1.83</sub>Al<sub>1.17</sub>O<sub>4</sub> spinel single crystal.

Table 1 summarizes parameters descriptive of the Knoop microhardness anisotropy of these spinel single crystals. The hardness anisotropy can be defined in terms of either the simple ratio of  $H_{\max}/H_{\min}$  or in terms of the hardness difference as  $(H_{\max}-H_{\min})/(H_{\max}+H_{\min})^{1/2}$ . Although these definitions as applied to the Knoop microhardness anisotropy are slightly different, it is evident that both yield similar trends and the same conclusions, namely that the extent of the Knoop microhardness anisotropy of the stoichiometric (MgO-1Al<sub>2</sub>O<sub>3</sub>) spinel is less than that of the nonstoichiometric (MgO-3Al<sub>2</sub>O<sub>3</sub>) spinel and also that the extent or degree of microhardness anisotropy appears to decrease as the indentation test load increases for both crystals. These features are presented in Fig.2 where the Knoop microhardness anisotropy is observed to decrease with increasing indentation test load. Comparing these two Knoop microhardness anisotropy profiles with the one reported by Akimune and Bradt,<sup>16)</sup> they are in good agreement. The Knoop microhardness anisotropy reported in their study was about 20% between the <100> and the <110> orientations, which is about the same as illustrated in Fig.2 for these two spinel crystals.

The representation of the microhardness anisotropy in Fig.2 suggests a possible relationship between the degree or extent of this anisotropy and the microhardness indentation test load. The form of the anisotropy versus the test load closely resembles the typical hardness versus indentation test load (or indentation size) trend. This suggests that there may exist some fundamental relationship between the microindentation hardness profiles and the indentation test load/size effect, the ISE. However, the details of that relationship are beyond the scope of this paper and will be addressed in a subsequent study.

It is apparent that there exist differences as well as similarities in the microhardness anisotropy profiles and the Knoop microhardnesses between these two different stoichiometry spinel single crystals. Any similarity must be certainly related to the crystal structure, as the same chemical species and chemical bonding are present in both crystals. However, the microhardness profiles of these two Mg-Al spinels are distinctly different. The stoichiometric spinel profile exhibits a central depression and well-defined plateau-like regions towards the <100> directions. This effect

is accentuated with increasing microindentation test load, whereas no plateau-like regions exist for the non-stoichiometric crystal, which exhibits a smooth parabolic profile. This difference can be further considered through the concept of the effective resolved shear stress (ERSS), as has been advanced by Brookes and coworkers.<sup>24)</sup>

The primary slip system for the stoichiometric (MgO-1Al<sub>2</sub>O<sub>3</sub>) spinel has been confirmed to be the {111}<1T0> by many studies as previously reviewed. For non-stoichiometric (MgO-xAl<sub>2</sub>O<sub>3</sub>, x>1) spinel, the operative slip system has been reported to be the {110}<1T0>. However, there exists some controversy as to whether the {111}<1T0> slip system is also operative for the non-stoichiometric Mg-Al spinels and to what extent it participates in the deformation.

Ito<sup>22)</sup> has measured the Knoop microhardness profile of Mn-Zn ferrite spinel single crystals on the (100), as well as on the (110) and the (210) planes. On the (100) plane of the MnFe<sub>2</sub>O<sub>4</sub>, Ito's Knoop microhardness profile is very similar to that reported for the nonstoichiometric spinel in this study. He concluded that both the {111}<1T0> and the {110}<1T0> slip systems were responsible for the microhardness profile of MnFe<sub>2</sub>O<sub>4</sub>. Dekker and Rieck<sup>23)</sup> have studied the Vickers microhardnesses of various spinel single crystals. On the {100} of a Mn<sub>1.83</sub>Al<sub>1.17</sub>O<sub>4</sub> single crystal, they observed that the <100> directions are harder than the <110> directions, which compares favorably with the hardness anisotropies for the Mg-Al spinels in this study and Mn-Zn ferrite spinels measured by Ito.<sup>22)</sup> However, they used the Vickers indenter which creates a much deeper impression than the Knoop indenter at comparable indentation test loads. This requires that more material flow out of the

Table 1. Knoop Microhardness Anisotropy of the MgO-xAl<sub>2</sub>O<sub>3</sub> Single Crystals on the (100).

Microindentation Test Load (g)	$\frac{H_{\max}}{H_{\min}} \times 100\%$		$\frac{(H_{\max}-H_{\min})}{(H_{\max}+H_{\min})^{1/2}} \times 100\%$	
	MgO-1Al <sub>2</sub> O <sub>3</sub>	MgO-3Al <sub>2</sub> O <sub>3</sub>	MgO-1Al <sub>2</sub> O <sub>3</sub>	MgO-3Al <sub>2</sub> O <sub>3</sub>
50	118.8	133.8	17.2	29.2
100	116.0	121.3	14.9	19.3
200	113.0	121.7	12.2	19.7
300	112.0	117.4	11.3	16.1

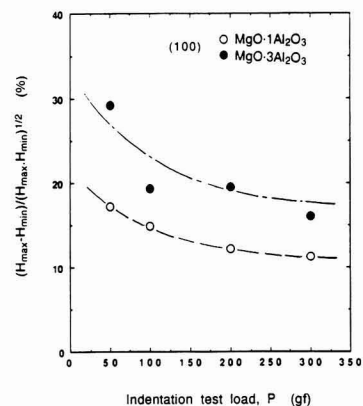


Fig. 2. Effect of the indentation test load on the microhardness anisotropy of spinel single crystals on the (100).

impression and probably promotes extensive slip on secondary and perhaps even tertiary slip systems, nevertheless the orientation of the profile is similar.

For the basis of discussion, it is logical to attempt to apply the ERSS concept as advanced by Brookes and co-workers under the assumptions that the  $\{111\}\langle 1\bar{1}0\rangle$  is the dominant slip system for the stoichiometric  $\text{MgO}\cdot 1\text{Al}_2\text{O}_3$  spinel, while the  $\{111\}\langle 1\bar{1}0\rangle$  and the  $\{110\}\langle 1\bar{1}0\rangle$  may both contribute significantly to the anisotropy of the non-stoichiometric spinel. The ERSS diagrams can be readily constructed for the Knoop indentations on the (100) planes. Detailed information on ERSS calculations has been introduced by Brookes et al.,<sup>24</sup> and is not included here. The interested reader should refer to his original paper. For the ERSS calculations, each individual ERSS line is first calculated, then the resultant ERSS diagram is constructed by a summation of the most dominant ERSS curves (dotted lines), those which have the highest magnitude ERSS within the region from the [001] to the [010] on the (100) plane. The microhardness profile is then expected to be the inverse of the ERSS diagram, if those slip systems dominate the microhardness.

Figure (3a) presents the resulting ERSS diagram for the  $\{111\}\langle 1\bar{1}0\rangle$  primary slip system, while Fig.(3b) illustrates the ERSS diagram for the  $\{110\}\langle 1\bar{1}0\rangle$  primary slip system. These two ERSS diagrams are essentially the opposite, that is  $45^\circ$  out of phase. As the ERSS diagram is inversely related to the microhardness anisotropy profile, a comparison of Fig.3 with Fig.1 clearly establishes that it is the  $\{111\}\langle 1\bar{1}0\rangle$  primary slip system which dominates the deformation processes which determine the microhardness profiles for both of these  $\text{MgO}\cdot x\text{Al}_2\text{O}_3$  ( $x=1, 3$ ) spinel single crystals. However, further discussion is appropriate.

Figs.(3a) and (1a) can be directly compared. In the calculated ERSS diagram of Fig.(3a) for the  $\{111\}\langle 1\bar{1}0\rangle$ , it is apparent that there are three distinct regions. A central high ERSS region extends over about  $30^\circ$  and is flanked by two lower ERSS symmetrical regions extending about  $30^\circ$  from the  $\langle 100\rangle$  toward the [011]. This is practically the exact inverse of the Knoop microhardness anisotropy in Fig.(1a), which also exhibits three distinct regions. Thus it must be concluded that the microhardness profile of the stoichiometric  $\text{MgO}\cdot 1\text{Al}_2\text{O}_3$  spinel on the (100) is determined primarily by the  $\{111\}\langle 1\bar{1}0\rangle$  slip system. This is in agreement with

Hornstra's original prediction<sup>1)</sup> and the experimental observations of Choi et al.,<sup>2)</sup> Newey and Radford,<sup>4)</sup> Doukhan et al.<sup>5,6)</sup> and Mitchell et al.<sup>8)</sup> The form of the microhardness profile for the stoichiometric  $\text{MgO}\cdot 1\text{Al}_2\text{O}_3$  spinel follows the behavior predicted by the ERSS diagram for the  $\{111\}\langle 1\bar{1}0\rangle$  primary slip systems.

However, the microhardness profile of the nonstoichiometric  $\text{MgO}\cdot 3\text{Al}_2\text{O}_3$  spinel presents some contradictions, or at least is not as clear in origin as that for the stoichiometric single crystal. Whereas several researchers<sup>4, 6,9,13)</sup> have reported the  $\{110\}\langle 1\bar{1}0\rangle$  to be the primary slip system in nonstoichiometric spinel, particularly for deformation at elevated temperatures, the calculated ERSS diagram for that slip system yields the incorrect maxima and minima for the experimentally observed microhardness profile. From the results of this study, it must be concluded that the  $\{110\}\langle 1\bar{1}0\rangle$  does not dominate the microhardness profile of  $\text{MgO}\cdot 3\text{Al}_2\text{O}_3$  on the (100). Rather, the microhardness profile for the nonstoichiometric crystal is in agreement with that predicted for the  $\{111\}\langle 1\bar{1}0\rangle$  slip system dominance the same as for the stoichiometric crystal. The origin of the dominance of the  $\{111\}\langle 1\bar{1}0\rangle$  slip system is not clear, it may be related to the highly compressive stress state beneath the indenter or to the fact that the deformation was introduced at room temperature.

Although the overall microhardness profile for the  $\text{MgO}\cdot 3\text{Al}_2\text{O}_3$  crystal on the (100) generally ascribes to the form predicted for the  $\{111\}\langle 1\bar{1}0\rangle$  primary slip system, if Figs.(1a) and (1b) are compared, there is no doubt that the nonstoichiometric crystal has a different shape to its microhardness profile. The plateau-like regions of the stoichiometric  $\text{MgO}\cdot 1\text{Al}_2\text{O}_3$  spinel are not present and there is no evidence for three separate regions of microhardness behavior on the (100) of the  $\text{MgO}\cdot 3\text{Al}_2\text{O}_3$  single crystal. rather the profile appears to be quite smooth and parabolic in form.

If the specific microhardnesses are considered for these two spinel single crystals, then it becomes evident that the nonstoichiometric crystal becomes harder for those orientations which are near to the  $\langle 100\rangle$ . This is precisely the orientation where the ERSS diagram for the  $\{110\}\langle 1\bar{1}0\rangle$  predicts the highest resolved shear stress or the greatest propensity for slip on the  $\{110\}\langle 1\bar{1}0\rangle$ . This suggests that it should be the lowest hardness when the  $\{110\}\langle 1\bar{1}0\rangle$  slip system is dominant. However, that slip system is not dom-

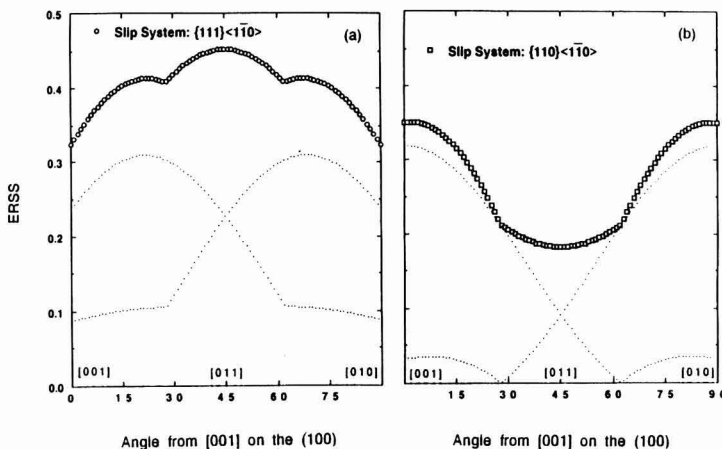


Fig. 3. The calculated ERSS diagrams for (a) the  $\{111\}\langle 1\bar{1}0\rangle$  and (b) the  $\{110\}\langle 1\bar{1}0\rangle$  slip systems.

inant during the indentation measurements, yet it might be active. One possible situation that allows for the {110}<110> slip and increased hardness is that for those orientations near to the <100> in the MgO·3Al<sub>2</sub>O<sub>3</sub> crystal, both the {111} and {110} slip systems are active. Researchers have observed the presence of multiple slip near to indentations<sup>22)</sup> and Ito has done so for the spinel structure. If the two slip systems were simultaneously active, perhaps there would occur much greater work hardening near to the <100> orientations, thus leading to the higher hardness which are observed in the MgO·3Al<sub>2</sub>O<sub>3</sub> and are evident in Fig.(1b).

3.2. The Indentation Load/Size Effect, Meyer's Law

Addressing the Knoop microhardness values as presented in Figs.(1a) and (1b) at each level of individual indentation test load, there is not any absolute way in which to distinguish as to which of the two crystals is consistently the harder. For example, except for the <100> directions, the stoichiometric (MgO·1Al<sub>2</sub>O<sub>3</sub>) spinel generally appears to harder than the nonstoichiometric (MgO·3Al<sub>2</sub>O<sub>3</sub>) spinel. To clearly distinguish the microhardness difference between the crystals, it is constructive to analyze the load dependence of the hardness behavior of the two crystals. Many microhardness studies<sup>25-29)</sup> have shown that Meyer's Law:

$$P = Ad^n \dots\dots\dots (2)$$

can be generally applied to describe the indentation load/size effect for a variety of materials and single crystals, both metals and ceramics, as well as for different indenter geometries (Knoop, Vickers and Brinell). In eq.(2), P and d have their original meanings as in eq.(1), while A and n are descriptive parameters. The conventional Meyer's Law of eq.(2) can be expressed in the logarithmic form as:

$$\log P = \log A + n \log d \dots\dots\dots (3)$$

Applying eq.(3) to the hardness results depicted in Figs.(1a) and (1b), the indentation load/size effect can be directly addressed for these crystals.

Figure 4 illustrates the Meyer's Law relationship on the (100) plane for the two Mg-Al spinels. Four orientations from the [001] to the [011] at 15° intervals are presented. It is evident that the Meyer's Law relationship is followed by

the experimental data as the linear regression coefficients (r<sup>2</sup>) of the plots all exceed 0.99. It is also apparent that the Meyer's Law exponent, or the n-value, is different for the [001] and the [011] as the n-value for the former is less than that of the latter for both of these spinel single crystals. Table 2 summarizes the two Meyer's Law parameters, the A-values and the n-values, for these two spinel single crystals. Note that the [001] and [010] Meyer's Law parameters are identical in each crystal and that the results are symmetrical about the [001] for each. It appears that there may exist some fundamental relationship between these two Meyer's Law parameters as the A-value appears to be inversely related to the n-value. This observation is confirmed in Fig.5, which has an r<sup>2</sup> of 0.92 for the linear regression analysis. This figure illustrates that the same n-A relationship exists for both the stoichiometric and the nonstoichiometric spinel single crystals, although the stoichiometric spinel exhibits larger n-values than the nonstoichiometric crystal. Secondly, for A=0, the n-value extrapolates to 2.03±0.04, which confirms the applicability of Meyer's Law to these hardness results.

Considering the Meyer's Law behavior, the n-values of these two spinels are significantly different. Those for the stoichiometric spinel are consistently larger than those for the nonstoichiometric spinel, revealing that the indentation load/size effect is not the same for these two single crystal spinels. Since n=2 is indicative of an indentation load/size independent condition, it is logical that the greater the de-

Table 2. Meyer's Law Parameters of the MgO·xAl<sub>2</sub>O<sub>3</sub> Single Crystals on the (100).

(100)[uvw]	A (g·μm <sup>2</sup> )	n	A (g·μm <sup>2</sup> )	n
	<b>MgO·1Al<sub>2</sub>O<sub>3</sub></b>		<b>MgO·3Al<sub>2</sub>O<sub>3</sub></b>	
[001]	0.23±0.01	1.80±0.02	0.37±0.01	1.67±0.01
15°	0.19±0.02	1.85±0.02	0.30±0.01	1.70±0.02
30°	0.18±0.01	1.88±0.01	0.23±0.02	1.76±0.01
[011]	0.16±0.01	1.85±0.01	0.22±0.01	1.77±0.02
60°	0.16±0.02	1.88±0.02	0.22±0.01	1.78±0.02
75°	0.19±0.01	1.84±0.01	0.32±0.02	1.68±0.01
[010]	0.23±0.02	1.80±0.01	0.36±0.01	1.68±0.01

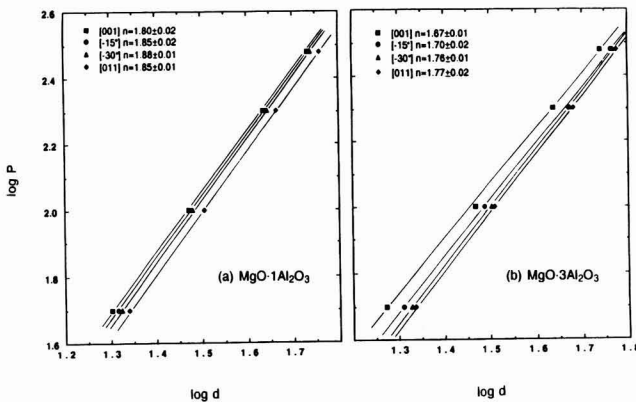


Fig. 4

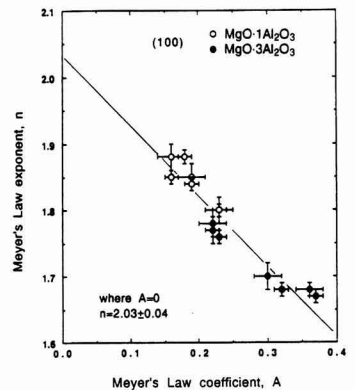


Fig. 5

Fig. 4. The classical Meyer's Law relationship on the (100) of the MgO·1Al<sub>2</sub>O<sub>3</sub> (a) and the MgO·3Al<sub>2</sub>O<sub>3</sub> (b) spinel single crystals.

Fig. 5. The relationship of the classical Meyer's Law parameters A and n for the spinel single crystals.

viation of the  $n$ -value from two, the greater is the indentation load/size effect. Hence these results reveal that the stoichiometric  $MgO \cdot 1Al_2O_3$  spinel single crystal experiences less of an indentation load/size effect during microindentation hardness testing than does the non-stoichiometric  $MgO \cdot 3Al_2O_3$  spinel single crystal.

**3.3. The Indentation Load/Size Effect, Normalized Meyer's Law**

The indentation load/size effect has been recently addressed for the microhardness of  $LaB_6$  single crystals through a normalized form of Meyer's Law by Li and Bradt.<sup>21)</sup> They applied the criterion of indentatation hardness/load independence, which is defined by a variation of hardness ( $H$ ) with respect to a change of indentation test load ( $P$ ) equal to zero, as:

$$\frac{\partial H}{\partial P} P = 0 \dots \dots \dots (4)$$

to derive a normalized form of Meyer's Law, which is:

$$P = \frac{2 P_c}{n} \left( \frac{d}{d_0} \right)^n \dots \dots \dots (5)$$

where  $P_c$  is the critical indentation test load beyond which the indentation load/size effect is diminished, and  $d_0$  is a characteristic indentation size related to  $P_c$ . According to other studies of the normalized form of Meyer's Law applied to different single crystals, including  $LaB_6$ <sup>21)</sup>,  $TiO_2$ <sup>29)</sup> and  $SnO_2$ <sup>30)</sup>, the Meyer's Law exponents or the  $n$ -values determined for experimental results analyzed by eq.(5) are identical to those for the classical Meyer's Law of eq.(2). The normalized form of Meyer's Law does, however, solve the dimensionality problem of the A-value and also reveals the physical significance of the Meyer's Law through  $P_c$  and  $d_0$ .

To apply eq.(5) to the analysis of the indentation load/size effect,  $P_c$  and  $d_0$  must first be determined from the experimental microhardness results. For indentation load/size independence, the microhardness can be considered as a "true" hardness ( $H_0$ ). Under this condition,  $d_0$  can be related to  $H_0$  and calculated from:

$$d_0 = \left( \frac{2 H_0}{14229 n A} \right)^{1/(n-2)} (\mu m) \dots \dots \dots (6)$$

where the load-independent "true" hardness can be determined by experimental microhardness results, as described by Larmie<sup>31)</sup> and Li et al.,<sup>32)</sup> in the form of:

$$d = (14229/H_0)^{1/2} P^{1/2} + \delta (\mu m) \dots \dots \dots (7)$$

where  $\delta$  is related to relaxation effects on unloading.

Figure 6 illustrates the  $d$  versus  $P^{1/2}$  plots for the evaluation of  $H_0$  of the (100) planes for the two spinel single crystals. The "true" hardness ( $H_0$ ) values are obtained from the slopes of the linear regression lines. Table 3 summarizes the resulting "true" hardness values. For the stoichiometric spinel, they range from 1180 to 1274  $kg/mm^2$  and are consistently higher than the values of 1033 to 1145  $kg/mm^2$  for the nonstoichiometric spinel with respect to all directions on the (100) plane. This comparison clearly reveals that the stoichiometric spinel is harder than the nonstoichiometric spinel structure. Many studies<sup>4,9,12,13)</sup> of plastic deformation of Mg-Al spinels at elevated temperatures confirm that the stoichiometric spinel is stronger than the nonstoichiometric spinels. At room temperature, the above conclusion is similar as revealed by the load-independent "true" hardnesses determined in this study.

**Table 3.** "True" Hardnesses and Characteristic Indentation Sizes of the  $MgO \cdot xAl_2O_3$  Single Crystals on the (100).

(100)[uvw]	$H_0$ ( $kg/mm^2$ )	$d_0$ ( $\mu m$ )	$P_c$ (g)	$H_0$ ( $kg/mm^2$ )	$d_0$ ( $\mu m$ )	$P_c$ (g)
	<b><math>MgO \cdot 1Al_2O_3</math></b>			<b><math>MgO \cdot 3Al_2O_3</math></b>		
[001]	1274±51	61.97±2.48	344±21	1148±46	58.81±2.44	279±20
15°	1292±52	62.77±2.51	358±20	1034±47	65.67±2.83	313±22
30°	1309±52	67.75±2.03	422±25	1065±43	68.26±2.73	349±21
[011]	1180±47	63.63±2.55	336±20	1033±41	65.73±2.63	314±19
60°	1324±53	67.36±2.69	422±30	1067±42	66.22±2.65	329±23
75°	1280±60	65.62±2.63	387±23	1013±41	63.59±2.54	288±17
[010]	1273±65	60.58±3.03	328±22	1158±48	58.71±2.35	281±20

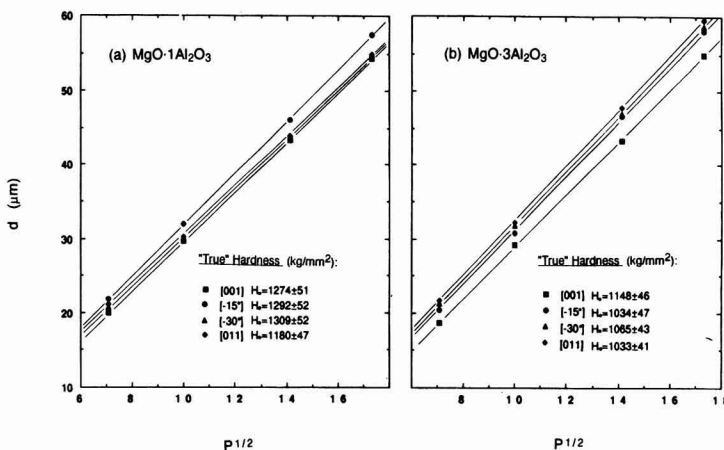


Fig. 6. The "true" hardness plots for the  $MgO \cdot 1Al_2O_3$  (a) and the  $MgO \cdot 3Al_2O_3$  (b) spinel single crystals.

The calculated “true” hardnesses can be applied to determine the characteristic indentation size ( $d_0$ ) through eq.(6). Table 3 summarizes the characteristic indentation sizes, the  $d_0$ -values, for these two spinel single crystals. With respect to the average value of  $d_0$  on the (001) plane, that for the stoichiometric spinel is essentially the same as that for the nonstoichiometric spinel:  $64.24 \pm 2.56 \mu\text{m}$  versus  $63.81 \pm 2.55 \mu\text{m}$ . These calculated  $d_0$  values are comparable to the measured indentation sizes at the 300g indentation test load for these spinel crystals, which is consistent with the observed indentation load/size effect on the (100) planes for these two spinel single crystals.

According to the calculated “true” hardness and the characteristic indentation sizes (the  $d_0$ -values), the critical indentation loads (the  $P_c$ -values) can be determined and these are summarized in Table 3. The critical indentation loads are anisotropic with respect to indentation orientation on the (100). The stoichiometric  $\text{MgO} \cdot 1\text{Al}_2\text{O}_3$  spinel has slightly higher  $P_c$ -values than the nonstoichiometric  $\text{MgO} \cdot 3\text{Al}_2\text{O}_3$  spinel. However, for both crystals, the  $P_c$ -values are about 300-400g, at which the indentation load/size effect is significantly reduced, consistent with the experimental results.

Once these characteristic indentation sizes, the  $d_0$ -values, have been calculated, the normalized Meyer’s Law in the logarithmic form of eq.(5), which is:

$$\log P = \log (2P_c/n) + n \log(d/d_0) \dots \dots \dots (8)$$

can be applied to these crystals. Figures (7a) and (7b) illustrate these relationships of  $\log P$  versus  $\log(d/d_0)$  for the stoichiometric spinel and the nonstoichiometric spinels, respectively. The slopes of the regression lines yield the normalized Meyer’s Law exponents which are identical to those of the classical Meyer’s Law. It can be concluded that the normalized form of Meyer’s Law is consistent with the experimental observations that the indentation load/size effect on the microhardness is significant when the indentation load is less than the critical indentation load ( $P_c$ ), or the indentation size is less than the characteristic indentation size ( $d_0$ ). The normalized Meyer’s Law provides a convenient way to assess the extent of the indentation load/size effect on the microhardness in terms of the physical prop-

erties: a critical indentation test load( $P_c$ ) and a characteristic indentation size ( $d_0$ ).

Comparing the normalized form of Meyer’s Law with the classical Meyer’s Law, the physical meaning of the classical Meyer’s Law coefficient ( $A$ ) can be better understood. It is revealed to be related to the critical indentation test load ( $P_c$ ) and the characteristic indentation size ( $d_0$ ), as well as the Meyer’s Law exponent, the  $n$ -value. This is evident when eqs.(2) and (5) are combined, yielding the Meyer’s Law coefficient ( $A$ ) expressed as:

$$A = \frac{2 P_c}{n d_0^n} \dots \dots \dots (9)$$

This illustrates that the  $A$ -value is indeed inversely related to the  $n$ -value as previously discussed and confirmed by the results presented in Fig.5. Sargent and Page<sup>33</sup> have also studied correlations between the  $A$ -values and the  $n$ -values, but for polycrystalline ceramics rather than single crystals. They observed that there exists a degree of correlation where the  $n$ -value appears to be inversely related to the  $\ln(A)$ . However, for polycrystalline ceramics, the grain boundary effect also directly affects the indentation measurement results. As a consequence, the  $A$ - $n$  relationship is not as obvious for polycrystalline specimens, as it is revealed for the single crystals in this study and illustrated in Fig.5.

As clearly presented by the above discussion, some features of the indentation load/size effect on the microhardness can be quantitatively described by applying the normalized form of Meyer’s Law. However, the physical significance of the Meyer’s Law exponent, or the  $n$ -value remains unresolved even in the normalized form. Although the  $n$ -value has been defined and confirmed as a parameter directly associated with the indentation load/size effect,<sup>34</sup> there exists no consistent agreement among many researchers as to its fundamental origin. Some explanations include the material resistance pressure effect,<sup>23</sup> dislocation source hardening,<sup>26</sup> interaction between the dislocations and the surface,<sup>35</sup> work hardening<sup>25</sup> and the elastic recovery effect.<sup>36-40</sup> It has been substantiated, however, that harder materials often experience the more significant indentation load/size effect in the microindentation hardness test, al-

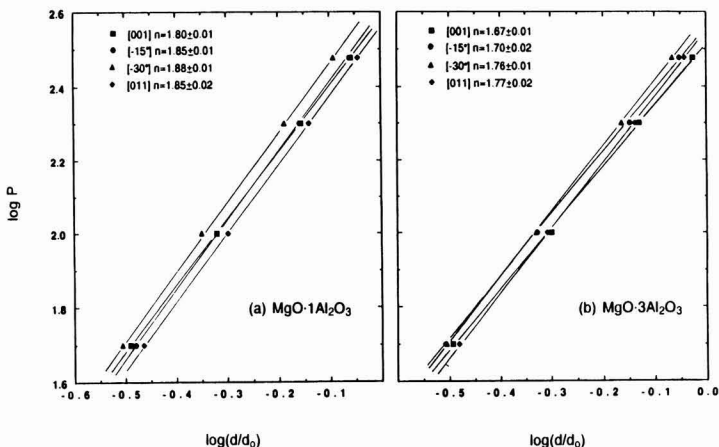


Fig. 7. The normalized Meyer’s Law relationship on the (100) of the  $\text{MgO} \cdot 1\text{Al}_2\text{O}_3$  (a) and the  $\text{MgO} \cdot 3\text{Al}_2\text{O}_3$  (b) spinel single crystals.

though these two spinels do not follow that trend. Further investigation of the Meyer's Law exponent, the  $n$ -value, is required to gain additional insight of the response of the material to the indentation load.

#### 4. Summary and Conclusions

The Knoop microhardness profiles were determined on the (100) planes of stoichiometric ( $\text{MgO} \cdot 1\text{Al}_2\text{O}_3$ ) spinel and nonstoichiometric ( $\text{MgO} \cdot 3\text{Al}_2\text{O}_3$ ) spinel single crystals for indentation test loads from 50 to 300g. The microhardness results indicate that the hardnesses of the two Mg-Al spinel single crystals are highly anisotropic on the (100) planes. The extent of the hardness anisotropy for the stoichiometric spinel is consistently less than that for the nonstoichiometric spinel. Analysis of the indentation load/size effect on the extent of the microhardness anisotropy illustrates that the latter decreases with an increase of the indentation test load. The trend appears to follow a power law, but this phenomenon requires further investigation.

The Knoop microhardness profiles were compared with the calculated ERSS diagrams. The latter were calculated with the assumption that the  $\{111\}\langle 1\bar{1}0 \rangle$  slip system is dominant for the stoichiometric spinel and yielded good agreement with the experimental microhardness profile. As the consequence of these analyses, it is suggested that at room temperature the Knoop microhardness anisotropy of the stoichiometric and the nonstoichiometric spinel crystals are both controlled by the  $\{111\}\langle 1\bar{1}0 \rangle$  primary slip system. The  $\{110\}\langle 1\bar{1}0 \rangle$  slip system appears to make only a minor contribution, even for the nonstoichiometric spinel and perhaps only near the  $\langle 100 \rangle$  orientations.

The indentation load/size effect was addressed through both the classical Meyer's Law and the normalized form of the Meyer's Law. The normalized Meyer's Law was confirmed to be consistent with the classical Meyer's Law through the experimental data, as the power law exponents or  $n$ -values are the same. According to the Meyer's Law analysis, the Meyer's Law coefficient ( $A$ ) is inversely related to the Meyer's Law exponent ( $n$ ) for both of these spinel single crystals. The  $n$ -values for the stoichiometric spinel are consistently higher than those of the nonstoichiometric spinel. The calculated critical indentation test load ( $P_c$ ) and the characteristic indentation size ( $d_0$ ) were consistent with the experimental results. The results suggest that the Meyer's Law parameters are anisotropic in nature, revealing that the indentation load/size effect varies with both the spinel stoichiometry and the crystallographic orientation.

#### References:

- 1) J. Hornstra, *J. Phys. Chem. Solids*, 15, 311-323 (1960).
- 2) D.M. Choi and H. Palmour III, *Materials Science Research*, Vol.3, ed. by W.W. Kriegel and H. Palmour III, Plenum Press, New York, (1966) 473-482.
- 3) M.H. Lewis, *Phil. Mag.*, 17, 481-499 (1968).
- 4) C.W.A. Newey and K.C. Radford, *Anisotropy in Single-Crystal Refractory Compounds*, Vol.2, ed. by F.W. Vahldiek and S.A. Mersol, Plenum Press, New York (1968) 321-338.
- 5) N. Koukhan, R. Duclos and B. Escaig, *J. de Phys. Colloq.*, C9, 379-387 (1973).
- 6) N. Doukhan, R. Duclos and B. Escaig, *ibid.*, C7, 556-571 (1976).
- 7) L. Hwang, A.H. Heuer and T.E. Mitchell, *Deformation of Ceramic Materials*, ed. by R.C. Bradt and R.E. Tressler, Plenum Press, New York (1975) 254-270.
- 8) T.E. Mitchell, L. Hwang and A.H. Heuer, *J. Mater. Sci.*, 11, 264-272 (1976).
- 9) W.T. Donlon, T.E. Mitchell and A.H. Heuer, *Phil. Mag.*, A40, 351-366 (1979).
- 10) H. Suematsu, T. Suzuki and T. Iseki, *J. Am. Ceram. Soc.*, 72, 306-308 (1989).
- 11) H. Suematsu, T. Suzuki and T. Iseki, *J. ibids.*, 72, 1449-1452 (1989).
- 12) G. Welsch, L. Hwang, A.H. Heuer and T.E. Mitchell, *Phil. Mag.*, 29, 1371-1379 (1979).
- 13) R. Duclos, N. Doukhan and B. Escaig, *Acta Metall.*, 30, 1381-1388 (1982).
- 14) L.G. Berry and B. Mason, *Mineralogy*, W.H. Freeman and Company, San Francisco (1959) 596.
- 15) B.B. Young and A.P. Millman, *Trans. I.M.M.*, 73, 437-466 (1964).
- 16) Y. Akimune and R.C. Bradt, *J. Am. Ceram. Soc.*, 70, C84-C86 (1987).
- 17) D. Viechnicki, F. Schmid and J.W. McCauley, *J. Appl. Phys.*, 43, 4508-4512 (1972).
- 18) G.K. Bansal and A.H. Heuer, *Phil. Mag.*, 29, 709-722 (1974).
- 19) S.J. Zinkle, *J. Am. Ceram. Soc.*, 72, 1343-1351 (1989).
- 20) E. Meyer, *Zeitschrift, V.D.I.*, 52, 645 (1908).
- 21) H. Li and R.C. Bradt, *Mater. Sci. Eng.* to be published.
- 22) T. Ito, *J. Am. Ceram. Soc.*, 54, 24-26 (1971).
- 23) E.H.L.J. Dekker and G.D. Rieck, *J. Mater. Sci.*, 9, 1839-1846 (1974).
- 24) C.A. Brookes, J.B. O'Neill and B.A.W. Redfern, *Proc. Roy. Soc. London*, A322, 73-88 (1971).
- 25) B.W. Mott, *Micro-indentation Hardness Testing*, Butterworths Scientific Publication, London, (1956) 101-139.
- 26) N. Gane and J.M. Cox, *Phil. Mag.*, 22, 881-891 (1970).
- 27) D.J. Clinton and R. Morrell, *Mater. Chem. Phys.*, 17, 461-473 (1987).
- 28) C. Hays and E.G. Kendall, *Metallog.*, 6, 275-282 (1973).
- 29) H. Li and R.C. Bradt, *J. Am. Ceram. Soc.*, 73, 1360-1364 (1990).
- 30) H. Li and R.C. Bradt, *ibids.*, 74, 1053-1060 (1991).
- 31) H.A. Larmie, Ph. D. Dissertation, Univ. of Washington, Seattle, WA, (1988).
- 32) Z. Li, A. Ghosh, A.S. Kobayashi and R.C. Bradt, *J. Am. Ceram. Soc.*, 72, 904-911 (1989).
- 33) P.M. Sargent and T.F. Page, *Proc. Brit. Ceram. Soc.*, 26, 209-224 (1978).
- 34) P.M. Sargent, *Microindentation Techniques in Materials Science and Engineering*, ed. by P.J. Blau and B.R. Lawn, ASTM STP 889, Phil., PA (1984) 160-174.
- 35) G.P. Upit and S.A. Varchenya, *The Science of Hardness Testing and Its Research Applications*, ed. by J.H. Westbrook and H. Conrad, ASM, Metal Park, Ohio (1973) 135-146.
- 36) P.M. Sargent and T.F. Page, *Scripta Metal.*, 15, 245-250 (1980).
- 37) J.L. Loubet, J.M. Georges, O. Marchesini and G. Meille, *J. Tribology*, 106, 43-48, (1984).
- 38) J.L. Loubet, J.M. Georges and G. Meille, *Microindentation Techniques in Materials Science and Engineering*, ed. by P.J. Blau and B.R. Lawn, ASTM STP 889, Phil., PA., (1984) 72-89.
- 39) M.F. Doerner and W.D. Nix, *J. Mater. Res.*, 1, 601-609, (1986).
- 40) G.M. Pharr and R.E. Cook, *J. Mater. Res.*, 5, 847-851 (1990).

# Fabrication and Characterization of CVD-Deposited TiC-SiC Composites

Chihiro Kawai and Masaya Miyake

Itami Research Laboratories, Sumitomo Electric Industries, Ltd.

1-1-1, Koya-Kita, Itami-shi, 664 Japan

Composites with several compositions in TiC-SiC system were fabricated by chemical vapor deposition and the several properties were measured. The CVD conditions used were  $\text{TiCl}_4\text{-SiCl}_4\text{-CH}_4\text{-H}_2$  system, deposition temperature of 1350°C and total gas pressure of 60 Torr. The TiC-SiC composites with various compositions were fabricated by stepwise change in the Ti/(Ti+Si) ratio in the feed gas on the basis of thermodynamic calculation for the system. The obtained composites were fully dense with columnar structure perpendicular to the substrate plane and had (220) orientation in parallel thereto. Thermal expansion coefficients of the TiC-SiC composites parallel to substrate ranged from 4.5 to  $7.4 \times 10^{-6} \text{K}^{-1}$  and Young's modulus perpendicular to the substrate ranged from 220 to 467 GPa depending on the composition. These measured values agreed with those calculated from some rules of mixture in composite.

[Received January 16, 1991; Accepted July 18, 1991]

**Key-words:** CVD, TiC, SiC, Composite, Young's Modulus, Thermal expansion coefficient, Functionally gradient material

## 1. Introduction

In recent years, a reinforcing technique for high temperature service structural ceramics such as SiC, TiC,  $\text{Si}_3\text{N}_4$ , etc. with high elastic continuous fibers such as carbon fibers and SiC fibers have undergone various experiments in order to improve fracture toughness and reliability of these ceramics. These fiber-reinforced ceramic composites exhibit various characteristics depending on the combination of fibers and ceramic matrix used, but one of the problems commonly involved in these composites is insufficient resistance to oxidation. In the case of carbon fibers used for the reinforcement, this problem is especially unavoidable, therefore, oxidation-resistant coatings must be applied on the composite surface. The oxidation-resistant coating popularly applied on high temperature service structural materials is a SiC coating fabricated by chemical vapor deposition process (hot CVD process). However, since relatively high deposition temperatures of higher than 1200°C are generally required, thermal stresses are generated at the boundary between the coated SiC layer and the substrate during cooling if thermal expansion coefficients of SiC and substrate material differ greatly from each other; Exfoliation of coated layer and crack generation in coated layer are thus caused, resulting in an insufficient oxidation resisting effect achieved by the coating.

When thermal expansion coefficient of a substrate differs

from that of SiC layer, as above mentioned, a modified technique for functionally gradient coating has been proposed as an oxidation resistant coating techniques. The method in this technique is that the thermal expansion coefficient of coated layer is arranged equivalent to that of a substrate at the boundary with the substrate, and is changed continuously to that of SiC toward the external surface of the layer, where oxidation resistant characteristics are required, so that a coated layer with a high oxidation resistance can be prepared without causing cracks and fractures in the coated layer. In the general case of hot CVD process, tensile residual stresses are generated in a coated layer when the thermal expansion coefficient of a coated layer is larger than that of the substrate, and compressive residual stresses are generated in a coated layer when thermal expansion coefficient of the coated layer is smaller than that of the substrate. Therefore, the modified technique for functionally gradient coating must suit the given conditions. As an example of the former case, studies<sup>1,2)</sup> were carried out on the functionally gradient coating in C-SiC system by arranging the thermal expansion coefficient of the coated layer gradient in the thickness direction in the range of 0 and  $4.5 \times 10^{-6} \text{K}^{-1}$  by the hot CVD process on a substrate of carbon fiber-reinforced carbon composite (C/C composite).

In our current study, the authors intended to investigate oxidation resistant coating technique on a substrate having a larger thermal expansion coefficient than SiC, and chose TiC-SiC system ceramics as the functionally gradient coating materials. In this investigation, a material design is necessary for optimization of the compositional distribution as to make the gradient function maximum. In order to carry out the material design as required, it is necessary to obtain various fundamental data such as tensile strength, thermal expansion coefficient, Young's modulus, and so forth of the TiC-SiC composites synthesized by the CVD process.

Regarding the study on the synthesis of TiC-SiC composites by CVD process, Touanen et al.<sup>3,4)</sup> and Stinton et al.<sup>5)</sup> carried out thermodynamic equilibrium calculations in various raw materials systems. Meanwhile, Goto et al.<sup>6-10)</sup> and Nickl et al.<sup>11)</sup> reported that they synthesized TiC-SiC composites by CVD process using feed gases of  $\text{SiCl}_4\text{-TiCl}_4\text{-CCL}_4\text{-H}_2$  system, compared the experimental results with the thermodynamic calculation results, and examined the texture of the composites. Regarding thermal and mechanical characteristics of TiC-SiC composites, it was reported that, in the case of sintered bodies, bending strength and fracture toughness were improved by the addition of TiC to SiC,<sup>12-17)</sup> while, Woydt et al.<sup>13)</sup> reported measured results of Young's modulus and thermal expansion coefficient of a sintered body in composition of 50vol%TiC-50vol%SiC. Regarding the characteristics of TiC-SiC composites synthesized by CVD process, however, fracture toughness was reported by

Goto et al.,<sup>9)</sup> but thermal expansion coefficient and Young's modulus have not been reported yet.

In our study, we synthesized TiC-SiC composites by CVD process using feed gases of SiCl<sub>4</sub>-TiCl<sub>4</sub>-CH<sub>4</sub>-H<sub>2</sub> system and measured Young's modulus and thermal expansion coefficient of the composites synthesized.

### 2. Thermodynamic Investigation

Prior to the experiments of the synthesis of TiC-SiC system composites by CVD process, we estimated by a computer simulation the deposit phases under thermodynamic equilibrium from the feed gases of SiCl<sub>4</sub>-TiCl<sub>4</sub>-CH<sub>4</sub>-H<sub>2</sub> system under various deposition conditions. In this computer simulation, we used a thermodynamic equilibrium calculation program (EKVICALC) and a data-base (EKVIBASE), both prepared by Svensk Energidata Co. (Sweden).

A theoretical formula for equilibrium calculation is expressed by simultaneous equations of equation (1), which concerns formation free energy in a system, and equation (2), which concerns material balance in a system.<sup>6)</sup> When total Gibbs' free energy in a CVD reaction system is expressed by *G*, a dimensionless quantity of *G*/*RT* is expressed by equation (1) below.

$$G/RT = \sum_i^m X_i^g [(g^0/RT)_i^g + \ln P + \ln (X_i^g/X)] + \sum_i^s X_i^c (g^0/RT)_i^c \dots \dots \dots (1)$$

Here, *X<sub>i</sub>* is mole number of chemical species *i*, *g*<sup>0</sup> is standard Gibbs' free energy of chemical species *i*, *R* is gas constant, *T* is absolute temperature, *P* is total pressure, and *X* is total mole number. Meanwhile, *g* represents gas phase, *c* solid phase species, *m* number of gas phase species, and *s* number of solid phase species. Chemical equilibrium in a system is attained when *G*/*RT* takes a minimum value under a condition that the material balance expressed by equation (2) below is satisfied.

$$\sum_i^m a_{ij} x_i^g + \sum_i^s a_{ij} x_i^c = b_j \dots \dots \dots (2)$$

Here, *a<sub>ij</sub>* is number of element *j* in chemical species *i*, and *b<sub>j</sub>* is total number of element *j*.

Table 1 shows the chemical species used in thermodynamic calculation in our experimental system, which include 50 kinds of gas phase species, 3 kinds of liquid phase ones and 14 kinds of solid phase ones. Goto et al.<sup>6)</sup> used the same raw materials system as we used, and carried out equilibrium calculation using chemical species of 49 kinds of gas phase species and 8 kinds of solid phase species. The species they used included Ti<sub>3</sub>SiC<sub>2</sub>, which we did not use. The difference between the thermodynamic calculation results of theirs and ours is assumed to be due to the differences of kind and number of data reserved in respective data-bases, and it is difficult to simply judge which calculation is more accurate.

Figure 1 shows an equilibrium phase diagram of SiCl<sub>4</sub>-TiCl<sub>4</sub>-CH<sub>4</sub>-H<sub>2</sub> system at a coating temperature of 1350°C under a pressure of 60Torr in the case that the ratio of total

flow rate of SiCl<sub>4</sub>, TiCl<sub>4</sub> and CH<sub>4</sub> in the feed gas against total gas flow rate is 1:7, and the ratio of CH<sub>4</sub> gas flow rate against H<sub>2</sub> gas flow rate (CH<sub>4</sub>/H<sub>2</sub>) is in the range of 5.0 to 5.3×10<sup>-2</sup>. The phases to deposit under thermodynamic equilibrium are shown in the figure. When coating temperature was increased up to 1550°C in the same conditions of gas flow rate and gas pressure, there was no substantial change observed in the phase diagram. In order to control the composition of deposited phases of TiC-SiC system as free from free carbon, Ti<sub>5</sub>Si<sub>3</sub> and TiSi, we chose a composition line A (CH<sub>4</sub>/H<sub>2</sub> = 5.0 to 5.3×10<sup>-2</sup>) in the diagram.

Goto et al.<sup>6,7)</sup> calculated the thermodynamic equilibrium in the condition of CCl<sub>4</sub>/H<sub>2</sub> = 1.7 to 4.6×10<sup>-2</sup>, which was relatively close to our experimental condition of CH<sub>4</sub>/H<sub>2</sub> = 5.0 to 5.3×10<sup>-2</sup>, and reported that there were no intermetallic compounds such as Ti<sub>5</sub>Si<sub>3</sub> and TiSi formed in the temperature range of 1300° and 1600°C. Here, CCl<sub>4</sub>/H<sub>2</sub> is the concentration ratio of carbon source gas against hydrogen gas in the feed gas. This result agreed with ours. However, they calculated that free carbon was deposited in addition to TiC and SiC in the case of CCl<sub>4</sub>/H<sub>2</sub> = 4.6×10<sup>-2</sup>. This result was different from our calculation result. We assume this difference was caused by the difference of carbon source gases used.

### 3. Experiments

#### 3.1. Fabrication

Using a CVD apparatus of external heating type with the heating element of carbon electrode, we carried out a coating on a substrate of isotropic graphite (grade IG-11, made by Toyo Carbon Co.) with dimensions of 25×25×5mm.

Figure 2 illustrates a schematic diagram of the CVD

Table 1. Chemical species in SiCl<sub>4</sub>-TiCl<sub>4</sub>-CH<sub>4</sub>-H<sub>2</sub> system.

<Gas species>									
Ti	TiCl	TiCl <sub>2</sub>	TiCl <sub>3</sub>	TiCl <sub>4</sub>	Ti <sub>2</sub> Cl <sub>6</sub>	Cl <sub>2</sub>	Si		
Si <sub>2</sub>	Si <sub>3</sub>	SiC	SiC <sub>2</sub>	Si <sub>2</sub> C	SiCl	SiCl <sub>2</sub>	SiCl <sub>3</sub>		
SiCl <sub>4</sub>	SiH	SiH <sub>2</sub>	Si <sub>2</sub> H <sub>4</sub>	SiHCl <sub>3</sub>	SiH <sub>2</sub> Cl <sub>2</sub>	SiH <sub>3</sub> Cl			
C	C <sub>2</sub>	C <sub>3</sub>	CCl	CCl <sub>2</sub>	CCl <sub>3</sub>	CCl <sub>4</sub>	C <sub>2</sub> Cl <sub>2</sub>	C <sub>2</sub> Cl <sub>4</sub>	
C <sub>2</sub> Cl <sub>6</sub>	CH	CH <sub>2</sub>	CH <sub>3</sub>	CH <sub>4</sub>	C <sub>2</sub> H <sub>2</sub>	C <sub>2</sub> H <sub>4</sub>	C <sub>2</sub> H <sub>6</sub>		
C <sub>3</sub> H <sub>4</sub> (propyne)					C <sub>3</sub> H <sub>4</sub> (propadiene)	C <sub>3</sub> H <sub>6</sub> (propene)			
C <sub>3</sub> H <sub>8</sub> (cyclopropane)					C <sub>2</sub> H <sub>6</sub>	CH <sub>3</sub> Cl	C <sub>2</sub> H <sub>5</sub> Cl	H	HCl
<Liquid species>									
Ti	TiCl <sub>4</sub>	Si							
<Solid species>									
Ti	Ti(alpha)	Ti(beta)	TiC	TiCl <sub>2</sub>	TiCl <sub>3</sub>	TiH <sub>2</sub>	TiSi		
TiSi <sub>2</sub>	Ti <sub>5</sub> Si <sub>3</sub>	Si	SiC(alpha)	SiC(beta)	C(diamond)				

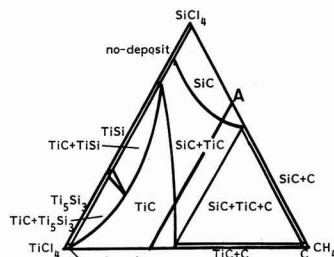


Fig. 1. Phase diagram in SiCl<sub>4</sub>-TiCl<sub>4</sub>-CH<sub>4</sub>-H<sub>2</sub> system at 1350°C, 60Torr.

$$H_2(\text{SiCl}_4 + \text{TiCl}_4 + \text{CH}_4) = 6$$

apparatus. By fixing the CH<sub>4</sub> flow rate constant and by controlling the flow rates of SiCl<sub>4</sub> and TiCl<sub>4</sub> in the feed gas, we varied the Ti/(Ti + Si) ratio, which is the concentration ratio of chemical species in the feed gas, and had TiC-SiC system composites deposited in various thicknesses from about 0.2 to 2.0mm on the substrate. The afore-mentioned control of flow rates of SiCl<sub>4</sub> and TiCl<sub>4</sub> in feed gas was carried out by adjusting the flow rate of carrier gas of H<sub>2</sub> for respective SiCl<sub>4</sub> and TiCl<sub>4</sub> vapors, which were kept at a constant temperature. H<sub>2</sub> gas concentration in feed gas was controlled nearly constant by introducing the H<sub>2</sub> gas from an independent supply system. Table 2 shows the CVD process conditions for synthesis of TiC-SiC composites along the composition line A given in Fig.1. The thickness of deposited layer was determined by optical microscopic observation of the cross-section of the layer. The deposited phases were identified by X-ray diffraction analysis, the composition of the deposited layer was quantitatively determined by chemical analysis, and the texture of the deposited layer was observed using an optical microscope, a scanning electron microscope (SEM) and a transparent electron microscope (TEM).

3. 2. Characterization

Using the specimens of deposited layers after the graphite substrates were removed, we measured the density by Archimedeian method, and measured the thermal expansion coefficient in parallel direction to the substrate surface in the temperature range from room temperature to 600°C using a thermal expansion measurement apparatus by differential transformer method. Concerning the measurement of Young's modulus, test specimens were prepared by cutting the specimens of deposited layers after the substrates were removed in a size of 10x-10mm, and by polishing them on surfaces parallel to the substrate surface. We measured

Table 2. The CVD conditions for fabrication of TiC-SiC composites.

point	a	b	c	d	e	f	g
SiCl <sub>4</sub> (l/min)	0.52	0.31	0.26	0.18	0.14	0.09	0
TiCl <sub>4</sub> (l/min)	0	0.15	0.18	0.23	0.32	0.37	0.31
CH <sub>4</sub> (l/min)	0.25	0.25	0.25	0.25	0.25	0.25	0.25
H <sub>2</sub> (l/min)	4.75~5.04						

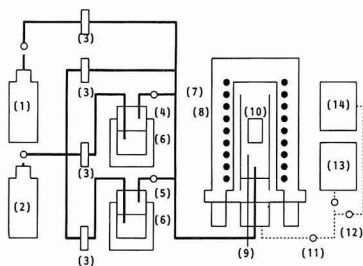


Fig. 2. Schematic diagram of the CVD apparatus. (1) CH<sub>4</sub> gas, (2) H<sub>2</sub> gas, (3) flowmeter, (4) TiCl<sub>4</sub> reservoir, (5) SiCl<sub>4</sub> reservoir, (6) electric thermo-bath, (7) CVD furnace, (8) graphite heater, (9) thermocouple (10) substrate, (11) pressure regulator, (12) exhaust exchange-valve (13) rotary pump, (14) water pump.

the propagation velocity of supersonic beam through the specimen above prepared in the thickness direction at the room temperature using a supersonic pulse, and calculated the Young's modulus from the propagation velocity.<sup>18)</sup> In connection to this measurement of Young's modulus, we measured the thickness of test specimens at 10 different points on the surface using a micrometer.

When we investigate the coatings of TiC-SiC system with gradient composition, we need to know the physical properties of the coatings in parallel direction to the substrate surface. But it was difficult for us to measure Young's modulus in this direction, because thin plate-like specimens in a maximum thickness of about 2mm only were obtained in our experiment. We were therefore obliged to measure the Young's modulus in a direction perpendicular to the substrate surface.

As seen in Fig.3, a supersonic beam supplied from a supersonic probe propagates through water and is reflected by a reflector. When the difference of propagation time between the cases that specimen exists and does not exist in this passage of supersonic beam is expressed by ΔT, it is expressed by equation (3) below.

$$\Delta T = 2d(1/V_w - 1/V_d) \dots \dots \dots (3)$$

Here, d is thickness of specimen, V<sub>w</sub> is propagation velocity in water, and V<sub>d</sub> is propagation velocity in specimen. When density and Poisson's ratio of specimen are respectively expressed by ρ and ν, Young's modulus (E) at a constant temperature is expressed by equation (4) below. Poisson's ratio of the TiC-SiC composites we applied was 0.24.

$$E = \rho V_d^2 \frac{(1 + \nu)(1 - 2\nu)}{(1 - \nu)} \dots \dots \dots (4)$$

4. Results and Discussion

4.1. Fabrication

Figure 4 shows two relationships between Ti/(Ti + Si) and composition of deposited phase respectively obtained by calculation and measurement. Here, Ti/(Ti + Si) is the ratio of Ti atomic concentration against total atomic concentration of Ti and Si in the feed gas. We could synthesize the composites in the full compositional range from 100%TiC to 100%SiC by controlling the composition of feed gas. SiC content in the composite by measurement tended to be higher than that by calculation, and this tendency became more remarkable with the increase of Ti/(Ti + Si) atomic ratio.

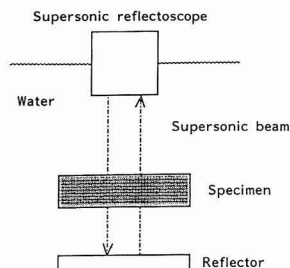


Fig. 3. Schematic diagram of supersonic pulse method for measurement of Young's Modulus.

Figure 5 shows the relationship between composition of deposited phase and deposition rate. The deposition rate slightly decreased with the increase of TiC content in the deposited phases, but it could be deemed as nearly constant.

Based on the experimental condition that  $(Ti + Si)/C$  value, which is the ratio of total atomic concentration of Ti and Si against that of C in the feed gas, is nearly constant, we assume that SiC is deposited preferentially to TiC with the increase of  $Ti/(Ti + Si)$  value when a mixed gas of  $SiCl_4$  and  $TiCl_4$  is used.

According to the study by Goto et al. using the feed gases of  $SiCl_4$ - $TiCl_4$ - $CCL_4$ - $H_2$  system,<sup>6)</sup> TiC content in the deposited composites by measurement was higher than that by calculation when a coating temperature of 1300°C was applied. This result was contrary to ours, though the temperature applied was nearly the same. They also reported that SiC content in the composites tended to increase with the increase of coating temperature, so that the SiC content by measurement became higher than that by calculation when the coating temperature was increased to 1600°C, and that this tendency became more remarkable with the increase of  $Ti/(Ti + Si)$  value. These results suggest that the deposition rate of SiC increases with the increase of coating temperature and with the increase of  $Ti/(Ti + Si)$  value, and that the deposition preferentiality of SiC and TiC is reversed at a certain temperature.

Our study results agreed well with those by Goto et al., if we exclude our result that the deposition rate of SiC was higher than that of TiC at a relatively low coating temperature of 1300°C. We assume that the higher deposition rate

of SiC at 1300°C in our study is mainly attributed to the different kind of carbon source in the feed gas we used from that Goto et al. used, namely, the critical temperature to determine the deposition preferentiality of SiC and TiC decreases when  $CH_4$  is used as the carbon source in the feed gas.

#### 4.2. Microstructures

Figure 6 shows the optical microscopic structures of TiC-SiC system composites on their cross-sectional surfaces. Dense columnar structures developed perpendicular to the substrate surface are observed, which agreed with the results Goto et al. reported.<sup>9,10)</sup> As shown in Fig.7, the density values measured nearly agreed with those calculated on the basis of the law of mixture in components. When the micrographs and the compositions of the composites are compared and contrasted to each other, it is estimated that the dark parts in the micrographs correspond to SiC and the bright parts to TiC. In the region of SiC-rich composition in the micrographs, it was as if SiC in the dark parts and TiC in the bright parts did not finish growing completely by themselves. It was also observed that wedge-shaped structures were partially contained in the columnar structures.

Figure 8 shows a TEM micrograph of the columnar structure containing this wedge-shaped structure. The wedge-shaped crystal was found to take an inclination of about 30 degree to the columnar crystal, which developed

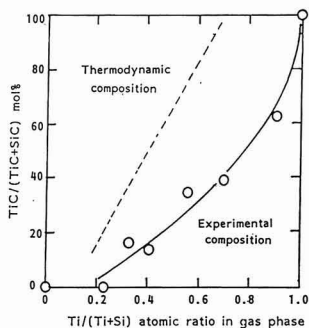


Fig. 4. Relationship between the composition of TiC-SiC composites and the feed gases composition.

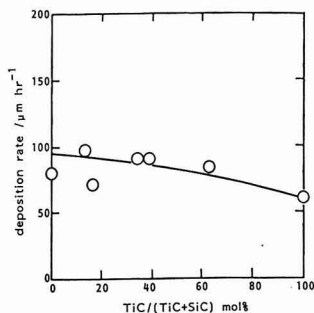


Fig. 5. The deposition rate of TiC-SiC composites.

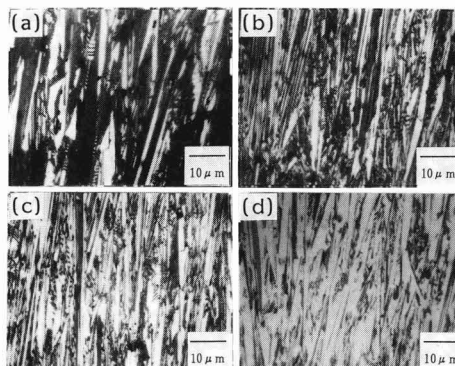


Fig. 6. The cross-sectional surface of TiC-SiC composites.

- (a) TiC 13.8 mol%, (b) TiC 34.3 mol%,  
(c) TiC 38.7 mol%, (d) TiC 62.8 mol%.

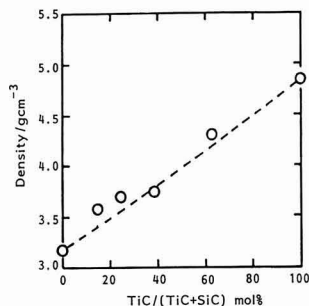


Fig. 7. Relationship of the composition of TiC-SiC composites and the density.

perpendicular to the substrate surface.

Figure 9 shows the X-ray diffraction patterns of various phases in the TiC-SiC composites. As both TiC and SiC take the same cubic crystalline structure (face-centered cubic), and have extremely similar lattice constants (SiC:  $a=4.358\text{\AA}$ , TiC:  $a=4.3285\text{\AA}$ ), they showed sharp X-ray diffraction lines at nearly the same position, but showed different orientations depending on the composition of deposited phase. The single TiC phase exhibited a strong (200) orientation, while the single SiC phase did not but exhibited two strong orientations of (200) and (111). In contrast, the TiC-SiC composite phase exhibited a strong diffraction from (220) plane and a very weak diffraction from (111) plane; the former diffraction became stronger and the latter became weaker with the increase of SiC content in the composite. Since (111) and (220) planes are calculated as crossing each other at an angle of about 35 degree based on the angle between the planes, the diffraction lines for the (111) plane are supposed to have been reflected from the wedge-shaped structures.

We assume that those strong (220) orientations the com-

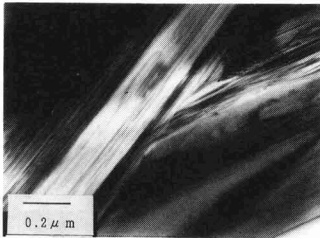


Fig. 8. The cross-sectional surface of 34.3 mol% TiC-SiC composite.

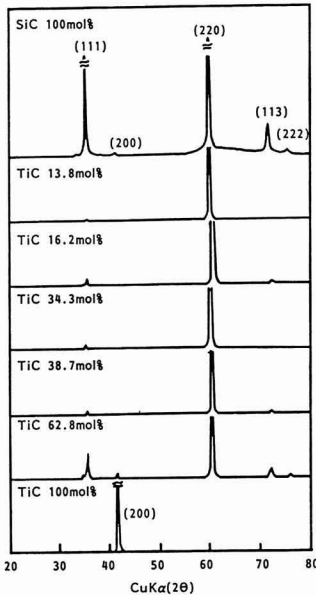


Fig. 9. X-ray diffraction patterns of TiC-SiC composites.

posite phases exhibited are attributed to the similar behaviors of TiC and SiC crystals to epitaxial growth as if these two kinds of crystals act mutually as the nucleus for the crystal growth of the other crystal.

4.3. Young's Modulus

Regarding the calculation equation of Young's modulus of composite materials, a model equation proposed by Voigt and one proposed by Reuss are available.<sup>19)</sup> Equations (5) and (6) shown below are obtained by applying these model equations to our experimental system. Upper and lower limit values of Young's modulus of the composite materials are determined by these equations (5) and (6). That is, the upper limit value of Young's modulus ( $E_U$ ) is calculated by equation (5) when a unidirectional stress is give parallel to the layer of the composite materials, and the lower limit value of Young's modulus ( $E_L$ ) is calculated by equation (6) when a unidirectional stress is given perpendicular to the layer, if we presume that the specimen is simply constructed with a perpendicular layer or one parallel to a given unidirectional stress. In the case of actual composite materials produced, the calculated limit values of Young's modulus ( $E_{cal}$ ) are obtained as an intermediate value between  $E_U$  and  $E_L$  due to the effect of combined orientation of crystal structure.

$$E_u = E_{TiC}V_{TiC} + E_{SiC}V_{SiC} \dots \dots \dots (5)$$

$$E_L = \frac{E_{TiC}E_{SiC}}{(E_{TiC}V_{SiC} + E_{SiC}V_{TiC})} \dots \dots \dots (6)$$

Here,  $E_{TiC}$  and  $V_{TiC}$ , and  $E_{SiC}$  and  $V_{SiC}$  respectively indicate Young's modulus and volume fraction of TiC and SiC.

In the case of TiC-SiC composites fabricated in our experiments, the crystal structure grew perpendicular to the substrate surface independent of the composition of the composites, and Young' modulus was measured in the perpendicular direction to the substrate surface. Unde such conditions the calculated value of Young's modulus ( $E_{cal}$ ) in the perpendicular direction to the substrate surface is expressed by equation (7) below, if equation (5) is presumed to be applicable to this calculation.

$$E_{cal} = E_U \dots \dots \dots (7)$$

Figure 10 compares the measured and calculated values of Young's modulus of TiC-SiC composites in the perpendicular direction to the substrate surface at room temperature.

The measured Young's modulus values of the single phases of TiC and SiC almost agreed with the respective literature values,<sup>20,21)</sup> and those of TiC-SiC composites changed almost continuously with the change of composition of the composite in the whole range of Young's modulus of 220 and 467GPa. These experimental values of 220 and 467GPa obtained for the respective terminal compositions were used as  $E_{TiC}$  and  $E_{SiC}$  in our calculation. The error in the measurement of specimen thickness, as seen in Fig.10, is assumed to be attributed to the different specimen thicknesses. In fact, the error size became smaller with the increase of specimen thickness. The measured values were a little smaller than the calculated ones. This difference is assumed to have been caused by the coexistence of columnar structures perpendicular to the substrate surface and other structures which grew in different directions.

4.4. Thermal Expansion Coefficients

Regarding thermal expansion coefficient  $\alpha$  of composite materials, equation (8) proposed by Turner<sup>22)</sup> is available.

$$\alpha = \frac{\sum \alpha_i V_i E_i}{\sum V_i E_i} \dots \dots \dots (8)$$

We calculated the thermal expansion coefficient of the TiC-SiC composites using this equation, and experimentally measured the mean thermal expansion coefficient of the composites in the range of room temperature and 600°C in the parallel direction to the substrate surface. **Figure 11** compares these two results. Respective Young's moduli and respective thermal expansion coefficients of TiC and SiC used in our calculation were our measured values.

Our measured values of thermal expansion coefficient of respective single phases of TiC and SiC almost agreed with the literature values.<sup>20,21)</sup> Our measured values of thermal expansion coefficient of the TiC-SiC composites in the intermediate composition range between 4.5 and 7.4×10<sup>-6</sup>K<sup>-1</sup> changed almost continuously with the change of composition of the TiC-SiC system composite, and almost agreed with the calculated values.

Regarding SiC-containing ceramic composites, Sasaki et al.<sup>23)</sup> and Uemura et al.<sup>21)</sup> respectively synthesized the C-TiC system composites and the C-SiC system composites by CVD process, and characterized the properties of these composites. They reported that Young's modulus and thermal expansion coefficient of these composites did not change continuously with the change of their composition. According to their interpretations, such discontinuous changing behaviors were caused by the content of a number of pores generated in the composites when C was compounded in TiC or SiC in the form of composite, and by the composition dependent change of the texture of the composites.

In the case of our TiC-SiC composites, we assume that Young's modulus and thermal expansion coefficient changed almost continuously with the change of composition of the composite, because pores of third component did not exist in the composites, and because the composites contained uniform columnar structures perpendicular to the substrate surface independent from the composition of the composite.

Regarding Young's modulus and thermal expansion coefficient of the TiC-SiC composites fabricated by the sintering process, Woydt et al.<sup>13)</sup> reported that they measured a Young's modulus of 4.586GPa and a thermal expansion coefficient of 5.7×10<sup>-6</sup>K<sup>-1</sup> in the case of the composite with

composition of 50vol%TiC-50vol% SiC (about 40mol%TiC-60mol%SiC) fabricated by hot press sintering process. The thermal expansion coefficient of 5.7×10<sup>-6</sup>K<sup>-1</sup> agreed well with what we obtained in our experiment, but the thermal expansion coefficient they reported was larger than that which we obtained in our experiment. Regarding the texture of sintered composite body, they did not say anything, but Endo et al.<sup>14)</sup> reported that the texture of sintered body fabricated by the hot press process (having the same composition as the sintered body fabricated by Woydt et al.) did not exhibit columnar structure as those which we obtained in our study. We suppose that the difference of the measured values of Young's modulus is mainly attributed to the orientation of the composite tested, but we could not clarify the reasons for the difference any further.

5. Conclusion

The authors fabricated TiC-SiC composites by CVD process, measured Young's modulus and thermal expansion coefficient, and compared the measured values of respective properties of the composites with the calculated ones, obtaining the following conclusions.

- 1) TiC-SiC composites having various compositions ranging from 100mol% TiC to 100mol%SiC were synthesized by adjusting the Ti/(Ti + Si) atomic ratio in the feed gas based on the thermodynamic calculation results with a feed gas of SiCl<sub>4</sub>-TiCl<sub>4</sub>-CH<sub>4</sub>-H<sub>2</sub> system. In the synthesis process condition of a temperature of 1350°C and a pressure of 60Torr, the deposition rate of the composite was about 60 to 100µm/h. The experimentally measured composition of the composites synthesized was higher in SiC content than the calculated one.
- 2) It was confirmed that the TiC-SiC composites were mainly composed of dense columnar structures which grow perpendicular to the substrate surface. It was also confirmed that the composites partially contained wedge-shaped structures, which were supposed to exhibit (111) orientation, different from (220) orientation exhibited by columnar structures.
- 3) Young's modulus of the TiC-SiC composites measured in a direction parallel to the growing direction of the composite changed nearly continuously with the change of composition of the composite in the range of modulus

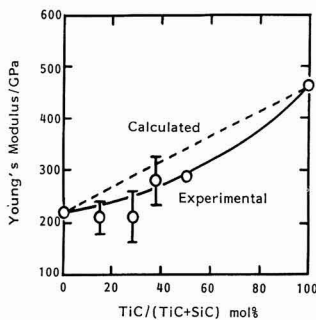


Fig. 10. Young's Modulus of TiC-SiC composites.

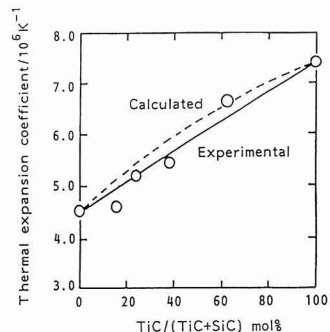


Fig. 11. Thermal expansion coefficients of TiC-SiC composites.

value of 2.20 and 4.67GPa. These measured values were a little smaller than the calculated ones. The reason for such difference was assumed to be due to the partial existence of wedge-shaped structures, which had a different orientation from the columnar structures.

- 4) Thermal expansion coefficient measured in a direction perpendicular to the growing direction of the TiC-SiC composites changed nearly continuously with the change of composition of the composite in the range of 4.5 and  $7.4 \times 10^{-6} \text{K}^{-1}$ . These measured values nearly agreed with the calculated ones.

Remarks: Part of this paper was presented at the 1990 Autumn Symposium of the Ceramic Society of Japan, held in September 1990.

(This study was performed through Special coordination Funds of the Science and Technology Agency of Japanese Government.)

#### Acknowledgements

The authors wish to thank Mr. Michio Shimada, senior researcher of the Research Laboratory for Ships for his assistance in our current study.

#### References:

- 1) C. Kawai and Y. Igarashi, Proc. 3rd Sympo. on functionally gradient materials (1989), 79-83.
- 2) S. Uemura, Y. Sohda and Y. Kude, *ibid.*, 69-73.
- 3) M. Touanen, F. Teyssandier and M. Ducarroir, *J. Physiq., Colloq. C5*, supp. 50, 5, 105-113 1989.
- 4) M. Touanen, F. Teyssandier and M. Ducarroir, *J. Mater. Sci. Lett.*, 8, 98-101 (1989).
- 5) D.P. Stinton, W.J. Lackey, R.J. Lauf and T.M. Besmann, *Cer. Eng. Sci. Pro.*, 5, 668-676 (1984).
- 6) T. Goto and T. Hirai, *J. Chem. Soc. Jpn.* 11, 1939-1945 (1987).
- 7) T. Goto and T. Hirai, Proc. 10th Int. Conf. on CVD (1987) 1070-1079.
- 8) T. Goto and T. Hirai, Proc. abstract, Spring Mtg. Funtai-Funmatsu-Yakin Kyokai (1987) 184-185.
- 9) T. Goto and T. Hirai, *Funtai-oyobi-Funmatsu-Yakin*, 34, 487-490 (1987).
- 10) T. Goto and T. Hirai, Proc. Ceram. Soc. Jpn. Ann. Mtg. 2 (1987) 545-546.
- 11) J.J. Nickle, K.K. Schweitzer and P. Luxenberg, *J. Less-Common Metals*, 26, 335-353 (1972).
- 12) H. Endo, M. Ueki and H. Kubo, *J. Mater. Sci.* 25, 2503-2506 (1990).
- 13) M. Woydt, J. Kadoorit, H. Hausner and K.H. Habig, *Ceram. Forum. Int.*, 67, 123-130 (1990).
- 14) H. Endo, K. Tanemoto and H. Kubo, *Sinter* 87, 2, 1052-1057 (1988).
- 15) H. Endo, M. Ueki, A. Kubo and J. Sugawara, *Zairyo-to-Purosesu*, 2, 1360 (1989).
- 16) H. Endo, M. Ueki and A. Kubo, *ibid.* 1, 431 (1988).
- 17) S.G. Seshadri, M. Srinivasan and K.M. Keeler, *Ceram. Eng. Sci. Proc.*, 8, 7-8, 671-684 (1987).
- 18) M. Shimada and S. Amada, Proc. 3rd Sympo. on Functionally gradient Materials (1989) 125-128.
- 19) W.D. Kingery, H.K. Bowen and D.R. Uhlmann, *Introduction to Ceramics*, John Wiley & Sons, New York (1976) 774.
- 20) G.V. Samonov, *High-Temperature Materials*, 2, Properties Index, Plenum Press, New York (1964) 179.
- 21) S. Uemura, Y. Sohda and Y. Kude, Proc. 1st Int. Sympo. on Functionally Gradient Materials (1990) 237-241.
- 22) P.S. Turner, *J. Res. National Bureau Standards* (1946) 239.
- 23) M. Sasaki and T. Hirai, Proc. 1st int. Sympo. on Functionally Gradient Materials (1990) 231-235.

---

This article is a full translation of the article which appeared in *Nippon Seramikusu Kyokai Gakujutsu Ronbunshi* (Japanese version), Vol.99, No.11, 1991.

# Preparation of Porous SiO<sub>2</sub>-ZrO<sub>2</sub> Glass from Sol Containing Polyethylene Glycol

Tetsuo Yazawa, Akiko Miyake\* and Hiroshi Tanaka

Government Industrial Research Institute, Osaka

8-31, Midorigaoka 1-chome, Ikeda-shi, 563 Japan

\*Shinko Pantec Co., Ltd.

4-78, Wakihama-cho 1-chome, Chuo-ku, Kobe-shi, 651 Japan

Porous SiO<sub>2</sub>-ZrO<sub>2</sub> glass was prepared from a sol containing polyethylene glycol (PEG) by the sol-gel method. After air-drying at room temperature, the gel was baked at 600°C. The ZrO<sub>2</sub> content in the porous glass was 30wt%. The median pore diameter of the porous glass was 2nm regardless of the molecular weight and amount of PEG added. The reproducibility of the pore size distribution as good, and the pore volume and surface were linearly proportional to the amount of PEG added. Alkali resistance of the porous glass was much larger comparing to the porous SiO<sub>2</sub> glass.

[Received March 22, 1991; Accepted July 18, 1991]

**Key-words:** Porous glass, Polyethylene glycol, Sol-gel method, Alkali resistance, Zirconium oxide, Organic polymer

## 1. Introduction

As inorganic porous materials, porous glasses can be experimentally produced by various processes, including a process by sintering of glass powder given with a controlled size distribution, a process based on phase separation and accompanied heat treatment of glasses at a temperature slightly than the glass transition point, a process by deposition of crystals in glasses and subsequent dissolution of chemically weak parts in the glass, and a process by the sol-gel method. Currently, the process based on phase separation is most common for the production of porous glasses. However, this process involves several problems such as a restricted selection of the composition of porous glasses, and difficulty obtaining a pore diameter smaller than 4nm. For instance, when we intend to make ZrO<sub>2</sub>, a high chemically resistant component contained in the skeleton of porous glasses, its content is badly restricted due to the vitrification region of starting glasses and the heat treatment condition for phase separation.<sup>1,2)</sup> In contrast, when the sol-gel method is used, the vitrification region is enlarged considerably and, in addition, the intermediates are porous bodies. Therefore, this method can be used for the production of porous glasses. Accordingly, many experiments have been conducted on the production of porous glasses, including porous SiO<sub>2</sub>-ZrO<sub>2</sub> glasses. However, these experimental results proved that various problems remained in the preparation of an even pore size and in the reproducibility thereof.

This paper reports our study results, in which we used the sol-gel method and successfully prepared porous SiO<sub>2</sub>-

ZrO<sub>2</sub> glasses containing 30wt% of ZrO<sub>2</sub> in their skeleton and contained pores in a median diameter of 2nm with good reproducibility. As afore-mentioned, porous glasses having a pore diameter smaller than 4nm are difficult to prepare by the process based on phase separation. When the pore diameter of 2nm is compared with that of various other inorganic materials, it is found, for instance, that the largest pore diameter of zeolite ranges from 1.2 to 1.3nm,<sup>6)</sup> that of intercalation compound ranges from 0.7 to 0.9nm,<sup>7)</sup> and that of molecular sieved active carbon, which belongs to a recent development, ranges from around 0.7 to 0.9nm.<sup>8)</sup> Therefore, the porous glasses having pore diameter of 2nm are deemed to be materials occupying a unique position among various inorganic porous materials.

## 2. Experimental Procedure

### 2.1. Preparation of Porous Glasses

Figure 1 illustrates a scheme of preparation process of porous glasses. We used 3 grades of polyethylene glycol (PEG), which is a linear polymer, such as PEG 600 having a mean molecular weight of 570 to 630, PEG 6,000 having that of 7,400 to 9,000, and PEG 20,000 having that of 18,000 to 25,000 (all of which were made by the Nakarai Yakuin Kagaku Kogyo Co.). Ethanol solution of tetraethoxy-silane (TEOS) containing one of the PEGs was added with water and hydrochloric acid in respective ratios

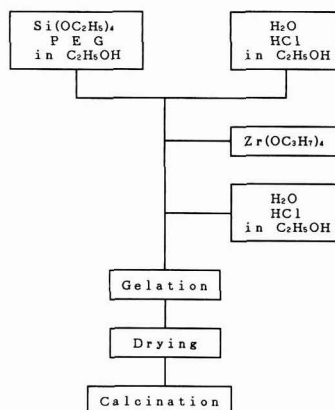


Fig. 1. Preparation process of porous glass.

of 1mol and 0.01mol to 1mol of TEOS, and was stirred for around 1h to make reaction. We call this reaction the first hydrolysis. Next, this solution was added with n-propoxide zirconium (NPZ) and stirred for around 1h. After that, it was added with ethanol solution containing water and hydrochloric acid in respective ratios of 1 to 8mol and 0.01mol to 1mol of TEOS. Thus the second hydrolysis took place.<sup>9)</sup> After stirring for around 10min, the gel formed was air-dried at room temperature and then baked at 600°C. The solution temperature during the stirring was controlled at room temperature when PEG 600 was used, and at 40°C when PEG 6,000 or PEG 20,000 was used in order to homogenize the solution.

## 2.2. Measurement of Pore Size Distribution

Both pore size distribution and pore volume were determined from the adsorption isotherm, of nitrogen at -196°C based on the Cranston Inkley method,<sup>10)</sup> in which a cylindrical model was presumed for a pore. Mean while, pore surface area was determined based on the BET formula (using an apparatus of Sorptometer 1,800, made by the Carlo Erbe Co.). Prior to these measurements, samples were pretreated at 150°C under a vacuum pressure of 452Pa

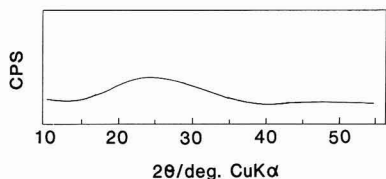


Fig. 2. XRD pattern of porous glass.

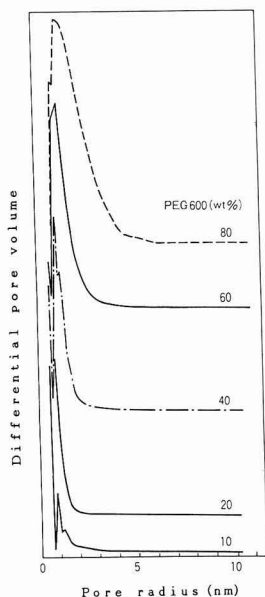


Fig. 3. Pore size distribution of porous glasses prepared from PEG 600.

for 2h.

## 2.3. Measurement of Alkali Resistance

Porous glasses (having pore surface area of 280m<sup>2</sup>/g) were prepared from the sol, which was prepared by adding water in the ratio of 2mol to 1mol of TEOS, and by adding PEG 600 by 20wt%. They were classified in the size range from 250 to 425μm. 5g of this glass powder was taken, washed with ethanol, dried under vacuum at 125°C, and then weighed. This powder sample was put in a sealed container made of teflon, in which it was dipped in 1N-aqueous solution of sodium hydroxide at 80°C for 140h. After rinsed, the sample was dried sufficiently in the same drying condition as applied to the original sample, and then weighed. Alkali resistance of the glass was determined from the weight loss ratio. For comparison we used porous SiO<sub>2</sub> glass (composition: SiO<sub>2</sub>=97wt% and B<sub>2</sub>O<sub>3</sub>=3wt%) having a pore diameter of 4nm and a pore surface area of 150m<sup>2</sup>/g. This pore surface area was almost the same as that of porous SiO<sub>2</sub>-ZrO<sub>2</sub> glasses prepared in this experiment.

## 3. Results and Discussion

### 3.1. X-ray Diffraction (XRD)

Figure 2 shows an XRD pattern of the porous glass sample we prepared. A very broad hollow appearing in the 2θ range of 15 and 25 degrees is assigned to amorphous SiO<sub>2</sub>. This XRD pattern without any sharp diffraction peak suggests that the porous glass we prepared is in the amorphous state.

### 3.2. Relationship Between Added Amount As Well As Molecular Weight of PEG and Pore Size

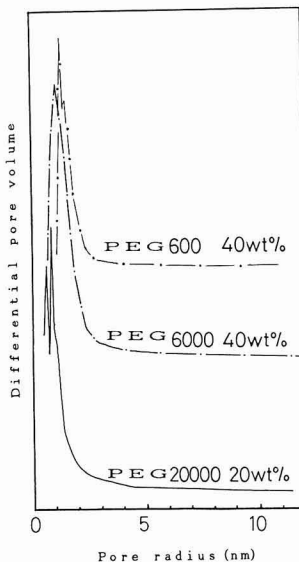


Fig. 4. Pore size distribution of porous glasses prepared from PEG 600, 6000 and 20000.

**Distribution**

Figure 3 shows respective pore size distributions when water was added in the ratio of 2mol to 1mol of TEOS and PEG 600 was added in various ratios from 10 to 60wt%. It is seen that the pore size distribution is a little broad in the case of the addition ratio of PEG 600 of 80wt%, but the median pore diameters are nearly the same regardless of the addition ratio of PEG 600 in the case of the various ratios other than 80wt%. Figure 4 shows the pore size distributions when various grades of (PEG as PEG 600, PEG 6,000 and PEG 20,000) having different molecular weight were added. It is seen that the pore size distribution does not depend much on the molecular weight of PEG added. Figure 5 shows the relationship between pore volume and pore surface area of the porous glasses prepared by adding PEG 600 in various ratios. It is seen that pore volume and pore surface area are almost linearly correlated. If a pore is presumed to take a cylindrical shape, then pore volume  $v$ , pore surface area  $s$  and pore diameter  $d$  are expressed in a relation of  $s=4v/d$ ; pore diameter  $d$  was thereby calculated as 2.34nm from the inclination of the linear relation line in Fig.5. Meanwhile, according to a study result on the adsorption of PEG from its aqueous solution onto molecular sieved active carbon,<sup>11)</sup> it was reported that the length of PEG molecule increased with the increase of molecular weight of PEG, but its diameter did not change so much with the increase of the molecular weight as to have been indicated as 1.4nm, 1.72nm and 1.678nm, respectively when the PEG used had various molecular weights of 600, 6,000 and 20,000. These diameters of PEG molecule reported almost agreed with the pore diameter of 1.34nm we calculated from the inclination of a relation line in Fig.5. Judging from this result of the agreement between the diameter of PEG molecule and the pore diameter, as well as from the result that pore diameter was independent of molecular weight and addition amount of PEG, as aforementioned (Figs.3 and 4), we assume that PEG molecules are contained in the SiO<sub>2</sub>-ZrO<sub>2</sub> matrix in such

unbroken state as shown in Fig.6.

**3.3. Relationship Between Amount of PEG Added and Pore Volume and Pore Surface Area in Porous Glasses**

Using the porous glass samples prepared in the same various conditions as mentioned in section 3.2, we investigated the effect of the amount of added PEG on the pore volume and the pore surface in the porous glasses. Figures 7 and 8 show the respective results. It is observed that both pore volume and pore surface area increased with the increase of the amount of PEG added. Volume and pore surface area in porous materials generally depend on pore size, but when linear polymers like PEG are contained in the matrix in such unbroken state as shown in Fig.6, a different behavior is shown to take place where both pore volume and pore surface area can be changed independent of pore size, as we previously mentioned in section 3.1.

A peculiar phenomenon is often experienced where porous glasses exhibit a black colour due to carbonization of residual organic materials during baking, especially when porous glasses containing fine pores in diameter of less than 5nm are prepared by the sol-gel method. These black-coloured porous glasses are found to have extremely reduced pore volume and pore surface area thereby, When PEG is added, however, such black colouring of porous glasses does not take place. The reasons for this different behavior are assumed to be that the pores generated by the baking of PEG provide passages for the gases generated during baking of the dried gels, and that the gases generated by the baking of residual organic materials are released through these passages together with the gases generated by

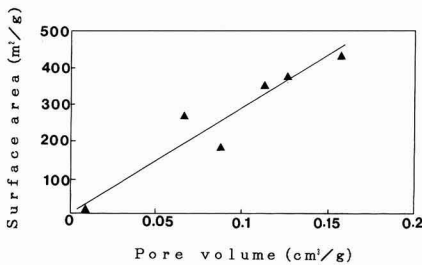


Fig. 5. Relation between pore volume and surface area of porous glasses.



Fig. 6. Structural state of PEG in SiO<sub>2</sub>-ZrO<sub>2</sub>.

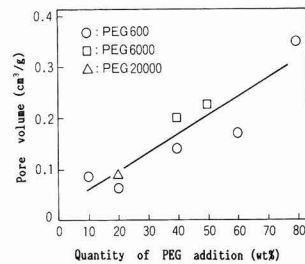


Fig. 7. Relation between quantity of PEG addition and pore volume of porous glasses.

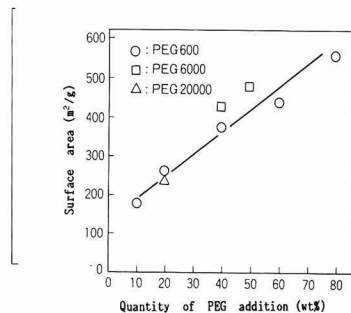


Fig. 8. Relation between quantity of PEG addition and surface area of porous glasses.

the baking of PEG.

### 3.4. Effect of Water Amount Added on Pore Size Distribution

In the course of the second hydrolysis of the sol, which was added with 70wt% of PEG 600, we added water in various ratios from 1 to 8mol against 1mol of TEOS content, and measured the pore size distribution in the porous glasses prepared. The results are shown in Fig.9. It is seen that the amount of water added has little effect on the pore size distribution as far as the ratio of water added is in the range as experimented.

### 3.5. Alkali Resistance

Table 1 shows the results of our alkali resistance test of the porous glass samples. As porous SiO<sub>2</sub> glass is dissolved completely in this test condition, its weight loss ratio is expressed as 100%. In contrast, the weight loss ratio of the porous SiO<sub>2</sub>-ZrO<sub>2</sub> glass we prepared was 7.4%. When compared with the weight loss ratio of 19.5% of slide glass, which is not porous, it is not difficult to evaluate the porous glasses we prepared as extremely alkali resistant.

### 3.6. Thermal Resistance

We experimentally investigated the thermal resistance of the porous SiO<sub>2</sub>-ZrO<sub>2</sub> glasses, which we prepared from a sol added with 30wt% of PEG, after baking at various temperatures from 600° to 900°C for 24h. As an additional test condition, we applied a baking time of 48h in the case of baking temperature of 600°C. Table 2 shows the pore volume and the pore surface area of the samples after baking in various baking conditions. It was learnt that, when the baking temperature was 600°C, both pore volume and pore surface area changed little with the change of baking time from 24h to 48h, but when the baking temperature was increased, they both decreased with the increase of temperature until they disappeared at 900°C, which implied the porous glasses were sintered completely. The overall results

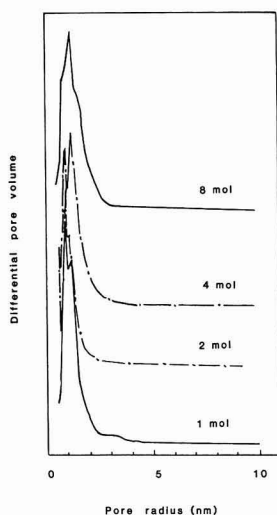


Fig. 9. Addition effect of water on pore size distribution at the second hydrolysis.

Table 1. Rate of weight loss of glass samples.

Glass	Rate of weight loss (%)
SiO <sub>2</sub> -ZrO <sub>2</sub> porous glass	7.4
SiO <sub>2</sub> porous glass by phase separation	100.0
Slide glass	19.5

Composition of slide glass

SiO<sub>2</sub> 68, Na<sub>2</sub>O 8.0, CaO 6.0, K<sub>2</sub>O 7.5,  
Al<sub>2</sub>O<sub>3</sub> 2.5, BaO 3.3 (wt%)

Table 2. Thermal resistance of porous glasses.

Conditions °C	h	Pore volume cm <sup>3</sup> /g	Surface area m <sup>2</sup> /g
600	24	0.12	280
600	48	0.12	275
700	24	0.034	173
800	24	0.0086	33.4
900	24	0	0

here suggest that the porous SiO<sub>2</sub>-ZrO<sub>2</sub> glasses we prepared are thermally resistant up to around 600°C.

## 4. Conclusion

Porous SiO<sub>2</sub>-ZrO<sub>2</sub> glasses containing about 30wt% of ZrO<sub>2</sub> were prepared by the sol-gel method, and the following results were obtained from the preparation process and the prepared products.

- 1) The said porous glasses containing fine pores in diameter of around 2nm could be produced with good reproducibility.
- 2) Pore volume and pore surface area in the said porous glasses increased almost linearly with the increase of the amount of PEG added.
- 3) Pore size in the said porous glasses was independent of the molecular weight of PEG added.
- 4) Alkali resistance of the said porous glasses was by far greater than that of porous SiO<sub>2</sub> glasses, even those having nearly the same pore surface area as the former glasses.
- 5) Thermal resistance of the said porous glasses was around 600°C.

The authors previously prepared multi-layer films of porous SiO<sub>2</sub>-ZrO<sub>2</sub> glasses,<sup>12)</sup> which were desalted in the ratio of about 90% (feed solution: 0.5wt% NaCl aqueous solution). The porous SiO<sub>2</sub>-ZrO<sub>2</sub> glasses we prepared in this study are expected to be used for separation films. It is supposed, in addition, that not only pore size but also pore morphology might be possibly changed by the selection of organic polymers to be added.

### References:

- 1) T. Yazawa, H. Tanaka, K. Eguchi and T. Arai, *Seramikkusu Ronbunshi*, 99, 351-353 (1991).
- 2) K. Eguchi, H. Tanaka, T. Yazawa and T. Yamaguro, *Proc. Ceram.*

- Soc. Jpn. Ann. Mtg., 1, (1986) 493-494.
- 3) M. Nogami, *Yogyo-Kyokaishi*, 93, 39-44 (1985).
  - 4) M. Nogami and K. Nagasaka, *J. Non-Cryst. Solids*, 109 79-84 (1989).
  - 5) T. Adachi, S. Sakuhana and M. Okada, *Yogyo Kyokaishi*, 95, 970-975 (1987).
  - 6) M.E. Dabis, C. Saldarriaga, C. Montes, J. Garces and C. Crowder, *Nature*, 331, 698-699 (1988).
  - 7) S. Yamanaka and S. Hattori, *Takousei Seramikkusu no Kaihatsu to Ouyou, CMC* (1984) 171-186.
  - 8) Y. Eguchi, *Hyohmen*, 10, 521 (1972).
  - 9) M. Nogami and K. Nagasaka, *Seramikkusu Ronbunshi*, 96, 925-929 (1988)
  - 10) R.W. Cranston and F.A. Inkley, *Adv. in Catalysis*, 9, 143-145 (1957).
  - 11) S. Kasaoka, E. Tanaka, Y. Sakata and R. Naito (1987) 2267-73.
  - 12) T. Yazawa, H. Tanaka, H. Nakamichi, K. Eguchi and T. Yokoyama, *Proc. Ceram. Soc. Jpn. Ann. Mtg.* (1990) 559.
- 

This article is a full translation of the article which appeared in *Nippon Seramikkusu Kyokai Gakujutsu Ronbunshi* (Japanese version), Vol.99, No.11, 1991.

# Sintering of High Purity ZrSiO<sub>4</sub> Powder

Toshiyuki Mori, Hiroshi Yamamura, Hidehiko Kobayashi\* and Takashi Mitamura\*

Tosoh Co., Ltd., Tsukuba Research Laboratory  
43 Miyukiga-oka, Tsukuba-shi, 305 Japan

\*Department of Applied Chemistry, Faculty of Engineering, Saitama University  
255, Shimo-ohkubo, Urawa-shi, 338 Japan

By measuring shrinkage and bulk density of the specimens at 900 ~ 1700°C, sintering of three kinds of high purity ZrSiO<sub>4</sub> powders prepared from 0.2 ~ 0.8M ZrOCl<sub>2</sub> and colloidal silica was studied. The flexural strength of their sintered bodies at room temperature to 1400°C was also evaluated to investigate the effect of sintering conditions. In the initial stage of sintering of high purity ZrSiO<sub>4</sub> powders with an average particle size of 0.5µm, grain boundary diffusion was a dominant factor. The apparent activation energy for sintering in the initial stage was 81 KJ/mol. On the other hand, when the average diameter of the particles is greater than 0.7µm, the bulk diffusion seemed to be overwhelming, and the apparent activation energy for sintering was higher than 130 KJ/mol. In the intermediate and final stages for sintering, the powders with relatively large sizes have resulted in high bulk density. However, the strength of the specimen obtained using powders with large grain sizes was low since the grain growth proceeded significantly. The sintered bodies of high-purity ZrSiO<sub>4</sub> with excellent flexural strength at high temperature were obtained by sintering the powder with the average particle size of less than 0.5µm up to more than 98% of theoretical density.

[Received April 1, 1991; Accepted July 18, 1991]

**Key-words:** High purity ZrSiO<sub>4</sub> powder, Particle size, Sintering Process, High temperature bending strength.

## 1. Introduction

Zircon (ZrSiO<sub>4</sub>) sintered bodies, studied for use mainly as refractories because they have a low coefficient of thermal expansion and low heat conductivity,<sup>1,2,4)</sup> are expected to be developed for use at high temperatures, such as mullite (3Al<sub>2</sub>O<sub>3</sub>·2SiO<sub>2</sub>) sintered bodies. They also have high chemical stability; they are resistant to glass corrosion.<sup>5,6)</sup> On sintering zircon, however, densification is now performed usually with TiO<sub>2</sub> or other additives being used as sintering aids.<sup>7,8)</sup>

The authors conducted studies on the synthesis of high purity ZrSiO<sub>4</sub> powder and succeeded in the synthesis of high purity ZrSiO<sub>4</sub> powder suitable for sintering.<sup>9,11)</sup> We also reported that, by using this powder as a starting material, ZrSiO<sub>4</sub> powder was densified with no sintering aid of oxide (which has been considered necessary for densification), and that the densified ZrSiO<sub>4</sub> has excellent properties at high temperatures.<sup>12)</sup> In the present study, we investigate some factors affecting the sintering of zircon prepared from synthesized high purity ZrSiO<sub>4</sub> powder, and evaluate their ef-

fects on the properties of the sintered body.

## 2. Experimental Method

### 2.1. Synthesis of High Purity ZrSiO<sub>4</sub> Powder

The starting materials were ZrOCl<sub>2</sub> (Tosoh Corporation) used as a zirconium material and colloidal silica (Nissan Chemical Industries, Ltd.) of 20wt% concentration used as a silica material. The ZrSiO<sub>4</sub> powder was synthesized by the following method.

Equal moles of ZrOCl<sub>2</sub> and colloidal silica were weighed, and hydrolysis was performed while refluxing by heating at 100°C for a specified time. To verify the completion of hydrolysis, hydrolyzed liquid was centrifugally separated at 15,000 rpm, and the Zr concentration in the aqueous solution obtained by filtering the supernatant liquid was analyzed. When unreacted ZrOCl<sub>2</sub> almost disappeared, the hydrolysis was regarded as being completed. After the hydrolyzed liquid thus obtained was dried, dechlorination was performed at 500°C. After dechlorination, the material was heated to 1400°C at a heating rate of 20°C/min, and then calcined for 8 hours to produce single-phase ZrSiO<sub>4</sub> powder.

By using the above method, three kinds of powders were prepared by changing ZrSiO<sub>4</sub> concentration into 0.2M, 0.4M and 0.8M to evaluate the difference in sintering.

The synthesized powders were evaluated by measuring the purity and particle size distribution. For the chemical analysis of powders, determination was performed by using the weight method by alkali fusion for Zr, the ICP emission method for Fe, Y, Ti, Ca, Mg, V, Cr, P, Ni, and Mn, the atomic absorption method by lithium tetraborate fusion for Na, the graphite atomic absorption method by lithium tetraborate fusion for Al, the weight method for Si, and the atomic absorption method for Cl. The particle size measurement of powder was performed after the powder was dispersed ultrasonically in distilled water for 30 minutes. For evaluating sintered bodies, shrinkage and three-point bending strength were measured and the microstructure of the sintered body was observed. The shrinkage was measured by using a thermal expansion meter (TMA), and the three-point bending strength was measured at room temperature and at temperatures in the range between 1000°C and 1400°C. The microstructure was observed with a scanning electron microscope (SEM) after thermal etching was performed.

### 2.2. Method for Evaluating Sintering of ZrSiO<sub>4</sub> Powder

The synthesized ZrSiO<sub>4</sub> powder was repressed at a molding pressure of 49MPa, and then compacts were prepared with a rubber press at 196MPa. The compacts were heated

to a specified temperature (1100°-1700°C) at a heating rate of 200°C/h, and kept at that temperature for a specified time (20min-48h) to prepare ZrSiO<sub>4</sub> sintered bodies.

The initial sintering stage of ZrSiO<sub>4</sub> was defined as the stage in which the shrinkage of sintered body is up to 5%. The change in shrinkage in this stage was measured by TMA, and the activation energy in the initial sintering stage was calculated from the shrinkage. In the intermediate and final stages, the sintering was evaluated by measuring the bulk density of the sintered body.

The obtained sintered bodies were cut into 3×40×40 mm specimens. The specimens were ground with #140 and #600 grindstones. After the bulk density was measured, the strength was measured at room temperature and at 1000°-1400°C, and the microstructure was observed with a SEM after thermal etching.

3. Results and Discussion

3.1. Initial-stage Sintering of ZrSiO<sub>4</sub>

Figure 1 shows the particle size distribution of three kinds of zircon powders and their SEM photographs.

Regarding the particle size distribution, the powder synthesized from 0.4M ZrOCl<sub>2</sub> aggregated less, and its particle size was very small--the average particle size being 0.51µm. The powders synthesized from 0.2M and 0.8M ZrOCl<sub>2</sub> have an average particle size of 0.96µm and 0.71µm, respectively. The SEM observation also revealed that these powders were aggregated.

The three kinds of powders used in this experiment have nearly the same level of purity and chlorine concentration.

Their values are summarized in Table 1. The reflux time is also given in Table 1. Although the factors affecting the cohesiveness and particle size of powder cannot be determined from this result, there seems to be a tendency for the obtained powder to aggregate strongly during drying of hydrolysis gel when a material with high concentration is used. The chlorine concentration is so sufficiently low that it does not affect the sintering.

In general, the rate of initial sintering is given by the following equation.

$$\Delta L/L_0 = (A\gamma\Omega D/kT)^n t^r \dots \dots \dots (1)$$

where, *r* is the surface energy,  $\Omega$  is a volume of void, *D* is the self-diffusion coefficient, *K* is the Boltzmann's constant,

Table 1. Chemical compositions of synthetic zircon powders.

	Zr O <sub>2</sub>	Si O <sub>2</sub>	Fe	Ti	Ca	Mg	Ni
0.2M powder	65.4	32.0	<0.01	0.005	<0.005	<0.002	0.002
0.4M powder	66.2	31.8	<0.01	<0.005	<0.005	<0.002	0.004
0.8M powder	65.4	32.0	<0.01	0.006	<0.005	<0.002	0.002

	Mn	V	Na	Al	Y	C1
0.2M powder	<0.001	<0.001	0.044	0.03	0.04	300
0.4M powder	0.001	0.002	0.023	0.15	0.04	200
0.8M powder	<0.001	<0.001	0.044	0.03	0.04	190

	reflux time(h)
0.2M powder	264
0.4M powder	312
0.8M powder	240

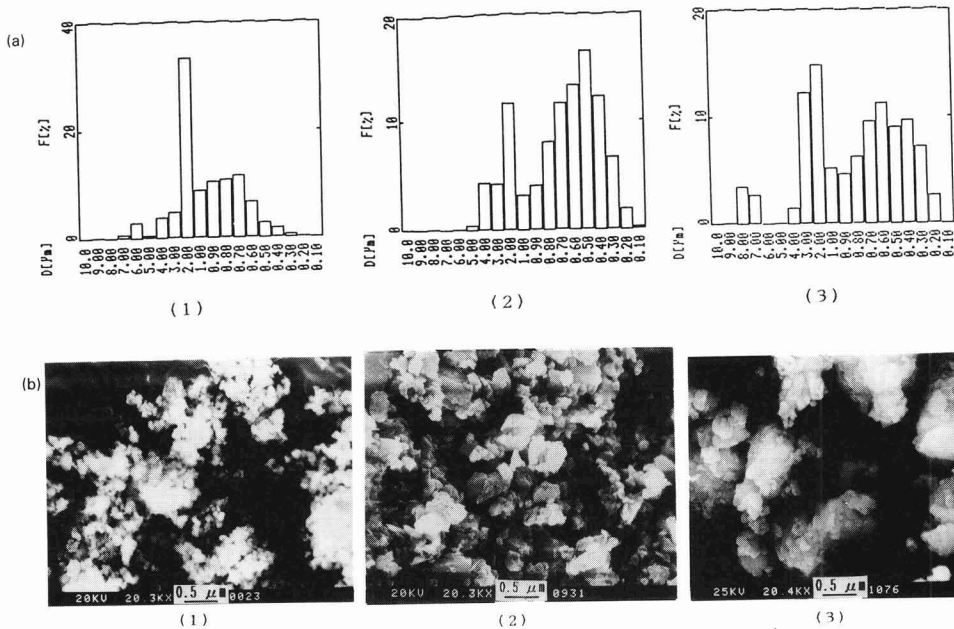


Fig. 1(a) Particle size distributions for three kinds of zircon powders: (1) 0.2M powder (2) 0.4M powder and (3) 0.8M powder. (b) SEM images of three kinds of zircon powders: (1) 0.2M powder (2) 0.4M powder and (3) 0.8M powder.

$r$  is the particle size, and  $A$ ,  $p$  and  $n$  are the constants that depend on the sintering mechanism.

**Figure 2** shows the linear shrinkage as a function of holding time at temperatures between 1100°C and 1350°C for the powder synthesized from 0.4M ZrOCl<sub>2</sub> shown in Fig.1. From the result of Fig.2, the slope of line was taken as 0.22 to 0.27. If the initial sintering proceeds due to grain boundary diffusion, the relation of  $n=0.25$  to 0.31 holds theoretically.<sup>13</sup> In the range of experiment shown in Fig.2, therefore, the sintering seems to proceed with the grain boundary diffusion being the dominant factor.

**Figures 3 and 4** show the linear shrinkage as a function of holding time at temperatures between 1100°C and 1350°C for the powder synthesized from 0.2M and 0.8M ZrOCl<sub>2</sub> shown in Fig.1, respectively. The slope of line was taken as 0.27 to 0.48 for the figures. If the initial sintering proceeds due to bulk diffusion, the relation of  $n=0.33$  to 0.50 holds theoretically.<sup>14,15</sup> In the range of experiment shown in Fig.3, therefore, the sintering seems to proceed with the bulk diffusion being the dominant factor.

From Eq.(1), the following equation is obtained.

$$\log(\Delta L/L_0) = \log K + \log t^n \dots \dots \dots (2)$$

where,  $K=(Ar\Omega D/kT)^n$ . **Figure 5** shows  $\log K$  as a function of the inverse of absolute temperature ( $1/T$ ). The activation energy of powder in the initial sintering stage obtained from the result of Fig.5 was 131KJ/mol, 81KJ/mol, and 147KJ/mol for the powder synthesized from 0.2M, 0.4M, and 0.8M ZrOCl<sub>2</sub>, respectively. From the above results, it is thought that, when ZrOCl<sub>2</sub> is used as a starting material, its concentration significantly governs the nature of powder and causes a difference in the mechanism of initial sintering.

Furthermore, when the powder synthesized from 0.4M ZrOCl<sub>2</sub> was used, the grain boundary diffusion was the dominant factor for sintering, and when the powder synthesized from 0.2M and 0.8M ZrOCl<sub>2</sub> was used, the bulk diffusion was dominant in sintering. This seems to be the reason for low activation energy of powder synthesized from 0.4M ZrOCl<sub>2</sub>.

The reason for the difference in activation energy in the initial sintering stage caused by the concentration of ZrOCl<sub>2</sub> is possibly the aggregation of material powder. For the

powders synthesized from 0.2M and 0.8M ZrOCl<sub>2</sub>, the aggregation of powder was strong, though the primary particle size is small. The difference in cohesiveness of material powder causes the difference in bulk density of compact, which may disturb the initial sintering.

**3.2. Intermediate and Final Sintering of Zircon Sintered Body**

**Figure 6** shows the bulk density as a function of sintering temperature for zircon sintered bodies sintered at temperatures between 1400°C and 1680°C for 4 hours. In the intermediate sintering stage up to relative density of 95% (bulk density of 4.46g/cm<sup>3</sup>), the process of densification for the powder synthesized from 0.4M ZrOCl<sub>2</sub> is nearly the same as that for the powders from 0.2M and 0.8M ZrOCl<sub>2</sub>. However, as shown in **Fig.7**, it was found that the powder synthesized from 0.2M ZrOCl<sub>2</sub> was densified most in the range

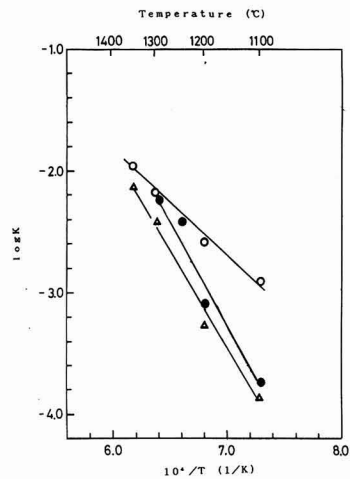


**Fig. 5.**  $\log K$  as a function of temperature. (●: 0.8M powder, ○: 0.4M powder, Δ: 0.2M powder)

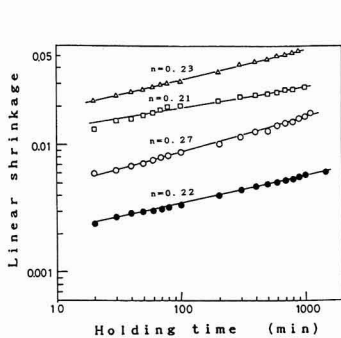


**Fig. 2**

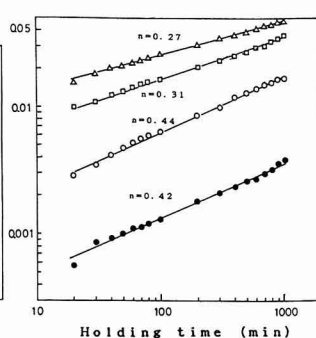


**Fig. 3**

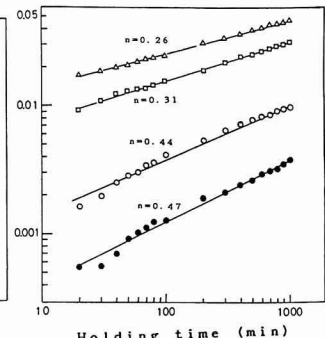


**Fig. 4**

**Fig. 2.** Linear shrinkage as a function of holding time for 0.4M powder. (●: 1100°C, ○: 1200°C, □: 1300°C, Δ: 1350°C)

**Fig. 3.** Linear shrinkage as a function of holding time for 0.8M powder. (●: 1100°C, ○: 1200°C, □: 1300°C, Δ: 1350°C)

**Fig. 4.** Linear shrinkage as a function of holding time for 0.2M powder. (●: 1100°C, ○: 1200°C, □: 1300°C, Δ: 1350°C)

above 95% of relative density ( $4.46\text{g/cm}^3$  of bulk density) when being sintered at  $1650^\circ\text{C}$ .

The powder synthesized from  $0.2\text{M ZrOCl}_2$  had the largest average particle size in the particle distribution measurement. To investigate the reason for increased bulk density, the powders were compared in cohesiveness by measuring the particle distribution after the dilution rate of dispersant (SN Wet 366, Sannopuko Co., Ltd.) was changed and a hydrophilic group was added to the powder surface. The result is shown in Fig.8.

As seen from Fig.8, only for the powder synthesized from  $0.2\text{M ZrOCl}_2$ , the aggregation of powder is loosened at a dilution rate of  $10^{-2}$  by the surface activity effect, and the average particle size determined from the particle distribution measurement decreases. The strength of cohesiveness of powder seems to be in the order of  $0.2\text{M} > 0.8\text{M} > 0.4\text{M}$  from the particle distribution measurement in Fig.1 and SEM observation, but the order seems to be  $0.8\text{M} > 0.2\text{M} \geq 0.4\text{M}$  when the result of Fig.8 is considered together.

The measured compact density was  $2.73\text{g/cm}^3$ ,  $2.59\text{g/cm}^3$ , and  $2.35\text{g/cm}^3$  for the powder synthesized from  $0.2\text{M}$ ,  $0.4\text{M}$ , and  $0.8\text{M ZrOCl}_2$ , respectively. The reason why the powder synthesized from  $0.2\text{M ZrOCl}_2$ , which is slightly cohesive, has a higher compact density than the powder synthesized from  $0.4\text{M ZrOCl}_2$ , which is least cohesive, may be because the aggregated particles of powder synthesized from  $0.2\text{M ZrOCl}_2$  that has aggregated by relatively weak cohesive force are loosened by the molding pressure during molding, resulting in the increase in compact density. This increase in density in molding may contribute to the densification, and lead to the increase in bulk density in the final sintering stage.

### 3.3. Mechanical Properties of Zircon Sintered Body

As described in 3.2, the sintering of high purity  $\text{ZrSiO}_4$  powder is greatly affected by the cohesiveness of powder caused mainly by the difference in concentration of starting material. Therefore, we investigated the effect of the difference in sintering on the nature of sintered body.

Figure 9 shows the three-point bending strength as a function of temperature for the samples sintered at  $1680^\circ\text{C}$  for 4 hours that have been synthesized by using three kinds of powders.

This figure indicates that for the powder synthesized from  $0.4\text{M ZrOCl}_2$ , the strength is almost unchanged in the range from room temperature to  $1400^\circ\text{C}$ , whereas for the powder synthesized from  $0.8\text{M ZrOCl}_2$ , the strength at room temperature is kept up to  $1300^\circ\text{C}$ , but decreases at  $1400^\circ\text{C}$ . To study the reason for this difference, the surface of sintered body was observed. The results are shown in Fig.10. These SEM photographs reveals that a dense and fine structure of average particle size of  $0.5\text{-}1\mu\text{m}$ , whereas the sintered body using the powder synthesized from  $0.8\text{M ZrOCl}_2$  has an average particle size of  $1\text{-}2\mu\text{m}$ , in which grain growth is greater and has larger voids than the sintered body using the powder synthesized from  $0.4\text{M ZrOCl}_2$ . The reason for the decrease in strength at  $1400^\circ\text{C}$  for the sintered body using the powder synthesized from  $0.8\text{M ZrOCl}_2$  may be that the grain boundary slides at  $1400^\circ\text{C}$  because of insufficient densification. The sintered body using the powder synthesized from  $0.2\text{M ZrOCl}_2$  has a higher bulk density and less voids than the other two sintered bodies, but has

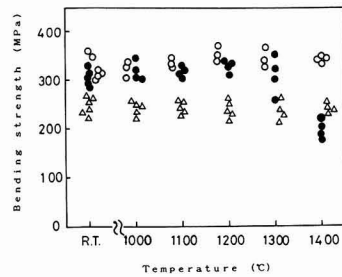


Fig. 9. Bending strength of the samples sintered at  $1680^\circ\text{C}$  for 4h as a function of temperature. (●:  $0.8\text{M}$  powder, ○:  $0.4\text{M}$  powder, △:  $0.2\text{M}$  powder)

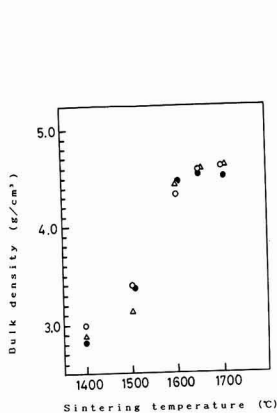


Fig. 6.

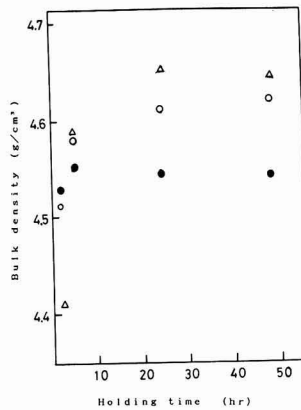


Fig. 7.

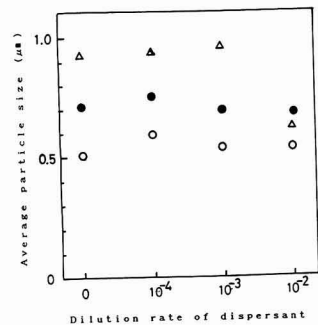


Fig. 8.

Fig. 6. Bulk density as a function of sintering temperature. (●:  $0.8\text{M}$  powder, ○:  $0.4\text{M}$  powder, △:  $0.2\text{M}$  powder) (Holding time: 4h)

Fig. 7. Bulk density as a function of holding time. (●:  $0.8\text{M}$  powder, ○:  $0.4\text{M}$  powder, △:  $0.2\text{M}$  powder) (Sintering temperature:  $1650^\circ\text{C}$ )

Fig. 8. Average particle size as a function of dilution rate dispersant. (●:  $0.8\text{M}$  powder, ○:  $0.4\text{M}$  powder, △:  $0.2\text{M}$  powder)

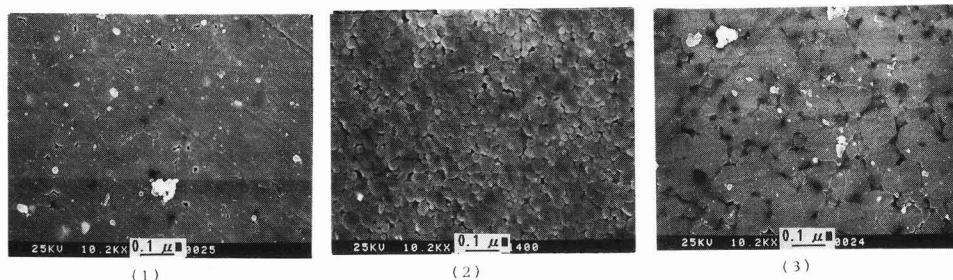


Fig. 10. SEM images of zircon sintered bodies. (sintering temperature: 1680C holding time: 4h) (1) 0.2M powder (2) 0.4M powder (3) 0.8M powder.

more grain growth than the sintered body using the powder synthesized from 0.4 ZrOCl<sub>2</sub>. This may be because of the nonuniformity of particle size of 0.2M powder. For the powder synthesized from 0.2M ZrOCl<sub>2</sub>, the cohesiveness of powder was so low that the aggregation is loosened in molding. On the other hand, however, it had the highest compact density among three kinds of powders. Therefore, the nonuniformity of particle size of powder probably increased the packing property of powder. Also, the nonconformity of particle size probably promoted the grain growth in sintering. It is difficult to identify the reason why the sintered body using the powder synthesized from 0.2M ZrOCl<sub>2</sub> has a lower strength than the sintered body using the powder synthesized from 0.4M ZrOCl<sub>2</sub>. However, one reason for lower strength as a whole is that the particle size in the sintered body is generally large. The decrease in strength at 1400°C probably did not occur because less voids lie in the sintered body as with the sintered body using the powder synthesized from 0.4M ZrOCl<sub>2</sub>.

From the above results, it was found that the excellent high-temperature properties of ZrSiO<sub>4</sub> single-phase sintered body appear to be due to the absence of impurities (which become glass phase of low melting point) and due to densification up to 98% or more of theoretical density.

#### 4. Conclusions

Sintering was performed at the normal pressure by using three kinds of high purity ZrSiO<sub>4</sub> powders. The conclusions are as follows:

- 1) The initial sintering of high purity ZrSiO<sub>4</sub> powder differed depending on the change of particle size of ZrSiO<sub>4</sub> powder due to the change of aqueous water concentration of ZrOCl<sub>2</sub>, which was a starting material. For the ZrSiO<sub>4</sub> powder with an average particle size of 0.5μm, the activation energy required for initial sintering was 81KJ/mol. When the average particle size exceeds 0.7μm, however, the initial sintering is greatly disturbed, and the required activation energy became 130KJ/mol or more.
- 2) In the intermediate and final stages of sintering of high purity ZrSiO<sub>4</sub> powder, the powder synthesized from 0.2M ZrOCl<sub>2</sub> had the highest apparent bulk density. The measurement of particle size distribution of powder using a dispersant revealed that the aggregation was easily loosened, so that the powder aggregated by weak cohesive force was collapsed, which increased the com-

act density; as a result the apparent bulk density increased. However, SEM observation revealed that significant grain growth was found in the sintered body as compared with the powder synthesized from 0.4M ZrOCl<sub>2</sub> that had the smallest average particle size; mechanical strength was not so high.

- 3) As a result of investigation on sintering of single-phase high purity ZrSiO<sub>4</sub> powders with different powder characteristics, it was found that the high-temperature characteristics of the sintered body (in which the strength did not decrease up to 1400°C) appeared when the sintered body, prepared by sintering while the average particle size was controlled to 0.5μm or less, had a dense and fine structure having a bulk density of 4.55g/cm<sup>3</sup> (relative density of 98%).

#### Acknowledgments

We wish to thank Mr.S. Motoki and Mr.C. Ishihara at the Analysis Research Department, Tosoh Corporation for chemical analysis of powder to evaluate zircon powders.

#### References:

- 1) S. Motoi, *Seramikkusu*, 7, 29 (1972).
- 2) M. Danhara, *ibid.*, 23, 960-962 (1988).
- 3) Y. Kagami, *TAIKABUTSU*, 39, 510-512 (1987).
- 4) K. Ichikawa and N. Tsukamoto, *Jirukon(Kagaku to Gijutsu) Uchidarokakuho* (1988) 229-242.
- 5) A. Ihara, *Seramikkusu*, 14, 513-519 (1988).
- 6) E.A. Tomas and R.W. Knauff, *Am. Ceram. Soc. Bull.*, 35, 1-5 (1956).
- 7) S. Motoi, *KOGYO KAGAKU ZASSHI*, 70, 638-643 (1967).
- 8) M. Sugai and S. Munemiya, *Jirukon(Kagaku to Gijutsu) Uchidarokakuho* (1988) 149-217.
- 9) H. Kobayashi, T. Kono, T. Mori, H. Yamamura and T. Mitamura, *Ceram. Soc. Jpn.*, 98, 567-572 (1990).
- 10) H. Kobayashi, T. Terasaki, T. Mori, H. Yamamura and T. Mitamura, *ibid.*, 98, 1109-1113 (1990).
- 11) H. Kobayashi, T. Terasaki, T. Mori, H. Yamamura and T. Mitamura, *ibid.*, 99, 42-46 (1991).
- 12) T. Mori, H. Hoshino, H. Yamamura, H. Kobayashi and T. Mitamura, *ibid.*, 98, 1017-1022 (1990).
- 13) M.F. Berard and D.R. Wilder, *J. Am. Ceram. Soc.* 52, 85-88 (1969).
- 14) W.D. Kingery and M. Berg, *J. Appl. Phys.*, 26, 1205-1212 (1955).
- 15) K. Kuribayashi and T. Sata, *Yogyo-Kyokaiishi*, 89, 41-46 (1981).

# The Effects of Surface Coating and Orienting of Whiskers on Mechanical Properties of SiC(w)/Si<sub>3</sub>N<sub>4</sub>

Tatsuji Matsui, Osamu Komura and Masaya Miyake

Sumitomo Electric Industries, Ltd.  
1-1-1, Koya-kita, Itami-shi, 664 Japan

In order to strengthen and toughen Si<sub>3</sub>N<sub>4</sub> ceramics by addition of SiC-whiskers, we tried to control interfacial properties between the whisker and matrix as well as orientation of the whiskers. For interfacial control, the effects of Al<sub>2</sub>O<sub>3</sub>, ZrO<sub>2</sub> and carbon coating on the surface of whiskers were studied. The flexural strength and the fracture toughness of Si<sub>3</sub>N<sub>4</sub> composite containing Al<sub>2</sub>O<sub>3</sub>-coated whiskers by decomposition of aluminum stearate were stronger (1107MPa) and larger (10.2MPam<sup>1/2</sup>) than those of the composite with non-coated whiskers. TEM observation revealed that Al<sub>2</sub>O<sub>3</sub>-coated whiskers in the composite had a smoother surface than non-coated whiskers and that a film-layer was formed at the interface between whisker and matrix. For orientation control, the flexural strength and the creep rupture resistance at 1250°C of Si<sub>3</sub>N<sub>4</sub> composite, reinforced with uni-directionally oriented whiskers by the doctor-blade method, were much stronger (1180Mpa) and much larger than those of monolithic Si<sub>3</sub>N<sub>4</sub> ceramics. After creep testing, the new stacking defects and dislocation in the whiskers were observed by TEM. On the basis of these results, the mechanisms of toughening and high-temperature strengthening of SiC(w)/Si<sub>3</sub>N<sub>4</sub> have been discussed.

[Received April 12, 1991; Accepted July 18, 1991]

**Key-words:** Silicon nitride, SiC whisker, Coating, Interfacial bonding, Uni-directional orientation, Fracture toughness, High-temperature strength

## 1. Introduction

Si<sub>3</sub>N<sub>4</sub> ceramics excel in wear, corrosion, and thermal shock resistance and have considerable strength and toughness, so that they are expected as structural materials for automobile and other mechanical parts. However, their fracture toughness or high-temperature strength is not sufficient as practical materials, and studies are now active to provide higher strength and toughness by adding whisker and long fiber.

The expected composite effects of whisker-reinforced ceramics include higher toughness<sup>4)</sup> by crack deflection,<sup>1)</sup> bridging owing to whisker pullout<sup>2)</sup> or debond<sup>3)</sup> of whisker/matrix interface, and higher high-temperature strength<sup>5)</sup> by controlling intergranular slip under stress shown in Fig.1. Conditions especially required to realize these effects are said to be:

- 1) proper control of interfacial bonding force between whisker and matrix;
- 2) orientation and dispersion of whisker as much as possible in the vertical direction to the face of crack propagation; and
- 3) whisker strength maintained even after sintering.<sup>6,7)</sup>

With regard to interfacial bonding force, there are some reports on the measurement of shear strength of fiber/matrix interfaces of SiC fiber reinforced Si<sub>3</sub>N<sub>4</sub><sup>8)</sup> and on the effect of the addition of Y<sub>2</sub>O<sub>3</sub>-SiO<sub>2</sub>, C, and BN to the whisker interfaces of SiC whisker-reinforced Si<sub>3</sub>N<sub>4</sub> on fracture toughness.<sup>9)</sup> As for the effect of whisker orientation, toughness was improved by uniaxial orientation through extrusion or injection molding.<sup>10,11)</sup>

At present, however, only a few reports are available on

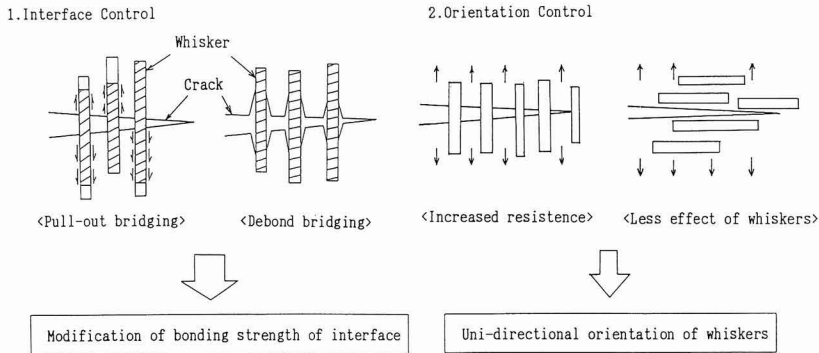


Fig. 1. Schematic illustration of control factor for toughening mechanism by whiskers.

bonding strength of whisker/matrix interfaces of whisker-reinforced materials, and it is quite hard to measure the factor directly. Moreover, no distinct knowledge has been obtained yet as to what kind of interfacial or reaction layers are the most effective to improve strength and toughness. In addition, study is also necessary with respect to the effects of whisker orientation on mechanical properties other than fracture toughness.

This project was intended to clarify a relation between the interfacial bonding force of whisker/matrix and strength and toughness of SiC whisker reinforced  $\text{Si}_3\text{N}_4$  ceramics ( $\text{SiC(w)}/\text{Si}_3\text{N}_4$ ), by examining the effects of whisker coating materials on strength, toughness and others. In the case of the effects of whisker addition after unidirectional orientation as well as those of different orientation property, studies were performed chiefly on fracture toughness, high temperature strength and high-temperature creep properties. Based on these results, the mechanism of whisker addition was investigated to improve toughness and high-temperature strength.

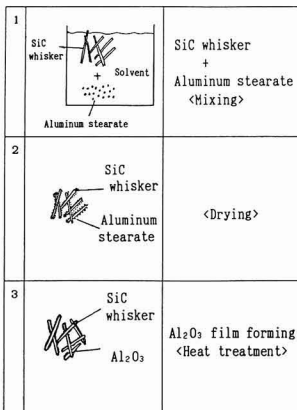


Fig. 2. Process of  $\text{Al}_2\text{O}_3$  coating on SiC whisker surfaces.

## 2. Method of Experiment

### 2.1. Coating Method of SiC Whisker Surfaces and Preparation of Sintered Bodies

Three kinds of whisker coating materials ( $\text{Al}_2\text{O}_3$ ,  $\text{ZrO}_2$  and C) were chosen to vary the interfacial bonding force of SiC whisker and  $\text{Si}_3\text{N}_4$  matrix. The interfaces of SiC whisker and  $\text{Si}_3\text{N}_4$  particles do not react below sintering temperatures ( $\sim 1700^\circ\text{C}$ ),<sup>10,12</sup> while predictions were made that  $\text{Al}_2\text{O}_3$  promotes an interfacial reaction, C inhibits the reaction, and  $\text{ZrO}_2$  plays an intermediate role. The difference in their reactivity was considered to change interfacial bonding force which might vary the strength or toughness of composite materials.

Figure 2 shows the method of forming a uniform  $\text{Al}_2\text{O}_3$  coating layer by the pyrolysis of an oxide precursor attached to whisker surfaces. A hundred grams of SiC whisker (Tokai Carbon Co., Ltd.; TWS-100; average diameter: about  $0.5\mu\text{m}$ ; length:  $5\text{--}15\mu\text{m}$ ;  $\beta$  type) and the same amount of aluminum stearate (Yasuda Medical Mfg.) were mixed in ethanol, dried, and treated at  $900^\circ\text{C}$  in air for 2hr to obtain  $\text{Al}_2\text{O}_3$  (estimated amount: about 10g). Also in the case of  $\text{ZrO}_2$  coating, the same process was applied with zirconyl nitrate (Research Laboratory for Hypepure Chemistry; 33g). The whisker/precursor ratio was determined such that the film thickness of oxide coating was about 1/50 of whisker diameter assuming uniform coating over SiC whisker surfaces. For the C-coated whisker, a commercial product was adopted. Figure 3 shows SEM images of non-,  $\text{Al}_2\text{O}_3$ -,  $\text{ZrO}_2$ -, and C-coated whisker.  $\text{Al}_2\text{O}_3$  and  $\text{ZrO}_2$  were dispersed uniformly over whisker surfaces in the form of particles, and X-ray diffraction found that the crystal form was  $\alpha$  type for  $\text{Al}_2\text{O}_3$  and monoclinic for  $\text{ZrO}_2$ . The surface of C-coated whisker (Tokai Carbon Co., Ltd.; TWS-100 with carbon treatment on its surface; film thickness: 5nm) was smooth and considered to be not crystalline but amorphous from the standpoint of X-ray analysis.

In the preparation of sintered bodies, as shown in Fig.4, the following materials were used: 20wt% of coated-whisker, 8wt% of  $\text{Y}_2\text{O}_3$  (The Shin-Etsu Chemical Co., Ltd.; SU) and 2wt% of  $\text{Al}_2\text{O}_3$  (Sumitomo Chemical Co., Ltd.; AKP50), both for sintering aids and 70wt% of  $\text{Si}_3\text{N}_4$  powder (Ube Industries, Ltd.; E10). They were mixed in ethanol, molded in sheet by filtration under reduced pressure, dried, stacked, and sintered by a hot press method. Specimens  $3\times 4\times 36$  in

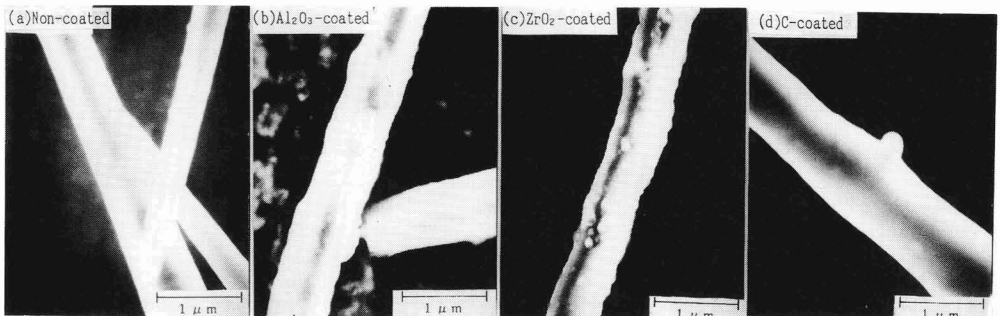


Fig. 3. SEM photographs of non-coated SiC whisker (a),  $\text{Al}_2\text{O}_3$ -coated (b),  $\text{ZrO}_2$ -coated (c) and C-coated (d) whisker.

size were cut out from the resulting sintered body, and density was measured by an Archimedean method. Strength (r.t. and 1250°C) was determined by a 3-point bending test with a span of 30mm. Fracture toughness was obtained by the SENB method in which the above specimen was slit 0.75mm deep by a diamond wheel (blade width: 0.1mm) in the vertical face to the pressing direction of a hot press. Moreover, residual stress in sintered bodies was measured by X-ray stress measurement under conditions of:  $\text{Si}_3\text{N}_4(323)$  face for a diffraction face, characteristic X-ray by a  $\psi$  constant method with  $\text{Cu-K}\alpha$ , and -733MPa/deg. for a X-ray stress calculation. The appearance of whisker/matrix interfaces was observed with a transmission-type electron microscope.

## 2.2. Orientation Method for SiC Whisker

As a method of whisker addition to enhance the composite effects of whisker on monolithic materials studies were conducted on the addition by unidirectional orientation through a doctor blade method. The properties of resulting composite materials were compared with those of monolithic materials to examine the effects of addition, and comparison was made between specimens with different directions of orientation.

Figure 5 illustrates the preparation of doctor blade sheets. As has been stated in 2.1, 20wt% of whisker (without coating), 70wt% of  $\text{Si}_3\text{N}_4$ , 10wt% of sintering aids, MPA and an organic binder were thoroughly mixed in ethanol, followed by defoaming and viscosity adjustment to provide a green sheet 0.3mm thick. The sheet was cut into tiles 100×100mm in size, which were stacked so as to have the same direction of whisker orientation, and then hot-pressed with the same conditions as in Fig.4. Four kinds of specimens 3×4×36mm in size were cut out from the obtained sintered body, according to the directions of hot pressing and doctor blade drawing as in Fig.6. The three-point bending strength (r.t. and 1250°C) and fracture toughness of each specimen were measured and the process of crack propagation was observed with a scanning electron microscope. In addition, creep tests were carried out at 1250°C in air under a 3-point bending stress of 343MPa, and the microstructures of parts of specimens after creep

rupture where tensile stress had been at work were observed with a transmission type electron microscope.

## 3. Results of Experiment

### 3.1. Coating Effects of SiC Whisker Surfaces

#### 3.1.1. Mechanical Properties of Coated Whisker Composite Materials

The relative density of composites containing non-coated whisker as well as  $\text{Al}_2\text{O}_3$ -,  $\text{ZrO}_2$ -, and C-coated whisker was over 99% after hot pressing, proving that all the materials were dense sintered bodies. Figure 7 shows the comparative results of each composite with regard to flexural strength ( $\sigma_{\text{RT}}$  and  $\sigma_{1250^\circ\text{C}}$ ) as well as fracture toughness ( $K_{\text{IC}}$ ) at r.t. and 1250°C.

The  $\sigma_{\text{RT}}$  value of non-coated whisker composites (hereafter referred to as non-coated materials) was 990MPa on the average, while that of  $\text{Al}_2\text{O}_3$ -coated whisker composites (hereafter  $\text{Al}_2\text{O}_3$ -coated materials) was 1107MPa on the average, higher than the former. In addition, the strength of C-coated whisker composites (hereafter as C-coated materials) was improved to 1054MPa, whereas that of  $\text{ZrO}_2$ -coated whisker composites (hereafter  $\text{ZrO}_2$ -coated materials) decreased to 864MPa.

The  $\sigma_{1250^\circ\text{C}}$  value of non-coated materials was 794MPa while that of C-coated material was 921MPa on the average, the highest of all, and a decrease in strength was low compared with the value at r.t.  $\text{Al}_2\text{O}_3$ - and  $\text{ZrO}_2$ -coated materials had lower high-temperature strength than non-coated

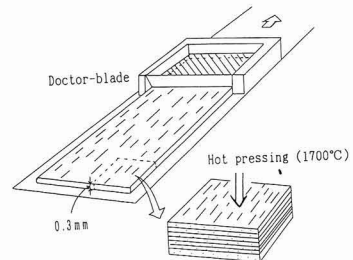


Fig. 5. Illustration of doctor-blade method.

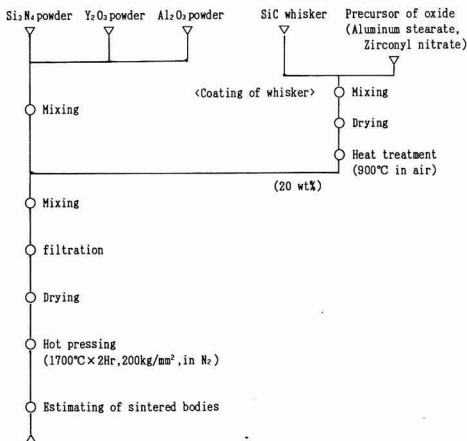


Fig. 4. Fabricating process of SiC(w)/ $\text{Si}_3\text{N}_4$  composites.

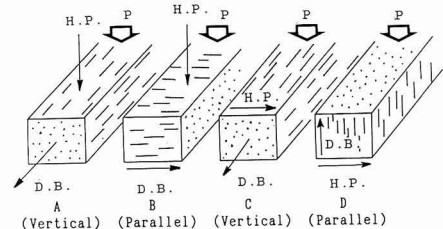


Fig. 6. Specimen for bending experiments classified according to the direction of power on 3-point bending (P), hot pressing (H.P.) and drawing of slurry by doctor-blade method (D.B.).

materials.

The  $K_{IC}$  value of non-coated materials was  $8.7\text{MPam}^{1/2}$  while that of  $\text{Al}_2\text{O}_3$  coated material was  $10.2\text{MPam}^{1/2}$ , showing a notable improvement in toughness. On the other hand,  $K_{IC}$  of  $\text{ZrO}_2$ -coated materials was  $7.4\text{MPam}^{1/2}$  and that of C-coated materials was  $7.8\text{MPam}^{1/2}$ , both lower than non-coated materials.

It was found that  $\text{Al}_2\text{O}_3$ -coated materials have improved strength at r.t. and toughness while they have low strength at high temperatures, that C-coated materials have lowered toughness and yet have notably improved strength at high temperatures, and that  $\text{ZrO}_2$ -coated materials have decreased strength at r.t. and high temperatures as well as toughness. These results suggest that  $\text{Al}_2\text{O}_3$  coating reacting at the interface of whisker and matrix provides the effect of improving fracture toughness, and that C and  $\text{ZrO}_2$  coating does not promote a reaction, tending to reduce toughness. For further study on the effect of  $\text{Al}_2\text{O}_3$  coating to increase toughness, the behavior of crack propagation through composites was observed along with the condition of whisker/matrix interfaces in the composites.

3.1.2. Behavior of Crack Propagation in Composites

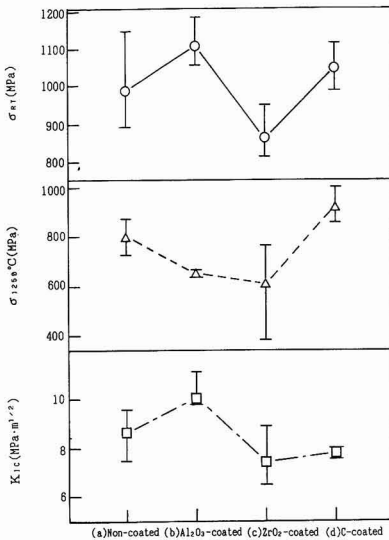


Fig. 7. Mechanical properties of composites containing whiskers (a) non-coated, (b)  $\text{Al}_2\text{O}_3$ -coated, (c)  $\text{ZrO}_2$ -coated and (d) C-coated.

A Vickers indenter was pressed onto the surfaces of sintered bodies of  $\text{Al}_2\text{O}_3$ - and C-coated materials, and the propagation of resulting cracks was observed with SEM. In the case of C-coated materials, there were many points where whisker/matrix interfaces peeled off and cracks deflected along them (Fig.8(ii)). As for  $\text{Al}_2\text{O}_3$ -coated materials, no such deflection was encountered but whisker bridging was rather common (Fig.8(i)).

3.1.3. Observation of Whisker/Matrix Interfaces

The effects of  $\text{Al}_2\text{O}_3$  coating were studied noticing whisker/matrix interfaces by means of TEM observation, as well as drawing a comparison with non-coating and C-coating in which the behavior of crack propagation was clearly different.

Figure 9 gives the condition of interfaces of non-coated materials (a), that of  $\text{Al}_2\text{O}_3$ -coated materials (b), and C-coated materials (c). In the case of non- and C-coated materials no special layers were encountered at their interfaces, suggesting that there are no interfacial reactions (Marked with "→"). By contrast,  $\text{Al}_2\text{O}_3$ -coated materials

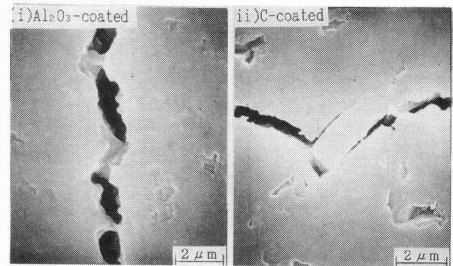


Fig. 8. Crack propagation in (i)  $\text{Al}_2\text{O}_3$ -coated and (ii) C-coated whisker containing composites.

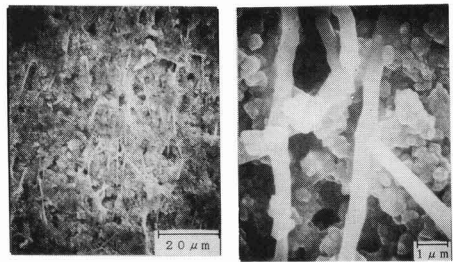


Fig. 10. Orientation of whiskers in doctor-blade sheets.

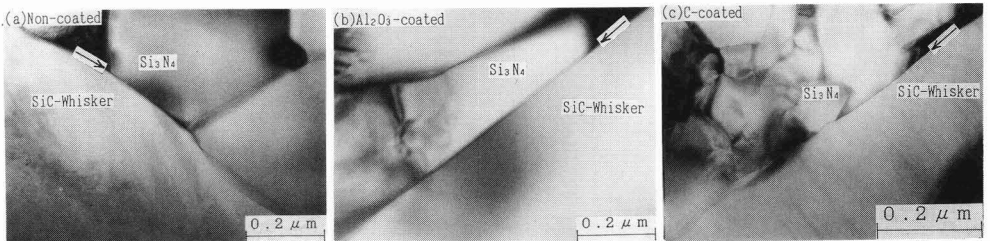


Fig. 9. TEM photographs of whisker-matrix interface of (a) non-coated, (b)  $\text{Al}_2\text{O}_3$ -coated and (c) C-coated whisker containing composites. The arrows show the interface.

developed film-like layers at the interfaces probably caused by Al<sub>2</sub>O<sub>3</sub> coating (Marked with “←”). The layers were detected even when samples were inclined during observation, proving that it is not due to overlapping of interfaces. Additionally, whisker in non-coated materials had a rough surface and was greatly strained by matrix particles, while in Al<sub>2</sub>O<sub>3</sub>-coated materials, whisker surfaces were quite smooth. The probable reason is that Al<sub>2</sub>O<sub>3</sub> coating improved interfacial wettability during hot-press sintering, thus reducing strain against and damage to the whisker.

### 3.2. Study on Orientation Effects of SiC Whisker

#### 3.2.1. Effects of Whisker Addition With Unidirectional Orientation and Difference in Orientation Property

Whisker in green sheets prepared by a doctor blade method was oriented almost in the same direction as shown in Fig.10. Evaluation was made with four kinds of specimens (A,B,C,D) cut out as in Fig.6 from a hot pressed body after stacking the above sheets. Differences in peak intensity ratios with (111) and (220) faces of β-SiC by X-ray diffraction showed the following facts: whisker in the specimens A and C of the sintered body is oriented vertically to the plane of crack propagation (hereafter referred to as vertically-oriented materials A and C), while in specimen B the orientation is parallel to the propagation plane and vertical to the propagation direction (hereafter parallel-oriented material B), and in the specimen D it is parallel to the propagation plane and direction (hereafter parallel-oriented material D). Figure 11 plots the measurements of  $\sigma_{RT}$ ,  $\sigma_{1250^\circ C}$  and  $K_{IC}$  of each specimen. The vertically-oriented material A had lower  $\sigma_{RT}$  than the monolithic material, but higher  $\sigma_{1250^\circ C}$  and  $K_{IC}$  in particular,  $\sigma_{1250^\circ C}$  increased nearly twice from 646 to 1180MPa. in addition,  $K_{IC}$  of the vertically-oriented material A was 1.15 times that of the parallel-oriented material D, and  $\sigma_{1250^\circ C}$  1.25 times that of the

latter. The vertically-oriented material C also showed the same trend as A in comparison with monolithic and parallel-oriented materials. This revealed that whisker-oriented composites had greatly improved fracture toughness and especially high-temperature strength.

In the next step, the behavior of crack propagation was observed to study the effect of  $K_{IC}$  improvement by vertical orientation, and further creep tests were performed to examine the effect of improvement of high-temperature strength.

#### 3.2.2. Behavior of Crack Propagation

A Vickers indenter was pressed onto the hot-press face of specimen A in order to examine the propagation behavior of cracks generated in various directions. Figure 12(i) shows the case of vertical whisker orientation to the direction of crack propagation, while (ii) the case of parallel orientation. In parallel orientation, cracks advance almost straight along the direction of whisker orientation, whereas in vertical orientation, crack deflection or whisker pullout is encountered everywhere, and this effect is considered to have improved  $K_{IC}$  of vertically-oriented materials.

#### 3.2.3. Influences on Creep Properties

Figure 13 shows creep properties of monolithic and composites (vertically-oriented material A and parallel-oriented material D). It was found that the strain rates of composites are lower than that of the monolithic material. Moreover, in comparison between the vertical-oriented material A and parallel-oriented material D, the former had greater strain amount leading to creep rupture time about twice as much,

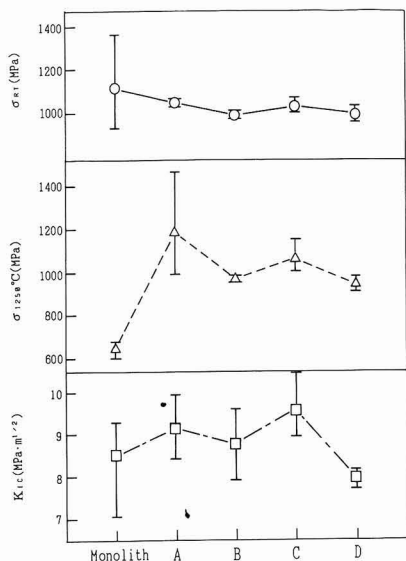


Fig. 11. Mechanical properties of monolith, specimen A (vertical), B (parallel), C (vertical) and D (parallel) classified according to whisker orientation as showed in Fig.6.

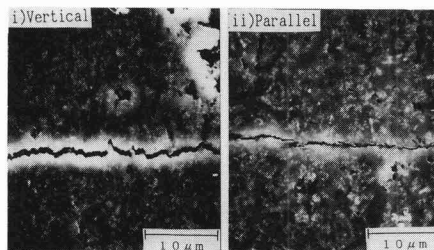


Fig. 12. Comparison of crack propagation configuration between (i) vertical and (ii) parallel orientation of whiskers.

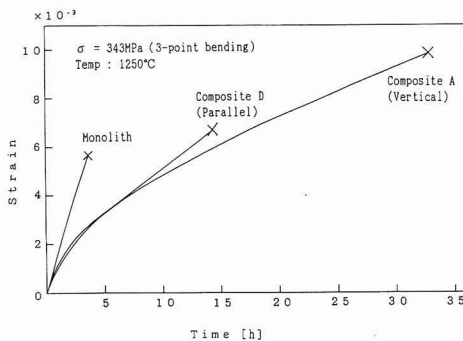


Fig. 13. Creep resistance properties of monolith, composites of specimen A (vertical) and D (parallel) showed in Fig.6.

and about nine times that of the monolithic material. That is, the vertically-oriented material had lower strain rate against loading stress and greater strain amount till rupture than the monolithic material, which probably resulted in longer creep rupture time.

## 4. Discussion

### 4.1. Effects of $\text{Al}_2\text{O}_3$ Coating of Whisker on Fracture Toughness

The fact that C-coating of whisker increased chances of interfacial peeling or deflection during crack propagation and  $\text{Al}_2\text{O}_3$  coating reduced them (Fig.8) suggest that there is a difference in an interfacial bonding force between C and  $\text{Al}_2\text{O}_3$  coating. Ashizuka et al.<sup>13)</sup> pointed out that in the case of C-coated SiC whisker/cordierite C-coating weakens the interfacial bonding force and causes peeling, which is the same trend as this result. The interfacial layer between whisker and matrix of  $\text{Al}_2\text{O}_3$ -coated materials (Fig.9) is different from an  $\text{Al}_2\text{O}_3$  layer (Fig.3) coated onto the whisker surface and changed into a film, so that some kinds of reactions must have occurred at the interface during sintering. Additionally, in  $\text{Al}_2\text{O}_3$ -coated materials, whisker bridging was mainly encountered during crack propagation. To explain the mechanism of providing higher toughness by bridging, Kelly<sup>2)</sup> proposed pullout bridging in which energy is relieved by the friction of whisker pullout during bridging while Becher et al.<sup>3)</sup> claimed debond bridging in which interfacial peeling causes bridging in the case of higher interfacial bonding force than pullout (Fig.1). It is not clear whether  $\text{Al}_2\text{O}_3$ -coated materials are related to pullout or debond, and yet at least the appropriate enhancement of a bonding force by an interfacial reaction is considered to correspond to the bridging mechanisms. Further, as in Table 1, results of the measurement of stress remaining in

composites showed that  $\text{Al}_2\text{O}_3$  coating reduces compressive residual stress against  $\text{Si}_3\text{N}_4$  in the composites to about 1/5. In other words, when the balance of tensile stress to compressive stress inside sintered bodies was taken into consideration, tensile residual stress against whisker could be lowered to 1/5, and the relaxation of tensile stress against whisker seemingly improved whisker strength. Another fact that roughness owing to strain against whisker surfaces was reduced suggests that composites had lowered deterioration and damage of whiskers and maintained the strength properties of whisker before sintering. From the above results, the functions of  $\text{Al}_2\text{O}_3$  as a coating material for whisker to improve toughness are probably due to the following two points.

- 1) Control of interfacial reactions: Formation of interfacial reaction layers to moderately enhance an interfacial bonding force.
- 2) Maintenance of whisker strength: Relaxation of strain or stress generated at the interface during sintering.

In the case of 1), excessive reactions at interfaces let cracks merely advance while cutting whisker — the effect of whisker composition is not at work. In addition, as is the case with C-coated materials in this experiment, the distinct occurrence of interfacial peeling or deflection does not always improve fracture toughness. In  $\text{Al}_2\text{O}_3$  coated materials in this study, whisker bridging during crack propagation probably resulted in improved toughness.

As for 2),  $\text{Al}_2\text{O}_3$  coated onto whisker is considered to form a liquid phase with  $\text{SiO}_2$  on the same surface in the process of sintering to improve interfacial wettability, thus relaxing strain and a difference in coefficients of thermal expansion caused by contraction in sintering, as well as resultant residual stress.

### 4.2. Effect of Orientation in Whisker Addition on High-Temperature Properties

When whisker was added with vertical orientation to the plane of crack propagation (vertically-oriented materials), strength at 1250°C increased about twice and creep rupture time about 9 times as much as the case without whisker addition (monolithic materials). Moreover, during creep tests, the vertically-oriented materials had about 1/8 the strain rate and about 1.7 times the strain amount till rupture compared with the monolithic material. Further, even in the same composites, vertically-oriented materials had a strain amount about 1.5 times that of parallel-oriented materials (parallel orientation to the plane of crack propagation). These results indicate that whisker composition leads to an increase in resistance to strain under high-temperature

Table 1. Comparison of properties of non-coated and  $\text{Al}_2\text{O}_3$ -coated SiC-whisker containing  $\text{Si}_3\text{N}_4$ .

	$K_{Ic}$ ( $\text{HP}\cdot\text{cm}^{1/2}$ )	Residual stress of $\text{Si}_3\text{N}_4$ ( $\text{kg}/\text{cm}^2$ )	Surface condition of whiskers	Layer at interface
non-coated	8.7	10.7		No
$\text{Al}_2\text{O}_3$ coated	10.2	2.1	smooth	Yes

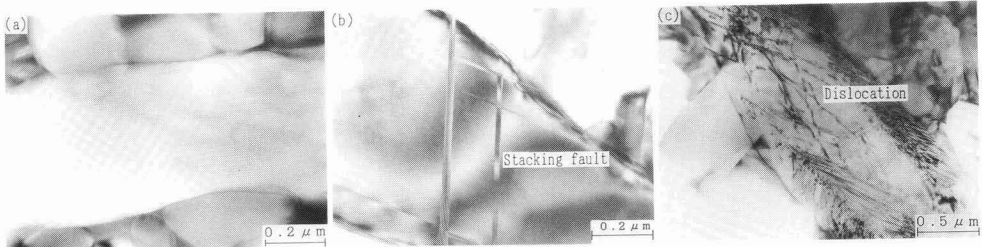


Fig. 14. TEM photographs of whiskers in composite (specimen A) before (a) and after (b, c) creep testing, showing the appearance of (b) stacking defects and (c) dislocation in the whisker.

stress. In other words, the intergranular slip of  $\text{Si}_3\text{N}_4$  matrix accompanying the softening of an intergranular glass phase at high-temperatures is hampered by the pinning effect of whisker. In addition, when whisker is oriented vertically to the plane of crack propagation, the strain amount of composites increases under high-temperature stress. The probable reason is that whisker orientation acts as bridging in  $\text{Si}_3\text{N}_4$  matrix, and even when the strain amount is increased by the intergranular slip of  $\text{Si}_3\text{N}_4$ , this whisker bridging against the direction of strain prevents the structure from easy rupture. Thus, added whisker with orientation increases rupture resistance even in case of the intergranular deformation of matrix. As a result, considerable stress is expected to be loaded on the whisker itself under high temperature stress. To confirm this, whiskers in specimens before and after creep tests were observed using TEM as in Figs.14(a), (b), (c), and new stacking defects or dislocation (Figs.14(b), (c)) were noticed inside the whisker after the tests. Nutt<sup>15)</sup> studied defects in SiC whisker and reported the presence of stacking defects, partial dislocation, and holes. Such initial defects may trigger new stacking defects with the help of external stress or act as nuclei to promote the movement of dislocation. Consequently, the generation of defects as in Figs.14(b), (c) suggests that the whisker shares stress during creep.

#### 4. Conclusion

The effect of surface coating for SiC whisker by the pyrolysis of oxide precursors was investigated as well as that of whisker orientation by a doctor blade method, and the following results were obtained. Surface coating effects:

- 1)  $\text{Al}_2\text{O}_3$  coating onto whisker surfaces improved strength at r.t and fracture toughness of composites to 1107MPa and  $10.2\text{MPam}^{1/2}$  ( $K_{IC}$ ) respectively;
- 2) Crack deflection was often encountered in C-coated materials while bridging of whiskers in  $\text{Al}_2\text{O}_3$ -coated materials, suggesting a difference in the condition of interfacial bonding;
- 3)  $\text{Al}_2\text{O}_3$  coating smoothed whisker surfaces, formed an intermediate layer between whisker and matrix, and reduced residual stress; and
- 4) These results indicated that  $\text{Al}_2\text{O}_3$  coating maintained whisker strength even after sintering and an interfacial bonding force between whisker and matrix changed to let a bridging mechanism dominate, thus improving toughness. Composite effects of whisker orientation were:
  - (1) The addition of whisker oriented vertically to the

plane of crack propagation provided composites with a high temperature strength of 1180MPa at 1250°C, about twice that of a monolithic material;

- (2) Strain fracture resistance during high-temperature creep increased and fracture time was greatly prolonged by about 9 times that of the monolithic material, thus proving a substantial improvement in creep properties by vertical orientation; and
- (3) Such orientation effects at elevated temperatures are probably attributed to an increase in the deformation resistance of matrix by whisker bridging as well as to stress sharing by the whisker itself.

#### note:

This work was mainly performed under the management of Engineering Research Association for High Performance Ceramics as a part of The Fine Ceramics R&D Project of Basic Technology for Future Industries supported by New Energy and Industrial Technology Development Organization.

(Published at the Annual Meeting in May, 1990 and also the 3rd Autumnal Symposium in September, 1990 of the Ceramic Society of Japan).

#### References:

- 1) K.T. Faber and A.G. Evans, *Acta Metall.*, 31, 565-576 (1989).
- 2) A. Kelly, *Roy. Soc. Lond. A.* 319, 95-116 (1970).
- 3) P.F. Becher, C.H. Hsueh, P. Angelini, and T.N. Tieg, *J. Am. Ceram. Soc.*, 71, 1050-1061 (1988).
- 4) K. Nihara, *Seramikkusu*, 21, 581-589 (1986).
- 5) Y. Godo, T. Yonezawa, A. Tsuge, and M. Kobayashi, *Proc. 2nd Autumnal Sympo. Ceram. Soc. Jpn.* (1989) 500-501.
- 6) S. Inoue, T. Uchiyama and K. Nihara, *Seramikkusu*, 21, 621-629 (1986).
- 7) K. Suganuma and K. Nihara, *ibid.*, 24, 937-944 (1989).
- 8) J.W. Laughner, R.T. Bhatt, *J. Am. Ceram. Soc.*, 72, 2017-2019 (1989).
- 9) N.D. Corbin, C.A. Willkens, J.L. Hammarstrom, V.K. Pujari, G.A. Rossi, K.N. Siebein, C.L. Chang and J.S. Hansen, *Proc. 26th Automot. Technol. Dev. Contract. Coord. Meet.* 1988, (1989) 235-241.
- 10) S. Kobayashi, T. Kandori and S. Wada, *Yogyo-Kyokaiishi*, 94, 903-905 (1986).
- 11) C.A. Willkens, N.D. Corbin, V.K. Pujari, R.L. Yeckley and M.J. Mangaudis, *Ceram. Eng. Sci. Proc.*, 9, 1367-1370 (1988).
- 12) F. Xia and Y.Z. Chin, *J. Met. Sci. Technol.*, 4, 201-204 (1988).
- 13) M. Ashizuka, M. Watanabe and N. Ikeyama, *Seramikkusu-Ronbunshi*, 98, 408-411 (1990).
- 14) S.R. Nutt, *J. Am. Ceram. Soc.*, 67, 428-431 (1984).

---

This article is a full translation of the article which appeared in *Nippon Seramikkusu Kyokai Gakujutsu Ronbunshi* (Japanese version), Vol.99, No.11, 1991.

# Effect of Coarse Quartz Grains on Mechanical Strength of Porcelain Body

Kenya Hamano, Yueh-Hong Wu\*, Zenbe-e Nakagawa\*\* and Minori Hasegawa\*\*

Department of Applied Chemistry, Faculty of Engineering, Kanagawa University  
3-27-1, Rokkakubashi, Kanagawa-ku, Yokohama-shi, 221 Japan

\*Hocheng Pottery MFG. Co., Ltd.

Taiwan, Rep. of China

\*\*Research Laboratory of Engineering Materials, Tokyo Institute of Technology  
4259, Nagatsuta, Midori-ku, Yokohama-shi, 227 Japan

The effect of coarse quartz grains on mechanical properties of triaxial porcelain body was examined. Bodies composed of 50 kaolin, 25 potash feldspar and 25% fine quartz, which was replaced in turn with 74~149 $\mu$ m coarse ones, were fired at 1400°C for 1h. Their bulk density was about 2.38g/cm<sup>3</sup> and hardly changed with the amount of coarse quartz. Bending strength of the fired specimens was markedly decreased from 1350kgf/cm<sup>2</sup> for the body free from the coarse quartz grains to about 900kgf/cm<sup>2</sup> by addition of only 0.03% of the coarse grains, and further decreased with an increase in the amount of the coarse quartz grains. Scattering in the bending strength values and also mean deviation of starting point of failure from the maximum stressed point decreased with increase in the content of the coarse quartz grains. From these relations, it was inferred that most failures of the specimens were started at the origin associated with the coarse quartz grains. The results clearly show that not only the control of the quartz grain size within an appropriate range but also the prevention of the contamination by coarse quartz grains are indispensable for the increase in the mechanical strength of a porcelain body.

[Received April 16, 1991; Accepted July 18, 1991]

**Key-words:** Porcelain body, Mechanical strength, Weibull coefficient, Quartz, Grain size, Coarse grains.

## 1. Introduction

The previous reports presented the following facts: The factors having effects on mechanical strength of kaolin-base porcelain body are the differences in thermal expansion coefficient and modulus of elasticity between the quartz grains and surrounding glassy matrix in the densified body. The prestressing effect due to the residual compressive stress at the glassy phase around the grain is large.<sup>1,2)</sup> This prestressing effect is affected by quartz grain size, and varies with the firing temperature. For the standard composition porcelain body of 50 Kaolin, 25 potash feldspar and 25 wt% fine quartz, the body containing 10-20 $\mu$ m quartz grains when fired at 1400°C for 1h and the body containing 5-10 $\mu$ m quartz grains when fired at 1350-1250°C for 1h have the highest strength. If the grain size is too small, the quartz grain is excessively melted, producing small prestressing effect. If the grain size is too large, the stress occurring in

cooling becomes too high, creating cracks in the surrounding glassy phase and quartz grain and reducing their strength.<sup>2)</sup> When the quartz grains in the size range that produces effective prestressing effect are contained, the strength of body becomes higher as more quartz grains are left unmelted in the rounded form in the body.<sup>2)</sup>

When the fracture surface of specimen is observed with a microscope after the strength test, large quartz grains are often found the surface or near the surface layer. This suggests that such coarse quartz grains are the sources of fracture. From this viewpoint, we studied the relationship between the amount of coarse quartz and the strength.

## 2. Materials and Preparation of Specimen

The materials used in this experiment were elutriated Korean Hadong Kaolin, Indian feldspar grains of 10-20 $\mu$ m obtained by elutriation, and screened quartzite of high purity for optical glass. Two kinds of quartz grain size ranges were used in this experiment. One was coarse size of 74-149 $\mu$ m that had been found to decrease the strength in the previous work. The other was grain size of 10-20 $\mu$ m screened by elutriation that had been found to give the highest strength when fired at 1400°C for 1h.

The chemical composition of raw materials is given in

**Table 1.** Chemical compositions of raw materials.

	SiO <sub>2</sub>	TiO <sub>2</sub>	Al <sub>2</sub> O <sub>3</sub>	Fe <sub>2</sub> O <sub>3</sub>	CaO	MgO	K <sub>2</sub> O	Na <sub>2</sub> O	lg. loss
Korean kaolin	46.37	0.16	37.42	0.93	0.42	0.26	0.73	0.42	13.00
Indian feldspar	65.66	0.01	18.69	0.08	0.10	0.01	12.32	2.89	0.20
Quartzite	99.74								

**Table 2.** Compositions of specimens (wt%).

	A	B	C	D	E	F	G	H	I
kaolin	50	50	50	50	50	50	50	50	50
feldspar	25	25	25	25	25	25	25	25	25
10~20 $\mu$ m quartz	25	24.9	24.9	24.7	24.5	24	23	20	0
74~149 $\mu$ m quartz	0	0.0	0.1	0.2	0.5	1	2	5	25

**Table 1.** From the result of X-ray diffraction, it was revealed that the Hadong Kaolin mainly contains metahalloysite and contains small amounts of hydrohalloysite, trace amounts of micaceous clay mineral, quartz and plagioclase, indian feldspar is potash feldspar into which small amounts of soda feldspar is dissolved; and the quartzite contains quartz only.

These materials were blended into nine kinds of specimens shown in **Table 2** on the basis of standard composition of 50 Kaolin, 25 potash feldspar and 25 wt% fine quartz, which was replaced in turn with 74-149 $\mu$ m coarse quartz. The mixing was performed by stirrer so that the quartz grain size is not changed. The mixture was heated while stirred using distilled water, and then evaporated. After being dried, the specimen was lightly ground in an agate mortar to prepare sample powder. The powder was preformed into a 5 $\times$ 5 $\times$ 40mm rectangular specimen under a pressure of 300kgf/cm<sup>2</sup> (1kgf/cm<sup>2</sup>=9.8 $\times$ 10<sup>4</sup>Pa) of a uniaxial press by using a bakelite-lined metallic mold, and then HIPed under a pressure of 800kgf/cm<sup>2</sup>. The compact was heated to 1400°C at a heating rate of 6°C/min using an electric furnace of silicon carbide heating element, held for 1h and then allowed to cool in the furnace (at a rate of

2°C/min on average to about 800°C) to prepare specimens for experiment.

### 3. Experimental Results and Discussion

First, the bulk density was measured by the mercury replacement method to estimate the degree of vitrification of compact. The measured values were calculated as the mean measurements from five measurements and plotted against the amount of coarse quartz particles as shown in **Fig.1**. The bulk density of fired body is almost unchanged though it decreases slightly as the amount of coarse quartz increases, so that it can be judged that the all specimens is in the same densification condition.

The powder X-ray diffraction has revealed that the constitutive phase of fired body is amorphous glass phase in addition to mullite and quartz, and that the quartz content increases as the amount of coarse quartz particles increases. In addition, polarization microscope observation was performed on the thin layer of fired body. **Figure 2** shows examples of polarization microphotographs of fired body containing 5% coarse quartz. In any body, the glass produced by the melting of feldspar spreads to form a matrix, in which mullite needle-shaped crystals are considerably developed. The fine quartz grains are melted from their surface and edge and shaped into a rounded form. The coarse quartz grains are also rounded, but cracks are found in and around the grains as seen in Fig.2.

The bending strength of fired body was measured. The measuring method is the three-point loading method with a span of 20mm and a cross head speed of 0.1mm/min. For the strength test, ten test pieces were used for the sample of 0% coarse quartz and 25% coarse quartz grains each, and twenty test pieces were used for other samples each, and the mean values were calculated. **Figure 3** plots the of bending strength test result against the logarithmic value of the amount of coarse quartz particles. The bending strength of body was 1350kgf/cm<sup>2</sup> on average when coarse particles

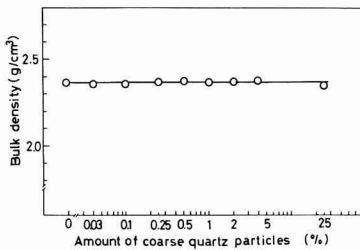


**Fig. 1.** Effect of addition of coarse quartz on bulk density of fired bodies.

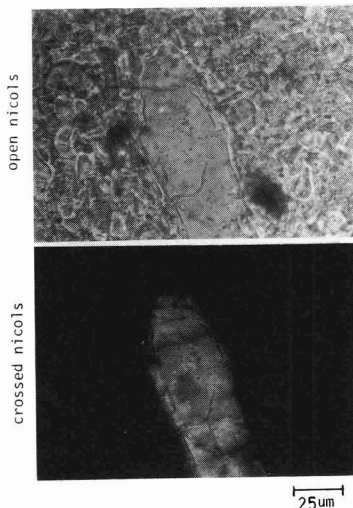


**Fig. 2.** Polarization microphotographs of fired bodies containing coarse quartz.

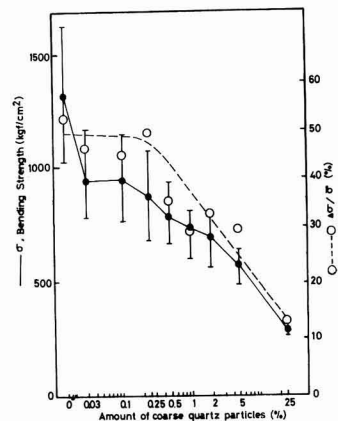


**Fig. 3.** Effect of addition of coarse quartz on bending strength of fired bodies and its deviation.

were not contained and prepared from only 10-20 $\mu$ m quartz, but suddenly decreased to about 900kgf/cm<sup>2</sup> when 0.03% coarse quartz particles were added. The strength continued to decrease as the amount of coarse quartz particles increased, being as low as 270kgf/cm<sup>2</sup> when all of quartz of 25% was coarse one. This shows that the effect of coarse quartz particles on the bending strength is very large.

The variation in strength value  $\Delta\sigma$  also decreases with the increase in the amount of coarse quartz particles. The ratio of  $\Delta\sigma$  to the average strength  $\sigma$  under each condition,  $\Delta\sigma/\sigma$ , is represented by the broken line in Fig.3. This deviation value is unchanged up to 0.25% coarse quartz, but suddenly decreases as the amount of coarse quartz particles exceeds 0.25%.

In this bending test (three-point loading method), fracture did not necessarily begin at the bottom center, which is the

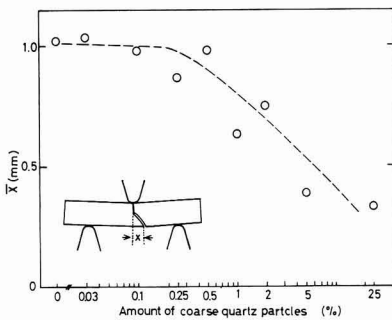


Fig. 4. Effect of addition of coarse quartz on length of deviation from center of specimens.

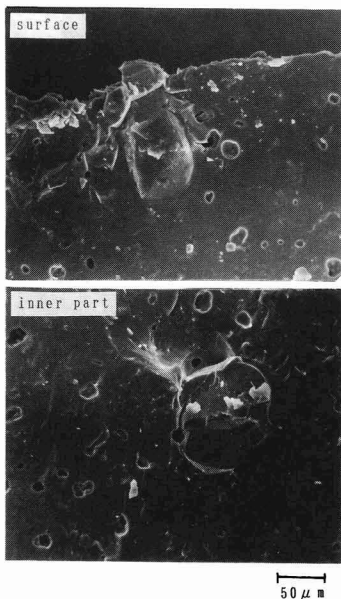


Fig. 5. Scanning electron micrographs of fired bodies containing coarse quartz.

maximum load point of test piece, and it often began at a point deviating from the center. Figure 4 shows the relation between the amount of coarse quartz particles and the length of deviation (X) from the center of the specimen. This result was obtained by measuring the length of deviation (X) for each test piece, and the mean value ( $\bar{X}$ ) was calculated for each condition. The length of deviation is unchanged up to 0.25% coarse quartz, but suddenly decreases as the amount of coarse quartz particles exceeds 0.25% and numbers of test pieces in which fracture began near the center, i.e. the maximum load center, increase. This relation is very similar to the plot of  $\Delta\sigma/\sigma$  in Fig.3.

Figure 5 shows the SEM photographs of fracture surface of specimen after subjected to the bending strength test. On the fracture surface, it can be observed that coarse quartz grains are present on the specimen surface as shown in A and also near the surface as shown in B, at which fracture began.

Summarizing these relationships, the coarse quartz grains contained in the body produces a high stress at the grain boundary due to the difference in thermal expansion coefficient of the grains and surrounding glass phase, and the stress sometimes exceeds strength value of the glass and quartz grain, creating cracks in the glass phase and quartz grain. Since some of these cracks are present on or near the surface of the specimen, the cracks, or ones formed by load superimposed on high residual stress, becomes the source of fracture of the entire specimen. As the amount of coarse quartz particles increases, the ratio of crack distribution on or near the surface of specimen increase. Therefore, the probability of presence at or near the maximum load point increases when the strength test is carried out. The fact that the change of strength deviation as a function of the amount of coarse quartz particles is in almost good agreement with the change of length of deviation from the maximum load point shows that the strength of specimen depends on the presence of coarse quartz grains.

Figure 6 shows the Weibull plot of bending strength of fired bodies. As the content of coarse quartz increases, the strength decreases, but the Weibull modulus increases. Figure 7 shows this relationship.

In consequence, the presence of coarse quartz grains in a densified porcelain body produces high stress during cooling owing to the difference in thermal expansion coefficient and modulus of elasticity between the quartz grains and the surrounding glass, which sometimes creates cracks. These

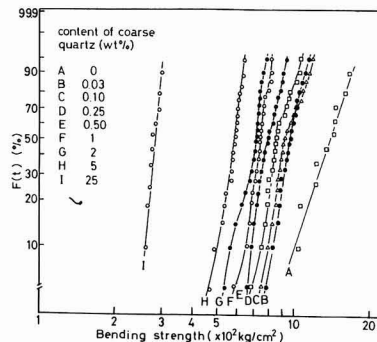


Fig. 6. Weibull plot of bending strength of fired bodies.

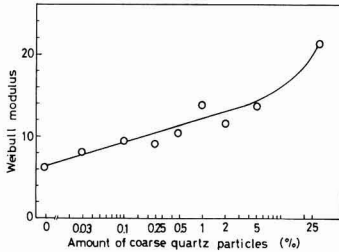


Fig. 7. Effect of addition of coarse quartz on Weibull modulus of bending strength of fired bodies.

become the source of fracture when the specimen is subjected to a load. Therefore, tiny amounts of coarse quartz grains of 0.03% contained in a body decrease the strength value to two-thirds. With the increase in the content of coarse quartz, the strength decreases further; at the same time, the variation in strength value becomes low, and the Weibull modulus becomes high.

For the materials for structural component, not only high strength but also high Weibull modulus is required. For porcelain bodies, as seen in this experiment, since fracture seems to occur from any defect, high Weibull modulus corresponds to the fact that the sources of fracture distributed near the maximum load point of specimen has increased, which naturally decreases the strength value.

Although it is ideal to make bodies having no defects, it is now necessary to minimize such defects to make bodies with high strength. As described in the previous report, it is naturally effective to decrease the quartz grain size contained in the body to some degree, and it is also necessary to thoroughly control the process in order to prevent coarse quartz grains that may become the sources of defects from entering the raw materials powder.

## 4. Conclusions

The effects of the amount of coarse quartz grains on the

mechanical strength of a triaxial porcelain body having nearly the same degree of densification were examined. The conclusions obtained in this experiment are summarized below.

- 1) The bending strength of body is decreased from 1350kgf/cm<sup>2</sup> to about 900kgf/cm<sup>2</sup>, i.e., to two-thirds by the addition of 0.03% coarse quartz grains. The strength decreases further as the amount of coarse quartz grains increases.
- 2) Variation in strength measurements become narrower with the increase in the amount of coarse quartz grains when more than 0.25% of coarse quartz grains are added. This tendency agrees well with the tendency of change of averaged length of deviation of crack formation point under three-point load from the maximum load point due to the addition of coarse quartz grains. This means that many fractures of porcelain body begin at the source caused by the presence of coarse quartz grains.
- 3) The Weibull modulus of body strength value increases as the amount of coarse quartz grains increases.
- 4) To increase porcelain body strength, it is necessary not only to control the grain size of quartz to be in an appropriate grain size range depending on the firing condition but also to prevent coarse quartz grains that may become the sources of fracture from entering the raw material powder.

(This paper represents results reported to the annual meeting of the Ceramic Society of Japan in May, 1985 and additional new work)

### Acknowledgments

We wish to thank Narumi Seito Co., Ltd. and Ohara Co., Ltd. for their supplying materials used in this experiment.

### References:

- 1) K. Hamano and E.S. Lee, Mechanical Behavior of Materials, Proc. 1971 Int. Conf. on Mechanical Behavior of Materials, Soc. Mater. Sci., Jpn., Vol.IV, (1972) 475-483.
- 2) K. Hamano, Y. Wu, Z. Nakagawa and M. Hasegawa, Seramikkusu Ronbunshi, 99, 153-157 (1991).

This article is a full translation of the article which appeared in Nippon Seramikkusu Kyokai Gakujutsu Ronbunshi (Japanese version), Vol.99, No.11, 1991.

# Quantitative Analysis of Pore Structure on Frost Durability of Inorganic Building Materials

Masahiko Nakamura, Takaaki Ohnishi and Masataka Kamitani\*

Department of Chemistry and Materials Technology, Faculty of Engineering and Design, Kyoto Institute of Technology

Goshokaido-cho, Matsugasaki, Sakyo-ku, Kyoto-shi, 606 Japan

\*Sekisui Chemical Co. Ltd., Kyoto Technology Center

Kamichosi-cho, Kamitoba, Minami-ku, Kyoto-shi, 601 Japan

The frost susceptibility of inorganic porous building materials was discussed from a viewpoint of quantitative analysis of internal pore structures. The analysis was undertaken on the basis of a couple of black-and-white image data, such as two dimensional pore-size distribution and three dimensional pore-connecting texture being constructed by a computer from original SEM photographs. The results were summarized as follows. The frost susceptibility showed excellent correlations with factors obtained by the quantitative analysis of pore-connecting textural. They are (a) an averaged shape factor (S) of the deviation from the perfect circle, a variance and a standard deviation about (S); (b) a distribution of (S) along with the polishing direction and a branching degree in a three dimensional connecting texture of pores; and (c) a fractal dimension calculated from the data of an accumulated pore-size distribution which was measured by the mercury-intrusion method. It is suggested that they should be used as promising factors for the indirect evaluation of the frost susceptibility of inorganic building materials.

[Received April 24; Accepted July 18, 1991]

**Key-words:** Frost durability, 3D pore structure, Image analysis, Fractal analysis, Building materials, Quantitative image analysis.

## 1. Introduction

Inorganic building materials have a porous structure because they are prepared from the state of powder as the raw materials through firing process. Therefore, the porous structure of the material is gradually destroyed by the repetition of freezing and thawing of water held in the porous structure, which deteriorates the basic performance of building material.

Generally, the above deterioration is called a "frost damage". For building materials to have excellent frost durability at low temperature region, it is effective to control the freezing and movement of moisture in such a porous structure by controlling the pore size distribution in the material and by the modification of the intend pore surface chemically and physically.<sup>1,2)</sup> Since the frost phenomena of building material is caused by the freezing of water held in the pore structure, it is needless to say that the pore structure is related closely to the mechanism by which frost damage is generated. Therefore there are some key factors for quantitatively characterizing the pore structure when the pore

structures in building materials are controlled to improve the frost durability. These are (a) pore size distribution, (b) pore shape distribution, and (c) pore-connecting texture. Several reports have been published in an attempt to improve the frost durability by the control and analysis of pore size distribution in ceramic building materials and cement-base building materials such as roof tiles, brick, and tiles.<sup>3-6)</sup> A few reports also have been published that deal with qualitative relation between the internal pore structure and frost durability.<sup>7,8)</sup> However, no report has been published on the quantitative analysis of the relation between the factors (b) or (c) with frost durability.

In the present work, we studied the relation between the various quantitative analysis results and actual frost durability as a basic study for proper design of inorganic building materials having excellent low-temperature durability (frost durability). The quantitative analysis was performed by image processing aided with a computer on the pore shape distribution and three-dimensional pore connecting texture in the polished cross section of some fired ceramic building materials (clay roof tiles) graded in frost durability.

## 2. Experiment and Analysis Method

### 2.1. Building Material Sample

Three kinds of clay roof tiles being graded in frost durability were used in this experiment. They were prepared from the raw material with the same composition so as to have the properties shown in **Table 1** by changing the firing temperature only.<sup>9)</sup> As the index of frost susceptibility shown in Table 1, the sample weight loss Q that has been used for evaluating the frost durability of aggregate for concrete<sup>10)</sup> was used. The material was sieved by two types of screens (1.9cm and 0.8cm mesh). The sieved material was dried at 105-110°C for 24h. After that, the accurately weighed lump sample (about 400g,  $W_0$ ) was impregnated by the boiling saturation method (5% salt water with accelerated deterioration effect was used), and then placed in a glass container with a lid that had an inside volume of

**Table 1.** Physical properties of building materials (fired clay roofing tiles) used as samples.

Sample name	Water absorp. (%)	Apparent porosity (%)	Saturat. coeffic.	Frost susceptibility (weight loss, Q) (wt%)
A	21.4	10.1	0.705	1.12
B	30.0	15.8	0.854	7.95
C	31.4	16.9	0.899	30.80

about 300cm<sup>3</sup>. After being allowed to stand in a freezer at -25±1°C for 16 hours, the sample was allowed to stand at room temperature (20°C) for 8 hours. This cycle was repeated at a specified times. After that, the washed and dried sample was sieved again and weighed accurately (W<sub>i</sub>). The weight loss Q due to breakage and fragmentation of grains in the starting lump sample was determined from the following equation.

$$(W_0 - W_i) / W_0 (\%) \dots \dots \dots (1)$$

The holding time for freezing and thawing is sufficient duration for the center of lump sample to reach a temperature equilibrium. In this experiment, 130 cycles was selected as the freezing-thawing cycle number to clearly specify the frost susceptibility.<sup>9)</sup> This cycle number has been confirmed by using many other samples.

**2.2. Image Processing Method**

The consolidated sample whose fine pores were filled with penetrable embedding resin was mirror polished, and a black-and-white image was prepared from the photographs obtained by SEM observation. To build the three-dimensional pore-connecting texture, the ordinate data of one frame was constructed with 256 pixels at the maximum both longitudinally and transversely by always fixing the fixed point in each black-and-white image; this was obtained by photographing under the same condition the above-described mirror polished surface prepared continuously at about 1µm intervals in parallel to each other and the subsequent image processing. The number of sheets of sample surface that were input into the computer was 10 for all samples because of the limited memory capacity of the computer and the limit of calculation time.

1) Quantitative Analysis of Pores for Two-dimensional Image Processing

One of the above-described 10 sequential black- and white images was analyzed on the shape distribution of pores. Although there are some methods for representing the pore shape, an averaged shape factor (S) of the deviation from the perfect circle was used in this experiment. The (S) is a shape evaluating factor contained in commercially available image processing software and is expressed by eq.(2).

$$S = L^2 / 4\pi A \dots \dots \dots (2)$$

where L is the peripheral length of pore and A is the pore area.

As seen from Eq.(2), S=1 for a perfect circle. In the shape measurement of this study, 1/256 the longitudinal and transverse dimensions of a black-and-white image is input as one pixel into the computer. When the pore area is considerably larger than one pixel, an exact shape factor can be obtained, but it contains many errors when the pore area is small. In the present analysis, therefore, the degree of deviation of the S value from S=1 for a perfect circle was calibrated beforehand on a circle with a known radius. S was determined for the pore image with the S value being in the range of 1 ≥ S ≥ 0.85. The relation between statistical factors such as the mean value S of shape factor, variance λ or standard deviation σ of S value and frost durability was investigated.

2) Analysis for three-dimensional pore-connecting texture

The relation between three-dimensional pore-connecting texture and frost durability was investigated as follows:

Analysis method ①: One set of ten sheets of sequential

black-and-white image planes that were in parallel to each other at intervals of about 1µm were prepared for each sample by computer image processing. When three-dimensional continuous pore structure data are built by piling the neighboring image planes, the determination of whether the pore is continuous was made as shown in Fig.1. When the neighboring pixels of the central pixel on the same plane and the neighboring pixels on the upper and lower planes have the same binary signal as the central pixel, they are given the same address number as the central pixel. The qualitative relation between branching degree and frost durability was investigated for the addressed three-dimensional connecting pores.

Analysis method ②: It is known that the pore distribution and the geometric connecting structure show fractal.<sup>11)</sup> Therefore, based on the pore size distribution data of sample obtained by the mercury-intrusion method, the quantitative relation between fractal dimension D obtained from eq.(3) and frost durability was investigated.

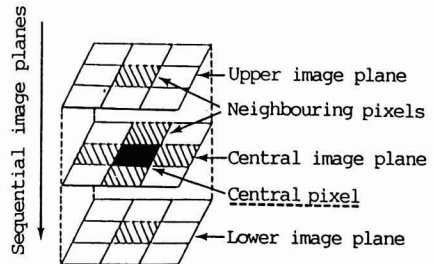
$$(V - V_{min}) / (V_{max} - V) = \{ (R - R_{min}) / (R_{max} - R) \}^{D-3} \dots (3)$$

where, R is the pore radius, V is the calculated volume of pore, D is the fractal dimension, and the suffixes of min and max indicate the minimum and maximum values of V and R when the logarithmic plot of (V - V<sub>min</sub>) / (V<sub>max</sub> - V) versus (R - R<sub>min</sub>) / (R<sub>max</sub> - R) has the highest linearity by substituting the pore size distribution curve data into eq.(3).

**3. Results and Discussion**

**3.1. Study by Two-dimensional Image Analysis**

Figure 2 shows the black-and-white image planes (black portion indicates the pore) for three kinds of clay roof tiles with different frost durability. Comparing pore shapes in Fig.2, it is qualitatively observed that the sample with higher frost durability is smoother in pore shape and lower in continuity. To quantitatively investigate the distribution of pore shape, therefore, the distribution of shape factor S calculated from Eq.(2) was determined for the images that are independent each other in each plane in Fig.2. The result is shown in Fig.3. From this figure, it is difficult to classify



When hatched pixels have same image signal as the central pixel, those neighbouring pixels were incorporated to a same group including the central pixel.

Fig. 1. Determination procedure for making the mutual linkages among neighboring pixels in the sequential image planes for computer-image processing.

the difference between three samples. However, when the data of Fig.3 is represented by the mean value  $S$ , variance  $\lambda$ , or standard deviation  $\sigma$ , a distinct difference is found between the three samples. In addition, the relation between these statistical factors and the index of frost susceptibility (weight loss  $Q$ ) was investigated. The result is shown in Fig.4, in which highly linear correlation is found for any of these factors.

3.2. Study by Three-dimensional Image Analysis

Figure 5 shows ten sequential black-and-white image planes obtained by polishing at intervals of about  $1\mu\text{m}$  for each sample. The changes of the pore area  $A$  and the pore-shape factor  $S$  along with the direction of sample polishing were investigated for the pores that are continuous (i.e. have the same address) from the top to the bottom image plane.



Fig. 2. Black-and-white images from SEM photographs for the analysis on the distribution of pore-shape factor ( $S$ ) indicating the deviation from the perfect circle.

The result is shown in Fig.6, which indicates that the sample having better frost durability has smaller changes.

Next, the branching degree of each pore from the top image plane to the bottom plane was investigated. The result was shown in Fig.7 by discriminating the pore having the same address in one image plane on the basis of three-dimensional continuity obtained by the computer on the criterion of Fig.1. Fig.7 indicates that the sample having better frost durability has lower branching degree and the sample that is more susceptible to frost has higher branching degree. This fact can be interpreted as follows by relating to the difference in frost susceptibility of water saturated sample obtained in this experiment. As known as a thermodynamic fact, the water held in the pore structure can locally freeze at a different temperature depending on the pore size. In the sample that has a continuous structure with

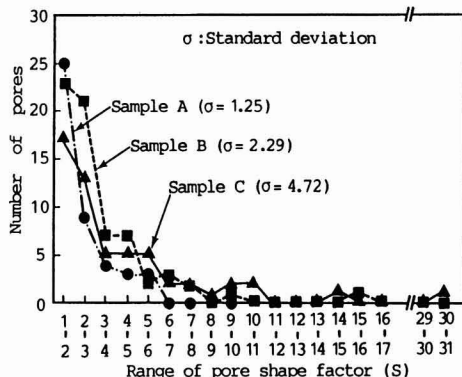


Fig. 3. Comparison of distribution of ( $S$ ) among three different samples.

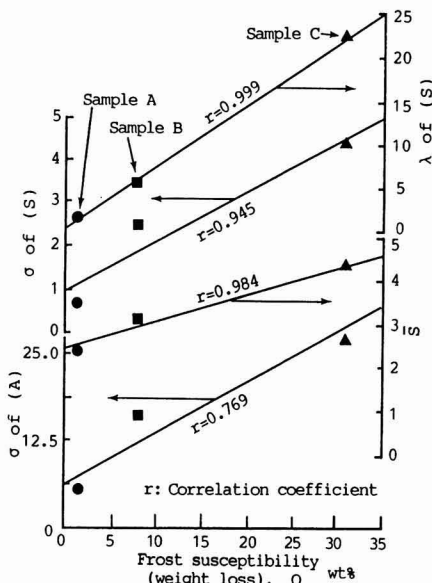


Fig. 4. Relationship of frost susceptibility ( $Q$ ) against ( $S$ ), variance ( $\lambda$ ) and standard deviation ( $\sigma$ ) concerning the value of ( $S$ ) and pore area ( $A$ ).

many pore branches (such that the water in fine branches is in the entrapped condition without being frozen), the amount of entrapped water increases, and finally the structure is destroyed under the static pressure generated when the system is cooled and the freezing of entrapped water proceeds. Particularly when the cooling speed is high, or

the pores branch finely, the structure is destroyed heavily because the accumulated fracture pressure cannot be released by the hydraulic flow of water and/or plastic deformation of ice through the fine pores.

Figure 9 shows the log-log plots between  $(V-V_{min})/(V_{max}-V)$  and  $(R-R_{min})/(R_{max}-R)$  calculated by Eq.(3) on the basis of the pore size distribution of three materials (see Fig.8). The relation between the fractal dimension  $D$  obtained from the line slope in Fig.9 and the index of frost susceptibility (weight loss  $Q$ ) is shown in Fig.10. This figure shows very close linear correlation.

The range of  $R_{min}$ ,  $R_{max}$ ,  $V_{min}$  and  $V_{max}$  value was determined by making reference to the results of another experiment<sup>9)</sup> in which the pore size range having closest correlation (see Fig.11) with the frost susceptibility  $Q$  was investigated for over 30 kinds of clay roof tiles including one used in this experiment, that is, by considering that the log-log plot between  $(V-V_{min})/(V_{max}-V)$  and  $(R-R_{min})/(R_{max}-R)$  has highest linearity in the widest possible range in the pore range of  $R < 0.7\mu\text{m}$ .

The fractal dimension calculated for three kinds of clay roof tile specimens used in this experiment was in the range of  $D=2.16-2.26$ . Judging from the value that is similar to the fractal dimension  $D=2.17$  for a human lung,<sup>12)</sup> it is thought that the connection of pore within clay roof tile is

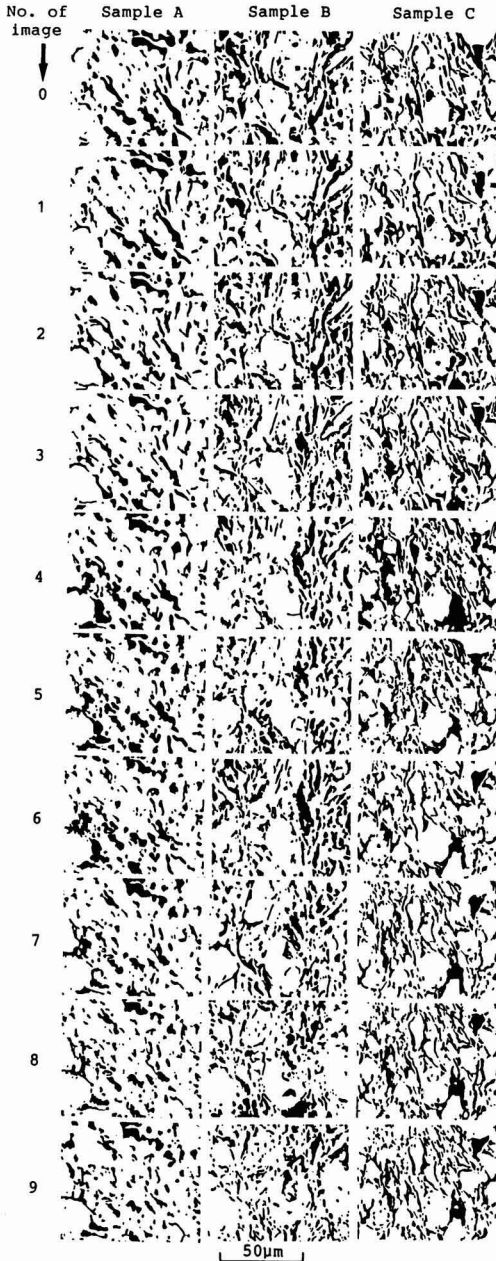


Fig. 5. Ten sequential black-and-white image planes for three different samples as the original data for creating three dimensional connecting structure of pores by computer.

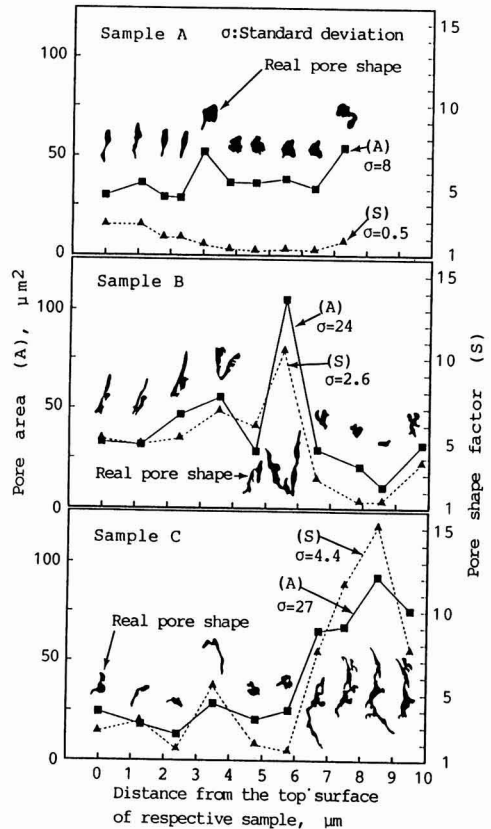
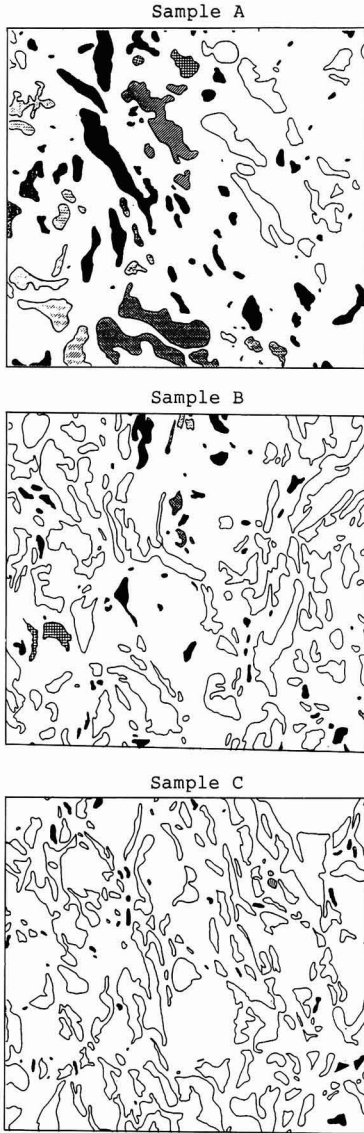


Fig. 6. Changes of the pore area (A) and the pore-shape factor (S) along with the direction of sample polishing.

similar to the spatial connection of human alveolus. When a space is filled with pores,  $D$  becomes 3. But the actual pores within the roof tile specimen show smaller  $D$  as compared with  $D=3$ . It is found that the specimen that is susceptible to frost (i.e. having high  $Q$ ) has a  $D$  value close to 3, and the pores branch finely within the specimen, the specimen having a pore structure with increased connection.

Considering the effect of defect density (that becomes a fracture starting point of brittle material) and the crack length included in the stress intensify factor term (in the



Same shadowed area indicates the same family of pores which are connected with each other.

Fig. 7. Configurational comparison of the branching degree in a three dimensional connecting texture of pores.

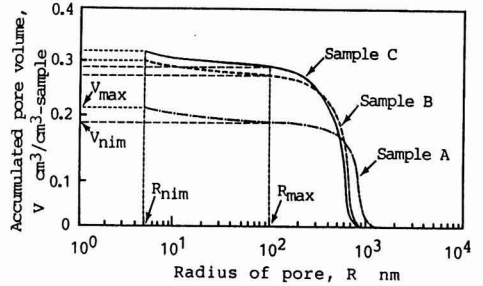


Fig. 8. Original data of pore size distribution for the fractal analysis.

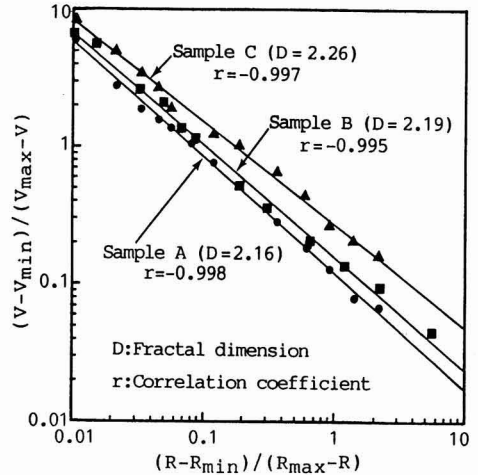


Fig. 9. Log-log plots between  $(V-V_{min})/(V_{max}-V)$  and  $(R-R_{min})/(R_{max}-R)$  in order to obtain the fractal dimension  $D$  in eq.2.

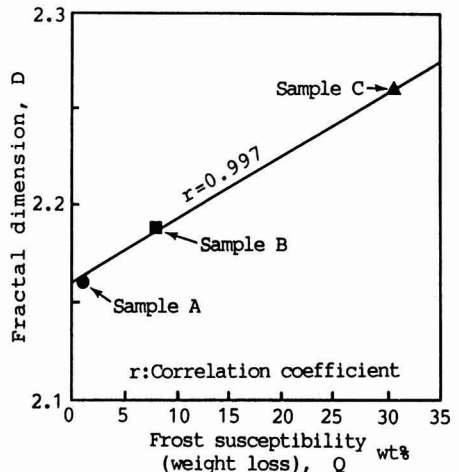


Fig. 10. Relationship between the fractal dimension and the frost susceptibility ( $Q$ ).

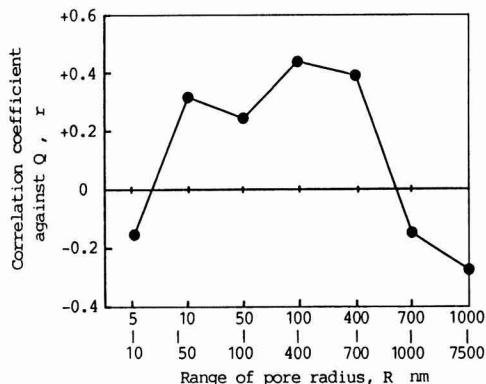


Fig. 11. Correlation of respective pore-size range against frost susceptibility ( $Q$ ), which were obtained from statistical analysis using over 30 kinds of clay-roofing tiles.<sup>9)</sup>

Griffith-Orowan theory) the irregularity (deviation from the perfect circle) of pore surface, which is morphological factor of pore, is related to the existence density of cracks for the case of structural fracture (*i.e.* frost damage) due to freezing of water within the porous structure. It is thought, therefore, that statistical factors of the mean value of  $S$  corresponding to the deviation from the perfect circle and  $\lambda$  or  $\sigma$  relating to the distribution of  $S$  reflecting the variety of pore shapes have a correlation with frost as high as the mean value of  $S$ .

As described above, several factors obtained by the quantitative analysis of two-dimensional distribution or three-dimensional connecting texture of pores dealt with in this experiment are useful tools not only for the analysis of frost mechanism but also as an indirect evaluation factor of frost susceptibility of building materials.

#### 4. Conclusions

To study the difference in frost susceptibility of inorganic porous building materials (represented as weight loss obtained from the freezing and thawing of sieved lump specimen saturated with water) from the viewpoint of pore structure of building material, quantitative analysis of shape distribution in the two-dimensional cross section and three-dimensional fractal dimension analysis based on pore size distribution were performed by using computer-aided image processing technology. The conclusions are summarized as follows:

1) The mean value, variance, and standard deviation of shape factor of the deviation from the perfect circle for pores of a two-dimensional image obtained from the black-and-white image data from an SEM photographs

of mirror polished building material surface show excellent correlation with the frost susceptibility.

- The distribution of the branching degree and the deviation from the perfect circle in the polishing direction obtained from the three-dimensional connecting texture built by a computer from the sequential black-and-white SEM image of polished surface at intervals of about  $1\mu\text{m}$  shows close correlation with the frost susceptibility. The factors relating to the pore structure are very effective when the degree of structural fracture caused by the hydraulic pressure of water entrapped in the pore connecting texture in unfrozen condition on freezing is evaluated indirectly.
- The fractal dimension calculated in the fractal dimension analysis based on the three-dimensional pore distribution data obtained from the mercury-intrusion method has close correlation with the frost susceptibility. This means that the fractal dimension for pore distribution becomes a factor that permits indirect evaluation of the frost susceptibility described in (2) because it represents the connection and spatial distribution of pores.

#### Acknowledgments

We wish to thank Prof. T. Odagaki at the Department of Physics and T. Kimura, a technical official at the Department of Chemistry and Materials Technology of Kyoto Institute of Technology for their assistance in computer software for carrying out this experiment. This work was partially supported by the Science Research Grant of Ministry of Education in Fiscal 1990 (Theme No.02555161; representative, M. Nakamura). The support is gratefully acknowledged.

#### References:

- M. Nakamura, *J. Soc. Powder Tech. Jpn.*, 26, 578-585 (1989).
- M. Nakamura, *Gypsum & Lime*, No.231, 113-121 (1991).
- O.J. Whittemore, Jr. and J.J. Sipe, *Powder Technol.*, 9, 159-164 (1974).
- G.G. Litvan, *Am. Ceram. Soc. Bull.* 63, 617-618 (1984).
- P.C. Aitcin and D. Vezina, *Cement, Concrete, Aggregates, CCAGDP*, 6, 38-42 (1984).
- R. Schmidt, *Interbrick*, 2, 40-43 (1986).
- M.R. Arnott and G.G. Litvan, *Am. Ceram. Soc. Bull.* 67, 1332 (1988).
- S.L. Marusin, *ibid.*, 69, 1332 (1990).
- M. Nakamura, A. Hama, S. Matumoto, S. Okuda and P.P. Hudec, *Yogyo Kyokaiishi*, 94, 1149-1156 (1986).
- P.P. Hudec, *Durability of Build. Mater.*, 1, 275-300 (1983).
- F. Ehrburger and R. Jullien, *Characterization of Porous Solid*, ed. by K.K. Unger et al., Elsevier, (1988) 441.
- H. Takayasu, *Fractal*, Asakura shoten, (1987) 36.

# Distribution of Electric Resistance of Dielectric Semiconductor Ceramics

Miho Uehara and Masakazu Tanahashi\*

Materials Characterization Department, Matsushita Technoresearch, Inc.  
3-15, Yagumo-Nakamachi, Moriguchi-shi, 570 Japan  
Corporate Research & Development Laboratory, Matsushita Electronic Components Co., Ltd.  
1006, Kadowa, Kadoma-shi, 571 Japan

**Direct observation of the distribution of electrical resistance within dielectric semiconductor ceramics by means of optical and scanning electron microscopes became possible by electrolytical etching of the ceramics conducted in diluted acid. By this method, the insulating layer of BaTiO<sub>3</sub> surface-layer type semiconductor ceramics and the grain-boundary of the SrTiO<sub>3</sub> semiconductor ceramics became observable by SEM or optical microscopes, and the distribution of the electrical resistance within the ceramics became measurable. It is considered that the latter insulating boundary layers are different from Bi diffused layers.**

[Received May 15, 1991; Accepted July 18, 1991]

**Key-words:** Dielectric semiconductive ceramic, Electrolytical etching, Surface dielectric layer, Boundary layer, Ceramic capacitor

## 1. Introduction

By utilizing the particular electrical characteristics realized by its inherent semiconductive and dielectric properties, semiconductor ceramics have been applied to produce various electronic components including capacitors, varistors, thermistors, etc.

Whereas the ceramics composition consisted mainly of semiconductor ceramics and dielectric parts existing on either the surface or at the grain boundaries, and the electrical characteristics of the grain boundary had been studied extensively,<sup>1,2)</sup> very few had been reported on the actual observation of the dielectric part except a case wherein a substantial materialistic unbalance such as segregation is produced.<sup>3,4)</sup>

This difficulty comes from the facts of nearly identical compositions of the semiconductor and the dielectric parts, producing no significant and detectable differences in the chemical composition and the element distribution.

Moreover, even if boundaries in the chemical composition were found, it would be nearly impossible to prove the coincidence of the composition boundary with the electrical boundary.

Thus, in our efforts to differentiate the above two boundaries, observations of the reoxidized insulating surface layer formed on a surface-layer type semiconductor ceramic (hereafter called SL-SC) capacitor and the grain-boundaries formed within a diffusion-material added grain-boundary type semiconductor ceramic (hereafter called DMA-GB-SC) capacitor are experimented.

SL-SC with a thin insulating layer on its surface is produced by reoxidizing the surface of a semiconductor ceramics which is produced by a sintering process in air which is followed by a reduction sintering process. Therefore, the chemical compositions of the layer and the semiconductor parts are identical except a slight oxygen deficiency in the surface.

Despite of a few past attempts to observe a cross-section of surface-insulation layer carried out using a reflection mode of optical microscope,<sup>5)</sup> and to observe a cross-section on which a potential difference is applied also by using a scanning electron-microscope (SEM),<sup>6)</sup> the observation of surface-insulation layer formed on SL-SC is a highly difficult task because of its indistinctive boundaries, and even if it became observable, its coincidence with the insulation layer could not be proved.

The DMA-GB-SC capacitors are formed by reduction sintering of semiconductor ceramics. After coating its surface by BiO<sub>3</sub>-CuO, the ceramics is subjected to a diffusion sintering in order to diffuse the oxides into the boundaries within the ceramics and to form an insulation layer on the surface. In this case again, although the distribution of the diffused material in the grain boundaries had been known,<sup>4)</sup> the coincidence of this with the insulation layer had not been established.

Thus, in these facts in mind, a method to observe and detect the boundary layers is developed by directing attentions of authors to the difference in the electrical resistances. With this method, the ceramics is electrolytically etched in acid solution to form surface indentations which are distinctively observable by either SEM or optical microscopes.

## 2. Experimental Method

### 2.1. Detection of The Reoxidized Layer of Surface-layer Type SC Capacitor

#### 2.1.1. Pretreatment

In order to observe and detect the surface insulation layer, a disc-shaped barium titanate SL-SC (capacitor of a diameter of 7.5mm, thickness of 300 $\mu$ m, static capacitance of 1000pF, insulation resistance of more than 10000M-Ohms) is vertically buried into a resin mold.

Then, the mold is cut to expose it cross-section on the upper and lower surfaces of the mold respectively. An electrode is deposited on the upper surface while specular-polish is applied onto the lower surface in order to make the observation and detection of the surface-layer easier.

At this state, the ceramics is conductive between the

lower and the upper surfaces, allowing easy determination of the conductivity by an ohm-meter.

### 2.1.2. Direct Measurement of Resistance Distribution

In this experiment, the ceramics specimen is cut to expose its diagonal cross-section in order to obtain a larger cross-sectional area to be observed. By this, the 300 $\mu\text{m}$ -thick cross-section is enlarged up to a width of 6mm. A stainless-steel very fine needle is adapted on one of the probe terminals of digital multi-meter made by FLUKE. By this, a contact area on the specimen of a radius less than 20 microns is realized.

The electric resistance is determined as the needle probe is sequentially scanned along the thickness direction under a stereomicroscope, while the other probe terminal is fixed on the upper electrode.

### 2.1.3. Observation of The Electrolytically Etched Reoxidized Layer

The ceramics specimen is electrolytically etched in diluted nitric acid (diluted down to cause no further chemical etching) for 30minutes by applying  $-10\text{V}$  to a carbon electrode dipped into the electrolyte while the lower surface of the specimen is kept at a plus polarity before the SEM observation of the surface is made. The specular-polished surface prior the etching is observed also as a contrast.

### 2.1.4. Effects of Heat-Treatment on the Reoxidized Layer

By altering the heat-treatment time (to perform reoxidation sintering) applied to the barium-titanate ceramics manufactured by the same method up to the reduction sintering process, various ceramics specimens are prepared. The heat-treatment is applied at a rate of temperature rise and fall of 400 $^{\circ}\text{C}/\text{hr}$ , a keep temperature of 1000 $^{\circ}\text{C}$ , a keep time of either 2, 4, or 16h, conducted in air.

The reoxidized layers are observed by a method shown in Sec. 2.1.3 in order to determine the respective thicknesses.

## 2.2. Detection of Grain Insulation layer of Grain Boundary Type Semiconductor Ceramic Capacitor

In order to observe the grain-boundary insulation layer, a disc-shaped strontium titanate GB-SC capacitor (having a diameter of 6.0mm, thickness of 250 $\mu\text{m}$ , static capacitance of 18000pF, a diffusion material of BiO<sub>3</sub>, and an insulating resistance of 8000M-Ohms) is ground down to a thickness less than that of the ceramic grain size (10–30 $\mu\text{m}$ ), and the observation surface is specular-polished as shown in Fig.1(a). At this condition, the surface is conductive to the reverse side through the grains.

The finished thin ceramic specimens is pasted on

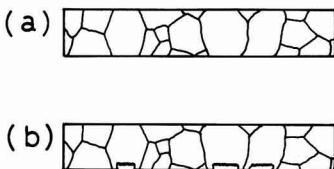


Fig. 1. Specimen for SEM observation of SrTiO<sub>3</sub> boundary layer.

(a) Polished to thin layer less than grain size.

(b) Electrolytically etched in dilute acid.

a doughnut-shaped insulating holder, and its reverse side is coated with a conductive paste to form an electrode there.

The specimen is then electrolytically etched in diluted nitric acid according to the method shown in Sec. 2.1.3. The specimen shown in Fig.1(b) is removed from the holder before the SEM observation is made. The specimens prepared by etching in the same diluted nitric acid without applying potential, and the specimens without etching are observed also.

## 3. Results and Discussion

### 3.1. Insulation Layer of the Surface-Layer Type Ceramic Capacitor

Figure 2 shows a result of the electrical resistance measurements conducted on the cross-section of ceramic specimen. Despite of a slightly higher apparent resistance of the conductive part due to the point contact, this shows distinctive differences between the semiconductor part and the insulation part, proving the existences of insulation layers on both surfaces.

The thickness of the surface insulation layer is found to be approximately 30 $\mu\text{m}$ , and beside these, parts having higher resistances are found even within the semiconductor parts.

Although the existence of reoxidized layer of the SL-SC capacitor is confirmed, and the partial thickness are determined by this method, a huge amount of resistance measurement have to be carried out in order to obtain a total image.

Figure 3 shows respective photographs of a specular-polished surface of the surface-layer type SC before and a surface after the application of electrolytic etching shown in Sec. 2.1.3. The latter photograph with a high contrast shows the surface roughened by the etch-off of the semiconductor parts and by the insulation parts unaffected by the etching.

The thickness of the insulation layer is even throughout the surface, and is approximately 30 $\mu\text{m}$ , and this coincides with the result of the direct observation.

Insulation parts are observed in a form of white islands existing within the semiconductor parts. According to an analysis carried out by using an energy-distributed X-ray microanalyzer, the island could be a part failed to change into semiconductor, and this contains titanium at a content

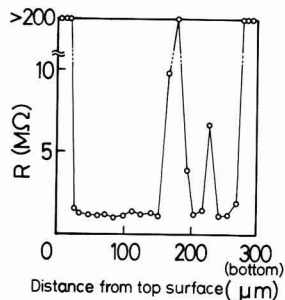


Fig. 2. Electric resistance of cross section of BaTiO<sub>3</sub> surface layer semiconductor ceramic capacitor. Total thickness is 300 $\mu\text{m}$ .

higher than that in BaTiO<sub>3</sub> parts.

Figure 4 shows photographs of the electrolytically etched surfaces of surface-layer SC specimens subjected to different reoxidizing conditions.

Figure 5 shows plots of the determined thickness of the insulation layer and the reciprocals of static capacitance taken against the reoxidation time.

Since these plots are on two straight lines which go through the origin, this proves that the static capacitance is solely dependent on the thickness of the insulation layer, and the reoxidation is made by the diffusion of oxygen atoms obeying the Fick concentration diffusion rule.

In the experiments conducted on the presently prepared specimens, specifying the thickness of the insulation layer by  $l$  and the re-oxidation time by  $t$ , an empirical relationship,  $l = 13.0\sqrt{t}$  is derived. This proves that the parts which became detectable by the electrolytic etching correspond exactly to the insulation layer (dielectric parts).

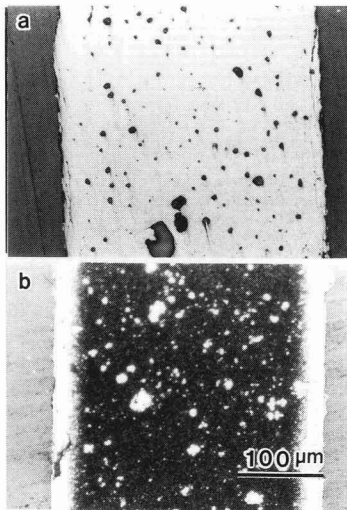


Fig. 3. Optical photograph of cross section of BaTiO<sub>3</sub> surface layer semiconductor ceramic capacitor.

(a) Specular polished, and (b) Electrolytically etched

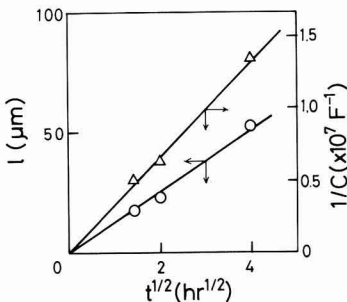


Fig. 5. Effect of reoxidation time on electric capacitance and thickness of insulating layer of BaTiO<sub>3</sub> surface layer semiconductor ceramic capacitor.

### 3.2. Grain Boundary Insulation Layer of the Grain Boundary Semiconductor Ceramics

Figure 6(a) shows a SEM photograph of specular-polished surface of GB-SC, Fig.6(b) shows the same surface after electrolytic etching, and Fig.6(c) shows the surface after chemical etching. These photographs show the bismuth diffusion layers appeared in a form of white traces along the grain boundaries.

Within the specimen, the grains realizing no conductivity between surface and reverse surface after electrolytic etching are keeping with their respective polished surface as they are, while two insulation layers formed within the grain boundaries of the etched grain are observed.

These two lines are attributed for the insulation layers originally formed at the neighborhood of the grain boundaries. These are left intact with their specular surfaces while the grains which are semiconductor are etched off.

Since this insulation layers are uniformly formed, this suggest that the growth of the grain boundary is controlled by the oxygen diffusion rate like the growth of the insulation layer of SL-SC.

Whereas a total disappearance of grain boundary for a width of 0.1µm is observed for all the specimens regardless its etching method, this could be attributed for the dissolve of strontium titanate which is denatured by the diffusion of the added BiO<sub>3</sub> along the grain boundaries since this disappearance coincide with the observed white insulation layer

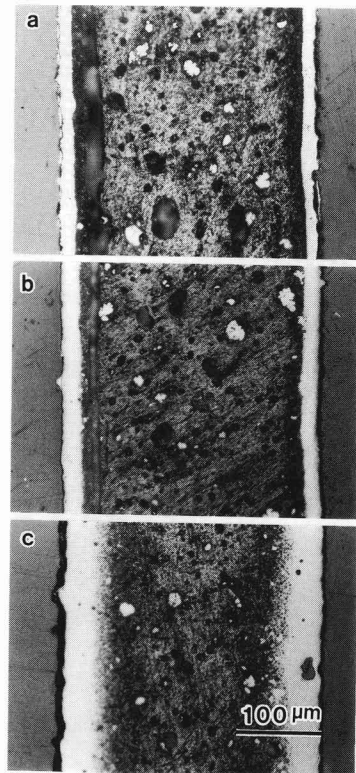


Fig. 4. Optical photograph of BaTiO<sub>3</sub> surface layers. Reoxidated at 1000°C for (a) 2H, (b) 4H and (c) 16H.

lines.

Therefore, the grain boundary which became observable after electrolytic etching is different from the bismuth diffusion layer, and this is formed at an internal part within the bismuth diffusion layer.

### 3.3. Electrolytic Etching of the Ceramics

As shown in Secs. 3.1 and 3.2, by using this method, ceramics having identical chemical properties can be discriminated by utilizing their differences in the respective conductivities. This is caused by the distribution of electrical

resistance existing even within a same semiconductor part, producing different etching modes therein.

Taking an example for a grain of the GB-SC, the semiconductor part neighboring to the grain boundary is etched stronger than those at the grain center. A resistance distribution formed at the sintering could be responsible for this.

Since the developed etching method is able to convert the resistance distribution into a form of surface irregularities, this method is applicable to other conductive ceramics.

## 4. Conclusion

An electrolytic etching method to be conducted in dilute acid is developed in order to observe electrical resistance distribution within semiconductor ceramics. By applying this method, particular surface irregularities which can be easily observed by optical microscope or SEM are formed.

The two-dimensional structure of reoxidized insulation layer formed on the surface-layer type semiconductor ceramics is determined and its formation obeying the Fick-type oxygen diffusion rule are identified.

The grain-boundary of the grain-boundary type semiconductor ceramics became observable first time as a form of insulation layer. This layer is considered to be different from the bismuth diffusion layer formed at the grain boundary.

Detailed study on the intergranular insulation layer of semiconductor ceramics capacitor will be continued by using this method.

(A part of this study was published at Electronic Materials Study Discussion of the Ceramics Society of Japan in October, 1988.)

### Acknowledgements

The authors wish to express their sincere appreciations to Messrs. M. Fujimura and H. Rokumaru of Miyazaki Matsushita Electric Co. Ltd. for their full supports and encouragements given to this project.

### References:

- 1) M. Kuwahara, Hyomenkagaku, 6, 340-346, (1985) in Japanese.
- 2) J. Tanaka, FC Report, 5, 244-251 (1987).
- 3) M. Inada, Jpn. J. Appl. Phys., 17, 673-677 (1978).
- 4) M. Fujimoto and W.D. Kingery, J. Am. Ceram. Soc., 68, 169-173 (1985).
- 5) Y. Matsuo and M. Fujimura, National Technical Report, 28, 6, 1135-1143 (1982) in Japanese.
- 6) S. Maruyama, Electro-Ceramics, 4, 57-60 (1973).

This article is a full translation of the article which appeared in Nippon Seramikkusu Kyokai Gakujutsu Ronbunshi (Japanese version), Vol.99, No.11, 1991.

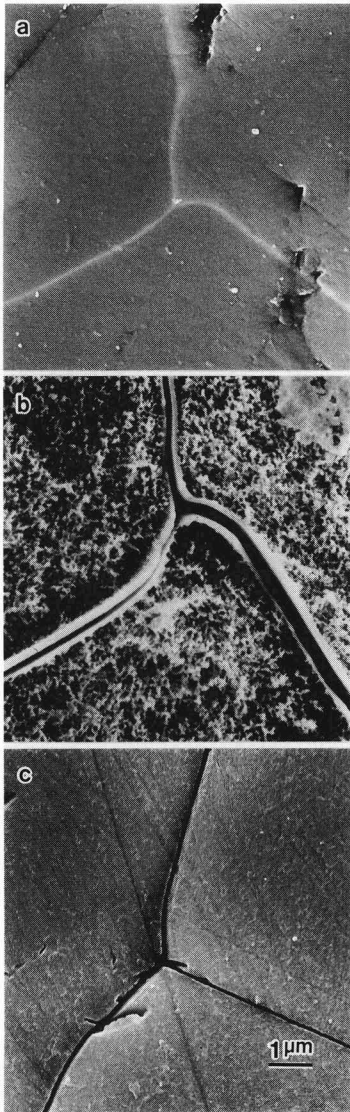


**Fig. 6.** SEM photograph of insulating layers of SrTiO<sub>3</sub> boundary layer capacitors.

(a) polished boundary, (b) electrolytically etched boundary and (c) chemically etched boundary.

# High Temperature Oxidation of Si<sub>3</sub>N<sub>4</sub> in O<sub>2</sub>-N<sub>2</sub> Atmospheres

Makoto Ishikawa, Nobuyuki Takeuchi, Shingo Ishida, Mitsuru Wakamatsu and Koji Watanabe\*

Department of Chemistry and Materials Technology, Kyoto Institute of Technology

Matsugasaki, Sakyo-ku, Kyoto-shi, 606 Japan

\*Technical Research Laboratory, Taiko Refractories Co., Ltd.

Makiyama-Shinmachi, Tobata-ku, Kitakyusyu-shi, 804 Japan

High temperature oxidation tests were carried out in a flowing O<sub>2</sub>-N<sub>2</sub> mixture for gas-pressure-sintered Si<sub>3</sub>N<sub>4</sub> containing Y<sub>2</sub>O<sub>3</sub> and Al<sub>2</sub>O<sub>3</sub> as sintering aids. The oxidation temperature and time were 1400°C and 15h, respectively and O<sub>2</sub> concentration in the gas mixture ranged from 1 to 100vol%. The oxidation reaction was monitored every minute by measuring of the evolved N<sub>2</sub> and NO gases with a quadruple mass spectrometer. The oxidation rate expressed as the N<sub>2</sub> evolution rate was in the order 1% O<sub>2</sub> > 21% O<sub>2</sub> ≥ 100% O<sub>2</sub>. In oxidation in high O<sub>2</sub> concentration, oxidation kinetics obeyed the parabolic law and a good conformity was obtained between the amount of N<sub>2</sub> evolved and the weight gain of the Si<sub>3</sub>N<sub>4</sub> sample after the oxidation. At a low O<sub>2</sub> concentration (1vol%), the oxidation rate was partly expressed by the first-order kinetics and a poor conformity was observed between the amount of N<sub>2</sub> evolved and the weight gain. It should be noted that the conformity improved when the gas flow rate was greatly increased.

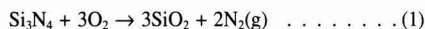
[Received May 17, 1991; Accepted July 18, 1991]

**Key-words:** Si<sub>3</sub>N<sub>4</sub>, Oxidation, Mass-spectrometer, N<sub>2</sub> gas, Weight gain

## 1. Introduction

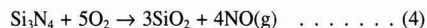
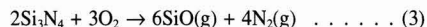
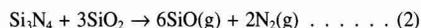
Silicon nitride (Si<sub>3</sub>N<sub>4</sub>) is a high temperature serviceable structural material with high mechanical property and a high thermal shock resistance. Thereby, it has been used commercially in various fields, notably as a turbocharger rotor. However, it has a problem of strong oxidation susceptibility in a high temperature oxidizing atmosphere. Therefore, a number of study results have been reported on the oxidation behavior of Si<sub>3</sub>N<sub>4</sub>.<sup>1-3)</sup>

The most popular quantitative evaluation method of oxidation reaction of Si<sub>3</sub>N<sub>4</sub> is based on the measurement of weight gain of Si<sub>3</sub>N<sub>4</sub> sample during oxidation. If this oxidation is assumed to proceed by the reaction shown in equation (1), the weight gain of Si<sub>3</sub>N<sub>4</sub> due to the formation of silica can represent the amount of Si<sub>3</sub>N<sub>4</sub> oxidized.



This method of determining the reaction rate by the weight gain has an advantage of easy measurement on the one hand, but it involves the following problems on the other hand. They are, for instance, (1) protective films on the sample surface are given with a thermal shock when the sample is

periodically taken out of a furnace for the measurement of its weight gain, and (2) time interval of the measurement cannot be arranged so short as desired, thereby, abrupt changes in the oxidation reaction are hard to be detected. A continuous measurement method of the weight change of sample using a thermo-balance can be a solution to these problems, but not only it is restricted in the shape and the weight of sample, but also actual reactions taking place can be only estimated from the oxide phases in the sample after the entire reactions. Especially when some other reactions to cause a weight loss of sample take place simultaneously, for instance, when active oxidation reactions to form SiO vapor (as shown in equations (2) and (3) below) take place, or when additives evaporate, the quantity of oxidation reaction will be assessed smaller than the actual one, if we only rely on the conventional method of measuring the weight gain of sample based on a reaction of equation (1). Furthermore, even when the reaction to form silica is taking place, the reaction actually taking place might possibly be eq.(4), instead of eq.(1) usually assumed. These two different reactions could not be distinguished by the measurement of the weight change of Si<sub>3</sub>N<sub>4</sub> sample.



Consequently, the authors have investigated the oxidation reaction mechanism of sintered Si<sub>3</sub>N<sub>4</sub> by means of mass spectrometric analysis of exhaust gases evolved during the oxidation test of the Si<sub>3</sub>N<sub>4</sub> samples. We previously reported the investigation results on the oxidation reaction of Si<sub>3</sub>N<sub>4</sub> in the condition of 100% oxygen concentration in the oxidation test atmosphere.<sup>4)</sup> This report concerns the effect of oxygen concentration in the test atmosphere on the oxidation reaction of gas-pressure-sintered Si<sub>3</sub>N<sub>4</sub> in the atmosphere of high temperature oxygen-nitrogen gas mixture.

## 2. Experimental Procedure

### 2.1. Test Samples

Test samples used in our experiments were sintered Si<sub>3</sub>N<sub>4</sub> bodies, which were prepared by adding 5wt% of Al<sub>2</sub>O<sub>3</sub> and 5wt% of Y<sub>2</sub>O<sub>3</sub> as sintering aids, and by sintering at 1750°C for 2h under a gas pressure of lower than 0.85MPa. Chemical composition of the sample analyzed by EDX is shown in Table 1. Test specimen was prepared in a rectangular prism shape in dimension of 3×4×40mm as specified by

industrial standard of JIS R 1601 for bending test of fine ceramics. The surfaces of the specimen were polished using #800 silicon carbide polishing papers, and then finished by ultrasonic cleaning in acetone.

## 2.2. Oxidation Test

Figure 1 shows a diagram of the oxidation test apparatus used.

The oxidation test was carried out by continuously supplying oxygen gas or oxygen-nitrogen gas mixture ( $O_2$ : 21vol% /  $N_2$ : 79vol% or  $O_2$ : 1vol% /  $N_2$ : 99vol%) at a flow rate of 20ml/min in a combustion tube made of mullite, which was placed in an electric furnace. The test specimen was placed in the combustion tube, which was held at the outside of the furnace without being heated. After the furnace was heated to 1400°C, this combustion tube was quickly inserted into the furnace and held there for 15h to be heated.

A part of the exhaust gas in the normal pressure (0.1MPa), which included the gases evolved during the oxidation test, in addition to the waste feed gas mixture, was introduced directly into the analysis chamber in a high vacuum ( $10^{-4}$ Pa) of a quadruple mass spectrometer through a leak valve, and the respective mass spectra of various gases in the exhaust gas were measured continuously. Mass numbers of the gas ions we measured ranged up to  $m/e$  value of 60 ( $m$ : mass number of ion,  $e$ : charge number of ion). By scanning in about 60sec, the mass spectrometer recorded continuously the data of ion intensity of the respective gas ions. Thereby, the data of ion intensity of all gas ion intensity obtained every minute.

In general, any ion intensity to appear in a mass spectrum is exhibited in a different value, depending on the apparatus of mass spectrometer used, or on the electron energy for ionization used, even when the same sample gas is used. Furthermore, even if the same apparatus and the same electron energy for ionization are used in the continuous mass spectrometric measurement, a minor fluctuation of the degree of vacuum in the quadruple chamber, including the ionization chamber, is unavoidable, when a single step pressure reduction is arranged for the continuous sampling of exhaust gas through the leak valve. Oxidation reaction mechanism of  $Si_3N_4$  was investigated in the past using a mass spectrometer,<sup>5)</sup> but it was not pursued sufficiently, because qualitative data were only available from the mass spectrometric measurement. To obtain the quantitative data of the gases evolved, the dependence of relative ion intensity on the degree of vacuum must be analyzed by all means. The authors confirmed that relative ionic strengths of various gases contained in the exhaust gas were not affected by such conditions in the mass spectrometric measurement as the degree of vacuum and others, as long as the concentrations of respective component gases in the feed

gas mixture were kept constant, and, based on these confirmed results, we corrected the ion intensity values we measured. As a result, by using a quadruple mass spectrometer, which has been regarded as only effective for the qualitative evaluation of gases, we were able to compare the relative ion intensity which corresponded to the concentrations of various gases in the exhaust gas evolved during the oxidation test, and, based on the ion intensity values measured of various standard gases respectively having a known concentration, we were further able to obtain the absolute values of the respective gas concentrations and to evaluate quantitatively the various gases in the exhaust gas evolved.

Using the samples before and after the oxidation test, we measured their respective weights, and investigated the relationship between the weight change of the sample and the amount of gas evolved. Concerning the surface of sample after the oxidation test, we identified the crystalline phases by X-ray diffraction (XRD) analysis, and examined the formed species using a scanning electron microscope (SEM), which was attached with an energy dispersive X-ray analysis (EDX).

## 3. Results

### 3.1. Gases Evolved and Weight Gains by Oxidation

Figure 2 shows the respective total amounts of various gases evolved and the weight gains of samples during the oxidation test of sintered  $Si_3N_4$  samples. The major component gases evolved were  $N_2$  and  $NO$ , regardless of oxygen concentration in the test atmosphere. A small amount of  $CO_2$  was confirmed to be additionally contained. It was recognized that the amount of  $N_2$  evolved by the oxidation reaction increased with the decrease of oxygen concentration in the atmosphere gas. Especially when oxygen concentration was 1vol%, a great amount of  $N_2$  was observed. This suggests the oxidation reaction took place violently. Meanwhile, the weight gain of sample showed a little difference in its dependence on the atmosphere gas condition from that in the same dependence of the amount of  $N_2$  evolved. That is, the weight gain increased with the

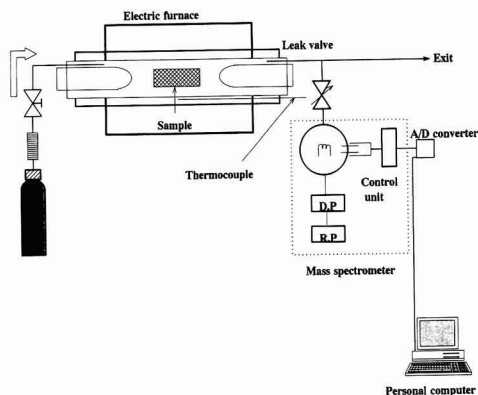


Table 1. Chemical composition of  $Si_3N_4$  sample.

Chemical composition (wt%)					
$Al_2O_3$	$Y_2O_3$	$K_2O$	$CaO$	$Fe_2O_3$	Cl
3.30	4.76	0.08	0.07	0.30	0.25

Fig. 1. Diagram of Oxidation apparatus.

decrease of oxygen concentration from 100% to 21vol% in the atmosphere gas, but turned to decrease greatly with the further decrease of oxygen concentration to 1vol%. In the case of oxygen concentration of 1vol%, the weight gain measured of the sample after oxidation test was lower than that calculated from the total amount of N<sub>2</sub> evolved, when the flow rate of atmosphere gas was as low as 20ml/min. However, it was high enough to correspond relatively well to that calculated, when the flow rate of atmosphere gas was 60ml/min.

Figure 3 shows the evolution rate of N<sub>2</sub> (μl/cm<sup>2</sup>min) during the oxidation test of sintered Si<sub>3</sub>N<sub>4</sub> sample at 1400°C plotted against the oxidation time. Four N<sub>2</sub> evolution rate curves in the figure correspond respectively to the various conditions of oxidizing gas atmosphere. In any atmosphere condition, N<sub>2</sub> evolution rate is observed to reach a maximum within a few minutes after the sample was quickly inserted in the high temperature oxidizing gas in the furnace, and to subsequently decrease rapidly or gradually. This behavior suggests that the initial oxidation of Si<sub>3</sub>N<sub>4</sub> takes place in a very short time, but the subsequent oxidation proceeds suppressively due to the formation of oxidized layer on the sample surface as protective films. However, it is also seen that the changing behavior or N<sub>2</sub> evolution rate against the oxidation time are a little different, depending on the oxygen concentration in the atmosphere gas. In the case of atmosphere gas with a high oxygen concentration such as 100% oxygen, or a gas mixture of 21vol% O<sub>2</sub> and 79vol% N<sub>2</sub> (hereafter called "air"), the oxidation of sample proceeds rapidly immediately after the sample starts to be heated, so that the N<sub>2</sub> evolution rate reaches a maximum of about 45 or 60μl/cm<sup>2</sup>min. In a few minutes after the rate reached a maximum, the N<sub>2</sub> evolution rate starts to decrease rapidly down to a half of the maximum value. After that, it is kept nearly constant for about 1h, and then decrease again rapidly. After decreasing for about 5h, it comes to almost zero.

On the other hand, in the case of oxygen concentration of 1vol% in the atmosphere gas, the oxidation rate of sample does not increase so rapidly immediately after the sample started to be heated as to show the maximum N<sub>2</sub> evolution rate of about 20μl/cm<sup>2</sup>min, which is around a half of that in the case of the atmosphere gas of 100% oxygen or air. It is also observed that the N<sub>2</sub> evolution rate does not decrease rapidly for several minutes after the initial violent oxidation, as observed in the case of the atmosphere of 100% oxygen or air, and that it stays at almost constant for about 15min

after the afore-mentioned decrease.

Figure 4 shows the NO gas evolution rate curves of the same Si<sub>3</sub>N<sub>4</sub> sample. In the case of the atmosphere gas with a high oxygen concentration, the curves of NO evolution rate resemble those of N<sub>2</sub> evolution rate. In the case of the atmosphere gas with 1vol% oxygen concentration, however, it is observed that the NO evolution takes place simultaneously with the N<sub>2</sub> evolution in the initial oxidation period, decreases rapidly until it comes to zero in the subsequent period, and then starts to take place again.

### 3.2. Oxide Films and Oxidation Products

According to our XRD analyses of the oxide phases formed on the surface of Si<sub>3</sub>N<sub>4</sub> sample after the oxidation test, there was no notable difference in the phases caused by the difference of atmosphere gas used. The crystalline phases there identified were cristobalite, Y2S (Y<sub>2</sub>O<sub>3</sub>·2SiO<sub>2</sub>) and Si<sub>3</sub>N<sub>4</sub>. In addition, we observed a broad peak, which was supposed to be assigned to amorphous silicas.

Figure 5 shows the SEM micrographs of the surface of oxidized surface layer of the samples after the oxidation test in various atmospheres. In the case of the sample oxidized in the atmosphere of 100% oxygen or of air, the surface of oxidized layer was smooth and consisted of dense glass phases and crystals of needle or prism type. These crystals of needle or prism type were identified by EDX analysis to have a composition in Y<sub>2</sub>O<sub>3</sub>/SiO<sub>2</sub> molar ratio of 1/2, thereby, they were regarded to be mainly composed of Y2S (Y<sub>2</sub>O<sub>3</sub>·2SiO<sub>2</sub>).

In the case of the samples oxidized in the atmosphere of 1vol% oxygen concentration, the surface of the oxidized layer was rough, and the needle type crystals were not observed much, but mainly unidentified crystals were ob-

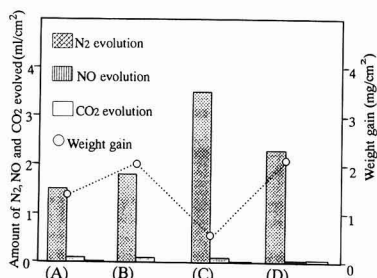


Fig. 2. Weight gain and amount of N<sub>2</sub>, NO and CO<sub>2</sub> evolved oxidized for 15h at 1400°C in O<sub>2</sub>-N<sub>2</sub> atmosphere; (A) O<sub>2</sub>, (B) O<sub>2</sub>(21%)-N<sub>2</sub>(79%), (C) O<sub>2</sub>(1%):20ml/min, (D) O<sub>2</sub>(1%):60ml/min.

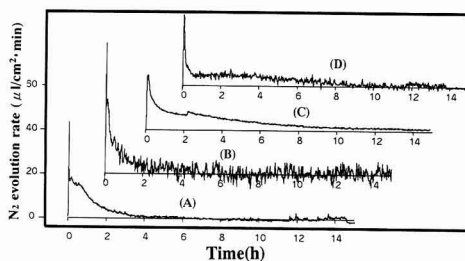


Fig. 3. N<sub>2</sub> evolution rate during the oxidation of Si<sub>3</sub>N<sub>4</sub> at 1400°C in O<sub>2</sub>-N<sub>2</sub> atmosphere; (A) O<sub>2</sub>, (B) O<sub>2</sub>(21%)-N<sub>2</sub>(79%), (C) O<sub>2</sub>(1%):20ml/min, (D) O<sub>2</sub>(1%):60ml/min.

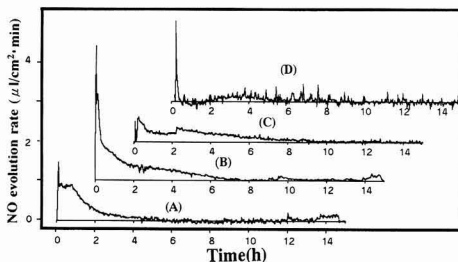


Fig. 4. NO evolution rate during the oxidation of Si<sub>3</sub>N<sub>4</sub> at 1400°C in O<sub>2</sub>-N<sub>2</sub> atmosphere; (A) O<sub>2</sub>, (B) O<sub>2</sub>(21%)-N<sub>2</sub>(79%), (C) O<sub>2</sub>(1%):20ml/min, (D) O<sub>2</sub>(1%):60ml/min.

served instead. These unidentified crystals were analyzed by EDX to mainly consist of silica. The EDX analysis of the amorphous part in the oxidized layer on the surface of the samples after oxidation test revealed that impurity element of low melting point as K, Ca, Fe, etc. was accumulated in a high concentration at the sample surface, compared to the sample surface before oxidation. The accumulation of these impurity matters was especially remarkable in the case of the atmosphere with 1vol% oxygen concentration, in which the oxidation reaction took place violently.

4. Discussion

When Si<sub>3</sub>N<sub>4</sub> is oxidized to form SiO<sub>2</sub> and N<sub>2</sub> as shown in equation (1), square of weight gain (corresponding to formed amount of silica) of Si<sub>3</sub>N<sub>4</sub> sample is generally assumed to obey the so-called parabolic law by changing linearly as a function of oxidation time.

$$W^2 = K_p t + C \dots\dots\dots (5)$$

where, *W* is weight gain, *t* is time, *K<sub>p</sub>* is a parabolic rate constant, and *C* is a constant related to initial oxidation. This parabolic relation expressed by equation (5) implies that oxidation reaction is rate-determined by mass transfer through glassy oxide films mainly consisting of silica, which were formed on the sample surface and act as an oxidation protective film. As another idea, a combined oxidation reaction formula as given in equation (6) below was proposed,<sup>6)</sup> which combined the oxidation reaction rate determined by the linear law in the initial stage of oxidation and that determined by the parabolic law in the progressed

stage of oxidation.

$$W^2 + AW = K_p t + C \dots\dots\dots (6)$$

Here, *W* is weight gain, *t* is time, and *K<sub>p</sub>*, *A* and *C* are constants.

In view of the corresponding relation confirmed between the amount of oxide phases formed by oxidation reaction and the amount of N<sub>2</sub> evolved during oxidation, we examined if a similar relation was effective when the integrated amount of N<sub>2</sub> evolved was used in place of the amount of N<sub>2</sub> evolved at each time. **Figure 6** shows the curves prepared by the integration of the evolution amount of N<sub>2</sub> continuously measured every minute during the oxidation test of Si<sub>3</sub>N<sub>4</sub> sample in the atmospheres with various oxygen concentrations, and **Fig.7** shows the modified curves of parabolic plots prepared from the data shown in Fig.6. In the case of the atmospheres with high oxygen concentrations (100% oxygen and air) used, the integration curves are observed to change their gradients rapidly to a lower inclination, thereby, a resistance to diffusion is indicated to have been caused by the protective films formed. However, when we examine the conformity of these integration curves with the parabolic law in Fig.7, we find that the oxidation reaction of Si<sub>3</sub>N<sub>4</sub> in the atmosphere with high oxygen concentration is not so simple as to be expressed by a single equation of diffusion-controlled rate determination. By this is mean, that the integration curve obeys the parabolic law to exhibit a constant gradient for around 2h immediate after the oxidation of sample is initiated, but it starts to deviate from the parabolic law after that and comes to nearly zero in inclination in the late period. Hasegawa et al.,<sup>7)</sup> Davidge et al.,<sup>8)</sup> and Tripp et al.<sup>9)</sup> reported similar behaviors

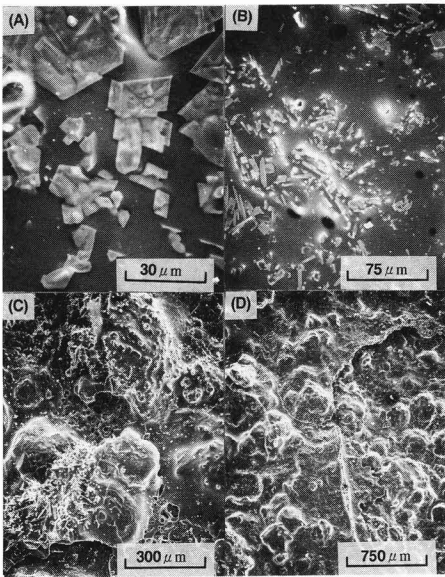


Fig. 5. Scanning electron micrographs of surfaces of Si<sub>3</sub>N<sub>4</sub> specimens oxidized for 15h at 1400°C in O<sub>2</sub>-N<sub>2</sub> atmosphere; (A) O<sub>2</sub>, (B) O<sub>2</sub>(21%)-N<sub>2</sub>(79%), (C) O<sub>2</sub>(1%) 20ml/min, (D)O<sub>2</sub>(1%) 60ml/min.

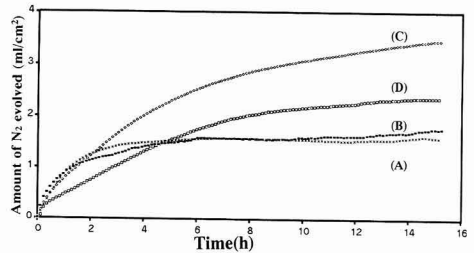


Fig. 6. Amount of N<sub>2</sub> evolved during the oxidation of Si<sub>3</sub>N<sub>4</sub> at 1400°C in O<sub>2</sub>-N<sub>2</sub> atmosphere; (A) O<sub>2</sub>, (B) O<sub>2</sub>(21%)-N<sub>2</sub>(79%), (C) O<sub>2</sub>(1%) 20ml/min, (D) O<sub>2</sub>(1%) 60ml/min.

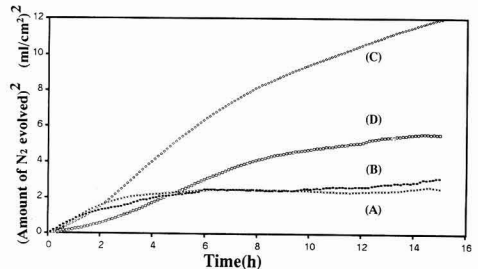


Fig. 7. Parabolic plots for oxidation of Si<sub>3</sub>N<sub>4</sub> at 1400°C in O<sub>2</sub>-N<sub>2</sub> atmosphere; (A) O<sub>2</sub>, (B) O<sub>2</sub>(21%)-N<sub>2</sub>(79%), (C) O<sub>2</sub>(1%) 20ml/min, (D) O<sub>2</sub>(1%) 60ml/min.

of the integration curves as we observed, which apparently indicated the presence of protective films to resist diffusion, but did not simply obey the parabolic law. Among them, the behavior of porous  $\text{Si}_3\text{N}_4$  body reported by Davidge et al. was very similar to what we observed. Meanwhile, the behavior of the integration curves we prepared seems to obey the logarithmic law.<sup>9)</sup> Porosity of our  $\text{Si}_3\text{N}_4$  samples was very low compared to that of porous  $\text{Si}_3\text{N}_4$  samples tested by Davidge et al. but it is hard for us to assume that such low porosity was caused by the closure of pores due to the progress of sintering, resulting in a rapid decrease of oxidation rate of  $\text{Si}_3\text{N}_4$ . Our EDX analysis revealed an accumulation of impurity elements (especially of Fe, K and Ca) in the glass phases in the oxidized surface layer. Judging from this phenomenon of the accumulation of impurity as well as from the fact that the  $\text{Si}_3\text{N}_4$  sample with a low content of impurity oxidized more violently than those with a high content of impurity,<sup>10)</sup> we assume that the accumulated impurity strengthens the function of oxide films as a protective film to oxidation. In other words, the relatively porous oxide phases formed on the surface of  $\text{Si}_3\text{N}_4$  sample in the initial oxidation period were densified as the result of densification of glass phases by the accumulated impurity, resulting in a rapid increase of the resistance to diffusion through the oxidized surface layer, so that the oxidation reaction of  $\text{Si}_3\text{N}_4$  sample almost stopped.

In the case of the atmosphere gas with 1vol% oxygen concentration the curves of evolution amount of  $\text{N}_2$  nearly obey the parabolic law in the period after 4 to 5h from the initiation of oxidation, as seen in Figs.6 and 7. However, the evolution amount of  $\text{N}_2$  increased linearly for 4h from the initiation of oxidation, as if it obeyed the linear law rather than the parabolic law. Therefore, a combined linear-parabolic law as expressed by equation (6) can be applied more suitably to the entire behavior in the oxidation of  $\text{Si}_3\text{N}_4$  samples. The behavior where the evolution amount of  $\text{N}_2$  obeyed the linear law in the initial oxidation period when oxide films were not formed sufficiently yet, as aforementioned, implies that the oxide films were not formed completely as to cover the whole surface of a  $\text{Si}_3\text{N}_4$  sample, or were formed completely but in a very porous state, therefore, the oxidation of the sample was rate-determined by reaction. In general, the oxidation of  $\text{Si}_3\text{N}_4$  sample (obeying the linear law while the protective films are being formed in the initial oxidation period) takes place for a very short time, so, it is difficult to detect by measuring the weight gain of the sample. In fact, in the case of the atmosphere with a high oxygen concentration, the oxidation of the sample was observed to obey the linear law for a very short time, and to change soon thereafter and start to decrease according to the parabolic law. However, in the case of the atmosphere with 1vol% oxygen concentration, linear law behaviour was observed for quite a long period. The reasons are categorized into the following two cases.

First, it took a long time before homogeneous protective films were formed over the whole surface of the sample. When we examined the oxygen concentration curve in the exhaust gas which we simultaneously measured with other gas concentrations in the oxidation test, we found that oxygen was consumed almost completely for the continuous long period in the initial oxidation period, since the flow velocity of the atmosphere gas was low and the furnace inner volume was very small. (Oxygen reaction ratio was higher than 80% in the period for 30min after the oxidation

reaction initiated). This experimental result can be seen as proof for the long of linear law behaviour. Secondly, period some reactions not forming the protective films are taking place. This case will include, as Billy indicated,<sup>11)</sup> an active oxidation of  $\text{Si}_3\text{N}_4$  forming  $\text{SiO}$  gas, a periodical exfoliation of oxide phase layer formed, a crack generation in the oxide phase layer due to crystallization, and a porosification of oxide films due to foaming by  $\text{N}_2$  and other gases. However, the phenomena of other active oxidation are mainly caused after the oxidation of  $\text{Si}_3\text{N}_4$  has progressed sufficiently, so it is hard to assume that they cause the linear progress of oxidation in the initial period, as we observed. Then, if such active oxidation of forming  $\text{SiO}$  has taken place, it necessarily is accompanied by a weight loss of  $\text{Si}_3\text{N}_4$  sample. In several reports, they confirmed the occurrence of active oxidation by the weight loss of  $\text{Si}_3\text{N}_4$  sample. In our current experiments, we could not observe the weight gain of the sample after oxidation, but we observed some inconformity in quantity between the amount of  $\text{N}_2$  evolved and the weight gain of the sample as shown in Fig.2. That is to say, in the case of the atmosphere with a high oxygen concentration, the weight gains measured of the sample almost conformed with the respective values calculated by the oxidation reaction equation (1) from the respective amounts of  $\text{N}_2$  evolved if we take account of the measurement allowances. Meanwhile, in the case of the atmosphere with 1vol% oxygen concentration, the amount of  $\text{N}_2$  evolved was larger than that in the case of the atmosphere with a high oxygen concentration, but the weight gain of the sample was smaller in the former case than that in the latter case. These phenomena suggest that some reaction to cause the weight loss of the sample, for instance, a reaction to form volatile  $\text{SiO}$ , is taking place partially. Singhal<sup>3)</sup> calculated that active oxidation reaction of forming  $\text{SiO}$  could take place at  $1400^\circ\text{C}$  at a low oxygen partial pressure of lower than  $10^{-2.5}$  atm. In fact, in several experimental reports,<sup>1,12)</sup> in which the weight loss was measured and the active oxidation reaction was confirmed to have taken place accordingly, the active oxidation reaction was reported to have taken place at a low oxygen partial pressure close to, or lower than  $10^{-2.5}$  atm. When oxygen concentration is 1vol% in a gas mixture at 1atm, the oxygen partial pressure in the gas mixture is calculated as  $10^{-2}$  atm, which is a little higher than the critical oxygen partial pressure of around  $10^{-2.5}$  atm calculated by Singhal and others. However, the oxygen concentration in the exhaust gas in the initial oxidation period is extremely low, as previously mentioned, and is lower than the critical oxygen partial pressure. If we take account of the oxidation reaction on the entire surface of a sample, we suppose that there might possibly be some part in the atmosphere gas, in which the oxygen partial pressure is reduced low enough to cause an active oxidation reaction. Also, it might be possible that the oxygen partial pressure in the atmosphere gas along the sample surface is influenced by the boundary layer between the sample surface and the gas flow, because the gas flow velocity was relatively low in our experiment. As a matter of general tendency, when a gas flow velocity is low or in the state of natural convection, it is supposed that the oxygen partial pressure is reduced by the effect of the presence of a boundary layer between solid surface and gas, thereby, the active oxidation tends to take place easily.<sup>13,14,15)</sup> In order to confirm the effect of the boundary layer above we carried out an oxidation test using the atmosphere gas with 1vol% oxygen concentration, in

which we increased the atmosphere gas flow rate to 60ml/min, which was three times as high as that of 20ml/min in our standard test. The test result revealed that the weight gain of the sample and the amount of gases evolved conformed well with each other, so the active oxidation to be accompanied by the weight loss of the sample did not take place. However, a part of the relation curve between the amount of  $N_2$  evolved and the test time was observed to obey the linear law for as long as several hours, in the same manner as observed in the case of gas flow rate of 20ml/min. This observed result suggests that a considerably long time is necessary in the case of gas flow rate of 60ml/min, as in the case of that of 20ml/min before the protective films were formed homogeneously on the whole surface of the sample. As the result, the amount of  $N_2$  evolved was smaller in the case of atmosphere gas flow rate of 60ml/min than in the case of that of 20ml/min. (in which active oxidation took place), it was larger in the case of atmosphere gas with 1vol% oxygen concentration and atmosphere gas flow rate of 60ml/min than in the case of atmosphere gas with a high oxygen concentration and atmosphere gas flow rate of 20ml/min. Concerning the weight gain of the sample, same comparative relations were obtained.

## 5. Conclusion

The authors prepared sintered silicon nitride ( $Si_3N_4$ ) samples by the gas-pressure-sintering method using alumina and yttria as sintering aids, and, in order to investigate the effect of oxygen concentration in the oxidizing atmosphere gas on the high temperature oxidation behavior of the  $Si_3N_4$  samples, we carried out an oxidation test of the sample using 3 kinds of  $O_2-N_2$  system oxidizing atmosphere gases with respective oxygen concentrations of 100%, 21vol% and 1vol% in an electric furnace at 1400°C. We carried out continuous quantitative measurements of the exhaust gases from the electric furnace using a mass spectrometer. The following results were obtained.

- 1) When the amount of oxidation reaction was estimated from the amount of  $N_2$  evolved, it was found that oxidation reaction became more violent in the order of oxygen concentration in the atmosphere gas of 1vol% > 21vol% ≥ 100%. Concerning the relationship between the weight gain of sample and the amount of  $N_2$  evolved, it conformed relatively well with the assumed reaction equation based on protective oxidation, in the case of high oxygen concentration in the atmosphere gas, but the weight gains were measured smaller than those calculated from the amount of  $N_2$  evolved using the same reaction equation in the case of 1vol% oxygen concentration in the atmosphere gas. Thereby, it was estimated that some active oxidation reactions accompanying the weight loss of sample like a reaction of forming SiO were taking place in the latter case.
- 2) Concerning the effect of atmosphere gas flow rate on oxidation reaction in the case of 1vol% oxygen concentration in the atmosphere gas, disconformity between the amount of  $N_2$  evolved and the weight gain of sample was not observed in the case of high gas flow rate (60ml/min), as observed in the case of low flow rate

(20ml/min).

- 3) Concerning the effect of oxygen concentration in the atmosphere gas on the relationship between the amount of  $N_2$  evolved and the oxidation time, in the case of high oxygen concentration, the relation curve basically obeyed the parabolic law, but deviated there from in the latter half of the oxidation period, finally decreasing its gradient to zero as if it obeyed the logarithmic law. The reason for such behavior was perhaps because impurity elements of low melting point accumulated in the protective films formed on the surface of  $Si_3N_4$  sample worked to densify the oxide phases (glass phases) in the protective films, resulting in a rapid increase of the resistance of the films to diffusion through the film. Meanwhile, in the case of 1vol% oxygen concentration in the atmosphere gas, the relation curve obeyed the parabolic law by exhibiting a gradual decrease of the oxidation rate in and after the middle part of oxidation period, but showed a long part of the curve of obeying the linear law in the initial oxidation period. Therefore, this relation curve is deemed to obey the combined linear-parabolic laws. This duration of obeying the linear law appeared in the relation curve regardless of the flow rate of atmosphere gas, therefore, a considerably long time would be necessary before homogeneous protective films were formed over the whole surface of  $Si_3N_4$  sample in the initial oxidation period.

## References:

- 1) W.C. Tripp and H.C. Graham, J. Am. Ceram. Soc., 59, 399-403 (1976).
- 2) Y. Hasegawa, H. Tanaka, M. Tsutsumi and H. Suzuki, *Yogyo-Kyokaiishi*, 88, 292-297 (1981).
- 3) S.C. Singhal, J. Mater. Sci., 11, 500-509 (1976).
- 4) M. Wakamatsu, N. Takeuchi, T. Hattori, K. Watanabe and M. Ishikawa, Proc. UNITECR '89, ed. by L.J. Trostel, Jr., (1989) 1694-1703.
- 5) S.S. Lin, J. Am. Ceram. Soc., 58, 160 (1975).
- 6) B.E. Deal and A.S. Grove, J. Appl. Phys., 36, 3770-3778 (1965).
- 7) Y. Hasegawa and K. Hirota, *Ceramics* (in Japanese), 18, 580-585 (1983).
- 8) R.W. Davidge, A.G. Evans, D. Gilling and P.R. Wilyman, *Special Ceramics*, 5, ed. by P. Popper, Brit. Ceram. Res. Assoc., Stoke-on-Trent, (1972) 329-343.
- 9) G. Tammann, W. Koster, Z. norg. alleg. Chem., 123, 196 (1922).
- 10) N. Takeuchi, M. Wakamatsu, S. Ishida, K. Watanabe and M. Tshikawa, Abstract papers for 1990 Autumn Mtg., Kyushu branch of Ceram. Soc. Jpn. (1990).
- 11) M. Billy, *Nitrogen Ceramics*, ed. by F.L. Riley, Martinus Nijhoff Publishers (1983) 403-418.
- 12) J.E. Sheehan, J. Am. Ceram. Soc., 65, C111-113 (1982).
- 13) M. Maeda, K. Nakamura, A. Tsuge, J. Master. Sci. Lett., 8, 195-197 (1989).
- 14) J.W. Hinze and H.C. Graham, J. Electrochem. Soc., 123, 1066-1073 (1976).
- 15) P. Barlier and J.P. Torre, J. Mater. Sci., 14, 235-237 (1979).

This article is a full translation of the article which appeared in *Nippon Seramikkusu Kyokai Gakujutsu Ronbunshi* (Japanese version), Vol.99, No.11, 1991.

# Composition and Microstructure of CVD-C, SiC Coating on SiC Fiber

J.X. Li, Yohtaro Matsuo and Shiushichi Kimura

Department of Inorganic Materials, Tokyo Institute of Technology  
2-12-1, Ookayama, Meguro-ku, Tokyo, 152 Japan

Nicalon-SiC fibers were coated with (C, SiC) at 1200°C and 1300°C by chemical vapor deposition to improve the thermal stability of the fibers and to modify fiber-matrix interface. A coating layer having thickness of 0.1 $\mu$ m-25 $\mu$ m was obtained by controlling the CVD conditions. According to the AES and SEM analyses, a carbon rich layer (0.1 $\mu$ m-0.5 $\mu$ m) was deposited on the fiber surface initially. Nuclei of silicon carbide were formed on the surface of the carbon rich layer and finally whiskers or domed grains of silicon carbide were grown. The deposition rates of the carbon rich layer and silicon carbide layer were about 0.02 $\mu$ m/min and 0.65 $\mu$ m/min, respectively. It was observed by XRD and TEM that domed grains, which were the mixtures of  $\beta$ -SiC and small amount of  $\alpha$ -SiC, consisted of subgrains and contained stacking faults in high density.

[Received May 22, 1991; Accepted July 18, 1991]

**Key-words:** Nicalon-SiC fiber, CVD-Coating, Composition, Carbon rich layer, Microstructure, Morphology

## 1. Introduction

The high toughness of fiber-reinforced ceramic matrix composites is mainly provided by crack bridging by reinforced fiber, debonding of fiber from matrix, friction slip between fiber and matrix, and fiber pullout. As well known the interfaces of fiber and matrix greatly affect the above-stated mechanism for higher toughness, so that appropriate interfaces are required to obtain high-performance composites. However, at present, there are few kinds of reinforced-fiber that can be used for ceramic matrix composites. One reason is that as in the case of alumina fiber, high sintering and operating temperatures cause strong chemical bonding between fiber and matrix, and composites are destroyed catastrophically as in monolithic materials, thus damaging the mechanism for higher toughness. Another reason is the high-temperature degradation of fiber itself (oxidation or thermal decomposition at high temperatures).<sup>1)</sup> To prevent these disadvantages, fiber surfaces are modified by ceramic coating with excellent thermal and oxidation resistance as well as good compatibility with fiber.<sup>2,3)</sup> The hopeful candidates among existing ceramic fiber for ceramic matrix composites are CVD-SiC fiber (Avco) and Nicalon fiber (Nippon Carbon Co., Ltd.).<sup>1,4,5)</sup>

CVD-SiC fiber is carbon fiber coated with SiC by a CVD method, and the composition of the CVD coating layer consists of  $\beta$ -SiC and a small quantity of  $\alpha$ -SiC. Columnar SiC grains grow rapidly from the fiber surface with the plane of the close-packed (111) of SiC vertical to the growth direc-

tion, and  $\beta$ -SiC contains a great deal of {111} stacking faults and microtwins.<sup>6,7)</sup> The CVD-SiC fiber has excellent thermal resistance, and yet its large diameter (about 140 $\mu$ m) prevents a mechanism for higher toughness from taking effect. On the other hand, in the case of Nicalon fiber, chemical reactions occur at high temperatures over 1000°C among SiO<sub>2</sub>, C, SiC contained in fiber, and the evolution of reaction products of CO and SiO causes great defects in the fiber surfaces,<sup>8,9)</sup> thus hampering its use for ceramic matrix composites as it is. In recent years, B, BN, and Si coating for Nicalon fiber is under study.<sup>3,9-13)</sup> When Si or B is coated on Nicalon fiber, Si diffuses promptly at high temperatures inside the fiber and matrix, while B forms glass with low melting point which makes the composite brittle and liable to easy destruction. The C or BN coating improves fracture toughness, but the former has an oxidation problem. Moreover, BN-coated fiber decreases its strength to 60% with treatment at 1200°C, and reactions with matrix pose a problem at high temperatures. These conditions indicate that it is necessary to develop a coating method which provides a layer with high compatibility between fiber and matrix, stable at high temperatures and capable of controlling the reaction of Nicalon fiber itself.

This study was intended to improve the thermal resistance of Nicalon fiber as well as to modify fiber/matrix interfaces by CVD- (C and SiC) coating on fiber surfaces: A CVD process and the morphologies of coating layers were examined along with the mechanism of layer formation, composition and microstructures.

## 2. Experimental Procedures

The fiber used in this study was non-sizing Nicalon-NL200 (Nippon Carbon Co., Ltd.), and fiber coating was conducted with a low pressure chemical vapor deposition system. As for a coating process, a carbon frame on which Nicalon fiber was attached while arranged in the same direction was put in a CVD furnace, heated to the specified temperature, and exposed to a raw material gas mixed with mixer to effect CVD coating. SiCl<sub>4</sub> and CH<sub>4</sub> were adopted as raw material gases for reaction and H<sub>2</sub> gas as a carrier gas. Since reaction temperature, pressure, gas flow rate, and gas mixing ratio generally have great influences on the morphology and composition of a coating layer in SiC coating on substrates by CVD,<sup>14-16)</sup> the reaction temperature and pressure were set to 1200°C, 1300°C and 20Torr, 40Torr; flowrate of SiCl<sub>4</sub> and CH<sub>4</sub> to 40 SCCM and 40 SCCM respectively, and that of H<sub>2</sub> to 120 or 170 SCCM (SCCM: gas flow rate at 1cc/min at 0°C and 1 atm). The reasons for adopting 1200°C and 1300°C as the reaction temperature are as follows. (1) To obtain pure  $\beta$ -SiC or a mixture of  $\beta$ -SiC

and C, a reaction temperature of about 1300°C was appropriate in this reaction system. (2) Coating at lower temperatures was desirable to prevent the high-temperature degradation of fiber during the heating stage of CVD process, while there was a report that free Si was formed on the side of low temperatures,<sup>14)</sup> so that the minimum CVD reaction temperature was set to 1200°C. Fiber samples coated under various conditions were observed with a scanning electron microscope for their surface morphology and cross-sectional microstructures. Moreover, fiber surface and depth direction analyses were performed by AES using JAMP-10S (JEOL, Ltd.) to investigate composition and distribution. The vacuum in the Auger analysis of the outermost surface of coated fiber was  $1 \times 10^{-7}$  Pa, and that in the depth direction analysis was  $6 \times 10^{-6}$  Pa (Ar atmosphere). The acceleration voltage of electrons was set to 10KV, sample current to  $1 \times 10^{-7}$  A, electron beam diameter to 0.5 $\mu$ m and the inclination angle of samples to 60°. The conditions of ion etching in the depth direction analysis were 3KV for the acceleration voltage of an ion beam,  $6 \times 10^{-7}$  A for sample current, and 17nm/min for etching speed (in the case of the standard sample SiO<sub>2</sub>). In addition, the crystal structures of coating layers were examined by TEM and XRD.

### 3. Experimental Results

#### 3.1. SEM Observation of Coating Layers

The surfaces of fiber coating under the above-stated conditions were observed with SEM photos as well as the measurement of the thickness of coating layers. Nicalon fiber samples coated at 1300°C, 20 Torr, and H<sub>2</sub> 120 SCCM with a CVD reaction time of 5, 30, and 60 minutes has coating layers about 0.1 $\mu$ m, 0.5 $\mu$ m, and 20 $\mu$ m thick respectively. **Figure 1** shows the surface conditions of fiber coated with a reaction time of 30 minutes (layer thickness: 0.5 $\mu$ m). As

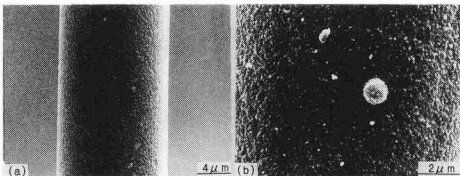


**Fig. 1.** SEM micrographs of Nicalon fibers with CVD coating (1300°C, H<sub>2</sub> 120SCCM, 30min), (a) surface of coated fiber, (b) showing a domed grain on the surface of coating layer.

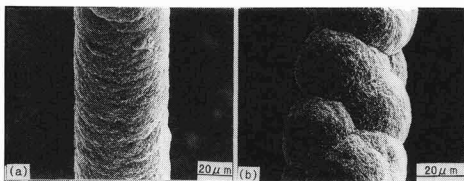


**Fig. 2.** SEM micrographs of Nicalon fibers with CVD coating (1300°C, H<sub>2</sub> 120SCCM, 60min), (a) fiber located in upstream of CVD chamber, (b) fiber located in downstream of CVD chamber showing large domed grains.

in Fig.1(a), the surfaces of coated fiber were smooth, and though the size of deposited grains was small, a few dome-shaped grains were deposited on the part of the coating layer surface as in Fig.1(b). The dome grains were about 4 $\mu$ m or less in size, and the number and size increased with a reaction time. The sample with a coating time of 5 minutes has the same surface condition as that in the case of 30 minutes.

**Figure 2** shows SEM photos of the surface of fiber coated with a reaction time of 60 minutes. In the case of fiber coated in the upstream of a CVD reaction furnace, dome grains are overlapped and hard to distinguish (Fig.2(a)), while in fiber coated in the downstream, dome grains about 20 $\mu$ m in diameter are recognized (Fig.2(b)). The reason is considered to be that super-saturation is higher (a reaction gas is thick), and the nucleation of SiC grains is more active in upstream than in downstream. As shown in Fig.1(b), the surface coating for 30 minutes has only a few small dome grains, and it is clear that the great dome grains as in Fig.2(b) grew rapidly with a reaction time over 30 minutes. These large dome grains are composed of sub-grains about 0.6 $\mu$ m in diameter, and there are grain boundaries between these dome grains (**Fig.3**).

**Figure 4** is an SEM photo of the fracture surface of fiber coated with a reaction time of 60 minutes. The noticeable point here is the presence of a thin intermediate layer at the interface of fiber and a coating layer. The thickness of the intermediate layer was found to be about 0.5 $\mu$ m. In the case of coating for 60 minutes, the formation of the coating layer was slow in the first 30 minutes of reaction in the CVD process (coating formation rate: about 0.02 $\mu$ m/min.), while

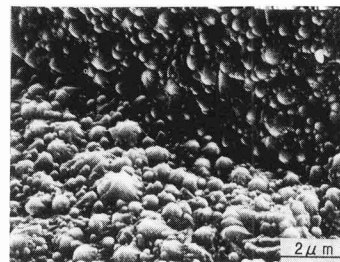


**Fig. 3.** SEM micrograph of a CVD-coated fiber surface showing a boundary of domed grains which consisted of subgrains.

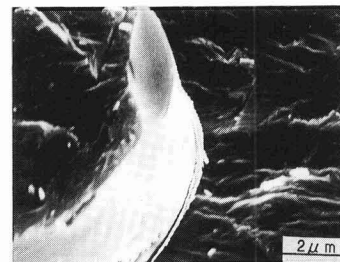


**Fig. 4.** The fracture surface of a coated fiber showing an intermediate layer at fiber-coating interface.

in the last 30 minutes of the reaction the growth rate was greatly accelerated (coating formation rate: about 0.65 $\mu\text{m}/\text{min}$ .). A difference between the formation rate near the surface of fiber after CVD coating and the subsequent formation rate was due to the different microstructures of coating layers, and the details will be described in the next paragraph.

In order to investigate the influences of an H<sub>2</sub> flared on the morphology, composition etc. of coating layers, the H<sub>2</sub> flared was increased from 120 SCCM to 170 SCCM (reaction time: 60 minutes), a coating layer 25 $\mu\text{m}$  thick was obtained with the same surface morphology as the case of H<sub>2</sub> 120 SCCM and the coating formation rate about 1.3 times that of the case of H<sub>2</sub> 120 SCCM. Under this condition also, an intermediate layer was detected from the fracture surface of fiber at the interface of a coating layer and fiber.

The influences of H<sub>2</sub> flared and pressure on the formation of coating layers were investigated with the conditions of 1200°C, H<sub>2</sub> 170 SCCM, and 20 Torr for pressure as a standard. **Figure 5** presents SEM photos of fiber surfaces coated under each condition. The coating conditions for (a), (b) and (c) in the figure are (H<sub>2</sub>:170 SCCM, pressure: 20 Torr), (H<sub>2</sub>:120 SCCM, Pressure:20 Torr) and (H<sub>2</sub>:170 SCCM, Pressure:40 Torr), respectively. A reaction time was constant at 30 minutes for all conditions. In Fig.5(a), the coating surface was cone-shaped and the thickness of the coating layer was about 3.5 $\mu\text{m}$  (distance from the fiber surface to the cone top). The SEM observation of the fracture face found an intermediate layer 0.1  $\mu\text{m}$  similar to that stated above at the interface of cone particles and fiber. When H<sub>2</sub> flared was changed from 170 to 120 SCCM, the coating layer smoothed (thickness: about 0.3 $\mu\text{m}$ ), and a few small par-

ticles and whisker-like deposited were encountered on the thin coating layer (Fig.5(b)). This means that a change in H<sub>2</sub> flared greatly affects the deposition rate and morphology of a coating layer. With a H<sub>2</sub> folw rate of 170 SCCM and reaction pressure 40 Torr increased from 20 Torr, the coating layer transformed into a mixture of whisker and dome particles from cone-shaped ones (Fig.5(c)).

The above results are summarized as follows. In the case of fiber coated at 1200 and 1300°C, the sample with the higher reaction temperature had higher rate of coating deposition larger size of particles of the coating layer, and the dome-type surface of the coating layer from the whisker-type one. An increase in H<sub>2</sub> folw rate tends to heighten the deposition rate. In coating at 1200°C, a change in H<sub>2</sub> flared has a greater influence on the morphology of the coating layer than in coating at 1300°C.

**3.2. Component Analysis of Coating Layers by AES**

The element analysis of the surfaces and depth direction of fiber coated at 1300 and 1200°C (thickness of coating layers: 0.5, 20 and 0.3 $\mu\text{m}$ ) was performed by AES. **Figure 6** gives the results of AES analyses of fiber coated under conditions as in Fig.1 (coating thickness: about 0.5 $\mu\text{m}$ ). Fig.6(a) is the Auger spectrum of the outermost surface of coated fiber (surface of the sample in Fig.1(a)), which detected O in addition to C and Si on the surface. Fig.6(b) is the result of element quantitative analysis in the depth direction, and sputtering from the surface to inside caused a decrease in the amount of detected Si and O and an increase in that of C. Fig.6(c) is an Auger spectrum after ion sputtering for 30 minutes, showing that the coating layer consists only of C. The element O detected near the surface by AES analysis is considered to be that adsorbed in air after

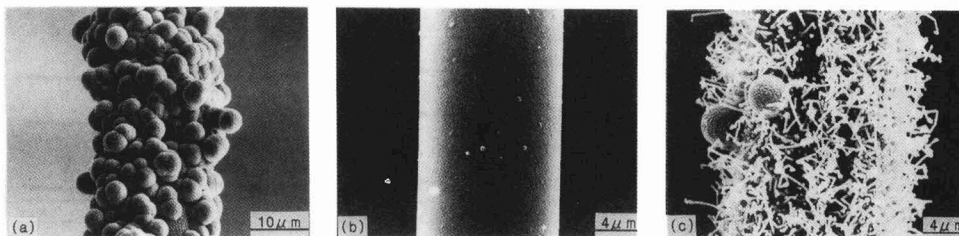


**Fig. 5.** SEM micrographs of CVD-coated Nicalon fibers: (a) fiber coated at 1200°C, H<sub>2</sub> 170SCCM, 20torr, (b) fiber coated at 1200°C, H<sub>2</sub> 120SCCM, 20torr, (c) fiber coated at 1200°C, H<sub>2</sub> 170SCCM, 40torr.

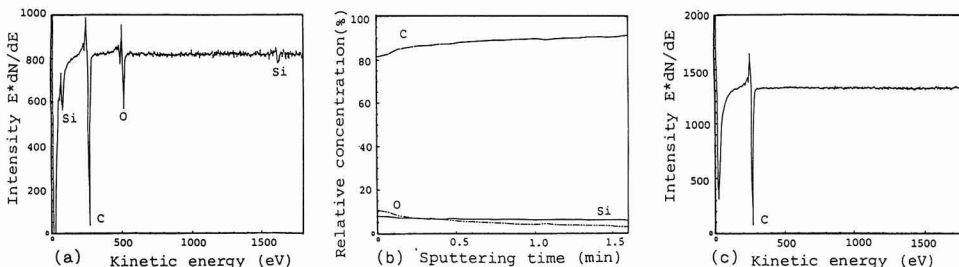


**Fig. 6.** Auger Electron Spectroscopy analysis for a CVD-coated fiber with a thickness about 0.5 $\mu\text{m}$ : (a) Auger spectrum of coated fiber surface, (b) depth profile, (c) Auger spectrum of coated fiber surface with 30min sputtering.

CVD coating.

Figure 7 presents the result of AES analysis with fiber coated under conditions as in Fig.2 (thickness of coating layer: about 20μm). Si, C and O were detected from the outer-most surface of the coating layer, and the elemental ratio of Si to C is about 1:1 from a depth of about 20μm (sputtering time: about 2 min.) (Fig.7(a)). Fig.7(b) is an Auger spectrum for the fracture face of coated fiber at the center of its coating past, and O was not detected. The above results suggest that the composition of the coating layer are composed only of SiC except for an intermediate layer near the fiber surface.

Figure 8 shows the analytical results of the depth direction from the surface of fiber coated at 1200°C (coating conditions: same as in Fig.5(b); thickness of coating layer: about 0.3μm). Compared with the case in Fig.6(b), much C, Si and O were detected on the outermost surface of the coating layer, and yet their amount dropped as the measuring point became deeper from the surface.

3.3. XRD and TEM Analysis

Figure 9 presents the results of XRD analysis with fiber without coating (a), that treated at 1300°C (b) and that with coating 20μm thick (c). Both samples of the patterns (a) and (b) consist of β-SiC fine crystals. Fig.9(c) is the result with the coated fiber, showing a peak at 2θ=33.5° characteristic of α-SiC as well as others (probably overlapped peaks for β- and α-SiC). That is, the crystal structure of the coating layer is composed of β-SiC (3C) and α-SiC(2H).

There are some reports that in the crystal structure of SiC the energy of stacking faults is low at {111} of β-SiC and {0001} of α-SiC, thus often causing face defects.<sup>6,7,17,18)</sup>

Figure 10 is the TEM photo of a coating layer deposited by CVD on the fiber surface. A number of stacking faults are contained in the CVD-SiC coating layer, and misorientation

is formed between fine particles. There is a curved grain boundary between fine particles with many defects.

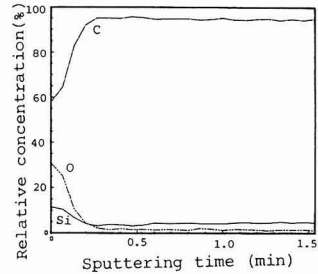


Fig. 8. Depth profile for a coated fiber with a coating thickness about 0.3μm.

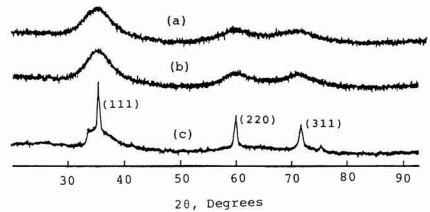


Fig. 9. X-ray diffraction patterns of fibers: (a) as-received, (b) heat-treated at 1300°C in Ar, (c) CVD-coated fiber with a coating thickness about 20μm.

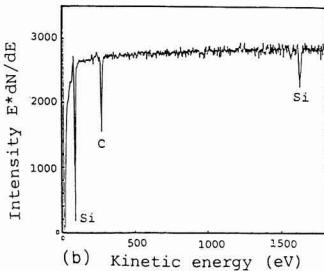
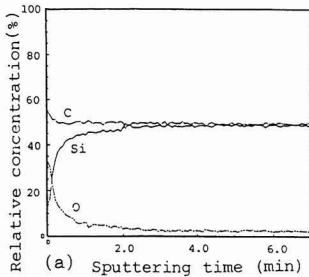


Fig. 7. Auger Electron Spectroscopy analysis for a CVD-coated fiber with a thickness about 20μm: (a) depth profile for coated fiber, (b) Auger spectrum of fracture surface of coating layer.

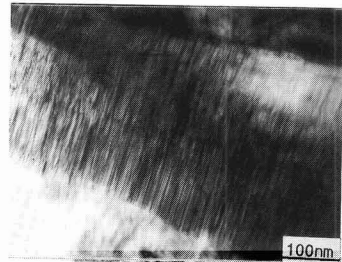


Fig. 10. TEM micrograph of coating layer.

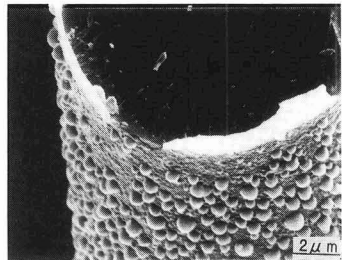


Fig. 11. SEM micrograph of CVD-coated fiber.

## 4. Discussion

In this experiment, coating layers with various surface conditions and thickness were obtained by controlling reaction temperature, pressure, gas flared and others during CVD. In the case of a coating layer 0.1-0.5 $\mu\text{m}$  thick, the composition near the fiber surface was C (Auger analysis), and about 10% of Si was dispersed in C near the surface of the coating layer. Dome-shaped  $\beta$ -SiC was formed on the surface of this carbon-rich layer, and grew 30 times as fast as the deposition rate of the carbon-rich layer. Normally, in structural materials, SiC coating is applied to substrates by CVD to provide wear and thermal resistance; yet there are few works on the mechanism of SiC deposition (thin film) near substrate surfaces, and most of them deal with the morphology, mechanical properties, and crystal structure of  $\beta$ -SiC.<sup>15,17-20</sup> On the other hand, in works on CVD-SiC thin films as electronic materials, a large number of line and plane defects are observed at the interfaces of substrates and  $\beta$ -SiC.<sup>21-23</sup> In this study, there are SiO<sub>2</sub> and free C in Nicalon fiber, so that the incompatibility of a fiber surface (substrate) and  $\beta$ -SiC face during CVD obviously hampers the nucleation of SiC. In the process of CVD, thermally-decomposed carbon was deposited in advance on the surface of Nicalon fiber, which probably facilitated SiC nucleation. The thickness of the formed carbon-rich layer is related to gas supersaturation, and with high supersaturation, many SiC nuclei are formed on the surface of the carbon-rich layer, thus reducing its thickness. Moreover, in the case of coating at 1200°C, a decrease in the flared of hydrogen led to a thicker carbon-rich layer. The reason is that with lower hydrogen flared the nucleation of SiC was slower and its deposition rate was lower. The number and growth rate of dome SiC particles attached to the surface of the carbon-rich layer were affected by gas supersaturation as stated above, and the particle size became larger as well as the number increased with reaction time. Moreover, when a carbon substrate was changed into a CVD reaction furnace, it tended to promote the deposition of SiC. **Figure 11** shows a SEM photo of fiber coated at 1300°C with a reaction time of 5 minutes. Plenty of SiC particles are formed on the surface of the carbon-rich layer 0.1 $\mu\text{m}$  thick.

In thick coating, it is necessary to provide fine coating for SiC particles to avoid the reduction of fiber strength. When coated fiber is used as a composite material, it is especially required to weaken interfacial bonding between coating layers and fiber as well as bonding between coating layers and matrix. As clearly shown in Fig.4, peeling occurred at the interface of the carbon-rich layer and fiber, indicating that the interface has weak bonding. Further, the same peeling was noticed between the carbon-rich layer and SiC layer.

## 5. Conclusion

In this study, fiber coating was conducted by CVD in an attempt to improve thermal resistance and modify the surface of Nicalon fiber, and the morphology, composition, crystal structures of coating layers were investigated to obtain the following conclusions.

1) When fiber is coated, first a carbon-rich layer is deposited

on the fiber surface. The layer has a thickness of about 0.1-0.5 $\mu\text{m}$  and a deposition rate of about 0.02 $\mu\text{m}/\text{min}$ . Once the carbon-rich layer is formed, SiC nuclei appear on the surface of this layer, and SiC particles grow with reaction time.

- 2) With coating at high temperatures, SiC particles formed on the surface of the carbon-rich layer are of dome, while with low reaction temperature, whisker-shaped ones are deposited and the amount increases with reaction pressure.
- 3) The SiC particles deposited in the form of dome consist of fine particles, and SiC contains a large amount of  $\beta$ -SiC as well as a small amount of  $\alpha$ -SiC. SiC has a number of stacking faults. The deposition rate of SiC was very high, reaching about 0.65 $\mu\text{m}/\text{min}$ . Moreover, the deposition rate becomes greater with reaction temperature and hydrogen flared.
- 4) When fiber is coated thickly, an intermediate layer and a carbon-rich layer are conjoined with an SiC layer as they are. There is a weak bonding force between the intermediate layer and fiber and the SiC layer, so that the treatment is expected to have the effect of improving the fracture toughness of composite materials by peeling and pullout at the interface.

### Acknowledgements

The authors are grateful to Mr. R. Ohki, Tokyo Institute of Technology, for his help in TEM; Mr. M. Kato, Sumitomo Metal Industries, Ltd. for his help in AES analysis; and Mr. A. Kimura (at present The Todyo Electric Power Co., Inc.), Mr. K. Fueda (at present Ube Industries, Led.), and Mr. K. Kuboyama, students of Department of Inorganic Materials, Tokyo Institute of Technology for their help in CVD experiments.

### References:

- 1) T. Mah, M.G. Mendiratta, A.P. Katz and K.S. Mazdiyasi, Am. Ceram. Soc. Bull., 66, 304-308 (1987).
- 2) B. Armas and C. Mombescure, 10th Conf. Int. On C. V. D., 1060-1069 (1985).
- 3) R.N. Singh and M.K. Brun, Ceram. Eng. Sci. Proc., 8, 636-643 (1987).
- 4) J.A. Dicarolo, J. Met., 37, 44-49 (1985).
- 5) T.F. Foltz, Ceram. Eng. Sci. Proc., 6, 1206-1220 (1985).
- 6) F.W. Wawner, A.Y. Teng and S.R. Nutt, SAMPE Quarterly, 39-45 (1983).
- 7) S.R. Nutt and F.E. Wawner, J. Mater. Sci., 20, 1953-1960 (1985).
- 8) T. Mah, N.L. Hecht, D.E. McCullum, J.R. Hownigman, H.M. Kim, A.P. Katz and H.A. Lipsitt, *ibid.*, 19, 1191-1201 (1984).
- 9) T.J. Clark, R.M. Arons, J.B. Stamatoff and J. Rabe, *ceram. Eng. Sci. Proc.*, 6, 576-588 (1985).
- 10) R.A. Lowden and D.P. Stinton, ORNL/TM-10667, Dec. 1987.
- 11) D.B. Fischbach and P.M. Lemoine, *Comp. Sci. Tech.*, 37, 55-61 (1990).
- 12) A.J. Caputo, D.P. Stinton, R.A. Lowden and T.M. Besmann, *Am. Ceram. Soc. Bull.*, 66, 368-372 (1987).
- 13) D.P. Stinton, A.J. Caputo and R.A. Lowden, *ibid.*, 65, 347-350 (1986).
- 14) J.E. Spruiell, ORNL-4326, Oak Ridge Nat. Lab. Tenn., Dec. 1968.
- 15) J. Chin, P.K. Gantzel and R.G. Hudson, *Thin Solid Films*, 40, 57-72 (1977).
- 16) D.P. Stinton, T.M. Besmann and R.A. Lowden, *Am. Ceram. Soc. Bull.*, 67, 350-391 (1988).
- 17) L.U. Ogbuji, T.E. Mitchell and A.H. Heuer, *J. Am. Ceram. Soc.*, 64, 100-105 (1981).
- 18) S.S. Shinozaki and H. Sato, *ibid.*, 61, 425-429 (1978).
- 19) T.D. Gulden, *ibid.*, 52, 585-590 (1969).

- 20) M.F. Gruninger, B.R. Lawn, E.N. Farabaugh and J.B. Wqachtman, *ibid.*, 70, 344-348 (1987).
  - 21) K. Shibahara, S. Nishino and H. Matsunami, *J. Cryst. Growth*, 78, 538-544 (1986).
  - 22) H.S. Kong, J.T. Glass and R.F. Davis, *J. Mater. Res.*, 4, 204-214 (1989).
  - 23) Y.C. Wang, H.S. Kong, J.T. Glass and R.F. Davis, *J. Am. Ceram. Soc.*, 73, 1289-1296 (1990).
- 

This article is a full translation of the article which appeared in *Nippon Seramikkusu Kyokai Gakujutsu Ronbunshi* (Japanese version), Vol.99, No.11, 1991.

# Mechanical Dampers Using Piezoelectric Composites

Yoji Suzuki, Kenji Uchino, Hironori Gouda\*, Masao Sumita\*,  
R.E. Newnham\*\* and A.R. Ramachandran\*\*

Department of Physics, Sophia University  
7-1, Kioi-cho, Chiyoda-ku, Tokyo, 102 Japan

\*Department of Organic and Polymeric Materials, Tokyo Institute of Technology  
2-12-1, Ookayama, Meguro-ku, Tokyo, 152 Japan

\*\*Materials Research Laboratory, The Pennsylvania State University  
University Park, PA 16802, USA

**New piezoelectric mechanical dampers have been fabricated using composites of piezoelectric ceramic:polymer:carbon black. Significant vibrational damping was observed in the composites with a ceramic volume fraction more than 50%. Damping characteristics are controllable by changing the conductivity through the carbon black concentration.**

[Received June 7, 1991; Accepted July 18, 1991]

**Key-words:** Mechanical damper, Composite piezoelectric ceramic

## 1. Introduction

Piezoelectric ceramics are useful for damping vibration. The authors reported previously that piezoelectric ceramics can be used as dampers.<sup>1)</sup> Consider that a piezoelectric ceramic material is attached to the object whose vibration is to be damped. When vibration is transmitted to the piezoelectric ceramic material, the vibrational energy is converted into electrical energy by the piezoelectric effect, and AC voltage is produced on the ceramic material. If the piezoelectric ceramic material is open or shorted electrically, the generated electrical energy is changed back into vibrational energy without loss. The repetition of this process provides continued vibration. If a proper resistor is connected, however, the energy converted into electricity is consumed as Joule's heat by the resistor, and the energy changed back into mechanical energy is reduced, so that the vibration can be damped rapidly. Taking the connected resistance as  $R$ , the capacity of piezoelectric ceramic material  $C$ , the frequency of vibration to be damped  $\omega$ , damping takes place most rapidly when the connected resistor is selected in a manner that the matching condition of impedance,  $R=1/\omega C$ , is satisfied.<sup>1)</sup> The damping time constant can be freely changed by the connected resistor.

Ceramics, though useful for damping vibration as described above, are difficult to assemble directly into mechanical system because they are hard and brittle. To resolve this difficulty, we fabricated dampers using a composite with properly flexible polymer (piezoelectric composite for damping) by considering practical use and workability.

## 2. Principle

When electrically conductive particles such as carbon black (CB) are added to polymer increasingly, the electric conductivity of composite increases in the order of ten near the critical adding point.<sup>2)</sup> Therefore, when a composite of polymer, piezoelectric ceramic powder and carbon black is fabricated (see Fig.1), the electric conductivity of composite is greatly changed by the addition of small amounts of carbon black. This means that, by properly selecting the electric conductivity of composite in place of connection of external resistors, each ceramic powder forms a circuit with the carbon black, so that the vibrational energy is consumed on the same principle as described above.

## 3. Experimental Method

In this study, PLZT (7/65/35) with a high piezoelectric constant was used as a piezoelectric ceramic material, and polyvinylidene fluoride (PVDF) was used as a polymer. The reason for using PVDF is that PVDF is relatively stiff elastically, though the piezoelectricity of PVDF is not particularly important in this study. PVDF, PLZT and CB were mixed on the basis of volume ratio. In this experiment, samples were prepared by fixing the ratio of PLZT at 40% and 50%. To prepare the samples, CB and PLZT powder was added to PVDF softened at 200°C, and the materials were mixed and pressed for a short time. Figure 2 shows flowchart of the process for making samples. The electric conductivity of 0.5mm-thick sheet was measured. The sheet with a stable conductivity was cut into specimens of 100mm long × 15mm wide. The specimen was fixed by vice at one end. Initial tip displacement was given by a pulse

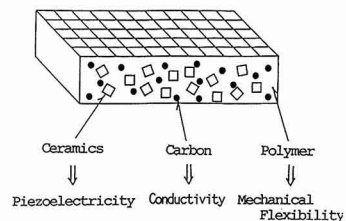


Fig. 1. Piezo-ceramic: Polymer: Carbon composite for mechanical dampers.

driving motor, and the residual vibration was detected with a non-contact displacement sensor (Kaman, SDP-2300) to determine the time over which the amplitude becomes 1/e (damping time constant). **Figure 3** shows the mechanical vibration measuring system.

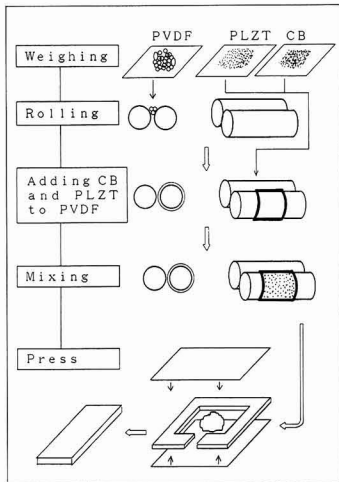


Fig. 2. Process of making samples.

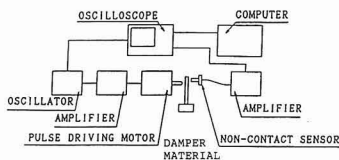


Fig. 3. Mechanical vibration measuring system.

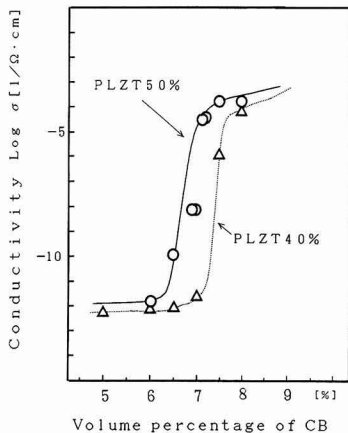


Fig. 4. Relation between conductivity and volume percentage of CB.

4. Results and Discussion

**Figure 4** shows the change in conductivity with the volume percentage of carbon black. The conductivity greatly changes depending on the volume percentage of CB. The volume percentage at which the conductivity begins changing suddenly is called a percolation threshold. The value of percolation threshold was 7% for 40% PLZT, and 6% for 50% PLZT; the value was lower when the ratio of PLZT was high. This difference may be caused by the facts that the volume percentage of carbon is not defined in relation to polymer, but in relation to the whole composite, and that the conductor circuit is easily formed when the ratio of ceramics is high because carbon particles aggregate around the ceramic particles.

The damping time constants of these samples were measured, producing the results shown in **Figs.5(a)** and **5(b)**. These figures show the relation between the damping time constant and the volume percentage of CB. In **Fig.5(a)**, the specimen with 40% PLZT was vibrated at 100Hz (the characteristic frequency of specimen was set at 100Hz for unification). The figure indicates that when the volume percentage of CB is about 7%, the damping time constant decreases; the vibration is damped rapidly. This value of volume percentage is nearly the same as the percolation threshold, and takes an intermediate value of conductivity between the maximum and the minimum. In **Fig.5(b)**, the specimen with 50% PLZT was vibrated at 100Hz. The figure indicates that when the volume percentage of CB is

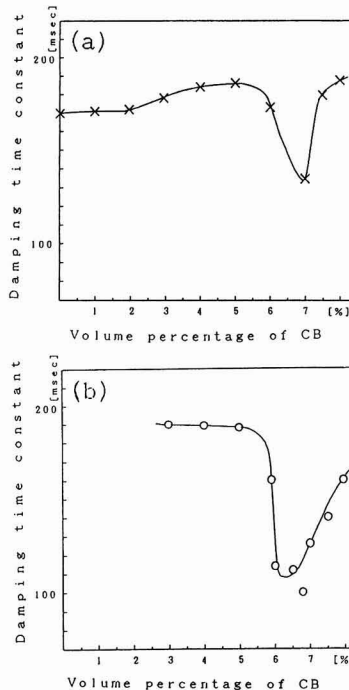


Fig. 5. (a) Relation between damping time constant and volume percentage of CB (PLZT 40%). (b) Relation between damping time constant and volume percentage of CB (PLZT 50%).

about 6%, the damping time constant decreases. Comparing Fig.5(b) with Fig.5(a), the lowest value of damping time constant is lower than that of specimen with 40% PLAT, but the damping time constant is higher at low volume percentage of CB (4% and lower) than that of specimen with 40% PLZT. This is probably because the specimen with more PLZT is stiffer elastically and has larger mechanical Q.

The volume percentage of CB at which the damping effect is largest in Figs.5(a) and 5(b) lies at the position where the conductivity is not so high in Fig.4. This is probably because CB forms an appropriate conductivity circuit partially around the ceramic particles in the composite in the condition where the CB begins forming network structure but does not complete the conductor circuit as a whole. This fact must be confirmed by observation with a microscope or other instruments. The specimen with 40% PLZT has less effect than that with 50% PLZT. Therefore, a fairly high ratio of piezoelectric ceramics is desirable.

Now, considering the relation of  $R=1/\omega C$ , it is expected that higher characteristic frequency of specimen shifts the curve of Fig.5 to the right slightly. By selecting a proper conductivity corresponding to the characteristic frequency, a damping effect appears.

## 5. Conclusions and Future Problems

A damper using piezoelectric composite of PVDF, PLZT and carbon black, which is a variant of damper using piezoelectric ceramics, was fabricated, and the relation between damping time constant and volume percentage of carbon was evaluated. The conclusions were as follows:

1) It was found that the damper using piezoelectric com-

posite is as useful for damping as the case where a resistor is connected to piezoelectric ceramics. The piezoelectric ceramics with a volume percentage of 50% has larger effect than that with 40%.

2) The damping effect appears by selecting conductivity corresponding to the specific frequency. Therefore, it is necessary to control the conductivity corresponding to the frequency to the damped through carbon black concentration at the fabrication stage.

However, it may be a problem in the future that sample fabrication is somewhat difficult when PVDF is used as a polymer because the change in conductivity is abrupt. A polymer whose conductivity changes slowly with the volume percentage of carbon black should be used.

As seen from Fig.5(b), the vibration was damped down to about 50% at the maximum depending on the volume percentage of carbon. In this experiment, however, electricity-machine coupling coefficient (efficiency of energy conversion) was low because the bending vibration mode of specimen was used. In the applications in which longitudinal vibration mode can be used, the damping characteristics may be improved further.

### References:

- 1) K. Uchino and T. Ishii, J. of the Ceramic Society of Japan, 96 (8) 863-67 (1988).
- 2) M. Sumida, J. of Japan Bonding Society, Vol. 23, No.3, 102-111(1987).

---

This article is a full translation of the article which appeared in Nippon Seramikkusu Kyokai Gakujutsu Ronbunshi (Japanese version), Vol.99, No.11, 1991.

# Synthesis of ZSM-5 Zeolite from Silica Stone Occurred in Ioh Island, Kagoshima Prefecture, Japan

Yoshihiro Hirata, Tadashi Kodama, Kinji Shimada and Yoshimi Ishihara

Department of Applied Chemistry and Chemical Engineering, Faculty of Engineering, Kagoshima University  
1-21-40, Korimoto, Kagoshima-shi, 890 Japan

ZSM-5 zeolite with the molar ratios  $\text{SiO}_2/\text{Al}_2\text{O}_3=61\text{--}75$  was synthesized hydrothermally at  $220^\circ\text{C}$  from silica stone containing  $\text{Al}_2\text{O}_3$  component of 1.40wt% (occurred in Ioh island, Kagoshima Prefecture, Japan), with tetrapropylammonium bromide (TPABr) and NaOH solution. The formation ratio, yield, and morphology of ZSM-5 were strongly affected by the concentration of NaOH solution. Increasing NaOH concentration decreased the yield and  $\text{SiO}_2/\text{Al}_2\text{O}_3$  ratio of ZSM-5. ZSM-5 zeolite formed from the silica stone smaller than  $44\mu\text{m}$  in NaOH solutions of concentrations higher than 1.0mol/l consisted of rectangular particles of about  $5\mu\text{m}$ . The  $\text{Al}_2\text{O}_3$  and  $\text{Fe}_2\text{O}_3$  components in the silica stone remained in the formed ZSM-5. It was possible to control the  $\text{SiO}_2/\text{Al}_2\text{O}_3$  ratio of ZSM-5 from 44 to 431 by adding  $\text{NaAlO}_2$  or amorphous  $\text{SiO}_2$  to the Ioh island stone. Roles of Na and TPA ions in the formation of ZSM-5 were also discussed.

[Received April 22, 1991; Accepted July 18, 1991]

**Key-words:** ZSM-5 zeolite, Silica stone, Cristobalite, Hydrothermal reaction, Tetrapropylammonium bromide, Sodium hydroxide solution, Silica/alumina ratio

## 1. Introduction

H type ZSM-5 zeolite, which was developed by Mobil Oil Corporation, is an excellent proton acid catalyst in converting methyl alcohol to hydrocarbon and  $\text{H}_2\text{O}$  below  $400^\circ\text{C}$ .<sup>1,2)</sup> The amount and acidic strength of proton in H-ZSM-5 depend upon molar ratio  $\text{SiO}_2/\text{Al}_2\text{O}_3$ .<sup>3-5)</sup> Substitution of Al for Si in the Si-O tetrahedron leads to introduction of proton in the zeolite along a general formula  $\text{H}_x\text{Al}_x\text{Si}_{1-x}\text{O}_2$ , indicating many acidic points for low  $\text{SiO}_2/\text{Al}_2\text{O}_3$  ratio. It is also pointed out that addition of organic cation such as tetrapropylammonium ion (TPA for short) plays an important role in synthesizing hydrothermally ZSM-5 zeolite.<sup>6,7)</sup> Unfortunately, limited understanding has been reported regarding the role of organic cation in the formation of ZSM-5. The purposes of this paper were (i) to confirm the possibility of hydrothermal synthesis of ZSM-5 zeolite from natural siliceous stone containing  $\text{Al}_2\text{O}_3$  component of 1.40wt% (silica stone in Ioh island, Kagoshima Prefecture, Japan; IIS for short), TPABr and NaOH solution, (ii) to understand concentration effect of TPABr and NaOH on the formation and molar ratio  $\text{SiO}_2/\text{Al}_2\text{O}_3$  of ZSM-5, and (iii) to discuss change of  $\text{Na}_2\text{O}$  and  $(\text{TPA})_2\text{O}$  contents with  $\text{SiO}_2/\text{Al}_2\text{O}_3$  ratio of ZSM-5.

## 2. Experimental Procedure

Silica stone in Ioh island of Kagoshima Prefecture, tetrapropylammonium bromide  $((\text{CH}_3\text{CH}_2\text{CH}_2)_4\text{NBr})$  and NaOH solution were used to synthesize hydrothermally ZSM-5 zeolite. As-received IIS contained cristobalite ( $\text{SiO}_2$ ), tridymite ( $\text{SiO}_2$ ) and a small amount of alunite  $((\text{K, Na})\text{Al}_3(\text{SO}_4)_2(\text{OH})_6)$  as crystalline phase under X-ray diffraction. The chemical composition of IIS dried at  $110^\circ\text{C}$  for 24hr was as follows (wt%): 2.95 Ig.loss, 94.16  $\text{SiO}_2$ , 1.40  $\text{Al}_2\text{O}_3$ , 0.36  $\text{Fe}_2\text{O}_3$ , 0.81  $\text{TiO}_2$ , 0.17  $\text{CaO}$ , 0.05  $\text{MgO}$ , 99.80 Total (molar ratio  $\text{SiO}_2/\text{Al}_2\text{O}_3=114$ ). Mixtures of IIS powder ( $<44\mu\text{m}$ ), TPABr and aqueous NaOH solution with oxide compositions  $a(\text{TPA})_2\text{O}\text{-}b\text{Na}_2\text{O}\text{-}c\text{Al}_2\text{O}_3\text{-}114\text{SiO}_2\text{-}c\text{H}_2\text{O}$  ( $a=2.72\text{--}36.7$ ,  $b=14.2\text{--}28.4$ ,  $c=1510\text{--}6620$ ) were settled into a teflon vessel (28mm diameter $\times$ 105mm height) and heated at  $160^\circ\text{--}220^\circ\text{C}$  for 3–72hr in an autoclave. After the hydrothermal reaction, solid products were removed from the solutions by filtration and dried at  $110^\circ\text{C}$  for 8hr in air. Phases in as-produced powders were identified by X-ray diffraction at a scanning rate of  $2^\circ/\text{min}$  ( $\text{CuK}\alpha$ , Model No.2013, Rigaku Co., Tokyo, Japan). Formation ratio of ZSM-5 in the solid product ( $f(z)$ ) was represented by the ratio of X-ray diffraction intensity regarding (501) plane of ZSM-5 and (101) plane of cristobalite:  $f(z)=I_z(501)/(I_z(501)+I_z(101))$ . The chemical compositions of solid products were examined by X-ray fluorescence (Rh) at 50kV (System 3080-E, Rigaku Co., Tokyo, Japan). About 200mg of the powder product was mixed with 4.5g of  $\text{Li}_2\text{B}_4\text{O}_7$ , and the mixture melted to form a 35mm-diameter glass sphere, which was chemically analyzed for Si, Al, Fe, Ti, Na and K contents. TG and DTA analysis of the products were carried out up to  $1000^\circ\text{C}$  at a heating rate  $10^\circ\text{C}/\text{min}$  (PTC-10A Type, Rigaku Co., Tokyo, Japan). Morphology of the products was observed by scanning electron microscopy at 75kV (H-700H Type, Hitachi Co., Tokyo, Japan).

## 3. Results and Discussion

### 3.1. Hydrothermal Synthesis of ZSM-5

#### 3.1.1. Reaction Time and Solid Products

Figure 1 shows reaction time dependence of weight ratio (yield) of the solid products to IIS, phase relation and molar ratio  $\text{SiO}_2/\text{Al}_2\text{O}_3$  of the products for the system  $2.74(\text{TPA})_2\text{O}\text{-}24.6\text{Na}_2\text{O}\text{-}c\text{Al}_2\text{O}_3\text{-}114\text{SiO}_2\text{-}2530\text{H}_2\text{O}$  at  $220^\circ\text{C}$ . The reaction products consisted of cristobalite and ZSM-5 zeolite at reaction time shorter than 12hr and changed to only ZSM-5 at longer time. The yield gradually reached a

constant value ( $-0.55$ ) with reaction time after a drastic decrease at the short time of 3hr. In the absence of TPABr, yield of the solid products containing no ZSM-5 after hydrothermal reaction for 12hr was 33% and close to the yield for 3hr as shown in Fig.1. This result and phase relation shown in Fig.1 suggest that (i) about 60wt% of IIS dissolved within 3hr, (ii) ZSM-5 formed through following two processes<sup>9)</sup>: (a) solid-liquid reaction in the IIS-TPABr-NaOH-H<sub>2</sub>O system and (b) crystallization from the liquid phase containing dissolved SiO<sub>2</sub> component, TPABr and NaOH. Increase in SiO<sub>2</sub>/Al<sub>2</sub>O<sub>3</sub> ratio with increasing time, that was accompanied by the increase in yield and in the amount of ZSM-5, reflects the crystallization of ZSM-5 from the liquid phase. Wet analysis of Al<sup>3+</sup> and Fe<sup>3+</sup> ions with chelatometric titration for the filtrate after the reaction for 12-72hr indicated that 99.0-100% of those ions in the starting IIS remained in the formed ZSM-5 zeolite. Above results and the difference in molar ratio SiO<sub>2</sub>/Al<sub>2</sub>O<sub>3</sub> between starting IIS and ZSM-5 formed after reaction for 72hr suggest that 54% of SiO<sub>2</sub> component of IIS was used for the formation of ZSM-5 and 46% of SiO<sub>2</sub> remained in the solution.

### 3.1.2. Effect of Concentration of NaOH and TPABr on the Formation of ZSM-5

Figure 2 illustrates effect of NaOH concentration on the yield of solid products (A) and on the formation ratio of ZSM-5 (B) for the reaction at 220°C for 12hr. Increase in the NaOH concentration higher than 1.2mol/l accelerated the dissolution of IIS (A), implying the formation of soluble sodium silicate. Influence of TPABr composition  $f(T)$ ,  $f(T)=[TPABr]/([TPABr]+[NaOH])$ , on the dissolution of IIS was small. On the other hand, formation ratio of ZSM-5 depended upon both concentrations of NaOH and TPABr. No ZSM-5 formed at  $f(T)=0$ . As seen in Fig.2(B), the amount of ZSM-5 increased with increase of NaOH con-

centration and  $f(T)$  value (TPABr concentration). However, at high  $f(T)$  values above 0.5 the amount of ZSM-5 showed maxima at certain NaOH concentrations. A comparison of results between Fig.2(A) and (B) suggests that (i) reaction of SiO<sub>2</sub> component and NaOH to form ZSM-5 did not proceed completely below the concentration  $[NaOH]=1.4\text{mol/l}$ , and (ii) decrease in the amount of ZSM-5 at low  $f(T)$  values below 0.2 was ascribed to the lack of template effect of TPABr to form ZSM-5 in addition to slow crystallization of ZSM-5 from highly concentrated NaOH solution (Fig.1). These phenomena, (i) and (ii), resemble partial destruction of the tetrahedral Si-O bond of SiO<sub>2</sub> (formation of non-bridging oxygen) by Na<sub>2</sub>O in glass formation and crystallization of glass in the Na<sub>2</sub>O-M<sub>x</sub>O<sub>y</sub>-SiO<sub>2</sub> system (M: cation), respectively. Existence of maxima in the formation ratio of ZSM-5 against NaOH concentration at high  $f(T)$  values, and shift of NaOH concentration corresponding to the maximum formation ratio of ZSM-5 to higher concentration with decreasing  $f(T)$  value might be associated with the solubility limit of TPABr at 220°C. Coating of the surface of IIS by undissolved TPABr may suppress chemical reaction between IIS and NaOH and as a result the formation ratio of ZSM-5 may not reach 100%. The solubility limit of TPABr at 220°C was estimated to be 1.2-1.3mol/l from the maximum formation ratio of ZSM-5 in Fig.2(B).

### 3.1.3. Chemical Compositions of Solid Products

Figure 3 summarizes SiO<sub>2</sub>, Al<sub>2</sub>O<sub>3</sub> and Na<sub>2</sub>O contents, and ignition loss with heating to about 1000°C for the solid products after hydrothermal reaction at 160-220°C as a function of formation ratio of ZSM-5. Based on the analysis of some TG-DTA data of the products, ignition loss observed below and above 350°C was interpreted to be the evaporation of H<sub>2</sub>O and decomposition of (TPA)<sub>2</sub>O, respectively.<sup>9,10)</sup> The structure change from cristobalite to ZSM-5 was accompanied by the decrease in SiO<sub>2</sub> and H<sub>2</sub>O

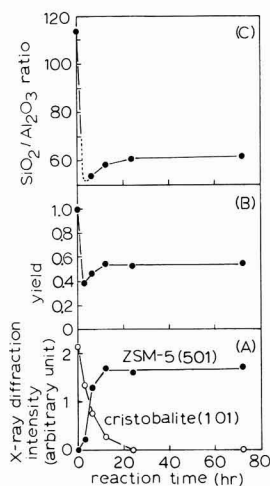


Fig. 1. Reaction time dependence of phase relation (A), yield (weight ratio) of the solid products to IIS (B), and molar ratio of SiO<sub>2</sub>/Al<sub>2</sub>O<sub>3</sub> (C) of the products for the system 2.74 (TPA)<sub>2</sub>O-24.6Na<sub>2</sub>O-Al<sub>2</sub>O<sub>3</sub>-114SiO<sub>2</sub>-1530H<sub>2</sub>O at 220°C.

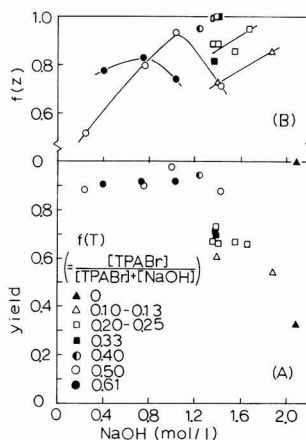


Fig. 2. Effect of NaOH concentration on the yield of solid product (A) and formation ratio of ZSM-5 (B) for the hydrothermal reaction at 220°C for 12hr. Formation ratio of ZSM-5,  $f(Z)$ , means X-ray diffraction intensity ratio of ZSM-5 and cristobalite:  $f(Z)=I_c(501)/[I_c(501)+I_c(101)]$ . TPA composition  $f(T)$  was defined as follows:  $f(T)=[TPABr]/([TPABr]+[NaOH])$ .

contents, and increase in  $(\text{TPA})_2\text{O}$  content. Composition change of  $\text{Al}_2\text{O}_3$  and  $\text{Na}_2\text{O}$  with the formation of ZSM-5 was minor as shown in Fig.3. Increase in  $(\text{TPA})_2\text{O}$  and  $\text{Na}_2\text{O}$  content with the formation of ZSM-5 means that these components have a crucial role for constructing ZSM-5 structure.

Figure 4 shows the  $\text{SiO}_2/\text{Al}_2\text{O}_3$  ratios of products after hydrothermal reaction at  $220^\circ\text{C}$  as a function of NaOH concentration. The molar ratio  $\text{SiO}_2/\text{Al}_2\text{O}_3$  decreased in the reaction using highly concentrated NaOH solution. This tendency can be compared with the result shown in Fig.2(A). Increasing NaOH concentration promotes dissolution of  $\text{SiO}_2$  component of IIS. However, most of the  $\text{Al}_2\text{O}_3$  component of IIS remained in ZSM-5, as mentioned in section 3.1(A). As a result, the  $\text{SiO}_2/\text{Al}_2\text{O}_3$  ratio strongly depends upon NaOH concentration. In addition, the molar ratio  $\text{SiO}_2/\text{Al}_2\text{O}_3$  increased for the products having high ZSM-5 formation ratio (Fig.1). This result is explained by the crystallization of ZSM-5 from the liquid phase. Consequently, the molar ratios of  $\text{SiO}_2/\text{Al}_2\text{O}_3$  are dominated by the concentration of NaOH and formation ratio of ZSM-5.

Figure 5 shows the controlling of wide range  $\text{SiO}_2/\text{Al}_2\text{O}_3$  ratios of ZSM-5 by adding amorphous  $\text{SiO}_2$  powder or  $\text{NaAlO}_2$  to IIS in NaOH solution. Experiments were done at  $220^\circ\text{C}$  for 24hr. The only solid products under X-ray diffraction were ZSM-5. Yield of ZSM-5 increased with an increase in molar ratio  $\text{Al}_2\text{O}_3/\text{SiO}_2$  of the starting materials as shown in Fig.5(A), suggesting an acceleration effect of  $\text{Al}_2\text{O}_3$  component on the crystallization of ZSM-5 from the liquid phase (see Fig.8). The  $\text{Al}_2\text{O}_3/\text{SiO}_2$  ratios of ZSM-5 were 1.3–1.9 times as high as those of starting materials (Fig.5(B)). As shown in Fig.5(B), the  $\text{Al}_2\text{O}_3/\text{SiO}_2$  ratio of ZSM-5 to starting materials decreased linearly with increasing  $\text{Al}_2\text{O}_3/\text{SiO}_2$  ratio of starting materials. This result is related to the yield of ZSM-5. Since the decrease in the yield at low  $\text{Al}_2\text{O}_3/\text{SiO}_2$  ratio of starting materials indicates the dissolution of large amount of  $\text{SiO}_2$  component (see

Figs.2 and 4), the  $\text{Al}_2\text{O}_3/\text{SiO}_2$  ratio of ZSM-5 becomes higher as the starting  $\text{Al}_2\text{O}_3/\text{SiO}_2$  ratio is decreased.

A difference in the  $\text{Al}_2\text{O}_3/\text{SiO}_2$  ratio of ZSM-5 between the IIS-TPABr-NaOH- $\text{H}_2\text{O}$  system and amorphous  $\text{SiO}_2$ - $\text{NaAlO}_2$ -TPABr-NaOH- $\text{H}_2\text{O}$  system was also compared at a molar ratio  $\text{Al}_2\text{O}_3/\text{SiO}_2=8.77\times 10^{-3}$  of starting materials in Fig.5(B). The former system using IIS gave higher  $\text{Al}_2\text{O}_3/\text{SiO}_2$  ratio of ZSM-5 than the latter system. Lower yield of ZSM-5 for the former system, which means lower  $\text{SiO}_2$  content of ZSM-5, can explain the above result.

### 3.2. Morphology of ZSM-5 Zeolite

Figure 6 shows morphology change of solid products with hydro thermal temperature for the system  $13.9(\text{TPA})_2\text{O}\cdot 14.2\text{Na}_2\text{O}\cdot \text{Al}_2\text{O}_3\cdot 114\text{SiO}_2\cdot 6540\text{H}_2\text{O}$ . Main products at low ( $160^\circ\text{--}180^\circ\text{C}$ ) and high ( $200^\circ\text{--}220^\circ\text{C}$ ) temperatures in the dilute NaOH solution (0.24mol/l) consisted of

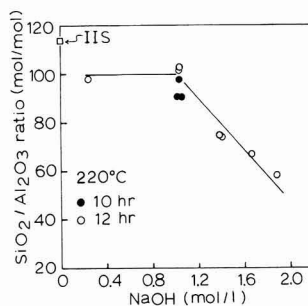


Fig. 4.  $\text{SiO}_2/\text{Al}_2\text{O}_3$  ratios of the solid products after hydrothermal reaction at  $220^\circ\text{C}$  for 10 and 12hr as a function of NaOH concentration.

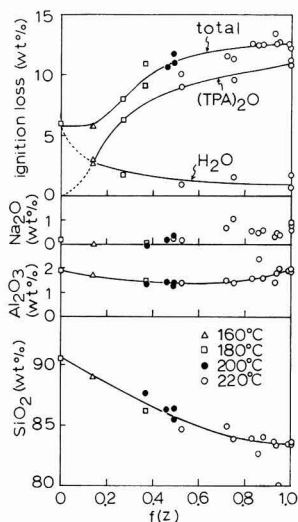


Fig. 3. Chemical compositions of the solid products after hydrothermal reaction at  $160^\circ\text{--}220^\circ\text{C}$  as a function of formation ratio of ZSM-5,  $f(z)$ .

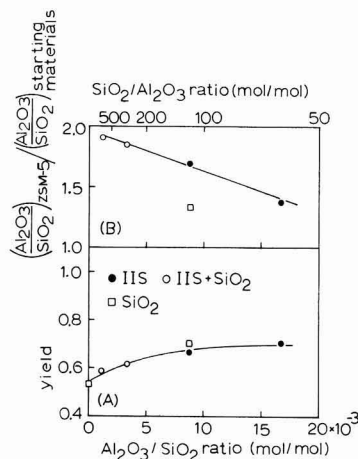


Fig. 5. Yield (A) and  $\text{Al}_2\text{O}_3/\text{SiO}_2$  ratio of ZSM-5 to starting materials (B) for the hydrothermal reaction at  $220^\circ\text{C}$  for 24hr as a function of  $\text{SiO}_2/\text{Al}_2\text{O}_3$  ratio of starting materials.

The  $\text{Al}_2\text{O}_3/\text{SiO}_2$  ratios of starting materials with the TPA composition  $f(T)=0.13$  were controlled by adding amorphous  $\text{SiO}_2$  or  $\text{NaAlO}_2$  to IIS in the NaOH solutions of 1.3–1.4mol/l. The symbols in Fig.5 represent the kinds of  $\text{SiO}_2$  sources of starting materials.

monodispersed spherical or rectangular particles of 1–2 $\mu\text{m}$  and agglomeration of rectangular primary particles in the submicron size range, respectively. The above change in the shape and size of products and formation ratio of ZSM-5 with reaction temperature (Fig.3) leads to the following explanations: (i) increase in the reaction rate between IIS and NaOH solution at high reaction temperature accelerates the dissolution of  $\text{SiO}_2$  component, (ii) increase in the concentration of  $\text{SiO}_2$  component and structure change of IIS with increasing temperature advance the nucleation of ZSM-5 zeolite; and (iii) grain growth of each ZSM-5 particle is suppressed due to the high nucleation rate of ZSM-5 at high temperatures and poor supply of  $\text{SiO}_2$  component in the dilute NaOH solution. On the other hand, larger rectangular ZSM-5 particles of about 5 $\mu\text{m}$  were formed in high concentrated NaOH solution.<sup>11)</sup> Figure 7 shows the ZSM-5 particles formed in the NaOH solution of 1.0–1.4mol/l. In this concentration range of NaOH solution, significant change in the particle shape was not observed as seen in Fig.7. However, the SEM photos seem to indicate that increase in the TPABr concentration promotes the formation of agglomerated ZSM-5. Growth of ZSM-5 particles in the concentrated NaOH solution would be ascribed to enough supply of dissolved  $\text{SiO}_2$  component. Formation of agglomerated ZSM-5, which was related to the increase in the TPABr concentration, may be due to higher nucleation of ZSM-5.

Figure 8 shows the effect of  $\text{Al}_2\text{O}_3$  content of ZSM-5 on the morphology. Decrease in the  $\text{Al}_2\text{O}_3$  content of starting materials caused (i) decrease in the size of ZSM-5 particle, and (ii) formation of irregular shape ZSM-5 particles. That is, Al ions promoted grain growth of rectangular ZSM-5.

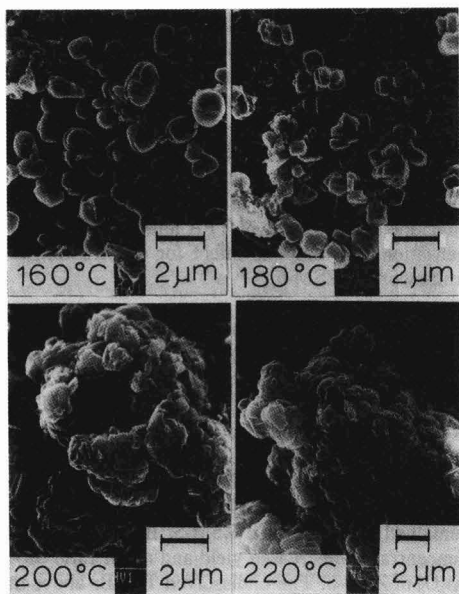


Fig. 6. Effect of hydrothermal temperature on the morphology of solid products after 12hr for the system  $13.9(\text{TPA})_2\text{O} \cdot 14.2\text{Na}_2\text{O} \cdot \text{Al}_2\text{O}_3 \cdot 114\text{SiO}_2 \cdot 6540\text{H}_2\text{O}$ .

### 3.3. Role of Na and TPA Ions on the Formation of ZSM-5

We discuss the role of Na and TPA ions on the formation of ZSM-5. As shown in Fig.3, the contents of these two cations in the solid products increased with formation of ZSM-5, suggesting following role of Na and TPA ions: template effect and charge compensation with substitution of Al for Si in constructing the ZSM-5 framework.

In the absence of TPA ion no ZSM-5 was formed as shown in Fig.2. This result indicates no template effect of only Na ion and high template effect of TPA ion accompanied with Na ion. Figure 9(A) shows  $\text{Na}_2\text{O}$  and  $(\text{TPA})_2\text{O}$  contents of TPA-Na type ZSM-5 formed by hydrothermal reaction at 220°C for 12–24hr, as a function of a  $x$  value in  $(\text{TPA})_y\text{Na}_{1-y}\text{Al}_x\text{SiMV}1-x\text{O}_2$ . ZSM-5 with the molar ratios of  $\text{Al}_2\text{O}_3/\text{SiO}_2=0-0.05$  contained  $(\text{TPA})_2\text{O}$  of  $2.5-3.0 \times 10^{-4}$  mol/g, indicating little dependence of TPA content on  $x$  value. However,  $\text{Na}_2\text{O}$  content increased with increasing  $x$  value. The  $\text{Na}_2\text{O}/\text{Al}_2\text{O}_3$  molar ratio corresponding to  $(1-y)$  value is shown in Fig.9(B). Fig.9(B) illustrates clearly charge compensation effect of both cations of Na and TPA. The contribution of Na ions to charge compensation increased with an increase in  $x$  value and reached 0.7–0.9 above 0.03 of  $x$ . In other words, the charge compensation effect by TPA ions is relatively high below 0.03 of  $x$  value. The molar ratios of  $(\text{TPA})_2\text{O}/\text{Al}_2\text{O}_3$  were also calculated to be 0.9–1.7 for  $x=0.021-0.048$ . Therefore, ZSM-5 formed in this experiment contained excess  $(\text{TPA})_2\text{O}$  compared with  $x$  value, indicating template effect of TPA ions. The above results conclude the two roles of TPA ions on charge compensation and template effect for constructing the framework of ZSM-5.

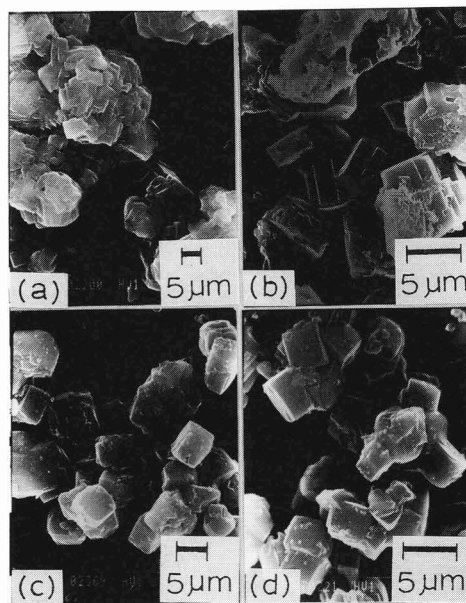
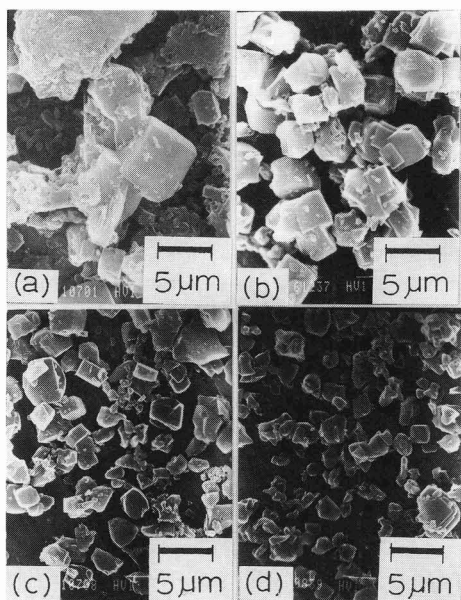


Fig. 7. Influence of TPABr concentration on the morphology of ZSM-5 formed at 220°C for 12hr in the NaOH solution of 1.0–1.4mol/l. TPABr concentration (mol/l) (a) 1.63, (b) 1.01, (c) 0.68, (d) 0.20.



**Fig. 8.** Effect of the  $\text{Al}_2\text{O}_3/\text{SiO}_2$  ratio of starting materials on the morphology of ZSM-5 formed at  $220^\circ\text{C}$  for 24hr in the NaOH solution of 1.3–1.4mol/l at the TPA composition  $f(\text{T})=0.13$ ,  $\text{Al}_2\text{O}_3/\text{SiO}_2$  ratio: (a)  $16.7 \times 10^3$  (b)  $8.8 \times 10^3$  (c)  $1.2 \times 10^3$  (d) 0.

## 4. Conclusions

ZSM-5 zeolite with the molar ratios  $\text{SiO}_2/\text{Al}_2\text{O}_3=61\text{--}75$  was synthesized hydrothermally at  $220^\circ\text{C}$  in Ioh island silica stone (IIS)–TPABr–NaOH– $\text{H}_2\text{O}$  system through solid-liquid reaction and crystallization of ZSM-5 from the liquid phase containing dissolved  $\text{SiO}_2$  component. The  $\text{Al}_2\text{O}_3$  and  $\text{Fe}_2\text{O}_3$  components in IIS ( $\text{Al}_2\text{O}_3$ : 1.40wt%,  $\text{Fe}_2\text{O}_3$ : 0.36wt%) remained in the formed ZSM-5. Increasing NaOH concentration decreased yield and molar ratio  $\text{SiO}_2/\text{Al}_2\text{O}_3$  of ZSM-5. The undissolved TPABr above the solubility limit suppressed the formation of ZSM-5. In the hydrothermal reaction at the  $\text{SiO}_2/\text{Al}_2\text{O}_3$  molar ratios of 60 to 825, which were controlled by adding amorphous  $\text{SiO}_2$  or  $\text{NaAlO}_2$  to IIS, the  $\text{Al}_2\text{O}_3/\text{SiO}_2$  ratio of ZSM-5 to starting materials decreased linearly with increasing  $\text{Al}_2\text{O}_3/\text{SiO}_2$  ratio of starting materials. The contribution of Na ions to charge compensation with substitution of Al for Si ions in ZSM-5,  $(1-y)$  value in the formula  $(\text{TPA}_y\text{Na}_{1-y})_x\text{Al}_x\text{SiMV1-xO}_2$  increased with increasing  $x$  value and reached 0.7–0.9 above 0.03 of  $x$ . ZSM-5 formed in this experiment contained excess TPA ions compared with  $x$  value, indicating two roles of TPA ions: charge compensation and template effect in constructing the framework of ZSM-5. ZSM-5 zeolite formed from IIS in the NaOH solution of concentration higher than 1.0mol/l consisted of rectangular particles of about  $5\mu\text{m}$ . Addition of Al component to IIS promoted grain growth of rectangular ZSM-5 particles.

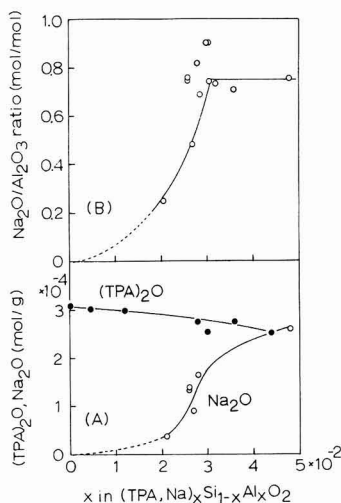


**Fig. 9.**  $\text{Na}_2\text{O}$  and  $(\text{TPA})_2\text{O}$  contents (A) and  $\text{Na}_2\text{O}/\text{Al}_2\text{O}_3$  ratio (B) of TPA–Na type ZSM-5 as a function of  $x$  value in  $(\text{Na}, \text{TPA})_x\text{Al}_x\text{Si}_{1-x}\text{O}_2$ .

## Acknowledgements

The authors gratefully acknowledge our colleagues, Prof. K. Somekawa, Y. Fukushige and H. Uemura for helpful suggestions. The authors also thank Y. Kamino, T. Kokusho and T. Sonoda of Kagoshima Prefectural Institute of Industrial Technology for chemical analysis of ZSM-5 zeolite. This research was partially supported by the Kagoshima Science Scholarship Foundation.

## References:

- 1) W.O. Haag, R.M. Lago and P.G. Rodewald, *J. Mol. Catal.*, 17, 161–169 (1982).
- 2) R.M. Dessau and R.B. LaPierre, *J. Catal.*, 78, 136–141 (1982).
- 3) T. Yashima, *Kagaku Kogyo*, 1983, 990–996 (1983).
- 4) A. Martin, U. Wolf, S. Nowak and B. Lucke, *Zeolites*, 11, 85–87 (1991).
- 5) R. Borade, A. Sayari, A. Adnot and S. Kaliaguine, *J. Phys. Chem.*, 94, 5989–5994 (1990).
- 6) J.B. Nagy, Z. Gabelica and E.G. Derouane, *Zeolites*, 3, 43–49 (1983).
- 7) N. Yoshimi, T. Maekawa and T. Yokogawa, *J. Ceram. Soc. Jpn.*, 98, 322–326 (1990).
- 8) E.G. Derouane, S. Detremmerie, Z. Gabelica and N. Blom, *Appl. Catal.*, 1, 201–224 (1981).
- 9) Y. Hirata, T. Kodama, K. Shimada and Y. Ishihara, *J. Ceram. Soc. Jpn.*, 99, 1255–1259 (1991).
- 10) A. Jentys, G. Warezka and M. Derewinski, J.A. Lercher, *J. Phys. Chem.*, 93, 4837–4843 (1989).
- 11) A. Nastro and L.B. Sand, *Zeolites*, 3, 57–62 (1983).

# Role of External Additives on the Surface Crystallization of Multi-component Non-Alkali Glasses

Hideyuki Kuribayashi, Rikuo Ota, Jiro Fukunaga and Tomoyuki Taguchi\*

Department of Chemistry and Materials Technology, Kyoto Institute of Technology

Matsugasaki, Sakyo-ku, Kyoto-shi, 606 Japan

\*New Glass Research Center, Yamamura Glass Co. Ltd.

2-1-18, Naruohama, Nishinomiya-shi, 663 Japan

The crystallization behavior of a glass in the  $\text{SiO}_2\text{-Al}_2\text{O}_3\text{-CaO-ZnO-TiO}_2\text{-B}_2\text{O}_3$  system with additives was investigated by means of DTA, XRD and SEM observation. The additives were wollastonite, silica, lime,  $\text{Fe}_2\text{O}_3$ , alumina, zirconia, zircon,  $36.6\text{CaO-}63.4\text{SiO}_2$  glass, titania, montmorillonite, kaolin, talc, and zeolite. The main results are as follows. 1) The most effective additives to reduce the double peaks of DTA curve into a single one were wollastonite,  $\text{TiO}_2$  and  $36.6\text{CaO-}63.4\text{SiO}_2$  glass. Among them, only external addition of wollastonite shifted the peak temperature downward. 2) Crystal precipitation was enhanced on the wollastonite contacted glass surface. 3) The precipitated crystalline phase was speculated to consist of tiny particles of anorthite, gehlenite, willemite and titanite crystals.

[Received April 6, 1991; Accepted July 18, 1991]

**Key-words:** Non-alkali glass, Surface crystallization, DTA, Wollastonite, External additive, Water vapor.

## 1. Introduction

Glass materials used for the insulated low dielectric layers of hybrid IC are especially required to have thermal resistance up to  $900^\circ\text{C}$ , insulation resistance over  $10^{12}\Omega$ , low dielectric constant less than 13, and migration resistance. Generally, non-alkali glass in the borosilicate system is used for these purposes. The authors earlier studied a  $\text{SiO}_2\text{-Al}_2\text{O}_3\text{-CaO-ZnO-TiO}_2\text{-B}_2\text{O}_3$  system with low-concentration  $\text{B}_2\text{O}_3$  by varying the amount of  $\text{SiO}_2$ ,  $\text{Al}_2\text{O}_3$ , CaO, ZnO,  $\text{TiO}_2$ , and  $\text{B}_2\text{O}_3$  in order to clarify the effect of each component on the glass crystallization of this system and changes in precipitated crystal phases.<sup>1-3)</sup> It was found that in the case of glass of this system, crystallization starts at the surface and the following crystals are precipitated: anorthite ( $\text{CaO-Al}_2\text{O}_3\cdot 2\text{SiO}_2$ ), gehlenite ( $2\text{CaO-Al}_2\text{O}_3\cdot \text{SiO}_2$ ), titanite ( $\text{CaO-TiO}_2\cdot \text{SiO}_2$ ), and willemite ( $2\text{ZnO}\cdot \text{SiO}_2$ ). In the ordinary preparation of glass ceramics, the two steps of heat treatment of crystal nucleation and crystal growth are adopted in most cases. However, the two-step heat treatment is not quite appropriate to prepare insulated low dielectric glass ceramics for IC with glass as a starting raw material. To prepare IC glass ceramics using glass with this composition requires a process in which glass powder is heated to a specified temperature ( $800\text{-}900^\circ\text{C}$ ) with a constant heating rate, where it is held for a short period of time (for example, about 10 minutes) to complete crystallization. Moreover, the glass powder must be fused to exhibit a per-

fectly smooth surface before the crystallization starts. Further, the crystallization should be completed in the narrow temperature range of  $800\text{-}900^\circ\text{C}$ . In the previous report,<sup>3)</sup> the two-step process was proposed as a crystallization step accompanying the heat treatment of glass of this system: (1) phase separation to an  $\text{Al}_2\text{O}_3$ -rich glass phase and a  $\text{TiO}_2\text{-ZnO}$ -rich glass phase, and (2) precipitation of titanite and gehlenite from the  $\text{Al}_2\text{O}_3$ -rich phase, and that of titanite and willemite from the  $\text{TiO}_2\text{-ZnO}$ -rich phase. The paper added the necessity of effecting means to promote phase separation in order to accelerate crystallization.<sup>3)</sup> Following these works, this study was intended to unify two crystallization peaks in the differential thermal analysis (DTA) at low temperatures by promoting surface crystallization with external additives. The external additives are agents added to glass samples to be crystallized, and are expected to affect crystallization from glass surfaces. Few reports have basically dealt with the effect of external additives on the acceleration of crystallization, with some exceptions such as the work by Partridge and McMillan<sup>4)</sup> that dust powder and fine flaws on the surface promotes ununiform nucleation. In this study, first various external additives were added to glass powder to investigate the behavior of crystallization. In the final step, the roles of the external additives in surface crystallization were discussed as well as the mechanism of surface crystallization.

## 2. Method of Experiment

### 2.1. Preparation of Glasses

The composition of the basic glass (No.0 glass) was the same as in the previous reports:<sup>1-3)</sup>  $\text{SiO}_2=35$  (39.8) in wt% (molar percent),  $\text{Al}_2\text{O}_3=15$  (10.1),  $\text{CaO}=20$  (24.4),  $\text{ZnO}=15$  (12.6),  $\text{TiO}_2=13$  (11.1), and  $\text{B}_2\text{O}_3=2$  (2).

The weighing and mixing of raw materials were arrived at according to the method stated in the previous report.<sup>1)</sup> The prepared raw material was melted at  $1450^\circ\text{C}$  for 2 hours in a platinum crucible, and part of it was discharged on an iron plate to form a glass block. The rest was allowed to flow on the water-cooled roller to obtain quenched glass flakes about 0.5 mm thick. The following two kinds of samples were prepared from the above glass. (1) One of them was powder glass containing external additives and was for the investigation of the influences of the external additives on crystallization. In this case, the external additives stated below were added to the glass flakes by 5 wt%, and the mixture was finely ground for 20 hours with a 500 cc alumina pot mill (dry) to prepare a mixed powder glass sample 3  $\mu\text{m}$  in average particle diameter (particle size dis-

tribution: 2-8 $\mu$ ). (2) The other is a block-shaped glass sample to investigate the behavior of crystallization of the external additives on the contact surface. A cube about 10 $\times$ 10 $\times$ 10mm<sup>3</sup> in size was cut out of annealed glass with a diamond cutter and mirror-finished with cerium oxide powder.

The following external additives were selected: corundum ( $\alpha$ -Al<sub>2</sub>O<sub>3</sub>), quartz (SiO<sub>2</sub>), calcium oxide (CaO), and rutile (TiO<sub>2</sub>), as well as iron oxide (Fe<sub>2</sub>O<sub>3</sub>), zirconia (ZrO<sub>2</sub>), zircon (ZrSiO<sub>4</sub>) and wollastonite (CaO-SiO<sub>2</sub>), were used as nucleation agents. Moreover, as mineral components containing water or OH groups, the following were also used: montmorillonite, talc, zeolite, and kaolin. In the addition of wollastonite crystals, the amount of addition was varied to 0.5, 1, and 10wt% to examine its effect on crystallization. As will be described later, wollastonite had the effect of promoting crystallization as an external additive, so that the addition of glass with wollastonite composition was attempted. However, since the wollastonite composition has a strong tendency to devitrify by the melting method, glass with composition close to wollastonite (CaO=36.6 and SiO<sub>2</sub>=63.4 mol%) was added as an external additive. Glass was prepared from a batch containing 2.5-15wt% of CaO-SiO<sub>2</sub> (wollastonite composition) in glass raw materials, and its behavior of crystallization was also studied (internal additive). **Table 1** lists these external additives or kinds of added components, particle size, and the amount of addition.

## 2.2. Behavior of Crystallization of Powder Glass

The behavior of crystallization of various powder glass samples prepared as in Section 2.1(1) was examined by differential thermal analysis (DTA). In the analysis, Rigaku's differential thermal analyzer (TG 8110) was used and about 500mg of a sample was heated at a rate of 20°C/min with  $\alpha$ -Al<sub>2</sub>O<sub>3</sub> powder as a standard sample. Such data were obtained from a DTA curve as exothermal peak temperature  $T_c^3$  (in the case of plural peaks,  $T_{c0}$ ,  $T_{c1}$ ,  $T_{c2}$ , and  $T_{c3}$  from the low temperature side), and peak width. Additionally, powder glass was treated at a constant temperature of 730°C for 1-48 hours, the order and amount of crystal precipitation were analyzed by powder X-ray diffraction

(XRD).

## 2.3. Reaction Between Glass Surface and External Additives

Wollastonite specimens to be brought into contact with polished glass surfaces were prepared as follows. First, natural wollastonite powder was pressed at 50kg/cm<sup>2</sup> into compacts about 10 $\times$ 10 $\times$ 5mm<sup>3</sup> in size. They were sintered at 1350°C for 1hour, cut by a diamond cutter, polished with #600 alumina paper, and finished by ultrasonic cleaning. The following experiment was performed using glass samples prepared as in Section 2.1(2) and wollastonite specimens. Each wollastonite sintered body was placed with its polished face on that of a glass sample, and heated at 730°C for 1-48hours in the electric furnace. After treatment, glass surfaces contacted by wollastonite and the condition of crystallization inside the glass samples were analyzed by XRD, as well as observed with SEM and a polarizing microscope. Before SEM observation, the samples were etched with a 5% HF solution for 5seconds. The composition of precipitated crystals was analyzed along with their crystal distribution. The component analyses were conducted in the range of 0.9 $\times$ 0.9-4.5 $\times$ 4.5 $\mu$ m<sup>2</sup> using a scanning electron microscope (JEOL, Ltd., T-220) and an energy-dispersion-type X-ray analyzer (EDX) (JEOL, Ltd., JED-2000).

## 3. Results of Discussion of Experiment

### 3.1. DTA Curves of Powder Glass

**Figure 1** shows the DTA curves of powder glass samples containing 5wt% of external or internal additives. Crystallization peak temperatures were summarized at the bottom of Table 1. The case (a) is without external additives. Exothermal peaks appeared at  $T_{c1}$ =877°C on the low-temperature side and at  $T_{c2}$ =892°C on the high-temperature side. The reason why they shifted further from those of DTA curves of No.0 glass ( $T_{c1}$ =862°C,  $T_{c2}$ =894°C) stated in the previous report<sup>3)</sup> to the high-temperature side is probably

**Table 1.** Additives to promote a nucleation of No.0 glass. The form of additives, crystalline or glass, particle size, quantity of additives, and peak temperatures ( $T_c$ ) are shown. The basic composition of No.0 glass is 35SiO<sub>2</sub>, 15Al<sub>2</sub>O<sub>3</sub>, 20CaO, 15ZnO, 13TiO<sub>2</sub>, 2B<sub>2</sub>O<sub>3</sub> in wt%. "Ext" indicates external additive; "Int" indicates internal additive with regard to No.0 glass.

Additive compound	(a)	(b)	(c)	(d)	(e)	(f)	(g)	(h)	(i)
	Non	Al <sub>2</sub> O <sub>3</sub>	SiO <sub>2</sub>	Fe <sub>2</sub> O <sub>3</sub>	CaO	ZrSiO <sub>4</sub>	TiO <sub>2</sub>	ZrO <sub>2</sub>	CaO-SiO <sub>2</sub>
		Corundum $\alpha$ -quartz					Rutile	+0.08T <sub>2</sub> O <sub>3</sub>	Wollastonite
Phase	Ext	Ext	Ext	Ext	Ext	Ext	Ext	Ext	Ext
Size/ $\mu$ m		0.7	110	2.3	4.0	18.5	4.5	6.0	8.5
Quantity	5wt%	5wt%	5wt%	5wt%	5wt%	5wt%	5wt%	5wt%	0.5, 1, 5, 10wt%
$T_{c1}$ /°C	877	892	893	913	925	882	903	905	861, 859, 863, 862
$T_{c2}$ /°C	892	903	911	942	950	914		917	
$T_{c3}$ /°C		926							
Additive compound	(j)	(k)	(l)		(m)	(n)	(o)		
	36.6CaO	CaO-SiO <sub>2</sub>	Montmorillonite		Kaolin	Zeolite	Talc		
	63.4SiO <sub>2</sub>	Wollastonite							
Phase	Ext	Int	Ext		Ext	Ext	Ext		
Phase	Glass	Melt	Cryst		Cryst	Cryst	Cryst		
Size/ $\mu$ m	130		3.2		18.5	2.8	1.5		
Quantity	5wt%	2.5, 5, 10	15wt%		5wt%	5wt%	5wt%		
$T_{c1}$ /°C	918	925, 944, 959, 978	858		865	869	897		
$T_{c2}$ /°C			896		872	879	904		
$T_{c3}$ /°C					914				

that the grinding conditions of powder glass in this experiment (5grams sampling, planetary mill, 30min. grinding) were different from those in the previous report.<sup>3)</sup> In the previous work, smaller particle size led to lower crystallization temperature under the same grinding method, but in this experiment, the result was contrary. Possible causes include particle size distribution, impurity contamination, and residual strain, but the mechanism is not clear at present. (b) In the case of samples containing corundum,  $T_{c1}$  and  $T_{c2}$  peaks shifted by 11°-15°C to the high-temperature side, and the third peak  $T_{c3}$  appeared. (c) In samples containing  $\text{SiO}_2$ , the peak temperature shifted by 15°-20°C to the high-temperature side, and  $T_{c2}$  entered the shoulder of the  $T_{c1}$  peak. (d) In samples with iron oxide, the peak temperature shifted by 36°-50°C to the high-temperature side. (e) In samples with calcium oxide, the peak temperature shifted by 48°-58°C to the high-temperature side. In the cases from (b) to (e), crystallization peaks are as broad as that of (a). (f) In samples with zircon, the peak temperature shifted by 5°-22°C to the high-temperature side. (g) In samples with rutile, the peak temperatures shifted to the high-temperature side and were unified. (h) In samples with zirconia, the peak temperature shifted by 25°-28°C to the high-temperature side. (i) In samples with wollastonite, the peak temperatures shifted to the low-temperature side and were unified. The peak temperature showed little change even when the addition of wollastonite was increased to 0.5, 1, 5, and 10wt%. (j) In samples with 36.6CaO·63.4SiO<sub>2</sub> glass, peaks shifted by 41°C to the high-temperature side and were unified. (k) In samples with wollastonite as an internal additive, peak temperatures shifted by 52°C to the high-temperature side and were unified. When the amount of addition was varied to 2.5, 5, 10, and 15wt%, the peak

temperature rose to 925°C, 944°C, 959°C and 978°C, respectively. In the above cases (f)-(k), crystallization peaks are sharper than that of (a), and are unified or close to it. (l) In samples with montmorillonite,  $T_{c1}$  shifted by 17°C to the low-temperature side, while  $T_{c2}$  did by 4°C to the high-temperature side. (m) In samples with kaolin,  $T_{c1}$  shifted by 12°C to the low-temperature side, and a small peak  $T_{c3}$  appeared. (n) In samples with zeolite, the peak temperature shifted by 8°-13°C to the low-temperature side. (o) In the sample with talc, the peak temperature shifted by

19°-12°C to the high-temperature side. In the above cases (l)-(o), peaks were not perfectly unified and yet sharper than in (a).

### 3.2. Effects of External Additives in Holding at Constant Temperature

#### 3.2.1. XRD of Powder Glass

**Figure 2** shows XRD patterns of powder glass (average particle diameter: 3 $\mu\text{m}$ ) with external additives treated at 730°C for 1 to 48 hours. (a) is No.0 glass without external additives. As stated in the previous report,<sup>3)</sup> anorthite ( $\text{CaO}\cdot\text{Al}_2\text{O}_3\cdot 2\text{SiO}_2$ ) is precipitated in 16 hours, and gehlenite ( $2\text{CaO}\cdot\text{Al}_2\text{O}_3\cdot\text{SiO}_2$ ), willemite ( $2\text{ZnO}\cdot\text{SiO}_2$ ), and titanite ( $\text{CaO}\cdot\text{TiO}_2\cdot\text{SiO}_2$ ) in 24 hours. The diffraction intensity of anorthite showed an increase with treatment from 36 to 48 hours, while that of other crystal phases hardly increased after 36 hours. (b) is the case of  $\alpha\text{-Al}_2\text{O}_3$  addition. Anorthite crystals began to precipitate when treatment reached 16 hours. However, compared with No.0 composition, the diffraction intensity of all crystal phases decreased substantially. It was found that  $\text{Al}_2\text{O}_3$  remained unreacted till the final step. The case (c) is the addition of cubic  $\text{ZrO}_2$  includ-

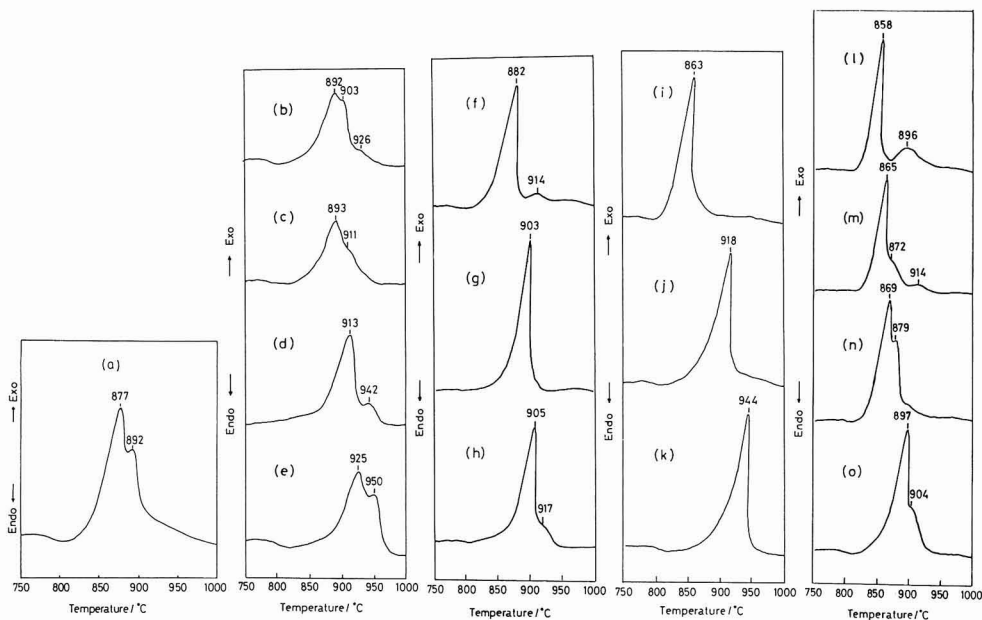


**Fig. 1.** DTA curves of No.0 glass with 5wt% additives (Table 1), heated at a rate of 20°C/min. (a) is No.0 glass with no additive. DTA curves of four groups of additives, (b) to (h), (i) to (k), and (l) to (o), are illustrated.

ing 8mol% of  $Y_2O_3$ . Anorthite began to precipitate after treatment reached 8hours, and gehlenite, willemite, and titanite precipitated after treatment of 24hours. Their diffraction intensity was almost constant over that point.  $ZrO_2$  proved to remain nearly unreacted. The case (d) is the addition of wollastonite. Anorthite precipitated after 8hour treatment, and gehlenite, willemite, and titanite after 16hour treatment. The diffraction intensity of these crystal phase was constant after 24hour treatment. On the other hand, most peaks of added wollastonite crystals disappeared after 4hour treatment.

### 3.2.2. XRD of Wollastonite-Contacted Surfaces

**Figure 3** shows XRD patterns of the surface of glass contacted with wollastonite and treated at  $730^\circ C$  for 1 to 48 hours. (a) is the XRD pattern of the free surface of glass. After heat treatment of 24hours, an anorthite peak was detected as well as those of gehlenite, willemite, and titanite, though slightly. The crosssection of the sample after heat treatment was examined by XRD; no crystal peaks were recognized even after 48hour treatment. (b) is the XRD pattern of the glass surface contacted with wollastonite. After 24hour treatment, the diffraction peaks of the four kinds of crystals were detected more strongly than in the case of (a).

### 3.2.3. SEM Observation of Wollastonite-Contacted Faces

**Figure 4** gives SEM photos of glass faces contacted with wollastonite or nothing, which were treated at  $730^\circ C$  for 48 hours.

The case (a) is without contact with wollastonite. After treatment at  $730^\circ C$  for 4 hours, columnar crystals about  $1 \times 0.4 \mu m$  in size were noticed though they were not detected by XRD. As treatment time increased to 8, 24, and 48hours, the columnar crystals grew but the number seemed unchanged. Moreover, the glass surface became rough, and the degree was intensified with treatment time. This is probably due to phase separation and was caused by different solution rates by etching. The case (b) is with contact with wollastonite. A number of columnar crystals precipitated after treatment of 8 hours. A part of the surface

without crystals became rough. The columnar crystals grew with treatment time, but the number seemed unchanged. The number of crystal particles is obviously greater than in the case of (a). There are striped microstructures probably indicating the direction of crystal growth in the enlarged photos (a) and (b) of the precipitated crystals. However, the grain boundaries of the four kinds of crystal particles (anorthite, gehlenite, willemite, and titanite) are not clear in the crystals. In order to distinguish the four kinds of crystal particles, the component analysis of columnar crystals and nearby glass was conducted by EDX. As a result, the concentration of Ca, Al, Si, Ti and Zn in the crystals and nearby glass was almost constant, and no difference in concentration was detected in both phases. Therefore, the grain boundary or condition of arrangement of each crystal particle in the columnar particles could not be recognized. SEM observation found that some pits were caused by etching with fluoric acid between the crystals and glass. Yet, when the sample surface without etching was observed by a polarizing microscope, no distinct cracks were encountered between the crystals and glass. It could not be determined whether the pits formed by etching were due to different solution rates by strain accompanying the compositional change or volume contraction of glass in the vicinity of the columnar crystals, or the presence of microcracks at the boundary face. After all, the columnar crystal was considered to be the aggregate of fine crystal particles less than  $1 \mu m$  in size that cannot be recognized by EDX.

### 3.3. Selection of External Additives For Crystallization

As has been stated earlier, the use of glass studied in this work as insulation film materials should meet the requirement for crystallization in heating (1) at appropriately low temperature, (2) in the narrow temperature range, and (3) as quickly as possible. In the cases of adding  $TiO_2$ , wollastonite and 36.6CaO-63.4SiO<sub>2</sub> glass, crystallization peaks were unified in the presence of external additives. In  $TiO_2$  addition, the peak temperature shifted to the high-temperature side, which is undesirable from the standpoint of (1). The peak temperature decreased only in the case of adding wollastonite. The crystallization peaks were also unified

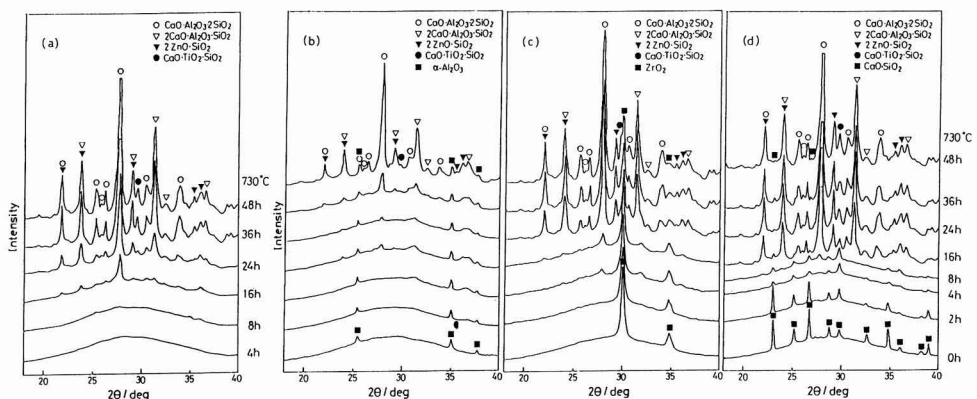


**Fig. 2.** XRD patterns of No.0 glass with additives, heat-treated at  $730^\circ C$  for 1 to 48h. (a) No.0 glass with no additives. (b) No.0 glass with 5wt%  $Al_2O_3$ . (c) No.0 glass with 5wt%  $ZrO_2$ . (d) No.0 glass with 5wt% external wollastonite ( $CaO \cdot SiO_2$ ).

when a wollastonite component was added as an internal additive, but the peak temperature increased and it is undesirable from standpoint (1). The glass transition point of this glass increased 4° to 18°C higher than that of No.0 glass, so that a rise in peak temperature was probably due to an increase in the viscosity of glass. As a result, it can be concluded that wollastonite crystals as an external additive are the most favorable agent to promote crystallization at low temperatures.

**3.4. Crystallization Mechanism in Presence of External Additives**

Based on experimental results in this study, the roles of external and internal additives in the promotion of crystallization were summarised as follows to study the mechanism of crystallization.

1) The addition of wollastonite (CaO-SiO<sub>2</sub>) as an external

additive induces the precipitation of anorthite (CaO·Al<sub>2</sub>O<sub>3</sub>·2SiO<sub>2</sub>) from an Al<sub>2</sub>O<sub>3</sub>-rich phase in the glass surface. The precipitation of anorthite promotes that of gehlenite as well as accelerates crystallization from the ZnO+TiO<sub>2</sub>-rich phase.

- 2) It is known that water addition lowers glass viscosity<sup>5-11)</sup> and promotes crystallization.<sup>12,13)</sup> When water or minerals containing OH groups are added, they are introduced in glass to reduce viscosity near the glass surface, thus probably promoting crystallization.
- 3) When DTA peaks are unified, the precipitation of anorthite precedes slightly, followed by that of other crystals.
- 4) **Figure 5** is the schematic diagram of a mechanism in which crystal particles grow while maintaining columnar forms. Quenched glass (a) first undergoes  $\sigma$  phase separation by heating (b). The previous report<sup>3)</sup> showed that the composition (mol%) of the precipitated crystal is A (anorthite):G (gehlenite):W (willemite):T (titanite)=78:18:1:3. The component amount of Al<sub>2</sub>O<sub>3</sub>-rich glass (A+G) is greater than that of ZnO+TiO<sub>2</sub>-rich glass (W+T), and after phase separation the former is expected to be a continuous phase. The

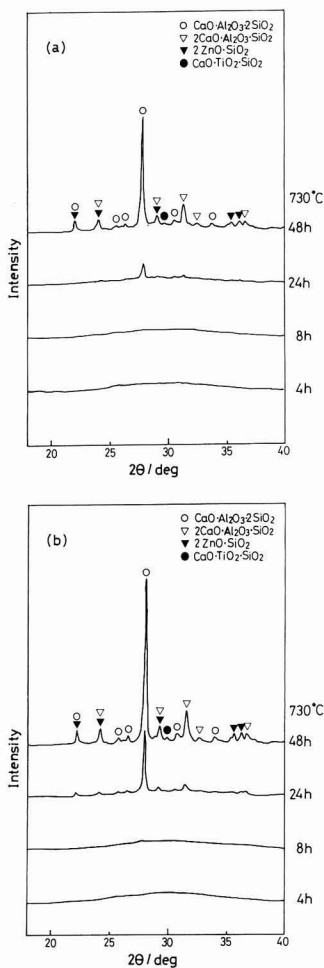


**Fig. 3.** XRD patterns of No.0 glass surface, heat-treated at 730°C for 1 to 48h in contact with wollastonite body (CaO·SiO<sub>2</sub>). (a) No.0 glass surface free from wollastonite body. (b) No.0 glass surface kept in contact with wollastonite body.

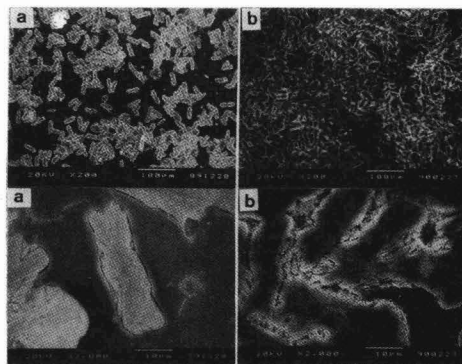


**Fig. 4.** SEM photographs of No.0 glass surface etched with 5% HF solution for 5sec, after a heat treatment at 730°C for 48h. (a) Free surface of glass. (b) Glass surface kept in contact with wollastonite body.

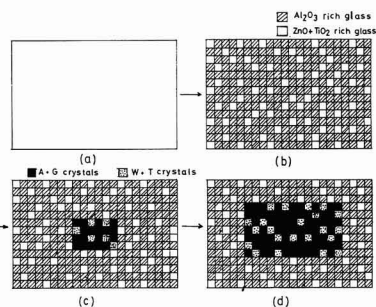


**Fig. 5.** A schematic drawing of crystal growth in No.0 glass. Phase separation proceeds from clear glass (a) to (b), and crystallization occurs in Al<sub>2</sub>O<sub>3</sub> rich phase and TiO<sub>2</sub>+ZnO rich phase (c). Crystalline particles grow in size (d). Distinctive patterns of individual crystalline phases, A (anorthite), G (gehlenite), W (willemite) and T (titanite), are not visualized.

nucleation of A and G occurs from the  $Al_2O_3$ -rich phase; then the crystals of W and T begin to precipitate from the ZnO+ $TiO_2$ -rich phase (c), and they grow (d). Each columnar crystal is surmised to consist of the fine crystals of A, G, W, and T (probably 1 $\mu$ m or less in particle diameter).

#### 4. Conclusion

Powder glass samples which were  $SiO_2$ - $Al_2O_3$ -CaO-ZnO- $TiO_2$ - $B_2O_3$  glass containing various additives were subjected to DTA, XRD, SEM, observation with a polarizing microscope, and component analysis to investigate the behavior of crystallization, and the following results were obtained.

- 1) The two crystallization peaks in DTA curves were unified by the addition of  $TiO_2$ , wollastonite, and 36.6CaO-63.4 $SiO_2$  glass. The peak temperature shifted to the low-temperature side only in the case of the external addition of wollastonite crystals.
- 2) Also in constant temperature heating, the external addition of wollastonite crystals accelerated the precipitation of anorthite as well as that of other crystals.
- 3) Plenty of fine columnar crystals were formed in the glass surface contacted with wollastonite, and the columnar crystals grew with heat treatment time while the number did not show an increase.
- 4) These columnar crystals were considered to be aggregates of the four kinds of crystals less than 1 $\mu$ m in size (anor-

thite, gehlenite, willemite, and titanite).

#### References:

- 1) H. Kuribayashi, R. Ota and J. Fukunaga, *Seramikkusu Ronbunshi*, 99, 36-41 (1991).
- 2) R. Ota, H. Kuribayashi and J. Fukunaga, *Zairyo*, 40, 395-399 (1991).
- 3) H. Kuribayashi, R. Ota, J. Fukunaga and T. Taguchi, *Seramikkusu Ronbun-shi*, (1991). In print.
- 4) G. Partridge and P.W. McMillan, *Glass Technol.*, 15, 127-133 (1974).
- 5) H. Scholze, *Glastech. Ber.*, 32, 278-281 (1959).
- 6) L. Merker and H. Scholze, *Galstech. Ber.*, 35, 37-43 (1962).
- 7) G. Hetherington and K.H. Jack, *Phys. Chem. Glasses*, 3, 129-133 (1962).
- 8) G. Hetherington, K.H. Jack and J.C. Kennedy, *ibid.*, 5, 130-136 (1964).
- 9) J.E. Shelby and G.L. McVay, *J. Non-Cryst. Solids*, 20, 439-449 (1976).
- 10) K. Matusita, T. Watanabe, K. Kamiya and S. Sakka, *Phys. Chem. Glasses*, 21, 78-84 (1980).
- 11) S. Sakka, K. Kamiya and Z.J. Huang, *Research Report, Facul. Engineer. Mie Univ.* 7, 137-159 (1982).
- 12) F.E. Wagstaff, S.D. Brown and I.B. Cutler, *Phys. Chem. Glasses*, 5, 76-81 (1964).
- 13) C.J.R. Gonzales-Oliver, P.S. Johnson and P.F. James, *J. Mater. Sci.*, 14, 1159-1169 (1979).

---

This article is a full translation of the article which appeared in *Nippon Seramikkusu Kyokai Gakujutsu Ronbunshi* (Japanese version), Vol.99, No.11, 1991.

# Properties of $Y_2O_3$ - $Al_2O_3$ - $SiO_2$ Glasses as a Model System of Grain Boundary Phase of $Si_3N_4$ Ceramics (Part 2)

## - Leaching Characteristics -

Kohei Oda and Tetsuo Yoshio\*

Yonago National College of Technology,  
4448, Hikonacho, Yonago-shi, 683 Japan

\*Faculty of Engineering, Okayama University,  
3-1-1, Tsushimanaka, Okayama-shi, 700 Japan

The leaching behavior of  $Y_2O_3$ - $Al_2O_3$ - $SiO_2$  glasses was studied in connection with the hydrothermal corrosion of  $Si_3N_4$ - $Y_2O_3/Al_2O_3$  ceramics. Leaching tests were conducted with the glass blocks under hydrothermal conditions at 300°C for 1 to 10 days. It was found that the weight loss of the glasses is less than 0.8mg/cm<sup>2</sup> after 10 days and the durability of the glasses is higher than that of  $SiO_2$  glass, Corning-1723 glass and  $Si_3N_4$ - $Y_2O_3/Al_2O_3$  ceramics. It was considered that the higher durability of the glass under hydrothermal conditions is due to the lower leach rates of  $Y_2O_3$  and  $Al_2O_3$ .

[Received March 14, 1991; Accepted July 18, 1991]

**Key-words:** Leach rate, Hydrothermal corrosion, Durability,  $Y_2O_3$ , Autoclave

## 1. Introduction

The authors have been studying the corrosion behavior of silicon nitride ceramics under water at high temperatures and pressures,<sup>1)</sup> as part of a study on the water resistance of ceramics aiming at the development of their applications as well as modification. So far, the authors have reported that the chemical stability of silicon nitride ceramics with additives in water at high temperatures and pressures depends mainly and greatly on a difference in the composition of additives constituting grain boundary phases, and that silicon nitride ceramics containing  $Y_2O_3$  and  $Al_2O_3$  has higher corrosion resistance than those containing MgO.

Based on these results, this study aimed to obtain information on the grain boundary phases of silicon nitride ceramics with  $Y_2O_3$  and  $Al_2O_3$  using simulated grain boundary glass. The physical properties of the simulated grain boundary glass were stated in the previous report.<sup>2)</sup> As a further step, the leaching characteristics of the simulated grain boundary glass were investigated under water at high temperatures and pressures. As a result, it was found that this  $Y_2O_3$ - $Al_2O_3$ - $SiO_2$  glass has excellent corrosion resistance under high-temperature and high-pressure water. Detailed characteristics are described in this paper.

## 2. Experimental Procedure

### 2.1. Preparation of Glass Samples

The glass sample used in this experiment was simulated grain boundary glass with the same composition as in the previous report<sup>2)</sup> --  $xY_2O_3(60-x)Al_2O_340SiO_2$  ( $x=30, 40, 45$ wt%) -- prepared in the same manner (these glass samples with  $x=30, 40$  and  $45$  wt% was denoted as YAS-1, -2 and -3, respectively). Some of these glass samples were polished with  $CeO_2$  powder to mirror faces to prepare glass block specimens  $8 \times 8 \times 4$ mm<sup>3</sup> in size, and the rest were ground to prepare glass powder specimens with 420-250 $\mu$ m in particle size.

### 2.2. Leaching Test

Glass powder specimens underwent a leaching test at 100°C for one day in a Teflon autoclave according to JIS R-3502 (chemical durability test for glass). The chemical analyses of leaching solutions were conducted by an ICP-AES method, and the leaching amounts of  $Y_2O_3$ ,  $Al_2O_3$  and  $SiO_2$  were measured to calculate the leach rate  $L$  (g/cm<sup>2</sup>-h) of each component.<sup>3)</sup>

Glass block specimens were subjected to a leaching test with an autoclave at 100°C and equilibrium water vapor pressure (8.6MPa) for 1, 6 and 10 days. In the procedure, as in the case of silicon nitride ceramics, hydrothermal treatment was carried out so that the volume of redistilled water  $V$ (cm<sup>3</sup>) was determined as  $V/A=10$  cm with regard to the geometric surface area of a sample  $A$ (cm<sup>2</sup>), in order to obtain the weight change of the sample per unit area before and after the leaching test. For comparison, the leaching test was also performed with quartz glass finished to mirror face  $3 \times 4 \times 4$ mm<sup>3</sup> in size under the same conditions. The chemical analyses of leaching solutions were conducted by an ICP-AES method.

## 3. Results and Discussion

### 3.1. Results of Glass Powder Leaching Tests

Figure 1 shows a relation between the leach rate of each component in leaching tests with simulated grain boundary glass powder in the  $Y_2O_3$ - $Al_2O_3$ - $SiO_2$  system and  $Y/Al$  (molar ratio). Moreover, for reference, Table 1 lists results obtained earlier by the authors-measurements of the leach rate of each component of glass with a composition of ((1-

$x)[0.5Na_2O \cdot B_2O_3 \cdot 3SiO_2] \cdot xM_2O_3$ ;  $x=0.05$ ,  $M=Al, Y$ ) consisting of basic glass ( $0.5Na_2O \cdot B_2O_3 \cdot 3SiO_2$ ) and 5mol% of  $Al_2O_3$  and  $Y_2O_3$  as additives.

As in the table, the relation between the leach rates  $L(i)$  of components is  $L(SiO_2) > L(Al_2O_3) > L(Y_2O_3)$ . Moreover, the addition of  $Al_2O_3$  and  $Y_2O_3$  tended to greatly inhibit the leaching of  $SiO_2$  as well. The leach rates of these components can be regarded as indexes expressing the leach rates of oxide components by water, that is, tendencies of leaching characteristics peculiar to the components, though there is a difference in matrix.

The leach rates of components of simulated grain boundary glass in the  $Y_2O_3-Al_2O_3-SiO_2$  system in this experiment as in Fig.1 are about 1/1000 compared with values in Table 1, showing that glass in this system has extremely high corrosion resistance. The study on the alkali resistance of aluminosilicate glass containing  $Y_2O_3$  by Makishima et al.<sup>5)</sup> also reported that aluminosilicate glass with  $Y_2O_3$  has higher corrosion resistance than quartz glass. Moreover, Day et al.<sup>6)</sup> reported that  $Y_2O_3-Al_2O_3-SiO_2$  glass is not corroded in distilled water at 50°C, and that etching or pitting does not occur. Those can be explained by the results of leach rates of components. The reason why the leach rate of  $SiO_2$  in Fig.1 shows lower value than that in Table 1 is probably that alkali borosilicate glass as a matrix fundamentally has low water resistance while  $Y_2O_3-Al_2O_3-SiO_2$  glass is non-alkali glass and the solubility of its  $Al_2O_3$  and  $Y_2O_3$  components to water is extremely low.

**3.2. Results of Leaching Tests With Glass Blocks**

Table 2 shows weight changes of block samples of  $Y_2O_3-Al_2O_3-SiO_2$  simulated grain boundary glass after treatment in the autoclave under the hydrothermal conditions of 300°C and 8.6MPa. Moreover, for comparison, Fig.2 plots the earlier results<sup>1)</sup> of  $Si_3N_4-Y_2O_3/Al_2O_3$  ceramics in which this glass component (measured under the same conditions) cor-

responds to the simulated grain boundary phase, as well as those of monolithic quartz glass since the major leached component is  $SiO_2$ . In addition, the similar test data with Corning-1723 glass ( $SiO_2$  57,  $Al_2O_3$  15,  $B_2O_3$  5, CaO 10, BaO 6 and MgO 7wt%) used as the window material of high-temperature and -pressure water containers (after reinforced with mica plates) are shown in the figure; these data serve as reference in studying the application of high-temperature and -pressure water resistance properties of the glass used in this experiment.

The block samples of  $Y_2O_3-Al_2O_3-SiO_2$  simulated grain boundary glass showed little weight change after hydrothermal treatment for 1 and 6 days. Even after hydro-thermal treatment for 10 days in which a weight change was detected, no substantial changes were encountered except for slightly clouded surfaces. It is clear that the simulated grain boundary glass in the  $Y_2O_3-Al_2O_3-SiO_2$  system has much higher corrosion resistance than  $Si_3N_4-Y_2O_3/Al_2O_3$  ceramics or quartz glass.

Table 3 summarizes the leaching amount of each component of leaching solutions after leaching tests with  $Y_2O_3-Al_2O_3-SiO_2$  simulated grain boundary glass,  $Si_3N_4-Y_2O_3/Al_2O_3$  ceramics, and quartz glass which were determined by ICP analysis. The table shows that weight changes given in Fig.2 are mainly due to the leaching of  $SiO_2$  and the weight loss of each sample is in good agreement with the leaching of  $SiO_2$ . By contrast, in the case of  $Al_2O_3$  and  $Y_2O_3$ , the contribution of these components to weight loss is negligible. That is, the leaching characteristics of glass blocks are closely related to the leach rates of components obtained by glass powder leaching tests

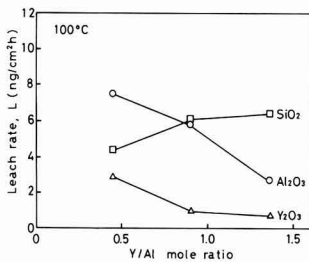


Fig. 1. Leach rates of  $Y_2O_3-Al_2O_3-SiO_2$  glasses as a function of Y/Al mole ratio.

Table 1. Leach rates of  $((1-x)[0.5Na_2O \cdot B_2O_3 \cdot 3SiO_2] \cdot xM_2O_3$ ;  $x=0.05$ ,  $M=Al, Y$ ) glasses calculated from the results of powder leaching test. (Ref.(3))

Additive oxide	L (μg/cm² · h)	
	L( $M_2O_3$ )	L( $SiO_2$ )
(Base glass)	—	35
$Al_2O_3$	2.3	6.2
$Y_2O_3$	0.6	5.2

Table 2. Specific weight loss for  $Y_2O_3-Al_2O_3-SiO_2$  glasses after hydrothermal treatment at 300°C and 8.6MPa.

Time (day)	Specific weight loss (mg/cm²)		
	YAS-1	YAS-2	YAS-3
1	ND	ND	ND
6	ND	ND	ND
10	0.08	0.59	0.79

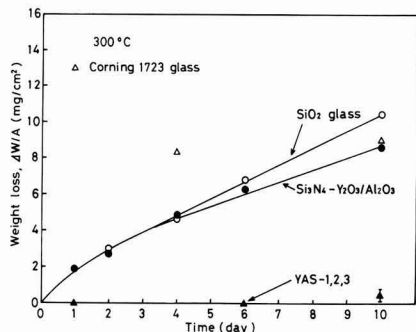


Fig. 2. Specific weight loss for YAS-1, YAS-2 and YAS-3 glasses,  $Si_3N_4-Y_2O_3/Al_2O_3$  ceramics and  $SiO_2$  glass treated under hydrothermal conditions at 300°C and 8.6MPa.

**Table 3.** Dissolution data for YAS-1, YAS-2 and YAS-3 glasses,  $\text{Si}_3\text{N}_4\text{-Y}_2\text{O}_3/\text{Al}_2\text{O}_3$  ceramics and  $\text{SiO}_2$  glass treated under hydrothermal conditions at 300°C and 8.6MPa.

Specimen	YAS-1			YAS-2			YAS-3			$\text{Si}_3\text{N}_4\text{-Y}_2\text{O}_3/\text{Al}_2\text{O}_3$			$\text{SiO}_2$ glass
	Leached amounts (mg/l)												
Time (d)	Si	Al	Y	Si	Al	Y	Si	Al	Y	Si	Al	Y	Si
1	0.30	0.15	0.34	0.44	0.04	0.23	0.59	0.10	0.17	100	0.81	0.00	-
2	-	-	-	-	-	-	-	-	-	210	1.66	0.01	155
4	-	-	-	-	-	-	-	-	-	299	2.80	0.03	260
6	1.01	0.38	0.22	1.06	0.13	0.35	1.50	0.10	0.26	420	2.55	0.01	338
10	2.89	0.31	0.16	16.0	0.24	0.24	14.9	0.13	0.18	607	1.73	0.26	516

though temperature is different, and they can be explained by the leach rates of components to some extent.

The corrosion of  $\text{Si}_3\text{N}_4\text{-Y}_2\text{O}_3/\text{Al}_2\text{O}_3$  ceramics under hydrothermal conditions proceeds with the following reaction:  $\text{Si}_3\text{N}_4 + 6\text{H}_2\text{O} \rightarrow 3\text{SiO}_2 + 4\text{NH}_3$ ; and the leaching of the products into water leads to weight loss.<sup>1)</sup> On the other hand, a glass phase with  $\text{Y}_2\text{O}_3$  and  $\text{Al}_2\text{O}_3$  constituting a grain boundary phase has high leaching resistance (as shown in the measurements of leach rates) so that it becomes a silicate hydrate containing these aid components, thus forming a corrosion phase. The corrosion layer of  $\text{Si}_3\text{N}_4\text{-Y}_2\text{O}_3/\text{Al}_2\text{O}_3$  ceramics consists qualitatively of the same components as  $\text{Y}_2\text{O}_3\text{-Al}_2\text{O}_3\text{-SiO}_2$  glass. As for the corrosion of quartz glass under the same conditions,  $\text{SiO}_2$  component is quite soluble to hot water judging from its leach rate and the lack of aid components leads to uncontrolled corrosion so that leaching weight loss increases monotonously with time. Corrosion layers are not formed on sample surfaces after corrosion tests, and corrosion is considered to proceed by a dissolution reaction in the surfaces.<sup>7)</sup>

As has been described above, the properties of high-temperature and -pressure water resistance of  $\text{Y}_2\text{O}_3\text{-Al}_2\text{O}_3\text{-SiO}_2$  glass as the simulated grain boundary glass phase of  $\text{Si}_3\text{N}_4\text{-Y}_2\text{O}_3/\text{Al}_2\text{O}_3$  ceramics were studied on the basis of the leach rate of each component. As a result, it was found that excellent high-temperature and pressure water characteristics of glass in this system are due to low leach rates of  $\text{Y}_2\text{O}_3$  and  $\text{Al}_2\text{O}_3$  components. These results suggest that controlling the composition of the grain boundary glass

phase may basically provide higher corrosion resistance for  $\text{Si}_3\text{N}_4$  ceramics and that they are candidates for window materials of high-temperature and -pressure water containers.

#### Acknowledgements

This research was supported financially in part by Nihon Itagarasu Zairyo Kogaku Zaidan.

#### References:

- 1) T. Yoshio, K. Oda, K. O'oka and K. Oda, *Yogyo-Kyokaiishi*, 94, 116-122 (1986); T. Yoshio, K. Oda and K. Oda, *ibid.*, 95, 435-441 (1987); T. Yoshio and K. Oda, *ibid.*, 95, 730-735 (1987).
- 2) K. Oda and T. Yoshio, *Seramikkusu-Ronbunshi*, 97, 1493-1497 (1989).
- 3) T. Yoshio and K. Oda, *ibid.*, 96, 159-164 (1988).
- 4) T. Yoshio and K. Oda, *MRS Int. Mtg. on Advanced Mater.*, Vol.4, MRS (1989) 337-342.
- 5) A. Makishima and T. Shimohira, *J. Non-Cryst. Solids*, 38 & 39, 661-666 (1980).
- 6) M.J. Hyatt and D.E. Day, *J. Am. Ceram. Soc.*, 70, C283-287 (1987).
- 7) T. Yoshio, A. Kohno and K. Oda, *Proc. 1st Fall Mtg. Ceram. Soc. Jpn.* (1988) 173-174.

This article is a full translation of the article which appeared in *Nippon Seramikkusu Kyokai Gakujutsu Ronbunshi* (Japanese version), Vol.99, No.11, 1991.

# Thermal Shock Resistance of High Thermal Conductive SiC Ceramics

Yukio Takeda\* and Kunihiro Maeda

Hitachi Research Laboratory, Hitachi Ltd.  
4026, Kuji-cho, Hitachi-shi, 319-12 Japan

The thermal shock resistance of high thermal conductive SiC ceramics by the water quench method was studied in comparison with other SiC ceramics. The critical temperature difference ( $\Delta T_c$ ) of the flexural strength was dependent on the kinds of SiC ceramics. The high thermal conductive SiC ceramics had the highest  $\Delta T_c$  value of 680°C. The hot-pressed SiC and pressureless-sintered SiC ceramics with smaller thermal conductivities had the  $\Delta T_c$  values of 450 and 350°C, respectively. The thermal shock damage resistance parameters ( $R'$ ) calculated from the thermal conductivities at 500°C were 22kW/m for high thermal conductive SiC, 16kW/m for hot-pressed and 12kW/m for pressureless-sintered SiC ceramics, which agreed qualitatively with the  $\Delta T_c$  values. The ratio of the calculated stress intensity factor ( $K_I$ ) for crack initiation at the water quenching to the critical stress intensity factor ( $K_{Ic}$ ) obtained from the flexural strength was in the range of 60-80%, and approximately constant in all examined SiC ceramics.

[Received March 27, 1991; Accepted July 18, 1991]

**Key-words:** Silicon carbide, Thermal shock behavior, Water-quench, Flexural strength, Fracture stress, Thermal shock fracture resistance parameter

## 1. Introduction

Silicon carbide (SiC) has a strong covalent bonding character and is superior in the properties of heat resistance and oxidation resistance; it is thus expected as an excellent materials for high temperature structural application. However, SiC ceramics are known to have a wide difference in their thermal, electrical and mechanical properties, depending on the sintering aids used.<sup>1-3</sup> Particularly when sintering aids of Be or its compounds are used, SiC ceramics additionally exhibit a higher thermal conductivity at room temperature than metallic aluminum, an electrical insulating property, and a thermal expansion coefficient close to that of silicon. This makes them commercially available as electrical insulating substrates for mounting Si semiconductor devices. Furthermore, these SiC ceramics exhibit high flexural strength up to 430MPa.<sup>4</sup> In view of these various excellent properties, high thermal conductive SiC ceramics are also expected to be suitable materials for parts subject to thermal shock at high temperature.

As remedial measures for the thermal stress fracture of ceramics materials, two methods described in the following are generally thought of:

1) to reduce the concentration of generated thermal stresses by a change of geometrical shape of the parts, and

2) to choose or develop a strongly resistant material to thermal stress fracture without changing the shape of the parts.

An example of method (1) is seen in the development of stationary ceramic blades of a gas turbine, in which the ceramic parts are designed in a structure separated into several pieces, so that the stress concentration is relaxed.<sup>5</sup> As an example of method (2), high thermal conductive SiC ceramics shall be suitable materials to develop because of their excellent thermal as well as mechanical properties.

Thermal shock fracture of ceramic materials has been investigated in various ways. The most popular evaluation method of this fracture has been the quenching of the materials at various temperature differences, and the arrangement of mean residual strength of the materials after quenched in relation to the temperature difference applied in quenching. In our current study, we investigated the high thermal conductive SiC ceramics added with BeO by comparing with other kinds of SiC ceramics, using the water quenching method.

## 2. Experimental Procedure

### 2.1. Test Samples

Table 1 shows three kinds of SiC ceramics test samples prepared by adding different kinds of sintering aids and by different sintering methods. Sample No.1 was prepared by hot-pressing with addition of BeO. (Hereafter, it is symbolized as SC-101). Sample 1 has high thermal conductivity at room temperature up to 270W/mK.<sup>1-3</sup> Samples No.2 and No.3 are SiC ceramics prepared for comparison purposes. Sample No.2 was prepared by hot-pressing with addition of AlN. (Hereafter, it is symbolized as SC-501.) Sample 2 has the highest flexural strength among the three samples.<sup>6</sup> Sample No.3 was prepared by pressureless sintering method with B additives. This sample was prepared by Hitachi Chemical Ceramics Co., Ltd..

Test specimens were prepared in dimension of 3×4×36mm, and polished on all surfaces in the surface roughness of less than 0.8μm. Specimen corners were chamfered by about 0.1mm.

Table 1. Properties of SiC ceramics used.

No.	symbol	additive	sintering method
1	SC-101	BeO	hot-press
2	SC-501	AlN	hot-press
3	Sintered SiC	B+C	pressureless sintering

**2.2. Measurement of Flexural Strength**

Flexural strength of the specimens was measured by the 4-point bending test method using a lower span of 30mm and an upper span of 10mm, and using a cross-head speed of 0.5mm/min at room temperature.

**2.3. Measurement of Thermal Shock Fracture Resistance**

After held at the respective specified temperatures for 20 to 30min, test specimens were quenched into water controlled at 20°C. The specimens thus given with thermal shock were measured for flexural strength at room temperature.

**3. Test Results and Discussion**

**3.1. Change of Strength after Water Quenching**

Figure 1 shows the relationship between temperature difference ( $\Delta T$ ) in quenching and flexural strength of the three kinds of SiC ceramics specimens after subjected to thermal shock by water quenching. In the case of SC-101, it is seen that flexural strength is maintained at 470MPa in the region of temperature difference in quenching up to 600°C, but it decreases rapidly after that, and then starts to gradually decrease with the increase of temperature difference in the region of  $\Delta T$  beyond 680°C, finally reaching a very small value at  $\Delta T$  of 900°C. It is considered that cracks generated in the specimen propagated semi-statically as early as at  $\Delta T$  of 680°C due to a high thermal conductivity of SC-101, so the strength did not decrease rapidly.<sup>7)</sup> In contrast, in the case of SC-501 and pressureless-sintered SiC ceramics, flexural strength decreased rapidly at  $\Delta T$  of 450°C and 350°C respectively, it reached a very low value at respective  $\Delta T$  of 500°C and 400°C. From these results, we determined the critical temperature differences ( $\Delta T_c$ ) of SC-101, SC-501, and pressureless-sintered SiC ceramics as 680°C, 450°C and 350°C respectively. It should be noted that  $\Delta T_c$  of 680°C of SC-101 having a high thermal conductivity is much larger than those of various SiC ceramics, which were reported as 400°C more or less,<sup>8)</sup> and is nearly equal to a high  $\Delta T_c$  value of Si<sub>3</sub>N<sub>4</sub> ceramics,<sup>9)</sup> which have been actively researched and developed as prospective structural ceramics in recent years. Consequently, SC-101 is proven to be a material excellent in thermal shock resistance property.

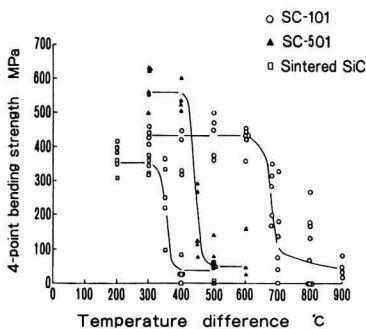


Fig. 1. Fracture stress of the three kinds of SiC ceramics quenched at various temperatures into water at 20°C.

**3.2. Thermal Shock Fracture Resistance Parameter**

Thermal shock damage resistance parameter is expressed by the following equations (1) and (2) when thermal shock is applied by the water quenching method.

$$R = S_t(1 - \nu)/(E \cdot \alpha) \dots \dots \dots (1)$$

$$R' = R \cdot \kappa \dots \dots \dots (2)$$

Here,  $R$  and  $R'$  are thermal shock damage resistance parameter,  $S_t$  is tensile strength,  $\nu$  is Poisson's ratio,  $\kappa$  is thermal conductivity,  $E$  is Young's modulus, and  $\alpha$  is thermal expansion coefficient.  $R$  or  $R'$  should be appropriately selected by the value range of Biot parameter  $\beta$ , which indicates the degree of thermal shock. When  $\beta$  is larger than 5, equation (1) for  $R$  should be used, and when  $\beta$  is smaller than 5, equation (2) for  $R'$  should be used.  $\beta$  is calculated by equation (3) shown below.

$$\beta = r_m \cdot h / \kappa \dots \dots \dots (3)$$

Here,  $r_m$  is a half thickness for a test specimen, which is 2.0mm in the case of this experiment, and  $h$  is heat transfer coefficient. Since water was the cooling media, we adopted the data reported by Midorikawa et al.<sup>8)</sup> as the heat transfer coefficient.

In order to determine  $\beta$ , the value of thermal conductivity is necessary to be known. The thermal conductivities of sintered SiC ceramics were measured by the laser-flash method.<sup>1)</sup> Test specimens for the thermal conductivity measurement were in dimension of 10mm in diameter and 5mm thick. Figure 2 shows the temperature dependence of thermal conductivity of the three kinds of SiC ceramics samples. It is seen that thermal conductivity is higher in the sequential order of SC-101, pressureless-sintered SiC ceramics and SC-501, and it decreases with the increase of temperature in any of those SiC ceramics samples. It shall be specially noted that thermal conductivity of SC-101 is higher than that of BeO, which is known to be a high thermal conductive material among various ceramics materials.

Using these thermal conductivity data, respective Biot parameters  $\beta$  of SC-101, pressureless-sintered SiC ceramics and SC-501 were calculated at the respective temperatures, at which  $\Delta T_c$  is given, obtaining 0.42, 1.3 and 1.2. All of the  $\beta$  values obtained were found to be smaller than 5. Therefore, as far as those experimental conditions are concerned,  $R'$  expressed by equation (2) is effective as the thermal shock damage resistance parameter for the SiC

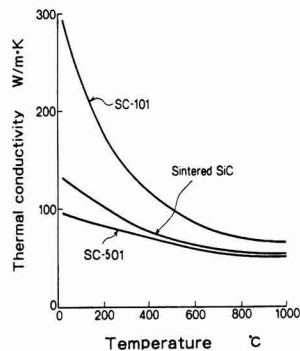


Fig. 2. Thermal conductivity as a function of temperature of the three kinds of SiC ceramics.

ceramics.

**Table 2** shows physical properties, mechanical properties and thermal shock fracture resistance parameters of the three kinds of SiC ceramics. *R'* values given in Table 2 were calculated using the thermal conductivity values of respective SiC samples at 500°C. *R* values are seen to be higher in the sequential order of SC-501, SC-101 and pressureless-sintered SiC ceramics. This sequential order of *R* agrees with that of flexural strength, which represents the mechanical properties, but does not agree with that of  $\Delta T_c$ . Meanwhile, *R'* values are seen to be higher in the sequential order of SC-101, SC-501 and pressureless-sintered SiC ceramics, and *R'* value of SC-101 is extremely high, upto 22kW/m, compared to two other SiC ceramics samples. This sequential order of *R'* agree with that of  $\Delta T_c$ ; *R'* value of hot-pressed Si<sub>3</sub>N<sub>4</sub> was calculated as 11kW/m<sup>9)</sup> based on the same assumption of SiC ceramics. Hot-pressed Si<sub>3</sub>N<sub>4</sub> is well known to have a strong thermal shock resistance among various kinds of ceramics. SC-101 is superior even to this hot-pressed Si<sub>3</sub>N<sub>4</sub> in terms of thermal shock fracture resistance parameter *R'*. These results prove that SC-101 is an extremely strong ceramic material in thermal shock resistance due to its high thermal conductivity. In other words, SC-101 is a suitable material for equipment parts subject to thermal shocks.

**3.3. Investigation of Fracture Kinetics**

In the study on thermal shock fracture using a sintered zirconia body, Ashizuka et al.<sup>11)</sup> introduced a relation as shown in equation (4) below, and investigated the behavior of this ceramics material on the basis of fracture kinetics.

$$K_I/K_{IC} = \alpha E \Delta T / (1 - \nu) \sigma_f f(\beta) \dots \dots \dots (4)$$

Equation (4) expresses the ratio of stress intensity factor *K<sub>I</sub>* when a quenching temperature difference of  $\Delta T$  is given to the ceramics material against critical stress intensity factor *K<sub>IC</sub>* of the material. Thermal stress fracture is caused when the thermal stress given to the material becomes larger than

**Table 2.** Relationship between physical and mechanical properties and thermal shock fracture resistance parameters of the three kinds of SiC ceramics.

Material	$\sigma_{bd}$ MPa	E GPa	$\nu$	$\alpha$ 10 <sup>-6</sup> /°C	$\kappa$ W/m·K	R °C	R' kW/m
SC-101	470	460	0.16	4	100	215	22
SC-501	550	480	0.16	4	65	240	16
Sintered SiC	350	450	0.15	4	70	165	12
Si <sub>3</sub> N <sub>4</sub>	850	310	0.27	3.2	17	626	11
Al <sub>2</sub> O <sub>3</sub>	300	400	0.27	9	8	61	0.5

the maximum tensile stress of the material. Therefore, fracture occurs in principle when *K<sub>I</sub>/K<sub>IC</sub>* value become 1. In equation (4), *f*( $\beta$ ) is a parameter indicating the deviation from an ideal quenching state, and is a function of  $\beta$ . In this study, *f*( $\beta$ ) was obtained using the results of Satyamrthy et al.<sup>12)</sup>

**Table 3** shows the various physical properties and the *K<sub>I</sub>/K<sub>IC</sub>* values calculated with these data for the three kinds of SiC ceramics. Here, tensile strength was calculated from flexural strength using equation (5) below.

$$\sigma_{bd} / \sigma_t = [4(m + 1)^2 / m + 2]^{1/m} \dots \dots \dots (5)$$

Here,  $\sigma_t$  is tensile strength,  $\sigma_{bd}$  is flexural strength measured by the 4-point bending test, and *m* is Weibull modulus. *K<sub>I</sub>/K<sub>IC</sub>* ratios using the  $\Delta T_c$  values were shown in Table 3, obtaining 61% for SC-101, 72% for SC-501, and 77% for pressureless-sintered SiC ceramics. The reason why SC-101 showed a small *K<sub>I</sub>/K<sub>IC</sub>* value as 61% is related to the high thermal conductivity of SC-101, which results in the relation that flexural strength does not change so rapidly with the increase of quenching temperature difference as in the case of two other SiC ceramics. As seen in Fig.1, all of the SiC ceramics tested in this study showed some allowance in the critical temperature difference  $\Delta T_c$ . Especially in the case of SC-101, it is difficult to determine the  $\Delta T_c$  value simply, because its flexural strength starts to decrease gradually with the increase of quenching temperature difference in the range of  $\Delta T_c$ , as seen in Fig.1. Then the temperature difference, at which flexural strength reached a remarkably decreased value, was adopted as 900°C for SC-101, 500°C for SC-501, and 400°C for pressureless-sintered SiC ceramics. *K<sub>I</sub>/K<sub>IC</sub>* ratios using these  $\Delta T_c$  values, were obtained 81, 80 and 87%, respectively. These resulted in similar values slightly larger than the previous values from 61 to 77%, but none reached 100%. The reasons for these results were not clarified, but if the fluctuations of respective values of  $\sigma_t$  and  $\Delta T_c$  in this measurement are taken into account and determination, these *K<sub>I</sub>/K<sub>IC</sub>* values calculated above are agreed fairly well with this estimation on the possibility of causing the thermal shock damage of SiC ceramics, which was predicted on the basis of fracture kinetics.

**4. Conclusion**

Three kinds of SiC ceramics samples having different characteristics were carried out thermal shock fracture resistance tests by the water quenching method. The results obtained are summarized in the following.

**Table 3.** Calculated *K<sub>I</sub>/K<sub>IC</sub>* for initiation of thermal shock fracture of the three kinds of SiC ceramics.

Material	Flexural Strength MPa	Tensile Strength MPa	Thermal Expansion x10 <sup>-6</sup> /K	Young's Modulus GPa	Poison's Ratio	$\Delta T_c$ K	<i>f</i> ( $\beta$ )	<i>K<sub>I</sub>/K<sub>IC</sub></i>
SC-101	470	329	4	460	0.16	680	7.43	0.61
SC-501	550	391	4	480	0.16	450	3.67	0.72
Sintered SiC	350	244	4	450	0.15	350	3.93	0.77

- 1)  $\Delta T_c$  was calculated as 680°C, 450°C and 350°C for the respective samples for SC-101, SC-501 and pressureless-sintered SiC ceramics.
- 2) Thermal shock fracture resistance parameter  $R'$ , which was calculated on the basis of the thermal conductivity value at 500°C, was determined as 22, 16 and 12kW/m for the respective samples of SC-101, SC-501 and pressureless-sintered SiC ceramics, and the sequential order of this value in size conformed to that of  $\Delta T_c$ .
- 3) The ratios of stress intensity factor  $K_I$  against critical stress intensity factor  $K_{IC}$  of the three kinds of SiC ceramics samples were in the range of about 60 and 80%.

#### References:

- 1) Y. Takeda, K. Nakamura, K. Maeda and M. Ura, *Adv. Ceram. Mater.*, 1, 162-165 (1986).
- 2) Y. Takeda, K. Nakamura, K. Maeda and Y. Matsushita, *J. Am. Ceram. Soc.*, 70, C266-267 (1987).
- 3) Y. Takeda, K. Nakamura, K. Maeda and Y. Matsushita, *Yogyo Kyokaiishi*, 95, 860-863 (1987).
- 4) Y. Takeda and K. Maeda, *Seramikkusu Ronbunshi*, 99, 715-717 (1991).
- 5) *Nikkei New Materials*, 91, 45 (1991).
- 6) Y. Takeda, K. Kosugi, S. Iijima and K. Nakamura, *Proc. 1st Int. Sympo. on Ceram. Components for Engine*, (1983) 529-537.
- 7) T. Nishida and E. Yasuda, *Seramikkusu-no-Rikigakuteki-Seishitsu, Nikkan-Kogyo-Shinbunsha* (1987) 221-240.
- 8) M. Midorikawa and T. Izeki, *YogyoKyokaiishi*, 94, 141-145, (1986).
- 9) A. Nakayama and H. Abe, *Zairyo*, 32, 685-688 (1983).
- 10) *Seramikkusu-no-Kikaiteki-Seishitsu*, ed. by Ceram. Soc. Jpn., (1979) 65.
- 11) M. Ashizuka, Y. Kimura, H. Fujii, K. Abe and Y. Kubota, *Yogyo-Kyokai-Shi*, 94, 577-582 (1986).
- 12) K. Satyamurthy, J.P. Singh, D.P.H. Hasselman and M.P. Kamat, *J. Am. Ceram. Soc.*, 63, 694-698 (1980).
- 13) R.W. Davidge, *Seramikkusu-no-Kyoko-to-Kakai* translated into Japanese by H. Suzuki and T. Izeki, published by Kyoritsu Shuppan-sha (1982) 144-150.

---

This article is a full translation of the article which appeared in *Nippon Seramikkusu Kyokai Gakujutsu Ronbunshi* (Japanese version), Vol.99, No.11, 1991.

# Bending Strength of SiC/Al<sub>2</sub>O<sub>3</sub> Composite Sheet obtained from Polycarbosilane/Alumina Powder/Binder Mixture

Kazuro Kawamura

Dept. of Materials Science and Engineering,  
The National Defense Academy  
1-10-20, Hashirimizu, Yokosuka-shi, 239 Japan

A SiC/Al<sub>2</sub>O<sub>3</sub> composite sheet was prepared from a green sheet composed of polycarbosilane (PCS) and Al<sub>2</sub>O<sub>3</sub> powder with the weight ratio of 2:1. The green sheet was fired in the temperature range of 1200° to 1400°C under N<sub>2</sub> gas atmosphere, and three point bending strength of the composite was examined. The strength in room temperature increased with firing temperature and showed the maximum value of 333MPa at 1300°C. Dispersion of Al<sub>2</sub>O<sub>3</sub> particles in the SiC matrix was effective to increase the strength of monolithic SiC sheet derived from PCS. When the composite was fired at 1400°C, however, the bending strength dropped rapidly in a similar manner as PCS-derived SiC fiber.

[Received April 17, 1991; Accepted July 18, 1991]

**Key-words:** Polycarbosilane, Silicon carbide, Silicon carbide/Alumina composite sheet

## 1. Introduction

There are many studies on the application of organic metal polymers as the ceramic precursor (precursor polymer). This is because this type of material has been regarded as more advantageous than powder materials in freedom of forming, sinterability and control of the composition. These advantages are also important in raising the efficiency of the manufacturing process.

Accordingly, we think that study in this field will be further enforced to include polymer design. However, problems exist in manufacturing ceramics by preparing and directly heat-transferring the precursor polymer. For instance, polycarbosilane (PCS), as the typical precursor polymer in producing SiC fibers, presents the following problems in heat-converting into SiC.

- 1) Contraction takes place in this substance as it reduces weight markedly in being made inorganic.
- 2) The firing temperature in which the strength becomes highest is 1200°C, and the strength deteriorates markedly at higher temperature.<sup>1)</sup>

Higher polymerization of PCS or making it cross-linked serves to improve the above phenomenon of 1). On the other hand, we can solve the demerit of 2) in some applications, although problems remain as this phenomenon is related with the progress of crystallization. For example, it is said that there is no deterioration in strength up to the temperature of 1300°C in fibre of Si-Ti-C-O system converted thermally from polytitanocarborosilane which is considered as

a partially transformed resin of PCS. This fibre shifts a little to higher temperature side in heat resistance than the SiC fibre converted from PCS.<sup>2)</sup> There is also a report<sup>3)</sup> that the bending strength was 57MPa at maximum in sintered body of PCS/ $\alpha$ -SiC powders fired at 1000° in 10wt% of PCS content. There is a recent report<sup>4)</sup> on polysilastylene as the SiC precursor. They obtained the strength of 275MPa with no deterioration in strength for their composite (mixed by wt%) with  $\beta$ -SiC fired at 1500° ~ 1700°C. These reports suggested to us that, if we use the organic silicone polymer as SiC precursor and want to get superior materials in high temperature strength, it would be better to mix with ceramic powders of the same or different system in sintering.

This study aimed at learning the structure and strength of the composite with heterogeneous ceramic powders, or the composite on the matrix of SiC converted from PCS/Al<sub>2</sub>O<sub>3</sub> powder.

## 2. Experimental Procedures

### 2.2. Specimens

We synthesized PCS from the starting substance of Dimethylchlorosilane in accordance with the literature.<sup>5,6)</sup> The obtained PCS was in foams with polymerization enough to swell (dissolve partially) in xylene. The Al<sub>2</sub>O<sub>3</sub> powders were the product (easily sinterable alumina) of Showa Denko K.K. The SiC/Al<sub>2</sub>O<sub>3</sub> composites were prepared in the following manner. Firstly we prepared a slurry of PCS/Al<sub>2</sub>O<sub>3</sub>/binder (we set the weight ratio of PCS/Al<sub>2</sub>O<sub>3</sub> as 2/1). Then we formed into sheet and fired into SiC/Al<sub>2</sub>O<sub>3</sub> composite sheet. We obtained the strength data by the bending test.

### 2.2. Heat-treatment and Measurement of Physical Properties

We sandwiched the specimen with a pair of alumina setters and fired in a tubular furnace at the temperature range of 1200°~1400°C in nitrogen gas atmosphere. The temperature was measured by platinum-platinum-rhodium thermocouple. The rising speed was 200°C/hr and the retention at the maximum temperature was 1hr.

The X-ray diffraction measurement was based on the powder method using CuK $\alpha$  for the ray. And the SEM observation was made on the fractured section coated with evaporated gold. Density was measured on a small specimen piece at 20°C in n-butanol using a Gay-Lussac picnometer. The bending test was carried out by the 3-point bending method, in 20mm of span at 0.5mm/min of cross

head speed. The size of the specimen was 6mm wide and 0.34–0.35mm thick.

### 3. Results and Observation

The white specimen before sintering turned to blackish gray by firing within the range of 1200°–1400°C. **Figure 1** shows the X-ray diffraction of the sintered sheet. The diffraction peaks marked with  $\mu$  correspond with  $\alpha\text{Al}_2\text{O}_3$ , and the broad and weak diffraction lines of arrow marks correspond with (111), (220), (211) of  $\beta\text{SiC}$  respectively from the lower angle. The diffraction lines of SiC are weaker in strength and broader than that of  $\text{Al}_2\text{O}_3$ . This diffraction pattern indicates that PCS converted SiC has a high degree of amorphism in the structure as well as small crystals.

The SEM photographs on the fractured section is shown in **Fig.2**. The structures in these pictures appeared the same for this range of firing temperature, and the effect of the firing temperature on the structure was not clear. We observed the peculiarity in structure that PCS converted SiC was formed uniformly in matrix and appeared to have surrounded the  $\text{Al}_2\text{O}_3$  grains.  $\text{Al}_2\text{O}_3$  in the matrix remained as grains, and the sintering did not seem to have progressed.

On the other hand, the change in density against the firing temperature was evident. The density increased linearly; from 2.49g/cm<sup>3</sup> to 2.62g/cm<sup>3</sup> to 2.72g/cm<sup>3</sup> at the firing tem-

peratures of 1200°, 1300° and 1400° respectively. This increase in density may have been caused by the progress in crystallization of the SiC components.

**Figure 3** shows the 3 point bending strength (average of 3 specimens). The maximum bending strength was 33MPa at 1300°C firing, and decreased above or below this firing temperature. The decrease in bending strength was particularly pronounced at a higher temperature. The deterioration in strength at 1400°C sintering was the phenomenon observed in the tensile strength of PCS converted SiC fiber.<sup>1)</sup> In other words, the bending strength of the SiC/ $\text{Al}_2\text{O}_3$  depends on the structural characteristics of SiC matrix. The small change from the strength behavior of SiC fiber was the fact that the bending strength became the maximum at 1300°C firing. The phenomenon to shift the temperature characteristics to the higher temperature side resembles the case of fibers of Si-Ti-C-O system converted from polytitanocarbosilane.

The weight reduction following the change from organic metal compounds to inorganic materials was large. In our samples, about 25% of weight reduction took place by turning to inorganic. Supposed that the remainder was all SiC, then the 2/1 mixing ratio of PCS/ $\text{Al}_2\text{O}_3$  corresponds with the SiC/ $\text{Al}_2\text{O}_3 \approx 3.8/1$  in the mol ratio after turning to inorganic. When we took higher mol ratio of  $\text{Al}_2\text{O}_3$  against PCS, we could not get the sintered body with measurable strength below the firing temperature of 1400°, for instance, in the ratio of PCS/ $\text{Al}_2\text{O}_3 = 1/1$ . We can predict this phenomenon

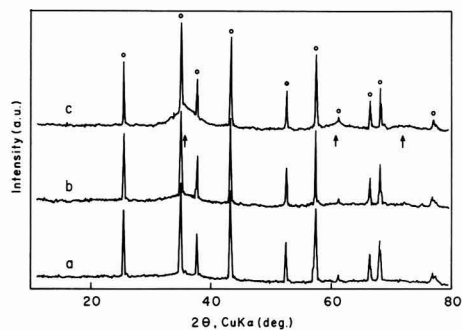


**Fig. 1.** X-ray diffraction profiles of SiC/ $\text{Al}_2\text{O}_3$  composite sheets obtained by firing of polycarbosilane (PCS) alumina powder/binder mixture. a:Firing temperature 1200°C, b:Firing temperature 1300°C, c:Firing temperature 1400°C.

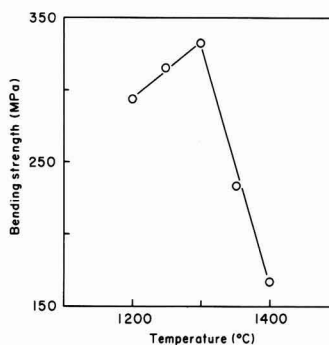


**Fig. 3.** Changes of bending strength with firing temperature for SiC/ $\text{Al}_2\text{O}_3$  composite sheet obtained from PCS/alumina powder/binder mixture.

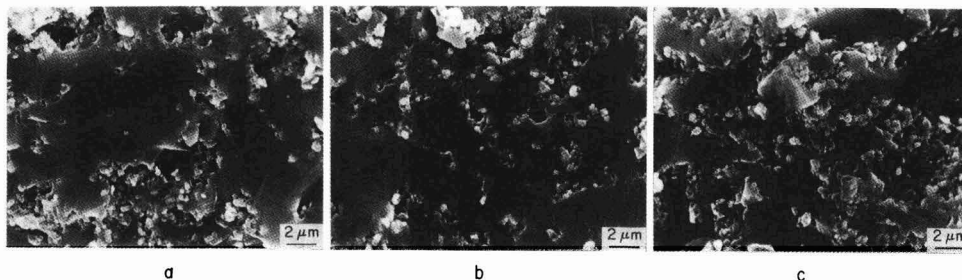


**Fig. 2.** SEM photographs of fracture surfaces of SiC/ $\text{Al}_2\text{O}_3$  composite sheets obtained by firing of PCS/alumina powder/binder mixture. a:Firing temperature 1200°C, b:Firing temperature 1300°C, c:Firing temperature 1400°C.

from the SEM photographs in Fig.2. This may be due to the fact that the continuity was lost in the SiC matrix structure, with more mixing ratio of  $Al_2O_3$ .

The writers et al. had tried to produce SiC sheet from PCS in the same manner before. In this case, the bending strength was  $281 \pm 6$  MPa at maximum at  $1260^\circ C$  sintering.<sup>7)</sup> The comparison of these two experiments points to the fact that the small addition of  $Al_2O_3$  powders to polycarbosilane served to increase the strength. As previously stated, the SEM photograph in Fig.2 indicates that the  $Al_2O_3$  grains remained as grains, and the sintering did not appear to have progressed. Accordingly, we cannot link the increase in strength upon the progress of sintering of  $Al_2O_3$ . However, we observed that the bonding between the SiC matrix and  $Al_2O_3$  is good. Therefore, we presume that the increase in strength was brought about by this good bonding effect. In this sense, the sintering in the system of PCS/SiC powder mixtures formulates the compounds of the same system. We can expect a marked effect of complex as the integration of the structure can easily occur at the boundary of these components. The sintering of  $Al_2O_3$  grain may progress at higher temperature, say  $1600^\circ C$  in this mixture. The crystallization, however, also progresses simultaneously in SiC matrix, causing the deterioration of strength. It appears, accordingly, that in applications like in our study where the PCS converted SiC in the matrix controls the strength, we cannot expect the increase in strength at the firing temperature, where the sintering of  $Al_2O_3$  progresses at higher temperature.

As the conclusion, it would be advisable to mix a small quantity of PCS as the binder, as stated at the beginning of

this paper, in an attempt to make a composite by combining PCS and ceramic powders. Moreover, it would be also advisable to consider the combination of the same compounds from the viewpoint of integration. This experiment, however, proved that a bonding effect can be expected in some applications by combining heterogeneous ceramics.

#### Acknowledgements

Special thanks to Messrs. J. Koga, T. Iwata and S. Yamanaka of Mitsubishi Materials K.K. for their assistance in the pursuit of this study.

#### References:

- 1) S. Yajima, Y. Hasegawa, J. Hayashi and M. Iimura, *J. Mater. Sci.*, 13, 2569-2576 (1978).
- 2) T. Yamamura, T. Ishikawa, M. Shibuya, T. Hisayuki and K. Okamura, *ibid.*, 23, 2589-2594 (1988).
- 3) S. Yajima, T. Shishido and K. Okamura, *Am. Ceram. Soc. Bull.*, 56, 1060-1063.
- 4) K. Niihara, M. Okumura, R. Takemoto, T. Yamamoto, J. Arima, K. Sugawara and T. Nishikawa, Preprint, *Ceram. Soc. Jpn. Ann. Mtg.* (1987) 249.
- 5) K. Okamura, Tanka Keiso Zairyo, C.M.C. (1985) 22.
- 6) K. Kawamura, S. Fujimoto, T. Iwata, S. Yamanaka, G. Maruyama and M. Ono, *Tanso*, 143, 115-120 (1990).
- 7) K. Kawamura et al., *ibid.*, to be published.

---

This article is a full translation of the article which appeared in *Nippon Seramikkusu Kyokai Gakujutsu Ronbunshi* (Japanese version), Vol.99, No.11, 1991.

# Preparation of SiC-Si<sub>3</sub>N<sub>4</sub> Composite Fine Powders from Chlorosilanes by R.F. Thermal Plasma

Masaaki Suzuki, Yoshinori Nakata and Takeshi Okutani

Government Industrial Development Laboratory, Hokkaido  
2-17-2-1, Tsukisamu-Higashi, Toyohira-ku, Sapporo-shi, 062 Japan

**Preparation of SiC-Si<sub>3</sub>N<sub>4</sub> composite fine powders from chlorosilanes, C<sub>2</sub>H<sub>4</sub> and NH<sub>3</sub> by R.F. thermal plasma was studied. SiC-Si<sub>3</sub>N<sub>4</sub> composite fine powders were prepared by injecting chlorosilanes (SiCl<sub>4</sub>, SiHCl<sub>3</sub>, SiH<sub>2</sub>Cl<sub>2</sub>), C<sub>2</sub>H<sub>4</sub> and NH<sub>3</sub> to the tail flame of R.F. plasma. When the powder was prepared from SiH<sub>2</sub>Cl<sub>2</sub>, C<sub>2</sub>H<sub>4</sub> and NH<sub>3</sub>, the powder composition depended on the C<sub>2</sub>H<sub>4</sub> and NH<sub>3</sub> flow rate. When C<sub>2</sub>H<sub>4</sub> flow rate was low, the powder contained SiC, Si, Si<sub>3</sub>N<sub>4</sub> and amorphous phases. As the C<sub>2</sub>H<sub>4</sub> flow rate increased, crystalline SiC, C and amorphous phases were present. The surface area of the powder was from 46.6 to 100m<sup>2</sup>/g and the particle size was from 0.02 to 0.2μm. TEM and SAED observation showed that these composite powders contained Si, SiC, Si<sub>3</sub>N<sub>4</sub>, C and amorphous particles. Si2p XPS spectra of the powder were separated into SiC, Si<sub>3</sub>N<sub>4</sub>, SiO<sub>2</sub> components. These composite powders were considered to be a mixture of SiC, Si<sub>3</sub>N<sub>4</sub>, C and amorphous particles. After heat treatment at 1773K for 1hr in Ar, amorphous phase disappeared and the crystalline phases in the powder were SiC and Si<sub>3</sub>N<sub>4</sub>.**

[Received June 10, 1991; Accepted August 22, 1991]

**Key-words:** R.F. Plasma, Composite fine powder, Chlorosilanes, C<sub>2</sub>H<sub>4</sub>, NH<sub>3</sub>, SiC, Si<sub>3</sub>N<sub>4</sub>, XPS

## 1. Introduction

Many studies have been conducted extensively in recent years on composite ceramics, with special attention on nanocomposite materials which combine fine ceramic particles.<sup>1)</sup> It is generally considered that the manufacture of composite ceramics with excellent features needs the preparation of composite fine powders, in which particle sizes, composition, crystal structure and the like are controlled from the stage of materials. SiC-Si<sub>3</sub>N<sub>4</sub> composite fine powders have so far been prepared by Electric Furnace Method,<sup>2)</sup> Laser Method,<sup>3,4)</sup> D.C. Plasma Method,<sup>5)</sup> Hybrid Plasma Method.<sup>6)</sup> We examined the conditions to prepare SiC-Si<sub>3</sub>N<sub>4</sub> composite fine powders by the R.F. Plasma and the characteristics of the prepared composite fine powders.

## 2. Experiment

We illustrate the schematic view of r.f. plasma torch in Fig.1. SiC-Si<sub>3</sub>N<sub>4</sub> composite fine powders were prepared by injecting chlorosilanes (SiCl<sub>4</sub>, SiHCl<sub>3</sub>, SiH<sub>2</sub>Cl<sub>2</sub>), NH<sub>3</sub> and C<sub>2</sub>H<sub>4</sub> into the tail flame of the plasma. Chlorosilane and

NH<sub>3</sub> react at ambient temperature to produce solid imide. Therefore, we introduced double walled nozzle to mix these reactant gases immediately before the plasma for the necessary reaction.

SiCl<sub>4</sub> and SiHCl<sub>3</sub> are liquid at ambient temperature and have high vapor pressure, so we used Ar gas as the carrier gas to the torch. The torch was a quartz tube of 45mm O.D. with triple walls. Plasma was manipulated by injecting Ar gas revolving to the tangent direction at both outer and inner tubes to stabilize the plasma. The flow rates of Ar gas were 8l/min for the outer tube, 5l/min for the inner tube, and 0.3l/min for the center tube. The output of the r.f. was 4MHz, 1.9kV. The location to inject reactant gas was at the distance L=5mm directly under the work coil. The temperature of the plasma was estimated to be in the range of 2100~2400K at L=5mm, by inserting a high melting point metal wire inside the plasma. Powders were collected from the collection bottle and electric precipitator, which were connected to the silica tube. Considerable volume of generated powders, however, adhered to the wall of the quartz tube. We collected these powders adhered to the quartz wall as samples. Powders contained NH<sub>4</sub>Cl as by-products. Since NH<sub>4</sub>Cl is sublimed at 610K, we removed NH<sub>4</sub>Cl by the heat treatment for 1hr at 623K in the Ar flow.

We obtained the specific surface area by the 1-point BET method, and carbon content of the powder by coulometry, and nitrogen and oxygen content by nitrogen and oxygen analyzer for ceramics (EMGA-650, Horiba). We examined the crystal structure by X-ray diffraction (XRD), as well as the shape and crystal structure of the particle by a transmission electron microscope (TEM) and a selected area electron

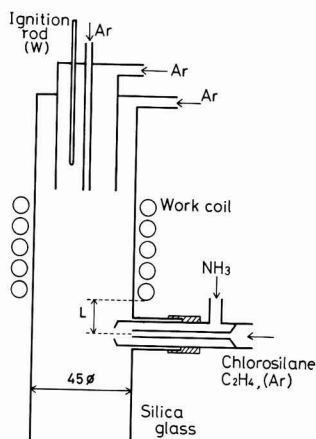


Fig. 1. Schematic view of R.F. plasma torch.

diffraction (SAED). We also examined the chemical state of the elements by X-ray photoelectron spectroscopy (XPS). We further examined the effect of heat-treatment on some samples.

### 3. Results and Observations

**Table 1** lists the composition, surface area and crystalline phase of the powders. Amorphous peak in the range of 20–25° (Cu, K $\alpha$ ) appeared in all samples by XRD. We observed crystalline SiC, Si, Si<sub>3</sub>N<sub>4</sub> besides amorphous phase when the C<sub>2</sub>H<sub>4</sub> flow rate was low. When the C<sub>2</sub>H<sub>4</sub> flow rate increased, the crystalline phase became SiC only. The same tendency was observed in the case of SiCl<sub>4</sub>, SiHCl<sub>3</sub>, and SiH<sub>2</sub>Cl<sub>2</sub>.

The composition of particles changed with the reactant gas flow rate. The total C content of the powders increased as the C<sub>2</sub>H<sub>4</sub> flow rate increased. And these powders also contained oxygen of 6–15wt%. One of the causes may be attributed to the oxidation of the powder surface, as the powders were handled in the air. We noticed the tendency of smaller oxygen content in the powders prepared from SiH<sub>2</sub>Cl<sub>2</sub> compared with those from SiHCl<sub>3</sub>, SiCl<sub>4</sub>. This tendency was pronounced in the formation of Si<sub>3</sub>N<sub>4</sub>. Si<sub>3</sub>N<sub>4</sub> powder prepared from SiH<sub>2</sub>Cl<sub>2</sub>-NH<sub>3</sub> contained about 10wt% of oxygen, while those from SiHCl<sub>3</sub>, SiCl<sub>4</sub>-NH<sub>3</sub> contained about 20wt%. We presumed that Si<sub>3</sub>N<sub>4</sub> powders prepared from SiHCl<sub>3</sub>, SiCl<sub>4</sub> were more easily oxidized in the air, as the reaction had not been completed up to inorganic Si<sub>3</sub>N<sub>4</sub> leaving the bond of N-H, Si-H, Si-Cl.

The powders prepared from SiH<sub>2</sub>Cl<sub>2</sub> contained less

oxygen as impurity and showed higher yield among the chlorosilanes. Therefore, we examined the SiH<sub>2</sub>Cl<sub>2</sub>-C<sub>2</sub>H<sub>4</sub>-NH<sub>3</sub> system in detail. **Table 2** indicates the flow rate of the gas, and the composition, surface area, and crystalline phase of powders. The crystalline phase showed the same tendency as in Table 1. When the NH<sub>3</sub> flow rate was 250SCCM, the C content of the powders increased slightly, even if we increased the flow rate of C<sub>2</sub>H<sub>4</sub>. The C content of the powders was 6.8wt% when the C<sub>2</sub>H<sub>4</sub> flow rate was 40SCCM. We could increase the C content of the powder when we injected NH<sub>3</sub> of 100SCCM diluted by Ar of 150SCCM.

**Figure 2** shows the change of the total C and N content of the powder with C<sub>2</sub>H<sub>4</sub> and NH<sub>3</sub> flow rate. Total C content increased as the C<sub>2</sub>H<sub>4</sub> flow rate increased, with more increase in lesser NH<sub>3</sub> flow rate. On the other hand, total N content did not depend on the flow rate of C<sub>2</sub>H<sub>4</sub>, but solely on the flow rate of NH<sub>3</sub>, and increased with the NH<sub>3</sub> flow rate. Figure 2 shows that we can control the composition of the powder by changing the flow rate of reactant gas.

**Figure 3** shows the TEM photographs of the fine powders prepared with various flow rates of C<sub>2</sub>H<sub>4</sub>, NH<sub>3</sub> and with constant flow rate of SiH<sub>2</sub>Cl<sub>2</sub>. These TEM photographs indicate that these powders consisted of particles of

**Table 1.** Reactant gas flow rate and composition, surface area, crystalline phase of the powder prepared from chlorosilanes.

Sample No.	Chlorosilane	Reactant Gas		Composition		Surface Area (m <sup>2</sup> /g)	Crystalline Phase		
		C <sub>2</sub> H <sub>4</sub> (SCCM)	NH <sub>3</sub> (SCCM)	C (wt%)	N (wt%)				
1	SiH <sub>2</sub> Cl <sub>2</sub>	10SCCM*	10	250	2.1	7.9	27.7	100.0	SiC, Si, Si <sub>3</sub> N <sub>4</sub> , Amo.
2	SiH <sub>2</sub> Cl <sub>2</sub>	10SCCM	20	250	4.0	6.8	29.9	76.3	SiC, Amo.**
3	SiH <sub>2</sub> Cl <sub>2</sub>	10SCCM	30	250	5.0	6.7	28.9	85.2	SiC, Amo.
4	SiHCl <sub>3</sub>	40mg/min	30	250	5.4	11.4	28.5	120.8	SiC, Amo.
5	SiHCl <sub>3</sub>	40mg/min	20	100	7.1	8.8	28.4	82.1	SiC, Amo.
6	SiHCl <sub>3</sub>	40mg/min	30	100	12.8	7.7	26.7	92.7	SiC, Amo.
7	SiCl <sub>4</sub>	40mg/min	8	100	3.7	14.4	25.3	61.8	SiC, Si, Si <sub>3</sub> N <sub>4</sub> , Amo.
8	SiCl <sub>4</sub>	40mg/min	20	100	14.1	9.1	23.2	95.0	SiC, Amo.
9	SiCl <sub>4</sub>	40mg/min	25	100	28.1	10.5	18.7	106.1	C, SiC, Amo.

\*SiH<sub>2</sub>Cl<sub>2</sub>=10SCCM+45mg/min, \*\*Amo.=Amorphous

**Table 2.** Reactant gas flow rate and composition, surface area, crystalline phase of the powder prepared from SiH<sub>2</sub>Cl<sub>2</sub>.

Sample No.	Reactant Gas			Composition		Surface Area (m <sup>2</sup> /g)	Crystalline Phase	
	SiH <sub>2</sub> Cl <sub>2</sub> (SCCM)	C <sub>2</sub> H <sub>4</sub> (SCCM)	NH <sub>3</sub> (SCCM)	C (wt%)	N (wt%)			
1	10	10	250	2.1	7.9	27.7	100.0	SiC, Si, Si <sub>3</sub> N <sub>4</sub> , Amo.
2	10	20	250	4.0	6.8	29.9	76.3	SiC, Amo.
3	10	30	250	5.0	6.7	28.9	85.2	SiC, Amo.
10	10	40	250	6.8	8.6	29.5	84.8	SiC, C, Amo.
11	10	5	*100	6.0	20.8	10.3	46.6	Si, Si <sub>3</sub> N <sub>4</sub> , SiC, Amo.
12	10	10	*100	8.7	10.4	20.7	56.4	SiC, Si <sub>3</sub> N <sub>4</sub> , Si, Amo.
13	10	15	*100	13.5	12.4	17.0	69.5	SiC, Si, Amo.
14	10	20	*100	15.5	10.3	18.9	80.0	SiC, Amo.

(\* 150SCCM Ar was added to 100SCCM NH<sub>3</sub>)

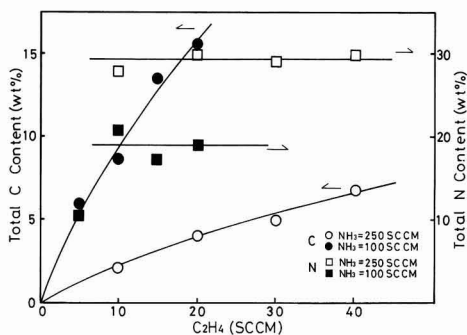


**Fig. 2.** Effect of reactant gas flow rate on total C and N content of the powder.

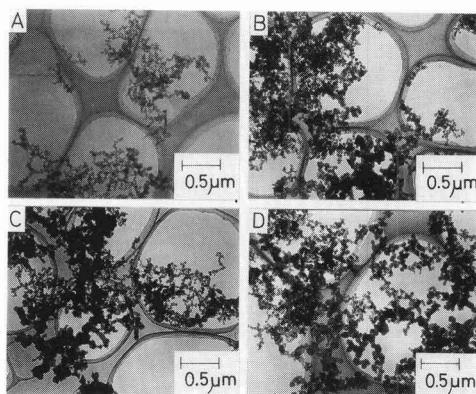


**Fig. 3.** TEM photographs of the powder.

(A) Sample No.1, C<sub>2</sub>H<sub>4</sub>=10, NH<sub>3</sub>=250SCCM, (B) Sample No.10, C<sub>2</sub>H<sub>4</sub>=40, NH<sub>3</sub>=250SCCM, (C) Sample No.12, C<sub>2</sub>H<sub>4</sub>=10, NH<sub>3</sub>=100SCCM, (D) Sample No.13, C<sub>2</sub>H<sub>4</sub>=15, NH<sub>3</sub>=100SCCM

0.02–0.2μm in sizes. In the case of low flow ratio of C<sub>2</sub>H<sub>4</sub>(A), the particles were smaller in size and spherical in shape, and many of them were rather uniform. As the flow ratio of C<sub>2</sub>H<sub>4</sub> increased, large particles (around 0.2μm) with various kind of peculiar shape, appeared. We carried out the SAED observation to find out what these particles were.

Figures 4 and 5 show the TEM photographs and SAED patterns on some peculiar shaped particles. The SAED patterns showed that smaller and spherical particles (a) of about 0.02μm were amorphous. Spherical particles (b) of about 0.1μm consisted of mainly Si, and a small quantity of cubic SiC. Angular particles (c) of 0.1–0.2μm were cubic SiC. Particles (d) of 0.1–0.15μm which were almost spherical but somewhere hexagonal were carbon. Although the composition of amorphous particles were not clear we could not find the mixing of Si, C, and N atoms in one particle by the SAED observation.

We also carried out the XPS measurement on some samples for the chemical state of elements in the powders. The XPS measurement can discriminate between the bond status of SiC, Si<sub>3</sub>N<sub>4</sub>, SiO<sub>2</sub> and others from their chemical shift. Figures 6 and 7 show the typical XPS spectra and the peak separation of Si2p and Cls. Si2p was the broad peak, and could be separated into 3 components of SiC, Si<sub>3</sub>N<sub>4</sub>, and SiO<sub>2</sub>. The area intensity ratio of these com-

ponents varied according to the composition of the powders. Cls was likewise able to be separated into SiC, graphite, and hydrocarbon, and the area intensity ratio of these components also varied according to the composition of the powders. N1s had rather wider half value width, but its peak position showed Si<sub>3</sub>N<sub>4</sub> and did not change with the composition of the powders.

These results implied that the powders obtained in this study were mixtures of SiC, Si<sub>3</sub>N<sub>4</sub>, Si, C, and amorphous particles. However, the composition and chemical state of the amorphous particles were not clear, and need further examination. Table 3 indicates the change of the powders by the heat-treatment at 1773K for 1hr in Ar. The heat treatment reduced their surface area, and the TEM observation revealed the increase in the particle sizes. The atoms heat treatment hardly changed the N content, but reduced the O content. Reduction in C content was observed in the samples, in which the XRD showed isolated C, although no change in the C content was seen in other samples. The amorphous phase was disappeared by the heat treatment and became crystalline SiC and Si<sub>3</sub>N<sub>4</sub>.

We believe that these powders can be used starting materials for composite ceramics containing both SiC and Si<sub>3</sub>N<sub>4</sub>.

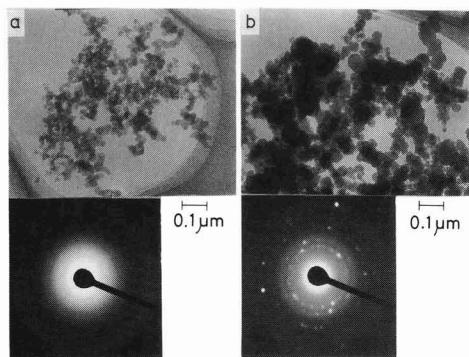


Fig. 4. TEM photographs and SAED patterns of various type of the particles found in the composite powder. (a) amorphous and (b) Si and small amount of SiC.

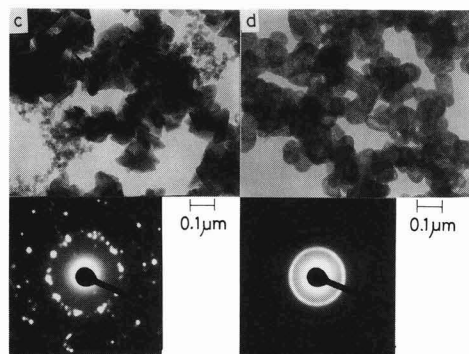


Fig. 5. TEM photographs and SAED patterns of various type of the particles found in the composite powder. (c) cubic SiC and (d) C.

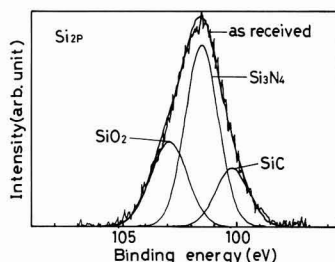


Fig. 6. Si<sub>2</sub>p XPS spectrum of sample No.3 and the result of peak separation.

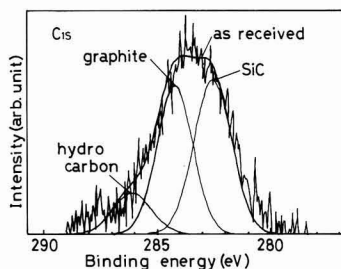


Fig. 7. Cl<sub>1</sub>s XPS spectrum of sample No.3 and the result of peak separation.

Table 3. The change of the powder properties by heat treatment.

Sample No.	Composition (wt%)	C	N	O	Surface Area (m <sup>2</sup> /g)	Crystalline Phase
10 (as received)	6.8 29.5 8.6				84.8	SiC, C, Amo.
(1773K, 1hr, Ar)	3.6 29.0 2.2				5.0	Si <sub>3</sub> N <sub>4</sub> , SiC
12 (as received)	8.7 20.7 10.4				56.4	SiC, Si <sub>3</sub> N <sub>4</sub> , Si, Amo.
(1773K, 1hr, Ar)	9.0 21.7 2.6				8.7	SiC, Si <sub>3</sub> N <sub>4</sub>

\*Amo=Amorphous

**References:**

- 1) K. Niihara, T. Hirano, A. Nakahira, K. Suganuma, H. Izaki and T. Kawakami, *Funtai oyobi Funmatsu Yakin*, 36, 169-172 (1989).
- 2) J. Hojo, H. Maeda and A. Kato, *Yogyo Kyokaiishi*, 95, 45-49 (1987).
- 3) G.W. Rice, *J. Am. Ceram. Soc.*, 69, C183-185 (1986).
- 4) M. Suzuki, Y. Nakata, M. Yamaguchi and T. Okutani, preprint, *Ann. Mtg., Ceram. Soc. Jpn.* (1990) 606.
- 5) J. Hojo, M. Nakamine and A. Kato, *Ceramic Transactions* 1, 277-284 (1988).
- 6) H.J. Lee, K. Eguchi and T. Yoshida, *J. Am. Ceramic Soc.*, 73 3356-3362 (1990).

---

This article is a full translation of the article which appeared in *Nippon Seramikkusu Kyokai Gakujutsu Ronbunshi* (Japanese version), Vol.99, No.11, 1991.

# Micro Mechanical Processing for Ordered Structure

Zenji Kato and Keizo Uematsu

Department of Material Science and Technology, Nagaoka University of Technology  
1603-1, Kamitomioka, Nagaoka-shi, 940-21 Japan

**A novel method for controlling the microstructure of a ceramic green body has been proposed. In this method, spherical granules with uniform size were placed mechanically in a regular array on a mesh, and then moved to a substrate (Micro mechanical processing). To demonstrate the potential of this method, alumina granules with size range 77-85 $\mu\text{m}$  were used as a model, and a hexagonal close packed structure was made. Uniaxial pressing of this array can create a uniform and orderly structured green body (Ordered structure).**  
[Received June 25, 1991; Accepted August 22, 1991]

**Key-words:** Regular array, Granule, Microstructure, Green body, Opticalmicroscope, Mesh.

## 1. Introduction

Defects present in ceramic structures greatly determine their characteristics. For the production of highly functional ceramics, the first thing is to remove the defects in the sintered structures as much as possible. The authors have been developing ceramic processing, in particular press forming, to assess the defects in granules and formed bodies,<sup>1)</sup> and to accurately measure density of granules.<sup>2)</sup> In this study, we have proposed a new method for controlling structures of green bodies, developed based on the knowledge acquired so far.

The proposed processing involves trays to produce the structure, uniformly configured to the order of several tens of microns, by mechanically arranging granules. Such an approach is named "micro mechanical processing," after its ability to control structures microscopically mechanically. It corresponds to the conventional physicochemical method to arrange monodisperse particles regularly,<sup>3)</sup> but is applicable, in principle, to production of larger-size green bodies. Moreover, the defects present in the green body prepared by the new method tend to be smaller in size. For example, the defect structures present in the green body consisting of uniformly sized and orderly arranged particles of several tens of microns (ordered structure) should be, in principle, several microns in size at the largest.

The newly developed method is also applicable to the production of composite material in which the particles are regularly arranged to the order of several dozen microns. Regularity of the particles depends largely on accuracy of particle arrangement and time required for the arrangement. Development of accurate and efficient method to arrange particles, therefore, is essential for the production of the desired structures. This article discusses the method for two-dimensionally arranging closely packed particles.

In this study, granules were placed on a mesh of adequate pattern to furnish the close-packed arrangement, fixed on

the mesh, and then uniaxially formed, to form the green body.

## 2. Experimental Procedure

Alumina particles were used in this study; they were dried and granulated by a spray drier, and then passed through 77 $\mu\text{m}$ - and 85  $\mu\text{m}$ -size sieves. A copper mesh with fine pores was used to arrange the granules regularly, where the pores, hexagonal in shape and 46 $\mu\text{m}$  in inscribed circle diameter, were arranged in a hexagonal close-packed pattern with a pitch of 83  $\mu\text{m}$ . **Figure 1** illustrates the method for arraying the granules; near close-pack condition will be realized by placing the granules one by one on the hexagonal arranged mesh pores.

**Figure 2** illustrates the test apparatus, which consists of a stereoscopic microscope (Nikon, SMZ-2B) in the upper

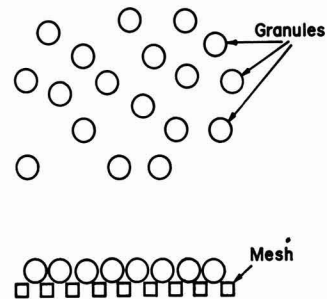


Fig. 1. Principle of granule array by a mesh.

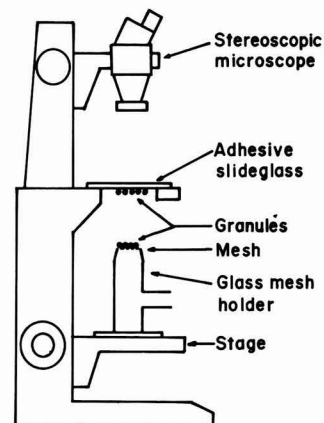


Fig. 2. Schematic diagram for apparatus to array granules.

portion and metallic stage on which the sample was placed in the lower portion. The granule-arraying mesh is fixed on the glass tube, kept vacuum inside, to induce air through the mesh pores. The sieved granules are placed on the pores carefully by the aid of the microscope, confirm that each granule is placed on each pore, before the vacuum is stopped. The granule-carrying mesh is then moved upwards slowly onto the slide glass plate coated with an adhesive uniformly to a thickness of approximately 40  $\mu\text{m}$ , while carefully observing the adhesive surface, to fix the granules. The granule assembly was formed uniaxially by a superhard die (inner diameter: 1cm) with mirror-polished. The structure was characterized by means of a scanning electron microscope (JOEL, STM-T100).

### 3. Results

Figure 3 shows an SEM micrograph of the granules. They are arrayed highly regularly in a regular hexahedron. Some of the particles around the center have seemingly obscure contours, probably due to insufficient deposition of gold and carbon, but actually they are as densely arrayed as those around them and contact each other closely, as revealed by stereoscopic microscope analysis. Some of the granules shown in the micrograph are non-spherical, because of insufficient sieving, which, however, will be solved in the future by improving the apparatus.

Figure 4 gives the SEM micrograph showing the granules formed uniaxially. They are pressed uniformly as a whole, approaching the hexahedral, corresponding to the close-pack structure. It is also observed that individual granules are not deformed uniformly, but ununiformly in such a way that peripheries are partly split. Those depressed at their centers are hollow granules deformed under pressure.

### 4. Discussion

Ulrich discusses processing to produce regular and fine structures for highly functional ceramic materials, viewed from chemistry,<sup>4)</sup> but the authors' attempt is the first dealing with relatively large structures.

The structures prepared in this study are characterized by a close-pack array with little space between the granules, as shown in Fig.4. The product prepared by the conventional forming process under elevated pressure suffers locally unstable packing conditions for granules before pressurization, with the result that the formed body is ununiform in density, having large pores locally. The method used in this study produces microscopically uniform body consisting of regularly arrayed granules, with only small defects believed to be formed at the interfaces.

High-strength materials should have as few defects as possible. It is however very difficult even for the method developed in this study to produce completely defect-free structures, as is the case with the conventional ceramic processing method, such as slip casting, injection molding and powder compression. Nevertheless, however, the newly developed method should produce ceramic structures with improved reliability, because the defects, even if

present, are well-controlled.

The method has the following advantages over the conventional method, and is expected to provide one conceptual model producing new ceramic materials:

- 1) Differently packed structures may be produced by changing the mesh pattern.
- 2) The composite structures may be controlled precisely by changing combination of meshes with different patterns.
- 3) A bulk material with regular structures may be produced by lamination.

For example, a 1cm thick formed body may be prepared by stacking roughly 100 layers when granules of 100  $\mu\text{m}$  or so in diameter are used.

It is necessary to solve two major problems before the proposed method is commercialized. First of all, more advanced control-related techniques are required than those used for the conventional processing method. The latest semiconductor-producing techniques can be used to align the granules with mesh pores and to produce the mesh pattern. The granule-arraying mesh can be easily produced by advanced etching techniques. It is easy to move the mesh to an accuracy of 1  $\mu\text{m}$  by means of an adequate device.

Second, it is necessary to produce dense granules of

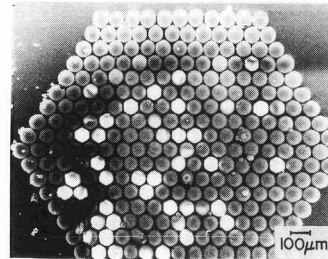


Fig. 3. SEM micrograph of regular arrayed granules.

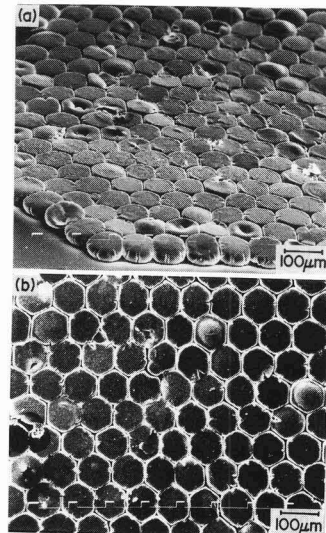


Fig. 4. (a), (b) SEM micrograph of uni-axially pressed structure of regular arrayed granules.

uniform size. It is believed that this problem can be also solved easily by advanced powder-producing techniques, such as those for microencapsulation.<sup>5)</sup>

**References:**

- 1) a. K. Uematsu, *J. Micromeritics Soc. Jpn.*, 28, 251-256 (1991)  
b. K. Uematsu, *FC Report*, 9, 187-193 (1991).
- 2) Z. Kato, J.Y. Kim, K. Saito and K. Uematsu, *Am. Ceram. Soc. Bull.*, 70, 129-131 (1991).
- 3) E.A. Barringer and H.K. Bowen, *Comm. Am. Ceram. Soc.*, 65, C199-201 (1982).
- 4) D.R. Ulrich, *Ultrastructure Processing of Ceramic, Glass and Composites*, ed. by L.L. Hench and D.R. Ulrich, Wiley Interscience, New York (1984) 6-11.
- 5) *Design of Microparticles*, ed. by M. Koishi, Kogyo Chosa-kai, (1987) 73-125.

---

This article is a full translation of the article which appeared in *Nippon Seramikkusu Kyokai Gakujutsu Ronbunshi* (Japanese version), Vol.99, No.11, 1991.

# Wetting Properties of W by Molten $\text{SiO}_2\text{-MgO-Al}_2\text{O}_3$ Ternary Eutectic Composition

Gyozou Toda, Shousaku Ishihara\* and Tsuyoshi Fujita\*

Central Research laboratory, Hitachi, Ltd.

Higashi Koigakubo, 1-280, Kokubunji-shi, Tokyo, 185 Japan

\*Production Engineering Research laboratory, Hitachi, Ltd.

292, Yoshida-cho, Totsuka-ku, Yokohama-shi, 244 Japan

The contact angle  $\theta$  of the melt with  $\text{SiO}_2\text{-MgO-Al}_2\text{O}_3$  ternary eutectic composition on W substrates and the penetrating behavior of the melt into W powder compacts were studied in the temperature range from 1350°C to 1650°C in  $\text{N}_2/\text{H}_2$  atmosphere.  $\theta$  decreased with increasing temperature and  $\theta$  in a wet  $\text{H}_2$  atmosphere was about 20° smaller than that in the dry  $\text{H}_2$  atmosphere. No time dependence of  $\theta$  nor reaction between the melt and W was observed at 1600°C. The shrinkage of W compacts after the penetration of the melt was observed when  $\theta$  was below 40°.

[Received June 25, 1991; Accepted August 22, 1991]

**Key-words:** Contact angle, Wetting,  $\text{SiO}_2\text{-MgO-Al}_2\text{O}_3$ , Tungsten, Penetration, Shrinkage.

## 1. Introduction

In the liquid-phase process to sinter or join ceramic or metallic materials, wettability of the solid surfaces with the liquid formed during the process greatly determines sintering characteristics and bonding strength.<sup>1,2)</sup> It is known that, in the production of the W/alumina circuit wiring substrate, the sintering aid for alumina is molten during the firing process and the liquid-phase penetrates into the thick film of the W conductor to bond alumina fast to the conductor.<sup>3,4)</sup>

Several researchers have discussed sintering of W/alumina circuit wiring substrates for strength of metallized tungsten and dependence of metallized structures on firing temperature.<sup>5-7)</sup> Bonding of Mo (or Mo-Mn), sharing common physical and chemical properties with W, to alumina has been studied for a long time,<sup>8-12)</sup> but mainly from the practical angles of their interactions, penetration of molten sintering aids into the space between the Mo particles, and metallized strength.

In this study, wettability of the W conductor with molten sintering aid was studied, in an attempt to collect the basic data for sintering of alumina-base circuit substrates. Production of this type of substrate normally depends on the eutectic composition of 3 to 4 elements, such as  $\text{SiO}_2\text{-MgO-Al}_2\text{O}_3$  and CaO, as the sintering aid;<sup>4,5)</sup> the  $\text{SiO}_2\text{-MgO-Al}_2\text{O}_3$  type aid (melting point: around 1350°C) was used in this study to investigate its wettability with the W plate and its penetration into the W compact.

## 2. Sample Preparation and Experimental Procedure

### 2.1. Sample Preparation

Assessment of wettability was done by measuring the contact angle, using the Sessile drop method, where the substrate was of 99.9% purity tungsten (approximately 20×20mm in area, 0.2mm thick), ground with 3  $\mu\text{m}$  diamond paste, decreased and then thermally treated at 1650°C for 30min in a hydrogen atmosphere.

The starting materials for the liquid droplets were powdered talc ( $3\text{MgO}\cdot 4\text{SiO}_2\cdot \text{H}_2\text{O}$ ) and clay ( $\text{Al}_2\text{O}_3\cdot 2\text{SiO}_2\cdot 2\text{H}_2\text{O}$ ),<sup>4)</sup> which were mixed in a ratio to give the 3-element eutectic composition (61.8wt% $\text{SiO}_2$ , 20.9wt%MgO and 17.3wt% $\text{Al}_2\text{O}_3$ , melting point: approximately 1350°C<sup>14)</sup>, ball-milled thoroughly in the presence of an adequate medium, dried, and formed into a shape 10mm in diameter and 8mm long under a pressure of approximately 25kg/cm<sup>2</sup>. This compact was heated at 1200°C for 1hr in air, and then cut into cube of 5×5×5mm (approximately 0.5g), to form the sample for the liquid droplets. For the experiments of penetrating the molten sintering aid into the W compact body, powdered tungsten (purity: 99.99%, average particle size: 1 $\mu\text{m}$ ) was formed into a shape 5mm in diameter and 5mm long, under the conditions to give a relative density of around 25% (which roughly corresponds to density of the vehicle-free paste for printing the wire substrate with a thick W film), to prepare the W compact. The same calcined sintering aid as used for measuring contact angle was molten for the penetration tests.

### 2.2. Experimental Procedure

One measure of wettability is contact angle,<sup>13)</sup> i.e., angle between the surface of a liquid droplet and the surface of a solid (including liquid) at the line of contact. **Figure 1** illustrates the apparatus used in this study to measure con-

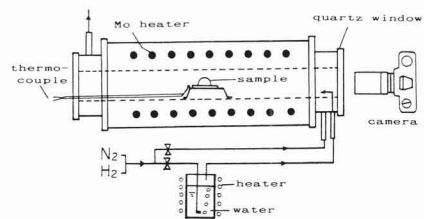


Fig. 1. Schematic diagram of apparatus for wetting measurement.

tact angle, consisting of the heating elements of molybdenum and combustion tube, where the measurement was done in a mixed atmosphere of  $N_2/H_2/H_2O$ . Temperature was measured by the W-5%Re:W-26%Re thermocouple unit. A droplet carried by tungsten plate was set in an electrical oven, and was observed by a camera set at one side of the peeping window for the changes with temperature increased at  $3^\circ C/min$ . The camera was equipped with a close-up bellows and a telephoto lens (400mm).

The film was enlarged 30 to 50 times by a coordinate analyzer, and the droplet silhouette was transferred to a semi-transparent paper, to read contact angle by a scaled protractor. Only the contact angles of those droplets spreading in almost complete circles were recorded.

The measured sample was then ground for its cross-section, to be analyzed by a scanning electron microscope (SEM) and by an energy-dispersion type X-ray diffractometer (EDX) for the elementary analysis.

For the test of penetrating the molten sintering aid into the W compact, the compact placed on the calcined aid was heated at  $3^\circ C/min$  in the apparatus shown in Fig.1, to observe the molten aid penetrating into the compact and changes in the compact shape in the radial direction.

### 3. Results and Discussion

#### 3.1. Effects of Temperature and Atmosphere on Contact Angle

Figure 2 shows the droplet sample on the tungsten plate, before and after melting at high temperature. It had an apparent melting point sufficiently close to that of the three-element eutectic composition of  $SiO_2-MgO-Al_2O_3$  (around



Fig. 2. Sessile drop profiles of  $SiO_2-MgO-Al_2O_3$  liquid on W.

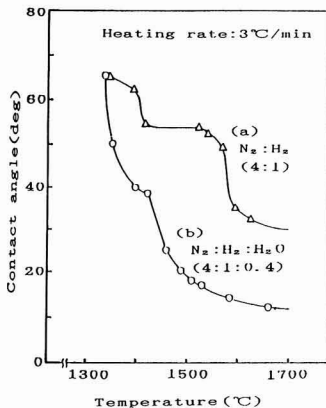


Fig. 3. Temperature dependence of the contact angle for  $SiO_2-MgO-Al_2O_3$  liquid on W. (a) dry  $H_2$  and (b) wet  $H_2$ .

$1350^\circ C^{14}$ ), in spite of the compounded powder, by which was meant that the droplet was of almost uniform composition. The cooled sample was completely transparent, with no precipitates, and was amorphous as revealed by the X-ray diffraction analysis.

Figure 3 shows contact angle changing with temperature, increased at  $3^\circ C/min$ , where (a) represents the data for the dry atmosphere of  $N_2/H_2$  ( $= 4/1$ , dew point:  $-50^\circ C$ ) and (b) the data for the wet atmosphere of  $N_2/H_2/H_2O$  (4/1/0.4). Contact angle  $\theta$  decreases as temperature increases in the presence of water, whereas it is almost constant at between  $1400$  and  $1500^\circ C$  in the dry atmosphere, about  $20^\circ$  higher than that observed in the presence of water at  $1600^\circ C$  or more.

Contact angle is generally determined by the balances between the interfacial tensions at the solid/gas, liquid/gas and solid/liquid interfaces, designated as  $\gamma_s$ ,  $\gamma_l$  and  $\gamma_{sl}$ , respectively:<sup>15)</sup>

$$\gamma_s = \gamma_{sl} + \gamma_l \cos\theta$$

The  $\theta$  value varying with atmosphere will result from changed balances between the interfacial tensions. Both droplet samples had the same composition, and the interactions between the starting particles constituting the samples were the same. It is therefore considered that  $H_2O$  adsorbed on the tungsten surfaces affects  $\gamma_s$  and  $\gamma_{sl}$ , assuming that  $\gamma_l$  is constant.

Figure 4 shows the effects of time on contact angle  $\theta$  for the sample kept at  $1600^\circ C$  in the  $N_2/H_2$  atmosphere. Contact angle was constant at around  $30^\circ$ , irrespective of time, indicating that there were neither changes in the droplet composition nor interactions between the droplet and the tungsten plate under the conditions used. The tested droplet was easily separated from the plate, and there was no reac-

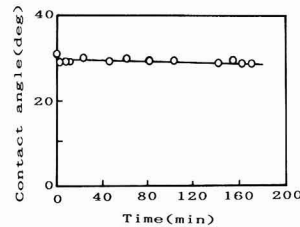


Fig. 4. Relationship between contact angle and holding time at  $1600^\circ C$ .

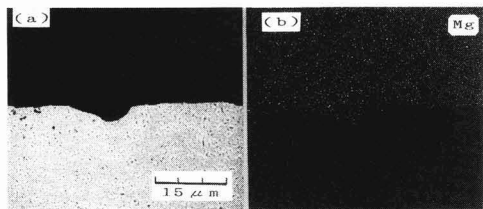


Fig. 5. The polished cross-section photographs of  $SiO_2-MgO-Al_2O_3$  glass/W interface. (a) SEM and (b) Mg mapping.

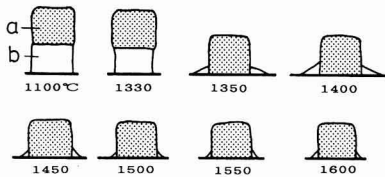


Fig. 6. Penetrating behavior of flux into W compact heating at 3°C/min. a:W compact, b:SiO<sub>2</sub>-MgO-Al<sub>2</sub>O<sub>3</sub> glass.

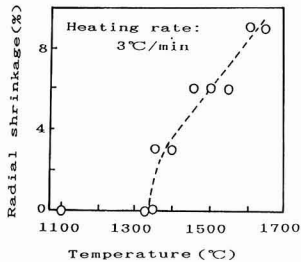


Fig. 7. The relation between radial shrinkage and temperature for W compact heating at 3°C/min.

tion layer observed by the SEM analysis (Fig.5).

### 3.2. Penetration of Molten SiO<sub>2</sub>/MgO/Al<sub>2</sub>O<sub>3</sub> into Tungsten Compact

Figure 6 shows the calcined sintering aid of the three-element eutectic composition of SiO<sub>2</sub>/MgO/Al<sub>2</sub>O<sub>3</sub>, placed under the tungsten compact and on the molybdenum plate, changing with temperature in a mixed N<sub>2</sub>/H<sub>2</sub>/H<sub>2</sub>O atmosphere (sketched from the photographs). The calcined sintering aid melted at around 1350°C penetrated the tungsten compact increasingly as temperature increased, the situations being represented by decreased  $\theta$  level, as shown in Fig.3.

As shown in Fig.7, it was also observed that the tungsten compact started to shrink in the radial direction as soon as the sintering aid was molten, and this trend was accelerated as temperature increased.

To summarize these results, the molten sintering aid penetrates into the tungsten compact, and it is necessary for the molten aid to have a contact angle of around 40° or less with the compact, to cause the latter to shrink.

## 4. Conclusions

The authors have measured contact angle of the molten, three-element eutectic composition of SiO<sub>2</sub>-MgO-Al<sub>2</sub>O<sub>3</sub> with the tungsten compact, and observed its penetration into the tungsten compact.

- 1) Contact angle  $\theta$  tends to decrease as temperature increases. It also varies with H<sub>2</sub>O content of a N<sub>2</sub>/H<sub>2</sub> mixture as the atmosphere gas; it is around 20° lower in a wet atmosphere than in a dry atmosphere, conceivably resulting from H<sub>2</sub>O adsorbed on the tungsten substrate surfaces.
- 2) Contact angle  $\theta$  is almost independent of time at 1600°C, and no interactions between the molten aid and tungsten substrate were observed.
- 3) Penetration of the molten aid into the tungsten compact and the resultant shrinkage of the compact proceed, when contact angle  $\theta$  is around 40° or less.

### References:

- 1) U.F. Zackay, D.W. Mitchell, et al., J. Am. Ceram. Soc., 36, 84-99 (1953).
- 2) K. Sugauma, Bull. Jpn. Inst. Metals, 29, 882-887 (1990).
- 3) C. Tonegawa, T. Hirao and A. Takami, Denshi Zairyo, 75-80 (1977-2).
- 4) D. Otsuka, M. Sekihata, T. Usami, Am. Ceram. Soc. Bull., 60, 540-545 (1981).
- 5) Y. Sumida and Y. Tozawa, Proc. Ann. Mtg., Ceram. Soc. Jpn. (1987) 647-648.
- 6) M. Ueyama and T. Yamamoto, Funtai to Funmatsu Yakin, 37, 851-856 (1990).
- 7) M. Ueyama and T. Yamamoto, *ibid.*, 38, 168-174 (1991).
- 8) A.G. Pincus, J. Am. Ceram. Soc., 44, 152-157 (1953).
- 9) S.S. Cole and G. Sommer, *ibid.*, 44, 265-271 (1961).
- 10) J.R. Floyd, Am. Ceram. Soc. Bull., 42, 65-70 (1963).
- 11) R.M. Fulrath and E.L. Hollar, *ibid.*, 47, 493-497 (1968).
- 12) E.A. Hayduk, Solid State Tech., 28, 321-324 (1985).
- 13) T. Sasaki, Experimental Chemistry, 7, Interfacial Chemistry, ed. by Chem. Soc. Jpn., Maruzen, (1956) 63-69.
- 14) Phase Diagram for Ceramist, Am. Ceram. Soc., (1969) 246.
- 15) D.T. Livey and P. Murray, Warmfeste und Korrosions bestandige Sinterwerkstoffe 2. Plansee Seminar, Metallwerk Plansee Ges. M.B.H., (1956) 375-404.

# Growth of Epitaxial PLZT Film by CVD

Hiroshi Funakubo, Katsuhiko Imashita and Nobuyasu Mizutani

Department of Inorganic Materials, Faculty of Engineering, Tokyo Institute of Technology  
2-12-1, O-okayama, Meguro-ku, Tokyo 152 Japan

(Pb, La) (Zr, Ti) O<sub>3</sub> films were prepared by CVD using Pb(DPM)<sub>2</sub>, La(DPM)<sub>3</sub>, Zr(O-t-Bu)<sub>4</sub>, Ti(O-i-Pr)<sub>4</sub> and O<sub>2</sub> as starting materials. PLZT films were grown with almost complete epitaxy on (100) MgO substrates. The deposition rate of the film was about 50-100nm/min. Some optical properties were almost the same as those of PLZT ceramics.

[Received August 4, 1991; Accepted October 17, 1991]

**Key-words:** Epitaxial PLZT film, CVD, Cold-wall type apparatus, Pb(DPM)<sub>2</sub>-La(DPM)<sub>3</sub>-Zr(O-t-Bu)<sub>4</sub>-Ti(O-i-Pr)<sub>4</sub>-O<sub>2</sub> system, Optical property

## 1. Introduction

The solid solution of (Pb<sub>1-x</sub>La<sub>x</sub>) (Zr<sub>1-x</sub>Ti<sub>x</sub>)O<sub>3</sub> [PLZT(100<sub>x</sub>/100<sub>y</sub>/100<sub>z</sub>)] is well known as a ferroelectric transparent material with strong electro-optic effect. It is known that these properties of PLZT depend on its composition, especially La content, and crystal structure,<sup>1)</sup> so that precise control of composition and crystallinity are required. In view of the application to integrated optics, it is of great interest to grow thin films of this material. The epitaxial thin films are especially useful for applications to various devices. The preparation of PLZT films by sputtering<sup>2-8)</sup> and ion beam deposition<sup>9)</sup> was reported, and epitaxial films were prepared by the sputtering method.<sup>3,5,7,8)</sup> However, the problem of precise control of composition and crystal structure in the bulk of the film still remains unsolved, because the sputtering ratio varies with each element. On the other hand, CVD is expected to achieve precise control of the film composition and crystallinity with facility. However, the preparation of the PLZT film by CVD has not been reported yet.

In this paper, almost epitaxially grown tetragonal PLZT films were prepared on (100) MgO substrates by adding La into Pb(Zr, Ti)O<sub>3</sub>, PZT, film which was previously reported.<sup>10)</sup>

## 2. Experimental

The PLZT film was prepared by adding La(DPM)<sub>3</sub> vapor into the Pb(DPM)<sub>2</sub>-Zr(O-t-Bu)<sub>4</sub>-Ti(O-i-Pr)<sub>4</sub>-O<sub>2</sub> system which was previously used as starting materials for the preparation of the PZT film. The schematic apparatus and experimental procedure for the PLZT film used in the present study were almost the same as that for PZT film.<sup>10)</sup> Freshly cleaved (100) MgO single crystal was used as a substrate. The deposition conditions for the PLZT films were summarized in Table 1. The La content in the film was controlled by

the heating temperature of La(DPM)<sub>3</sub>. The distance between the tip of the gas nozzle and the substrate was kept at 30mm, which was longer than that in the preparation of the PZT film (10mm), for improving of the surface flatness of the film.

## 3. Result and Discussion

The films deposited on the substrates were transparent and adhered well to the substrate. The growth rate of about 50-100nm/min was more than 10 times as fast as that of dc or rf sputtering methods but was almost half of that of the PZT film.<sup>10)</sup> This was mainly attributed to the fact that the concentration of the PLZT source gas near the substrate was lower than that of PZT for the longer distance between the tip of the gas nozzle and the substrate.

The PLZT films with different x, y and z were obtained by controlling the vaporizing temperature of each starting materials and the flow rate of each carrier gas. Figure 1 shows XRD patterns of (a) PLZT (0/50/50), (b) PLZT (6/50/50) and (c) PLZT (8/50/50) films. The composition of these films was determined by EDS measurements. Only (00l) and (h00) peaks of tetragonal phase were observed together with those of MgO and the intensities of (00l) reflections are significantly stronger than those of (h00) ones. Moreover, (00l) peaks shifted to the higher angle and approached to (h00) peaks with the increase of La content. This means that the lattice constants of a- and c-axes of tetragonal phase tended to become equal with increasing La content in the film. Such a result was reported for bulky PLZT.<sup>11)</sup> The degree of c-axis orientation, α,<sup>10)</sup> was increased to above 0.9 by adding La into PZT as shown in Fig.1(b) and (c). This suggested that PLZT films had highly [001] orientation.

Figure 2 shows (001) and (101) X-ray pole figures of the PLZT (6/50/50) film. This is almost the same of that of the PZT film.<sup>10)</sup> This result shows that there is not only the

Table 1. Deposition conditions of PLZT film.

Precursor	Pb : Pb(DPM) <sub>2</sub> La : La(DPM) <sub>3</sub> Zr : Zr(O-t-Bu) <sub>4</sub> Ti : Ti(O-i-Pr) <sub>4</sub>
Temperature of vaporizer	Pb : 165 - 170 °C La : 170 - 180 °C Zr : 49 - 54 °C Ti : 36 - 42 °C
Flow rate of carrier for each component	Pb : 180 ml/min (N <sub>2</sub> ) La : 150 ml/min (N <sub>2</sub> ) Zr : 20 - 40 ml/min (N <sub>2</sub> ) Ti : 20 - 40 ml/min (N <sub>2</sub> ) O <sub>2</sub> : 40 ml/min
Total gas flow rate	: 480 ml/min
Total gas pressure	: 20 Torr
Deposition temperature	: 650-700 °C
Substrate	• (100) MgO (10mm × 10mm × 0.5 mm)

crystal structural arrangement having an axis perpendicular to the substrate but also that with parallel one. From the result of Figs.1 and 2, the highly epitaxial nature of this film on (100) MgO substrate was ascertained as the same as that of the PZT film.<sup>10</sup>

Figure 3 shows SEM micrographs of PLZT (6/59/41) film. The PLZT film was dense and made up of fine grains. Moreover this film has a relatively flat surface and some roughness corresponds to the surface roughness of cleaved MgO substrate, as shown in Fig.3(a).

The transmittance spectra of the PLZT (6/59/41) film on MgO substrate with about 0.53μm in thickness were measured at normal incidence in the range 0.2-0.8μm. The measurement was done for the same film as shown in Fig.3. The transmittance rose from ca. 0.34μm and showed strong interference oscillations corresponding to the flat surface of the film. The transmittance at the wavelength of 0.589μm was about 57%. This transmittance was rather small compared with that prepared by the sputtering method.<sup>3,8</sup> The reduction of the transmittance was probably caused by the irregularity of the surface of the film and the interface between the film and substrate as shown in Fig.3(b). The refractive index was obtained from the wavelength spacing between adjacent peaks of the interference oscillations. The dependence of refractive index of the film on the

wavelength is shown in Fig.4. This was the typical dispersion curve near an electronic interband transition. The refractive index was ca. 2.56 at the wavelength of 0.589μm, which was almost the same of that of PLZT ceramics.<sup>11,12)</sup>

Generally dispersion data in the interband transition region are most often modeled with a single electronic oscillator. According to the notation of DiDomenico and Wemple,<sup>13)</sup> the refractive index is given by the expression

$$n^2 - 1 = (S_0 \lambda_0^2) / [1 - (\lambda_0 / \lambda)^2]$$

where  $\lambda_0$  is an average oscillator position and  $S_0$  is an average oscillator strength. Figure 5 shows  $1/(n^2-1)$  of PLZT film as a function of  $1/\lambda^2$  for the PLZT film using the data in Fig.4. The linear relationship was observed and this shows that the model with the single electric oscillator is

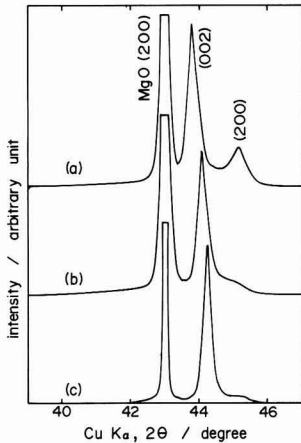


Fig. 1. XRD patterns of PLZT films on (100) MgO substrates. (a) PLZT (0/50/50), (b) PLZT (6/50/50), (c) PLZT (8/50/50).

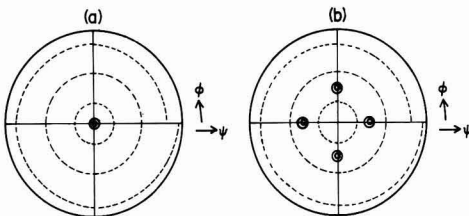


Fig. 2. X-ray pole figures of PLZT (6/50/50) film on (100) MgO substrate. (a) (001), (b) (101).

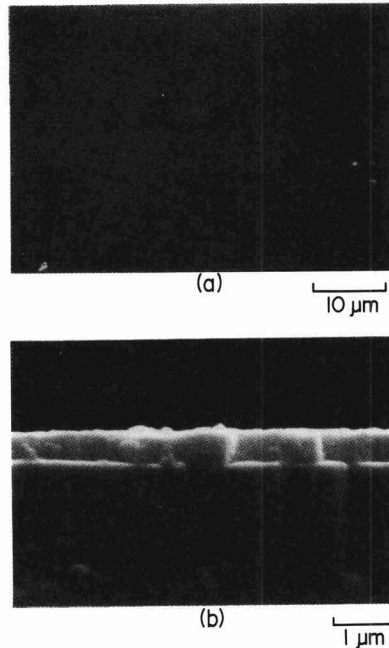


Fig. 3. SEM micrographs of (6/59/41) PLZT film. (a) surface, (b) fractured surface.

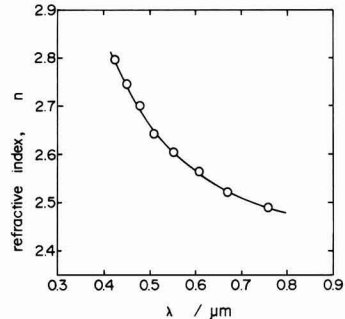


Fig. 4. The wavelength dependence of the refractive index of PLZT (6/59/41) film on (100) MgO substrate. Film thickness: ca. 0.53μm.

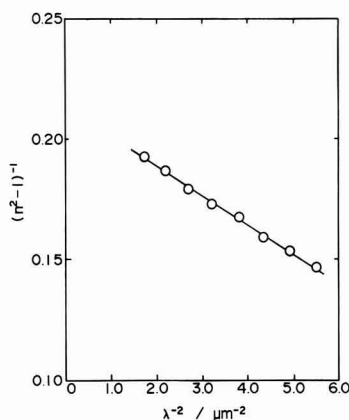


Fig. 5. The dependence of  $1/(n^2-1)$  on  $1/\lambda^2$  replotted using the data in Fig.4.

suit for the PLZT film prepared in the present study. Moreover,  $S_0$  and  $\lambda_0$  was estimated to be  $0.813 \times 10^{14} \text{m}^{-2}$  and  $0.24 \mu\text{m}$ , respectively, from the slope of the straight line and the infinite-wavelength intercept in Fig.5, respectively. These values were similar to those reported for (10/65/35) PLZT ceramics.<sup>12,14)</sup>

#### 4. Conclusion

Almost completely epitaxially grown  $(\text{Pb}_{1-x}\text{La}_x)(\text{Zr}_x\text{Ti}_{1-x})\text{O}_3$  films have been successfully prepared on (100) MgO substrate by CVD using  $\text{Pb}(\text{DPM})_2$ ,  $\text{La}(\text{DPM})_3$ ,  $\text{Zr}(\text{O}-t\text{-Bu})_4$ ,  $\text{Ti}(\text{O}-i\text{-Pr})_4$  and  $\text{O}_2$  as starting materials. The deposition rate of the film was about 50-100mm/min. Some

optical properties were almost the same as those of PLZT ceramics.

#### Acknowledgements

The authors would like to thank Dr. A. Saiki and Mr. R. Ooki of Tokyo Institute of Technology for the measurement of pole figure and EDS measurements, respectively.

#### References:

- 1) G.H. Haertling and C.E. Land, *J. Am. Ceram. Soc.*, 54, 1-11 (1971).
- 2) K. Tanaka, Y. Higuma, K. Yokoyama and T. Nakagawa, *Jpn. J. Appl. Phys.*, 15, 1381-1382 (1976).
- 3) M. Okuyama, T. Usuki and Y. Hamakawa, *Appl. Phys.*, 21, 339-343 (1980).
- 4) H. Matsunami, M. Suzuki, M. Ishida and T. Tanaka, *Jpn. J. Appl. Phys.*, 15, 1163-1164 (1976).
- 5) M. Ishida, S. Tsuji, K. Kimura, H. Matsunami and T. Tanaka, *J. Cryst. Growth*, 45, 393-398 (1987).
- 6) T. Fukami and T. Sakuma, *Jpn. J. Appl. Phys.*, 20, 1599-1600 (1981).
- 7) H. Adachi, T. Kawaguchi, K. Setsune, K. Ohji and K. Wasa, *Appl. Phys. Lett.*, 42, 867-868 (1983).
- 8) H. Adachi, T. Mitsuyu, O. Yamazaki and K. Wasa, *J. Appl. Phys.*, 60, 736-741 (1986).
- 9) L.L. Boyer, A.Y. Wu, G.W. Metzger and J.R. McNeil, *J. Vac. Sci. Tech.*, A7, 1199-1201 (1989).
- 10) H. Funakubo, K. Imashita, N. Kieda and N. Mizutani, *Seramikkusu Rombunshi*, 99, 248-250 (1991).
- 11) H.M. O'Bryan, Jr. and A.H. Meitzler, *Am. Ceram. Soc. Bull.*, 51, 479-485 (1972).
- 12) C.J. Kirkby, *Ferroelectrics*, 7, 157-159 (1974).
- 13) M. DiDomenico and S.H. Wemple, *J. Appl. Phys.*, 40, 720-753 (1969).
- 14) P.D. Thacher, *Appl. Opt.*, 16, 3210-3214 (1977).

This article appeared in English in *Nippon Seramikkusu Kyokai Gakujutsu Ronbunshi* (Japanese version), Vol.99, No.11, 1991.

# Comment on "Synthesis of Titanium Nitride Whiskers from Potassium Fluorotitanate (IV)"

C. Bamberger and J. Brynestad

Chemistry Division, Oak Ridge National Laboratory, Operated by Maytin Marietta Energy Systems, Inc.

Post Office Box 2008, Oak Ridge, TN 37831, USA

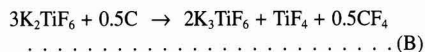
[Received August 22, 1990]

We have read with great interest the paper by Tabuchi, Kaneko and Iwasaki published on TiN whiskers in *J. Ceram. Soc. Japan Intl. Edn.*, 98, 44-49 (1990).

We commend them for the conversion of  $K_2TiF_6$  into TiN, however we strongly disagree with the reaction mechanisms. The occurrence of a reaction such as in eq.(3) in which elemental fluorine is evolved is highly unlikely; Ti(IV) will not thermally reduce to Ti(III), especially when present as a fluoride or complex fluorides. The only reductant known to be present in the system is carbon. While at 1600K the reaction



cannot proceed to the right because its  $\Delta G$  is +160kcal, it is conceivable that a reaction such as



may have a  $\Delta G$  not too far from zero. Unfortunately we do not have the necessary data for the calculation.

Using free energy calculations for the related reaction



at 1600K its  $\log K_p = -17.0$  which will indicate a significantly low equilibrium partial pressure of  $CF_4$ . However the system is dynamic and the  $CF_4$  would be consumed by reaction with the  $Al_2O_3$ , according to



for which  $\Delta G$  is -287kcal at 1600K.

Because there is no sufficient information available on what species (especially gaseous) are present, we are not able to postulate a thermodynamically reasonable equation for representing the formation of TiN from the  $TiF_3$ . It is conceivable, that although at very low partial pressures, oxyfluoride species such as  $AlOF$ ,  $TiOF_2$ ,  $COF_2$  may participate in the reaction. Thus it would be of interest to replace the  $Al_2O_3$  tube with one that does not contain oxygen, i.e. a refractory metal or even graphite.

The corrosion of the  $Al_2O_3$  tube can also possibly occur by the alternative reaction

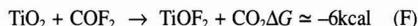


for which  $\Delta G$  is only +5kcal at 1600K.

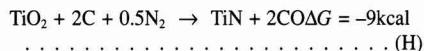
Because KF vapor is present at 1600K, the following reaction would take place with  $AlF_3$  (from either reaction (C) or (D) or both)



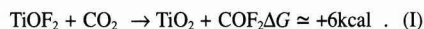
thus explaining the presence of K-fluoroaluminates as corrosion products of the  $Al_2O_3$ . Because the  $TiO_2$  could have formed on the  $Al_2O_3$  wall (eq.(D)) a reaction is needed to transport  $TiO_2$  to the graphite; the following reactions are feasible from a thermochemical point of view



In the presence of graphite the  $TiO_2$  can be converted to TiN according to:



and to close the cycle the carbonyl difluoride could be regenerated by:



which is the reverse of eq.(F). This would require a  $\Delta T$  between the  $Al_2O_3$  wall and the graphite tube.

The above reactions are just examples of what might occur in a complex system such as that used; the reactions postulated by us are thermodynamically feasible and thus do not require transport mechanism in which gaseous TiN needs to be present at 1600K and to nucleate on the graphite wall as indicated in the paper.

All the above discussion is predicated on the assumption that the system of Tabuchi et al. (especially the graphite) was clean of any impurities, mainly hydrogen or hydrocarbons.

---

This article appeared in English in *Nippon Seramikkusu Kyokai Gakujutsu Ronbunshi* (Japanese version), Vol.99, No.11, 1991.

# Reply to "Comment on 'Synthesis of Titanium Nitride Whiskers from Potassium Fluorotitanate (IV)'"

Mitsuharu Tabuchi, Yasunari Kaneko\* and Hiromichi Iwasaki\*

Graduate Course of Applied Chemistry, Faculty of Science and Engineering, Ritsumeikan University  
56-1, Tohjinkitamachi, Kita-ku, Kyoto-shi 603 Japan

\*Department of Chemistry, Faculty of Science and Engineering, Ritsumeikan University  
56-1, Tohjinkitamachi, Kita-ku, Kyoto-shi 603 Japan

[Received October 3, 1991]

We have investigated reactions related to eq.(3) from the thermodynamical point of view thoroughly and have arrived at the following conclusion.

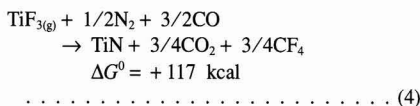
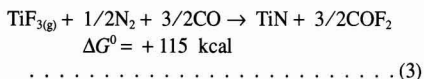
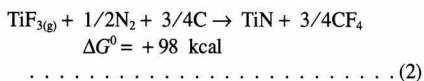
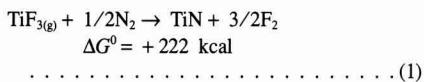
It is clear from Fig.3 in the paper that TiN is formed in association with converting  $K_2TiF_6$  into  $K_3TiF_6$ . When we consider reasonable reaction paths from  $K_2TiF_6$  to TiN, two processes must be taken into account. The first process is that from  $K_2TiF_6$  to  $K_3TiF_6$ . The second process is related to the formation reaction of TiN whisker and coating. It is presumed that gaseous species, such as  $TiF_4$ ,  $TiF_3$ ,  $TiOF_2$ , take part in the second process. The reactions (D-I) pointed out by the Bamberger and Brynestrud are involved in this process.

In the first process, carbon from the graphite tube would dominate the conversion reaction from  $K_2TiF_6$  to  $K_3TiF_6$ , because the product obtained by firing  $K_2TiF_6$  without the graphite tube nor boat under  $N_2$  flow at  $1000^\circ C$  was not  $K_3TiF_6$ , this crystalline phase could not be identified by X-ray diffraction.

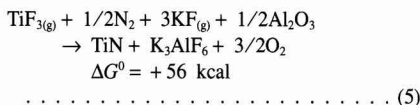
As for the second process, formation mechanism of TiN from  $TiF_4$ , which is cited through eq.(D-I) in the comment, is valid from the thermodynamical point of view. But it is difficult to think that  $K_3TiF_6$ , which is another product in reaction (B) is not converted into TiN and is transferred out of the system. It is doubtful for us that the formation mechanism can also explain the formation process of TiN from  $K_3TiF_6$ , because  $TiF_4$  could not be formed probably from  $K_3TiF_6$ , having trivalent titanium, in the reduced atmosphere.

Thus we must consider feasible conversion from  $K_3TiF_6$  to TiN. We could not find the standard Gibbs energy of formation ( $\Delta G^\circ$ ) of  $K_3TiF_6$  and  $KAlF_4$ . The white product in the neighborhood of gas outlet is considered to be  $K_3AlF_6$ , and we consider that  $K_3TiF_6$  is decomposed into  $TiF_3$  vapor ( $TiF_{3(g)}$ ) and KF vapor ( $KF_{(g)}$ ) at 1600K, because  $TiF_3$  and KF melt at 1500K and 1129K respectively. The  $\Delta G^\circ$  values of these compounds are available.<sup>1)</sup>

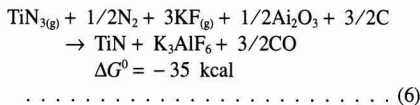
$TiF_{3(g)}$  can not change into TiN without the existence of carbon and  $Al_2O_3$  tube and/or  $KF_{(g)}$  at 1600K from thermodynamical point of view as follows:



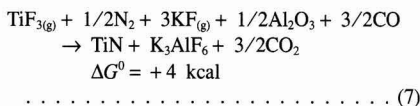
and



The reaction (5) is more feasible than reactions (1-4). But this reaction could not proceed to the right and after all, the following reactions (6) and (7) would occur.



and



These reactions could proceed to the right, probably in the neighborhood of  $Al_2O_3$  tube. These reactions look consistent with our experimental results in which TiN whisker was formed on the outer surface of the graphite tube and on the  $Al_2O_3$  tube occasionally. Both reactions (6), (7) and (D-I) are probably consistent with the growth mechanism of a TiN whisker, that is, TiN whisker grew by layer growth on the facets of it, as mentioned in the paper.

We could not find a more reasonable reaction path for the TiN formation on the facets of a whisker, this problem could be resolved by determining the gaseous species which take part in the formation process of the TiN whiskers from  $K_2TiF_6$ .

## References:

- 1) M.W. Chase, Jr., C.A. Davies, J.R. Downey, Jr., D.J. Frurip, R.A. McDonald and A.N. Syverud, JANAF Thermochemical Tables Third Edition Part I and II, Journal of Physical and Chemical Reference Data, 14 Supplement 1, Am. Chem. Soc. and Am. Inst. Physics for the National Bureau of Standards (1985).

# Information & Communications

## News

### Zirconia-base Ceramic Material

Ishikawa Prefecture's Industrial Research Institute has developed, jointly with Kanebo and Germany's Max Planck Institute, a new zirconia-base ceramic material suited for electrolyte in solid-phase electrolyte fuel cells, which are called fuel cells of the third generation. It is known that cubic zirconia, containing trace quantities of yttria, is suited for the solid-phase electrolyte, but the newly developed material is the conventional one to which roughly 5wt% of alumina is added to improve characteristics. Alumina is added by the special wet process in which hydrolysis is combined with coprecipitation, to keep sinter resistance low and make the sinter "plastically" processable. Electrical resistivity is approximately  $10^{-3}\Omega\text{m}$ , which is lower than that of the conventional material by one digit. Addition of alumina reduces particle size to  $0.4\mu\text{m}$ , which is equivalent to that of tetragonal zirconia, making the sinter more amenable to deformation at high temperature of 1400 to 1500°C. The institute has deeply drawn the sinter. The results were presented to the International Ionics Symposium, held in Canada. The institute also plans to develop a fuel cell with the new ceramic electrolyte, jointly with Kanebo.

### Ceramic Material for High-Efficiency Thermoelectric Devices

Prof. Kakue Matsubara of Yamaguchi University's Faculty of Engineering has been studying the effects of thin, amorphous film formation by ion-assisted deposition on temperature-related characteristics of thermoelectromotive force, in order to develop ceramic-base thermoelectric materials as part of a "project to develop thermoelectric materials by the plasma-ion process," an energy-related research program being promoted by Ministry of Education. Usefulness of the ceramic, produced by sintering plasma-treated iron and silicon microparticles under pressure, has been demonstrated as a material for high-efficiency direct thermoelectric conversion. Power-generation tests were conducted under a differential temperature of 600°C (heating temperature: 800°C, heat radiator end temperature: 200°C), to generate power of approximately 2W per unit area at the maximum voltage of 0.48V and amperage of  $18.5\text{A}/\text{cm}^2$ , using a specimen 13mm long and  $4\text{mm}^2$  in cross-sectional area. The results indicate that there are bright prospects of developing an element of still higher efficiency. The element is expected to greatly contribute to effective utilization of waste heat, esti-

mated to be equivalent to 200 million KJ of oil, and to the saving of fossil fuels and thereby to the abatement of CO<sub>2</sub> emission. The results were presented to the symposium, held at UK's Wales University.

### Uniform Film of Cubic Crystals of Gallium Nitride

The Agency of Industrial Science and Technology's Electrotechnical Laboratory has developed for the first time uniform film of gallium nitride which consists only of cubic crystals. Gallium nitride is attracting attention as a material which can realize blue light emission and superhigh-speed elements. The devices so far developed, however, are made of hexagonal crystals. The key to the success was the pretreatment of the gallium-arsenic substrate with nitrogen gas prior to the molecular beam epitaxy (MBE) process, in which the starting metallic material is deposited over the substrate under a vacuum, to form the film.

The pretreatment replaces arsenic by nitrogen, to form a superthin film of gallium nitride over the substrate. Evaporation of metallic gallium, while blowing nitrogen onto the substrate forms the uniform film consisting only of the cubic crystals. Its band gap, which determines semiconductor characteristics, is 3.8eV, higher than that of the film of the hexagonal system. The success should further enhance the possibility of gallium nitride films finding use in superhigh-speed semiconductor elements and light-emitting devices which cover a wide color range from red to ultraviolet region, says the laboratory.

### Ceramic Substrate for Fixing Disc

Kyocera has developed glass-coated ceramic substrate for fixing discs. It is an alumina disc, sandwiched by  $25\mu\text{m}$  thick glass films, with a total thickness of 0.635mm. It has a smoother surface than the conventional aluminum or glass substrate, allowing it to read information stored in finely sectioned areas in the disc. The 2.5-inch type can store information of 60 megabytes, a capacity roughly 1.5 times higher than that of the conventional disc.

The newly developed substrate, having sufficiently smooth surface, makes the disc come as close as  $0.05\mu\text{m}$  to the head. Alumina ceramic has various advantages over the conventional one; it is roughly 4 times stronger than aluminum or glass, polished more easily, and produces less defective devices in the assembly process. Two types are available: 1.8 and 2.5 inches in diameter. The sample price is 2,000 to 3,000 yen, which

will be reduced to 1,000 yen when they are mass-produced. The company expects to attain annual sales of 5 billion yen or so in five years.

### Discharge-Sintering for Production of Material with Inclined Functions

Sumitomo Coal Mining Co., Ltd. has developed a technique which allows production of material with inclined functions in much shorter time (one-tenth or less) than the conventional process. The key is a process called discharge-sintering in which pressure and voltage are applied simultaneously to the starting powder. The product made on a trial basis is a composite plate of zirconium dioxide and stainless steel, approximately 2mm in thickness, in which the chemical compositions are changed in three stages. A pressure of  $300\text{kg}/\text{cm}^2$  is applied to the powder mixture of three different compositions, simultaneously with DC pulse voltage, to trigger the discharge plasma phenomenon between the particles. The jigs that support and transmit pressure to the upper and lower sides of the plate are of different materials, to generate a temperature differential across the thickness (superhard alloy of tungsten carbide for the stainless side and graphite for the zirconia side). The technique produces the composite plate much easier than the conventional one, in 20 min or so. The company plans to sell sets of know-how and equipment to the makers.

### Insulator Tiles

Mitsui Mining has developed, jointly with Kawasaki Heavy Industries, a ceramic insulator tile for the external surfaces of the Japanese space shuttle planned for launch in 1999. It is characterized by uniform, three-dimensional structure of silica fibers and alumina fibers fixed by a ceramic material. These fibers are known for their insulating and heat-resistant properties, respectively. The tile is coated with glassy material. Its tensile strength is  $10\text{kg}/\text{cm}^2$ , which is roughly two times higher than those used by NASA. The development project was commissioned by the National Space Development Agency, in which Mitsubishi Heavy Industries and Fuji Heavy Industries, in addition to Kawasaki Heavy Industries, are participating.

### Production of Plate-shape, Single-crystalline Rutile by the EFG Method

Chichibu Cement has succeeded for the first time in the world, jointly with Tohoku University's Prof. A. Fukuda, in growing

plate-shape, single-crystalline rutile by the EFG method as one of the single crystal withdrawal growth methods. The starting powder, placed in a die provided with a slit, is placed in a crucible and heated by high-frequency current, and the molten powder, rising up through the slit by capillarity, is withdrawn and grows over the seed crystals to produce the single crystals. Temperature within the oven is finely controlled, to realize plate-shape (2×20×80mm), single-crystalline rutile. Two or more plates can be produced simultaneously. Single-crystalline rutile is produced by melting titanium dioxide as the starting material. The product, however, tends to be polycrystalline, and difficult to form into a plate of target width. The company plans to expand the size and, at the same time, to commercialize polarization plates and light-detecting elements for optical isolators in 1992.

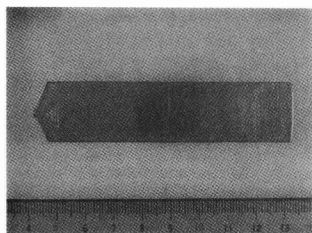


Fig. 1. Plate-shape, single crystalline rutile.

### Dummy Wafers of Single-crystalline Sapphire

Kyocera Corp. is going to mass-produce for the first time dummy wafers of single-crystalline sapphire, based on the EFG method developed by US Mobile Industries. Molten alumina, treated at 2,000°C, is withdrawn together with the seed crystals along the die into a plate. The plate is then cut into a disc, to produce the wafer, 4-nines (99.99%) in purity. Having a complete mirror face, sufficiently high strength and heat-resistance, it can be used repeatedly for a semi-permanent period in semiconductor production lines. This compares with only 3 months at the longest for which the wafer of quartz as the major wafer type at present can be used repeatedly. It is also suited for analysis, by fluorescent X-ray, of trace quantities of impurities in films. The company plans to produce 200 wafers monthly, mostly of 4-, 5- and 6-inch diameter types, and of 8-inch diameter types to some extent. The sample price of the 8-inch diameter type is 200,000 yen. It expects to attain annual sales of 1.2 billion yen in one year.

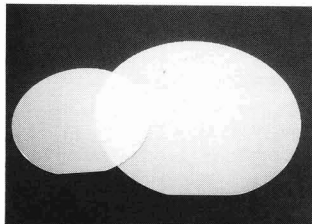


Fig. 1. Single crystalline sapphire wafer.

### Heat-resistant Parts of C/C Composite

Kawasaki Steel and Kawasaki Heavy Industries have jointly succeeded in production, on a trial basis, of carbon material reinforced with carbon fibers (C/C composite) for the Japanese space shuttle "HOPE" which the National Space Development Agency plans to launch. The former is responsible for forming carbon-fiber-reinforced plastic (CFRP) as designed, and the latter for sintering the composite at 1500 to 2000°C. The small pores in the sintered body are filled with coal tar, and the sintering process is repeated. It is finally coated with heat-resistant oxide film. The C/C composite thus prepared, in which carbon molecules are regularly arranged at a high density, can withstand heat of 1700C, generated when the shuttle dashes into the atmosphere. Its bending strength is 42kg/cm<sup>2</sup>, which is higher than that of superduralumin (40kg/cm<sup>2</sup>) used for the shuttle body. The composite material will be used for the front sections of the main wings and the vertical wings. It is 1m long, forming a monolith with the reinforcing frame. Distortion is 1mm or less.

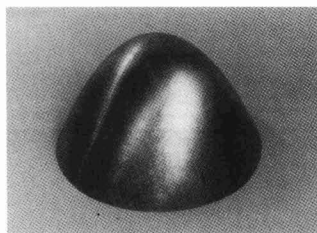


Fig.1. C/C composite material for nose of shuttle

### Competition in Development of Cerebral Magnetic Field Measurement Equipment which Employs SQUID

Fifteen Japanese firms are competing in the development of cerebral magnetic field measurement equipment. They include Toshiba, Hitachi, Shimadzu, Yokogawa Medical Systems, Siemens Asahi Medics, Furukawa Electric, Daikin Kogyo, Sumitomo Electric, Osaka Gas, Mitsui Metals, Sumitomo Heavy Industry, Fujitsu, Seiko Electronic Industry, Nippon Gaisai, Ulvac, Takenaka Construction, and Shimizu Construction.

Ten companies are participating in a consortium organized by MITI on superconductor sensor laboratory. Cerebral magnetic field measurement equipment is available for fields other than the diagnosis of cerebral diseases. Including diagnosis of heart diseases, estimation of pleasantness felt by humans, and the detection analysis of information processing by humans.

### Formal Contract between SSC Laboratory and Two Japanese Companies for Development of

### Superconducting Wires

Furukawa Electric Industry Co., Ltd. and Sumitomo Electric Industry Co., Ltd. have arranged with US SSC Laboratory to participate in the development of superconducting wires. SSC has the world's largest proton accelerator with circumference of 87km. SSC inquired as to whether or not the two companies wanted to participate in the development program. Both companies have experience in fabricating superconducting wires used for JT-60, linear magnetic levitation train, MRI, Japanese Tristan, accelerator, and other projects. Sumitomo will in develop the of superconductor to be used for the internal ring and Furukawa will develop that for the external ring. Seven manufacturers have participated in the program, of which two will be selected. The superconducting wire will be 6µm in diameter, and one thousand wires will be contained in a copper tube. The copper tube wire is necessary to enable turning electricity of 2750A under 5T. Meanwhile SSC announced that it has successfully developed a wire which allows turning electricity of 7000A.

### Turbo Helium Compressor for Cryogenic Refrigerator Used in Superconducting Generator

IHI has developed a turbo compressor which operates at 80K with a rotation speed of 100,000rpm. This turbo compressor will be used for cryogenic refrigerators which cool the magnetic coils of a superconducting generator, now under development as national project. Through this development, helium at flow rate of 113g/s can be compressed to 8 atm, 7 times that achieved by a conventional compressor. Full-scale testing has not yet been conducted and the total the refrigeration system has not yet been completed. The technology developed thus far is regarded as sound footing for the system.

The turbo compressor suction helium gas which is cooled prior to compression in order to increase compression efficiency. A 25kW motor is employed, and 3-D radius flow impellers were developed. A magnetic bearing was employed to support the shaft which connects the motor and impellers, thus eliminating the need for a lubricant. These measures prevented contamination of the system.

### Oxygen Sorption-Desorption Behavior and Superconductivity of Bi-Based Oxide Superconductor

Y. Deshinaru and his colleagues at Kyushu University verified the following:

- 1) The sorption-desorption of oxygen is accompanied by reversible changes in critical temperature  $T_c$  and in the length of the c-axis.
- 2) The relationship between the quantity of oxygen sorbed (or desorbed) and  $T_c$  varies with composition. The difference is particularly noticeable, when changing the Sr/Ca ratio ( $y$  level); the  $T_c$  level of the samples vary inversely and more significantly.
- 3) The Pb-doped sample has a higher hole

concentration, approximately  $1 \times 10^{-5}$  mol/g as oxygen, than the Pb-free sample,

4) The sample with  $y=0.8$  has a lower  $T_c$  level and a shorter  $c$ -axis than the sample with  $y=0$ , irrespective of oxygen content.

5) It is considered that the 2212 phase has the optimum hole concentration at a certain oxygen content to provide the maximum  $T_c$  level. The sample with  $(x, y)=(0, 0.8)$  is found to have the optimum oxygen content at  $\delta=0.15$ .

### Fabrication of Y System Superconductor Thick Film on Ag Substrate by Gas Deposition.

Dr. Murakami and his colleagues at the Superconductivity Research Institute of ISTEK fabricated a  $YBa_2Cu_3O_{7-x}$  thick film, 1mm wide and 1 to 100 $\mu$ m thick, on an Ag substrate by gas deposition using ultra-fine particles of  $YBa_2Cu_3O_{7-x}$ .

The gas deposition process was adopted for fabrication of a thick film with ultra-fine powders of Y system superconductor in order to take advantage of the features of the ultra-fine particles. The thick film displayed excellent properties, obtaining  $J_c=2300A/cm^2$  (77K).

It was shown that silver is more suitable as a substrate for the gas deposition method than ceramics. This was attributed to the better adhesion of ultra-fine powders to the silver substrates and to the sintering through the liquid phase.

With respect to thermodynamics, the silver substrates provided superior results. Furthermore, it was found that the gas deposition method depresses the melting point of ultra-fine particles; thus, causing the depression in the melting point of silver.

### Superconducting Magnetic Bearing

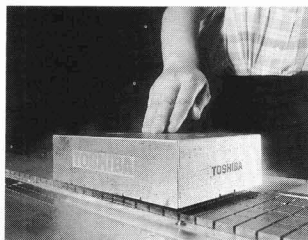
MPMG Group of The Superconductivity Research Lab., ISTEK, headed by Dr. M. Murakami, has jointly with Nippon Seiko K.K., developed a superconducting magnetic bearing using Y system superconductor prepared by MPMG process and permanent magnet.

The magnetic bearing was able to support 2.4kg heavy shaft which rotate at 30,000rpm. Conventionally superconducting magnetic bearing had been proposed by many and they were all applied repulsing force between superconductor and permanent magnet. Newly developed bearing applied attraction force so that the bearing realized stable and strong force.

This experiment demonstration possibility to manufacture large superconducting magnetic bearing, that precision processing of superconductor was possible, availability of superconducting magnetic bearing at limited space for precision machines.

### Development of Magnetic Levitation Transportation System which Employed Oxide Superconductor

Toshiba Corp. developed a demonstration system of a linear magnetic levitation transport system which employed Y system superconductor provided by Nippon Steel Corp. It was composed of vehicle mounting Y system superconductor and cooling liquid nitrogen, and truck composed of permanent magnet. The vehicle mounted 4 superconductor plate of 4.5cm in diameter and 1.5cm thick. The truck was composed of 4 columns of permanent magnets each row of which was composed of 4 magnets. Linear motors were arranged at both sides along with truck. The system can lift up vehicle by 5mm, and transport 3kg heavy load. Lateral 4kg force is not able to push away the vehicle from truck. It travel at speed of 25m/min. Change in current can control travelling speed.



### Special Resin for Repairing Dies

Sanki Bussan has developed gelled, special epoxy resin containing alumina particles, which can be used to repair (by filling or heaping) dies for plastic makers. The resin is a two-liquid mixing type with a hardening agent, having a tensile strength of 220kgf/cm<sup>2</sup> and compressive strength of 1000 kgf/cm<sup>2</sup>, when dried, which are equivalent figures to those of alumina. Furthermore, it is highly rigid and machinable.

The special resin is dried and hardened in 3 to 5 hrs at normal temperature. It is useful for repairing dies for metallic part production and injection molders by filling or heaping the damaged portions. It is also useful for modifying the dies by filling ribs, stopping gates and changing wall thickness.

Sanki Bussan, which developed the special resin, is a maker of die-related products such as mold bases. The resin, having mechanical strength equivalent to that of alumina, adheres well to glass and ceramic materials, and is useful for repairing dies of plastics and other materials.

The company has also been selling the release agent for the resin it has developed. The resin allows the die to produce master models and models to be cut easily

### YAG Laser Machine

Hitachi Construction Machinery Co. Ltd. is expanding sales of YAG laser machines. The company is aiming at a breakthrough of a

construction machine reliance and is actively expanding a new field. The company has already succeeded in the commercialization of a supersonic wave processing machine, and in development of a YAG laser machine. YAG laser machines are used for super-ultra fine processing in electronics -- related fields. YAG laser machining is used in place of electro-discharge machining and etching. Against such a background, the company is selling YAG laser machines abroad. One such machine employs a laser oscillator made by Lazak Co. (Switzerland). This oscillation device, which has almost complete single beam mode and high output, was developed to process new fine ceramic materials and is starting to be used widely also in the field of hard and brittle material including sintered carbide tools. Hitachi will expand business in Japan, and is starting exportation to Korea and other Southeast Asian countries. The company plans to export this machine even to U.S. in the near future.

### High-Grade Colored Stainless Steel Sheets

Nisshin Steel Co., Ltd. has started mass producing high-grade colored stainless steel sheets as a company calls Neues by using sputtering, a high speed vacuum vapor deposition techniques. This is the result of cooperative development efforts with Leibholz, Germany's largest producer of vacuum equipment, and also the first application of the sputtering technique to the production of wide stainless steel sheets.

The sputtering used for manufacturing high-tech products like semiconductors, magnetic discs and carbide tools is used to coat raw stainless steel sheets with ceramic materials such as titanium nitrate and titanium carbonate to produce stainless steel sheets coated in various colors such as silver, black, bronze or blue -- Neues. As coloring technique used for Neues is superior to conventional chemical coloring in color uniformity, tint, and color durability, the company expects Neues to find wide applications in high-grade interior building materials, materials for elevators and escalators, and other interior materials.

### Improved Technique for Production of Superconducting Membrane

A research group at the Toyo University's Faculty of Engineering, led by Prof. H. Imagawa, has developed a technique to simplify the superconducting ceramic production process. It is based on the supersonic spray-pyrolysis concept, in which the powder synthesis apparatus is modified in such a way that production of bismuth-base, high-temperature superconducting oxide and deposition of the oxide on a ceramic substrate are combined, and effected simultaneously by the same unit. The screen printing step, required by the conventional process to deposit the synthesized particles on a ceramic substrate, can be eliminated. The newly developed technique will attract attention as one which

can greatly save time in processing the superconducting ceramic membrane, which is difficult to mass-produce.

Supersonic spray-pyrolysis is generally known as the method for synthesizing bismuth-base, high-temperature oxide particles. This comprises (1) dissolution of the superconducting oxide in nitric acid, (2) atomization of the solution by supersonic waves, and (3) heating the atomized particles to 800 to 900°C, to synthesize the superconducting powder.

Deposition of the synthesized particles on a ceramic substrate to form the film has usually required a time-consuming procedure; the particles are collected from the reactor and then screen-printed on a substrate, spin coating being sometimes required.

The newly developed method is time-saving in that the particles are directly deposited on a ceramic substrate in the reactor in which they are synthesized.

The powder-synthesizing apparatus has a heating unit consisting of an electrical oven and quartz tube, which are combined in a characteristic manner. Specifically, the quartz tube is set in the electrical oven in such a way that part of the tube is projected out of the oven. This arrangement generates a temperature differential between the portion within the oven and that outside, to promote transportation and deposition of the particles.

**Fig. 1.** Supersonic spray-pyrolysis apparatus for powder synthesis

### **CCD Linear Image Sensor with Amplifier**

NEC Corp. has shipped samples of a high sensitivity CCD linear image sensor incorporated with amplifiers, the  $\mu$ PD3732D,  $\mu$ PD3733D, and  $\mu$ PD3734D.

The CCD linear image sensor consists of a photodiode light receiver, a transferring gate transferring electric charges from the photodiode to a register, a CCD register to serially transmit the charges, and an output circuit to output signals. The CCD linear sensor can be used in facsimiles and image scanners.

Amplifiers incorporated with the output circuit render high sensitivities of the CCD linear image sensor and incorporated peripheral circuits in the CCD chip allow compactness of the element including auxiliary circuits. The package is a ceramic 22-pin package with 1mm pin-pitch.

Mass production started in October at a level of 450 thousand pieces monthly. The unit prices for sample are 2,500 yen for the  $\mu$ PD3732D having 1760 elements, 2,800 yen for the  $\mu$ PD3733D having 2,088 elements, and 3,000 yen for the  $\mu$ PD3734D having 3,000 elements.

# Abstracts of Articles on Ceramics from the Selected Journals of the Academic Societies

Journal of The Physical Society  
of Japan  
Vol.60 No.6 June 1991  
p.2040-2050

## Spin Dynamics Studied by $^{89}\text{Y}$ NMR in High $T_c$ Superconductor $\text{YBa}_2\text{Cu}_3\text{O}_{6+x}$

Takashi OHNO, Tatsuo KANASHIRO and Kiyoshi MIZUNO<sup>†</sup>

Department of Physics, Faculty of Engineering, Tokushima University,  
Tokushima 770

<sup>†</sup>Faculty of Integrated Arts and Science, Tokushima University,  
Tokushima 770

$^{89}\text{Y}$  NMR shifts in the high  $T_c$  superconductor  $\text{YBa}_2\text{Cu}_3\text{O}_{6+x}$ , are compared with  $^{17}\text{O}$  NMR new data published by Yoshinari *et al.* and the orbital shift  $^{89}K_{orb}$  is estimated to be 155 ppm. The nuclear spin lattice relaxation rate  $^{89}(1/T_1T)$  for  $^{89}\text{Y}$  is found to be proportional to  $^{17}(1/T_1T)$  for  $^{17}\text{O}$  at 2, 3 plane sites, which supports the single spin fluid model. The relation  $T_1TK_S = \text{const.}$  is realized for  $^{89}\text{Y}$  nuclei in the oxygen depleted compounds  $\text{YBa}_2\text{Cu}_3\text{O}_{6+x}$ . It is found that the relation  $T_1TK_S = \text{const.}$  means that the energy width of dynamical spin susceptibility  $\chi''(q, \omega)$  with the wave vector  $q \rightarrow 0$ ,  $h\nu_0$ , is independent of temperature although the uniform susceptibility  $\chi_0$  strongly depends on temperature. It is also shown that the weight of the low  $q$  part of the spin excitation spectrum decreases with decreasing the hole concentration.

[ high  $T_c$  superconductor,  $\text{YBa}_2\text{Cu}_3\text{O}_{6+x}$ , NMR, Knight shift, spin-lattice relaxation, spin dynamics ]

Zairyo  
Vol.40 No.453 June 1991  
p.689-694

## Fractography and Fracture Analysis on Ceramics/Metal Joint

Hideo KOBAYASHI\*, Yoshio ARAI\*\* and Nobuo NAGASHIMA\*\*\*

Four point bending tests for  $\text{Si}_3\text{N}_4$ /steel joints were conducted and their fracture surfaces were examined by advanced fractographic method. Based on these results, the fracture mechanism was discussed by the fracture mechanics approach.

The crack initiates at the ceramics/adhesive interface. A part of crack front is arrested at the microcrack in the ceramics side of the interface. Another part of the crack front grows along the interface. Then, the stress intensity factor,  $K$ , at the arrested crack front increases as the profile of the whole crack front becomes like a Chevron notch. The unstable fracture occurs when  $K$  at the arrested crack front reaches  $K_{Ic}$  for ceramics.

**Key words** : Ceramics, Ceramics/metal joint, Fracture mechanics, Fractography, Interface strength

Japanese Journal of Applied  
Physics  
Vol.30 No.6 June 1991  
p.1198-1203

## Preparation of Superconducting Bi-Pb-Sr-Ca-Cu-O Compounds by Oxalate Coprecipitation

Dian-Hau CHEN, Cheng-Yie SHEI<sup>1</sup>, Shyang-Roeng SHEEN  
and Chau-Ting CHANG

Department of Chemistry, National Tsing Hua University,  
Hsinchu and Institute of Atomic and Molecular Science,  
Academia Sinica, Taipei, P.O. Box 23-166, Taiwan, R.O.C.

<sup>1</sup>Material Research Laboratories, Industrial Technology Research Institute, Hsinchu

$\text{Bi}_{1.4}\text{Pb}_{0.4}\text{Sr}_2\text{Ca}_2\text{Cu}_3\text{O}_y$  has been prepared from an ethylene glycol medium that contains starting metal nitrates via homogeneous coprecipitation using triethylammoniumoxalate and oxalic acid. The theoretical estimate on the conditions of oxalate coprecipitation and preliminary characterization of the properties of the  $\text{Bi}_{1.4}\text{Pb}_{0.4}\text{Sr}_2\text{Ca}_2\text{Cu}_3\text{O}_y$  obtained after the high-temperature treatment are reported. The preparation of this five-component system of Bi, Pb, Sr, Ca and Cu using triethylammoniumoxalate and oxalic acid has worked successfully in a large-quantity preparation of up to 200 g per batch.

**KEYWORDS** : (Bi, Pb) $_2\text{Sr}_2\text{Ca}_2\text{Cu}_3\text{O}_y$ , high-temperature superconductor, triethylamine, oxalate coprecipitation

Japanese Journal of Applied  
Physics  
Vol.30 No.6 June 1991  
p.1216-1217

### Preparation of $\text{YBa}_2\text{Cu}_3\text{O}_y$ Superconducting Thin Films by Radio-Frequency Plasma Flash Evaporation

Wataru FUKAGAWA\*, Kazunori KOMORI, Masao FUKUTOMI, Yoshiaki TANAKA,  
Toshihisa ASANO, Hiroshi MAEDA and Naokichi HOSOKAWA<sup>1</sup>  
National Research Institute for Metals, Tsukuba Laboratories, Tsukuba-shi, Ibaraki 305  
<sup>1</sup>ANELVA CORPORATION, Fuchu-shi, Tokyo 183

An attempt has been made to deposit superconducting thin films using low-pressure plasma flash evaporation. The rf plasmas used were sustained at 20-30 Torr by the 13.56 MHz rf generator operated at 10 kW. A dense and lustrous film was obtained at the deposition rate of about 10 Å/s. The best film on (100)MgO showed a sharp resistive transition with  $T_c$  ( $p=0$ ) as high as 91 K and the  $J_c$  of  $1.3 \times 10^6$  A/cm<sup>2</sup> at 77 K and zero field.

**KEYWORDS:**  $\text{YBa}_2\text{Cu}_3\text{O}_y$ , superconducting thin film, high-temperature plasma, plasma flash evaporation, atomic oxygen

Japanese Journal of Applied  
Physics  
Vol.30 No.6 June 1991  
p.1235-1238

### Reaction-Bonded Boron Nitride-Aluminum Nitride Ceramic Composites

Takao KANAI, Kei TANEMOTO and Hiroshi KUBO

R&D Laboratories-I, Nippon Steel Corporation, 1618 Ida, Nakahara-Ku, Kawasaki 211

Hexagonal boron nitride-aluminum nitride (h-BN-AlN, 75-25 wt%) ceramic composites are synthesized by reaction bonding. Metallic component-free, relatively dense composites are obtained by using h-BN and Al as starting materials and by optimizing sintering conditions. In comparison with reaction-bonded BN, higher bending strength, 98 MPa, and higher thermal conductivity, 66 W/(m·K), are attained for a  $\text{Y}_2\text{O}_3$ -added BN-AlN composite. A low thermal expansion coefficient of  $2.6 \times 10^{-6}/\text{K}$  is also achieved.

**KEYWORDS:** hexagonal boron nitride, aluminum nitride, ceramic composite, reaction bonding, bending strength, thermal conductivity

Japanese Journal of Applied  
Physics  
Vol.30 No.6A June 1991  
p.L991-L992

### Fabrication of Thick $\text{Bi}_{1.4}\text{Pb}_{0.6}\text{Sr}_2\text{Ca}_2\text{Cu}_3\text{O}_x$ Superconducting Tapes by an Extrusion Method Using Paraffin Wax

Suguru SUZUKI, Hiroki KATO, Kenji IWASHITA,  
Minoru TAKAHASHI and Yasuo HIKICHI

Ceramic Engineering Research Laboratory,  
Nagoya Institute of Technology, 10-6, Asahigaoka, Tajimi-shi 507

Thick  $\text{Bi}_{1.4}\text{Pb}_{0.6}\text{Sr}_2\text{Ca}_2\text{Cu}_3\text{O}_x$  superconducting tapes, which can flow practically high critical currents, are obtained continuously by the following process: (1) calcined  $\text{Bi}_{1.4}\text{Pb}_{0.6}\text{Sr}_2\text{Ca}_2\text{Cu}_3\text{O}_x$  particles, mixed with paraffin wax, are extruded through a nozzle to align platelike particles unidirectionally; (2) the paraffin wax, used as a matrix for workability, alone is burned out, taking care not to destroy the extruded configuration; (3) the burned out tapes are pressed to realize the denser configuration; and then (4) annealed at 850°C for 100 h in air.

**KEYWORDS:** superconductor,  $\text{Bi}_{1.4}\text{Pb}_{0.6}\text{Sr}_2\text{Ca}_2\text{Cu}_3\text{O}_x$ , critical current density, extrusion

Japanese Journal of Applied  
Physics  
Vol.30 No.6A June 1991  
p.L1000-L1002

### Effects of Annealing Conditions and Substrate Materials on the Superconducting Properties of $\text{Ba}_2\text{YCu}_3\text{O}_{7-y}$ Films Prepared by the Dipping-Pyrolysis Process at 750°C

Takaaki MANABE, Wakichi KONDO, Susumu MIZUTA  
and Toshiya KUMAGAI

National Chemical Laboratory for Industry, Tsukuba, Ibaraki 305

Superconducting  $\text{Ba}_2\text{YCu}_3\text{O}_{7-y}$  (BYCO) films were prepared on various substrates by the dipping-pyrolysis process. The effects of annealing parameters, environment and time were also investigated. The 2- $\mu\text{m}$ -thick films of  $\text{BaCO}_3$ - $\text{Y}_2\text{O}_3$ -CuO mixture were heat-treated at 750°C under a low-oxygen partial pressure ( $p(\text{O}_2)=2 \times 10^{-4}$  atm) followed by annealing under higher- $p(\text{O}_2)$  atmospheres. The resulting films showed high superconducting transition temperatures; values of  $T_{c, \text{onset}}(s)$  were 89 K on  $\text{SrTiO}_3(100)$ , 86 K on  $\text{LaAlO}_3(100)$ , 86 K on yttria-stabilized zirconia (YSZ), 83 K on MgO(100), and 76 K on sapphire.

**KEYWORDS:**  $\text{Ba}_2\text{YCu}_3\text{O}_{7-y}$  superconductor, film, dipping-pyrolysis process, metal acetylacetonates, oxygen partial pressure, low temperature, annealing, substrates,  $\text{SrTiO}_3$ , YSZ

Japanese Journal of Applied  
Physics  
Vol.30 No.6A June 1991  
p.L1003-L1005

### Low-Temperature Deposition of Y-Ba-Cu-O Superconducting Films by Thermal Chemical Vapor Deposition

Hisanori YAMANE, Masaharu HASEI<sup>1</sup>, Hideyuki KUROSAWA<sup>1</sup>  
and Toshio HIRAI

*Institute for Materials Research, Tohoku University, 2-1-1 Katahira, Aoba-ku, Sendai 980*  
<sup>1</sup>*Riken Co., 810 Kumagaya, Kumagaya 360*

Y-Ba-Cu-O superconducting films having a zero-resistance temperature of 84–85 K were prepared at 650°C on SrTiO<sub>3</sub>(100) single-crystal substrates without postannealing by thermal chemical vapor deposition using  $\beta$ -diketone metal chelates as sources and O<sub>2</sub> with low partial pressure as a reactant gas. The films mainly consisted of YBa<sub>2</sub>Cu<sub>3</sub>O<sub>x</sub> with *a*-axis and *c*-axis orientations normal to the film planes.

**KEYWORDS:** chemical vapor deposition, Y-Ba-Cu-O superconducting film, low-temperature growth,  $\beta$ -diketone metal chelates, O<sub>2</sub>, superconducting transition temperature, film surface structure

Japanese Journal of Applied  
Physics  
Vol.30 No.6B June 1991  
p.L1096-L1098

### Biaxial Alignment of High-T<sub>c</sub> Superconductor Polycrystals (III): Demonstration in a Bi-2212(Yb) Thick Film

Bao-Shan ZHANG, Feng CHEN, Rafael HIDALGO,  
Sheng-Qi WANG, Xin-Yu ZHANG, Jian-Zhong ZHANG,  
Robert S. MARKIEWICZ, Bill C. GIESSEN and Yuan-Zang LU<sup>1</sup>

*Departments of Chemistry and Physics and Barnett Institute,  
Northeastern University, Boston, MA 02115, USA*  
<sup>1</sup>*Division of Applied Physics, Harvard University, Cambridge, MA 02138, USA*

To produce polycrystalline superconductor ceramics with potentially higher critical currents by eliminating grain boundary weak links caused by grain orientation misfit, we use a method combining grain shape alignment and magnetic field alignment by orthogonal alignment forces. Continuing this work, we report here X-ray diffraction data demonstrating the first preparation of an ~80  $\mu$ m thick Bi<sub>2</sub>Sr<sub>2</sub>Ca<sub>0.7</sub>Yb<sub>0.3</sub>Cu<sub>2</sub>O<sub>x</sub> film having substantial biaxial grain alignment; a very high degree of *c*-axis alignment is combined with >30% preferential <100> axis alignment within the *a*-*b* plane (relative to a random <100> axis distribution in that plane). While films with this composition are not good superconductors, they demonstrate the feasibility of the method.

**KEYWORDS:** Bi cuprate superconductors, Bi<sub>2</sub>Sr<sub>2</sub>Ca<sub>x</sub>Cu<sub>2</sub>O<sub>x</sub>(Yb), rare earth magnetic moment, magnetic field alignment, plate shape alignment, double alignment, X-ray diffraction study, grain boundary weak links, elimination of weak links

Japanese Journal of Applied  
Physics  
Vol.30 No.6B June 1991  
p.L1106-L1109

### Superconductivity in Hydrogen-Doped Nd<sub>1.85</sub>Ce<sub>0.15</sub>CuO<sub>4</sub>

Kenkichiro KOBAYASHI, Yoshiharu GOTO, Shigenori MATSUSHIMA  
and Genji OKADA

*Faculty of Engineering, Ehime University, Matsuyama 790*

Hydrogenation of Nd<sub>1.85</sub>Ce<sub>0.15</sub>CuO<sub>4</sub> has been carried out at a low temperature of 110°C in 1 atm H<sub>2</sub>. The contents of hydrogen and oxygen of H-doped samples are estimated by pulse H-NMR measurements and thermogravimetric analysis. The T<sub>c</sub> values of H-doped samples are independent of the hydrogen content, whereas the volume fraction of superconductivity is significantly decreased with the increase in hydrogen content. These results are explained by the local disappearance of superconductivity in the neighborhood of a doped hydrogen atom.

**KEYWORDS:** superconductor, hydrogen doping, Nd<sub>1.85</sub>Ce<sub>0.15</sub>CuO<sub>4</sub>

Japanese Journal of Applied  
Physics  
Vol.30 No.6B June 1991  
p.L1114-L1117

### *In Situ* Preparation of Superconducting Bi<sub>2</sub>Sr<sub>2</sub>Ca<sub>n-1</sub>Cu<sub>n</sub>O<sub>y</sub> (*n*=1~5) Thin Films by Molecular Beam Epitaxy Technique

Ichiro TSUKADA and Kunimitsu UCHINOKURA

*Department of Applied Physics, The University of Tokyo,  
7-3-1 Hongo, Bunkyo-ku, Tokyo 113*

Superconducting Bi<sub>2</sub>Sr<sub>2</sub>Ca<sub>n-1</sub>Cu<sub>n</sub>O<sub>y</sub> (*n*=1~5) thin films have been prepared *in situ* by molecular beam epitaxy with highly condensed ozone as oxidizing gas. All films including thermally metastable phases of *n*=4 and 5 were obtained by sequential shutter control, and even the *n*=1 phase film showed superconductivity. The surface of the *n*=1 phase film was observed by reflection high-energy electron diffraction, and the modulated structure was clearly observed.

**KEYWORDS:** superconductivity, Bi<sub>2</sub>Sr<sub>2</sub>Ca<sub>n-1</sub>Cu<sub>n</sub>O<sub>y</sub>, ozone, metastable phase, molecular beam epitaxy, incommensurate modulated structure

Journal of The Physical Society  
of Japan  
Vol.60 No.5 May 1991  
p.1452-1455

**Unconventional Superconductivity and Magnetism  
in a Heavy Fermion Material CeCu<sub>2</sub>Si<sub>2</sub>**

Masa-aki OZAKI\* and Kazushige MACHIDA†

*Department of Physics, Kyoto University, Kyoto 606*

*†Department of Physics, Okayama University, Okayama 700*

By enumerating group-theoretically the antiferromagnetic (AF) states allowed under the known crystalline symmetry in a representative heavy Fermion superconductor (SC), CeCu<sub>2</sub>Si<sub>2</sub>, the conditions are examined under which a double transition of either SC ( $T_C$ ) or AF ( $T_N$ ) states occurs. It is predicted that for almost all simple AF states a splitting of the transition temperature  $T_C$  or  $T_N$  can be induced by a non-trivial coupling of the two order parameters, provided that the existing SC state belongs to a degenerate  $E_g$  representation.

[ CeCu<sub>2</sub>Si<sub>2</sub>, heavy Fermion superconductor, unconventional pairing state, antiferromagnetism, double transition ]

\* Present address: Niihama National College of  
Technology, Niihama 792.

## Bibliographic Information

1. Title	Journal of Ceramic Society of Japan, International Edition	ISSN : 0912-9200
2. Frequency	Monthly	1 volume per year (No.1 Jan. - No.12 Dec.)
3. Volume No.	100	
4. Cover data of (Vol. 95, No1)	January 1987	Vol.95 No.1 is the first Issue of English version
5. Index of contents	Given annually	bound in
6. Size	21cm×29.7cm	1700 pages per annum
7. Subscription rates (Air speed)	¥200,000	(12 issues)

## ORDER FORM

To: Circulation Div., the Journal of Ceramic Society of Japan, International Edition  
c/o Fuji Technology Press Ltd.  
Daini Bunsei Bldg., 1-11-7 Toranomon  
Minato-ku, Tokyo 105, Japan

Date: \_\_\_\_\_

Please enter my subscription to the **Journal of Ceramic Society of Japan, International Edition**

(for \_\_\_\_\_ copy/ies)

Name: \_\_\_\_\_

Position: \_\_\_\_\_

Address: \_\_\_\_\_

Signature: \_\_\_\_\_

Payment enclosed  
(Payment by credit card is preferred)

Bill me  
Air speed ¥200,000

Attention: Please indicate our ref. No.(AUTO, TEC, TECJ, CER, ROB, ...) when you make the remittance.  
All subscriptions can be paid in advance through any of the following methods.

1) Charge my:

AmEx  Visa  MC

Card No. .... Exp. Date .....

Mr/Mrs./Ms. ....

Address ..... City .....

Zip code ..... Country .....

2) Transfer to Fuji Technology Press Ltd      A/C No.10667 Fuji Bank Toranomon Branch, Minato-ku Tokyo

3) Bank Draft

4) Transfer to Fuji Gijyutsu Shuppan K.K.(Fuji Technology Press Ltd.) A/C No. Tokyo 7-145130, Postal Saving

## Attention!!

**You are now able to make remittance by credit card!**  
**You can enter subscriptions with only your name, card number and its expiry date. No bank charge nor preparation of Japanese yen bank draft is necessary.**

---

# Journal of Robotics and Mechatronics

Vol.3 No.2 Apr.1991

---

## Contents

---

### Special Issue on Bioelectronics

- Editorial for Special Issue on Bioelectronics . . . . . 73  
Hideto Ide

#### Papers:

- Measurement of Microscopic Displacement and Vibration of Tympanic membranes by Means of Fiber Optics . . . . . 74  
Eiji Toba, Kenchiu Riku, Kazuya Ito and Kiichiro Taguchi
- Nerve Response Depending on Temperature Changes in Carp 79  
Hideto Ide and Masao Ohtsuka
- Magnetic Stimulation of Spinal Roots . . . . . 84  
Shoogo Ueno and Osamu Hiwaki
- Proving the Carry-over Effect of Slow-Wave Sleep by Mathematical Models . . . . . 88  
Toshinori Kobayashi, Yoichi Tsuji, Yoshinobu Iguchi
- Comparison of Alpha Wave Frequency in Listening to Two Kinds of Music . . . . . 93  
Yoichi Tsuji, Kazuyuki Nagasawa, and Misao Itoi

#### Technical Papers:

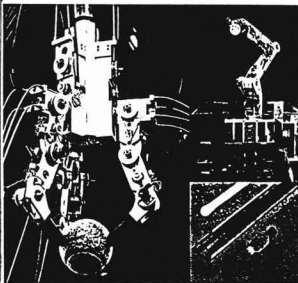
- Analysis of Temperature Distribution in the Human Body by Electromagnetic Heating . . . . . 96  
Yoshiyuki Kageyama, Hideto Ide and Masao Saito
- An Analysis of Relation between Blinking Patterns and Arousal Level . . . . . 101  
Ryosuke Hosaka
- Fundamental Study for Developing Posture-Changes in Beds to Prevent Bedsores . . . . . 105  
M. Nakane, A. Takahashi and S. Saito
- Equivalent Circuit of Nerve Axon by Duality Theory and its Analysis . . . . . 112  
Shuichi Yokoyama and Toshio Kakinuma
- Processing of Three-Dimensional Image Information and Its Application to Industry . . . . . 116  
Kazuhiro Homma
- Sensor Actuator for Automation of Carrying Line . . . . . 121  
Akinori Nakamura
- Symbol Encoding Method of Time Series Data and Markov Model . . . . . 124  
Takafumi Katayama, Eiji Suzuki and Masao Saito

#### Letters:

- Scented Envelopment and ERP Basis Waves . . . . . 128  
Yasuhiko Saito, Takuji Yamamoto, S Kanamura
- Magnetoencephalography (3) . . . . . 131  
Masaru Yarita

Journal of  
Robotics and Mechatronics  
Vol.3 No.2 Apr.1991

Special Issue on Computer Architecture for Robotics



## Bibliographic Information

1. Title	Journal of Robotics and Mechatronics	ISSN : 0915-3934
2. Frequency	Bimonthly	1 volume per year (No.1 Feb. - No.6 Dec.)
3. Volume No.	4	
4. Cover data of (Vol. 1, No1)	June 1989	
5. Index of contents	Given annually	bound in
6. Size	21cm×30cm	700 pages per annum
7. Subscription rates (Air speed)	¥72,000	(6 issues)

### ORDER FORM

To: Circulation Div., the Journal of  
Robotics and Mechatronics  
c/o Fuji Technology Press Ltd.  
Daini Bunsei Bldg., 1-11-7 Toranomom  
Minato-ku, Tokyo 105, Japan

Date: \_\_\_\_\_

Please enter my annual subscription to the **Journal of Robotics and Mechatronics**  
(for \_\_\_\_\_ copy/ies)

Name: \_\_\_\_\_  
Position: \_\_\_\_\_  
Address: \_\_\_\_\_  
Signature: \_\_\_\_\_

Payment enclosed  
(Payment by credit card is preferred)

Bill me  
Airmail ¥72,000

Attention: Please indicate our ref. No.(TEC, TECJ, CER, RB, ...) when you make the remittance.  
All subscriptions can be paid in advance through any of the following methods.

1) Charge my:

AmEx  Visa  MC

Card No. . . . . Exp. Date . . . . .

Mr./Mrs./Ms. . . . .

Address . . . . . City . . . . .

Zip code . . . . . Country . . . . .

2) Transfer to Fuji Technology Press Ltd      A/C No.10667 Fuji Bank Toranomom Branch, Minato-ku Tokyo

3) Bank Draft

4) Transfer to Fuji Gijyutsu Shuppan K.K.(Fuji Technology Press Ltd.) A/C No. Tokyo 7-145130, Postal Saving

## Attention!!

**You are now able to make remittance by credit card!**  
**You can enter subscriptions with only your name, card number and its  
expiry date. No bank charge nor preparation of Japanese yen bank  
draft is necessary.**

# What is the English Monthly Journal TECHNO JAPAN?

It is a professional international periodical designed to cater to people in a wide variety of key industrial and government positions. Its carefully selected contents, including complete reports, for example, on the current status and new developments in Japanese industry and technology, are tailored to meet the information needs of specialists all over the world. Each news article includes an expert's commentary based on in-depth data analysis and also incorporates sufficient data to enable readers to make their own independent judgements on various issues and topics. Techno Japan is a monthly journal whose reports contain information indispensable for those overseas specialists who keep track of current conditions and must project future Japanese and international economic and industrial trends. It is the most authoritative source of information about the most recent technological advances in virtually all fields of industry.



<p><b>TECHNO JOURNAL</b> <b>Liquid Crystal Polymer Blends (III)</b></p>	<p><b>Table 1 Properties of 100% polyimide (continued)</b></p> <table border="1"> <tr><th>Property</th><th>Value</th></tr> <tr><td>...</td><td>...</td></tr> </table>	Property	Value	...	...	<p><b>Table 2 Properties of 90% polyimide (continued)</b></p> <table border="1"> <tr><th>Property</th><th>Value</th></tr> <tr><td>...</td><td>...</td></tr> </table>	Property	Value	...	...				
Property	Value													
...	...													
Property	Value													
...	...													
<p><b>Table 3 Properties of 80% polyimide (continued)</b></p> <table border="1"> <tr><th>Property</th><th>Value</th></tr> <tr><td>...</td><td>...</td></tr> </table>	Property	Value	...	...	<p><b>Table 4 Properties of 70% polyimide (continued)</b></p> <table border="1"> <tr><th>Property</th><th>Value</th></tr> <tr><td>...</td><td>...</td></tr> </table>	Property	Value	...	...	<p><b>Table 5 Properties of 60% polyimide (continued)</b></p> <table border="1"> <tr><th>Property</th><th>Value</th></tr> <tr><td>...</td><td>...</td></tr> </table>	Property	Value	...	...
Property	Value													
...	...													
Property	Value													
...	...													
Property	Value													
...	...													

## Contents of TECHNO JAPAN

### Industrial & Technological News Articles

Every issue of Techno Japan contains more than 300 pieces of information.

News articles are classified as follows:

- Basic Industries:** Energy, Steels & Metals, Ceramics & Materials Science, Superconductivity
- Machinery Industries:** Miscellaneous Machines, Precision Engineering & Fine Finishing, Factory Automation, Transportation & Materials Handling
- Electronics Industries:** Electronic Devices, Telecommunications, Information Processing, Home Automation & Broadcasting, Electronics Instruments, Medical Engineering, Electronic Machine Manufacturing & Assembly
- Chemical Industries:** Chemicals, Polymers, Biotechnology

### Disaster Prevention, Agribusiness

### Systems Industries:

### Feature Articles

Long, highly informative feature articles of crucial interest to overseas governments and industries appear each month. As many as 55 pages in one issue may be devoted to such important and fascinating articles which enlarge the depth and breadth of readers' knowledge about subjects of current interest. Such high news value feature articles are carried individually or in a series.

### Economic Report and Statistics

Techno Japan's economic report and statistics is officially provided by the Economic Planning Agency. These reports help to promote mutual understanding among various nations.

### Research Institutes in Japan

# TECHNO JAPAN

**FUJI TECHNOLOGY PRESS LTD.**

Daini Bunsei Bldg., 11-7, Toranomon 1-chome, Minato-ku, Tokyo 105, Japan

